University of Southampton
Faculty of Engineering, Science and Mathematics
School of Civil Engineering and the Environment

The role of frictional heating in the development of catastrophic landslides

By

Francesco Cecinato

Thesis for the degree of Doctor of Philosophy

February 2009

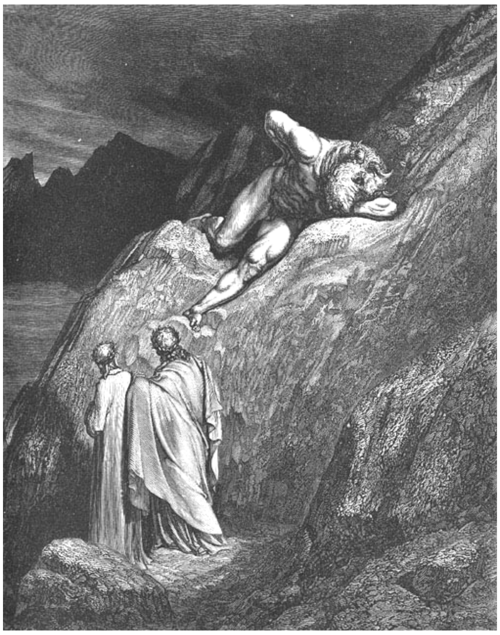

Era lo loco ov'a scender la riva
venimmo, alpestro e, per quel che v'er'anco,
tal, ch'ogne vista ne sarebbe schiva.

Qual e` quella ruina che nel fianco
di qua da Trento l'Adice percosse,
o per tremoto o per sostegno manco,

che da cima del monte, onde si mosse,
al piano è sì la roccia discoscesa,
ch'alcuna via darebbe a chi sù fosse;

[*The place where to descend the bank we came*
Was alpine, and from what was there, moreover
Of such a kind that every eye would shun it

Such as that ruin is which in the flank
Smote, on this side of Trent, the Adige
Either by earthquake or by failing stay

For from the mountain's top, from which it moved,
Unto the plain the cliff is shattered so,
Some path 'twould give to him who was above;]

(Dante Alighieri, *The Divine Comedy*, Hell, canto XII)

UNIVERSITY OF SOUTHAMPTON

ABSTRACT

FACULTY OF ENGINEERING, SCIENCE & MATHEMATICS
SCHOOL OF CIVIL ENGINEERING & THE ENVIRONMENT

Doctor of Philosophy

THE ROLE OF FRICTIONAL HEATING IN THE DEVELOPMENT OF CATASTROPHIC LANDSLIDES

by Francesco Cecinato

In this work, a new thermo-mechanical model is developed by improving on an existing one, applicable to large deep seated landslides and rockslides consisting of a coherent mass sliding on a thin clayey layer. The considered time window is that of catastrophic acceleration, starting at incipient failure and ending a few seconds later, when the acquired displacement and velocity are such that the sliding material begins to break up into pieces. The model accounts for temperature rise in the slip zone due to the heat produced by friction, leading to thermoplastic collapse of the soil skeleton and subsequent increase of pore water pressure. This in turn drastically decreases the resistance to motion and allows the overlying mass to move downslope ever more freely.

The proposed model is implemented numerically and validated by back-analysing the two well-documented catastrophic landslide case histories of Vajont and Jiufengershan. The model is then employed to carry out a parametric study to systematically investigate the development of catastrophic failure in uniform slopes. It was found that the most influential parameters in promoting catastrophic collapse are (1) the static friction-softening rate a_1, (2) the slope inclination β, (3) the soil permeability k_w, (4) the dynamic residual friction angle ϕ_{rd} and (5) the overburden thickness H. The most dangerous situation is when a_1, β and H are very large and k_w and ϕ_{rd} are very low. Of the above, the 'thermo-mechanical parameters' k_w and H deserve more attention as they have been introduced by the thermo-mechanical model and are not normally considered in standard stability analyses of uniform slopes. A second parametric study was performed to demonstrate that thermo-mechanical parameters alone can make a difference between a relatively non-catastrophic event and a catastrophic one. Hence, further insight into the design of landslide risk mitigation measures can be gained if, in addition to the standard site investigations, the permeability of the soil is measured and the depth of an existing or expected failure surface is measured or estimated respectively.

Contents

List of figures

List of tables

Declaration of authorship

I, FRANCESCO CECINATO, declare that the thesis entitled THE ROLE OF FRICTIONAL HEATING IN THE DEVELOPMENT OF CATASTROPHIC LANDSLIDES and the work presented in the thesis are both my own, and have been generated by me as the result of my own original research. I confirm that:

- this work was done wholly or mainly while in candidature for a research degree at this University;
- where any part of this thesis has previously been submitted for a degree or any other qualification at this University or any other institution, this has been clearly stated;
- where I have consulted the published work of others, this is always clearly attributed;
- where I have quoted from the work of others, the source is always given. With the exception of such quotations, this thesis is entirely my own work;
- I have acknowledged all main sources of help;
- where the thesis is based on work done by myself jointly with others, I have made clear exactly what was done by others and what I have contributed myself;
- parts of this work have been published as:

F. Cecinato, A. Zervos, E. Veveakis, I. Vardoulakis (2008). *Numerical modelling of the thermo-mechanical behaviour of soils in catastrophic landslides*. Proceedings of the 10th International Symposium on Landslides and Engineered Slopes, Chen et al. (Ed), Xi'An, China, 615-621.

F. Cecinato, A. Zervos (2008). *Thermo-mechanical modelling of catastrophic landslides*. Proceedings of the 16th Conference of the Association of Computational Mechanics in Engineering, M. Rouainia (Ed), Newcastle, UK, 144-147.

F. Cecinato, A. Zervos (2008). *Thermo-mechanical modelling for velocity prediction in catastrophic landslides*. Geophysical Research Abstracts, Vol. 10, EGU2008-A-02745. EGU General Assembly, Vienna, 13-18 April 2008.

Signed: …………………………………………………………………..

Date:…………………………………………………………………….

Acknowledgements

I would like to thank the following people or organisations who have, in one form or another, provided precious help, support and advice over the last three and a half years.

Dr. Antonis Zervos for his constant, invaluable supervision and the motivation and encouragement that made it overall possible to carry out this research.

Manolis Veveakis (NTU of Athens) for his help in tackling the constitutive modelling part of this work and for his comradeship.

Prof. Ioannis Vardoulakis for his advice, along with all the fellows at the geomaterials lab for having both scientifically and socially welcomed me during my 4-month visit at the NTU of Athens.

Prof. Chris Clayton and Prof. William Powrie for their comments and advice on my 9-month report and 18-month report respectively.

Prof. Guido Gottardi for having always encouraged me in pursuing research in soil mechanics since my undergrad times at the University of Bologna.

The Engineering and Physical Sciences Research Council that provided the studentship for carrying out this research.

Alessia, for her irreplaceable all-round support, the countless beautiful and the few troublesome, yet worthwhile, moments; and for having caught that plane.

My housemates Ale, Davide, Iain and Nino for their friendship and spirit of participation that made me experience a sense of common life like never before.

All the friends that I have luckily encountered during my English years, who have made my PhD life fuller, among which: Arturo, to whom I owe an awful lot, Argyro for her support in crucial moments and Filippo who has become a brother to me both in music and in life.

My family, who have always provided me with plenty of unbiased love.

All my ‘older’ Italian friends who have kept an eye on me from the distance, constantly providing sound advice, notably Ceci, Dippo, Lalla and Paolino.

Notation

General Symbols

a_1	rate of static friction softening
a_2	rate of dynamic friction softening
$\overline{a}$	Hueckel's hardening coefficient
c	compressibility
C	specific heat
C_f	thermal constant
$\mathbf{C}^{Te}$	stress-independent thermo-elastic tensor
c_v	consolidation coefficient
d	shearband thickness
D	dissipation
D_i	temperature-dependent thermal diffusivity
$\mathbf{D}^{me}$	elastic tensor
$\mathbf{D}^{te}$	thermo-elastic tensor
e	void ratio
E	Young's modulus
f	yield locus
f_{Td}	thermal deviatoric yield locus
f_{Ti}	thermal isotropic yield locus
F_1,F_2	heat equation (non-constant) coefficients
G	shear modulus
g	plastic potential
$\tilde{g}$	thermal friction sensitivity
H	depth of rupture surface (slide thickness)
$\tilde{H}$	hardening modulus
h_w	height of water table above the slip plane
I_p	polar moment of inertia
J	stress deviator
j	mechanical equivalent of heat

K	bulk modulus
K_T	temperature-dependent bulk modulus
k_m	thermal diffusivity
k_w	soil permeability
$\mathrm{L_A(B^C)}$	standard orthogonal array nomenclature
M	critical state parameter
m	mass
$\hat{M}$	evolution law of critical state parameter
M_J	generalised critical state parameter
n	porosity
N_p	specific volume intercept of iso-NCL line
p'	mean effective stress
q	deviatoric stress
R	radius of failure circle
t	time
u	excess pore pressure
u_H	pore pressure in static conditions
U_{max}	maximum total pore pressure
v	velocity
v_d	landslide velocity
v	specific volume
$\overline{v}$	overall average velocity
$\overline{v}^*$	predicted average velocity
W	block weight
x,y,z	spatial coordinates
x_d	landslide displacement
α, β_s	thermo-elastic expansion coefficients
α_c^{tp}	thermo-plastic contraction coefficient
α_s	seepage angle
β	slope angle
$\tilde{\beta}$	compressibility modulus
γ	rate of thermal softening

$\dot{\gamma}$	shear strain rate
γ_s	unit weight of soil
γ_w	unit weight of water
γ_{ij}	shear strain components
γ_s, γ_w	unit weights of soil and water
Γ	specific volume intercept of critical state line
$\boldsymbol{\delta}_{ij}$	Kronecker delta
$\boldsymbol{\varepsilon}$	strain vector
ε_v^p	volumetric plastic strain
ε_{ij}	strain components
ε_q	deviatoric strain
θ	temperature
θ_L	Lode angle
κ	slope of unloading-reloading line
λ	slope of isotropic normal compression line
λ_m	pore pressure coefficient
$\dot{\lambda}$	plastic multiplier
μ_F	incipient failure friction coefficient
μ_m	mobilised friction coefficient
$\hat{\mu}$	evolution law of friction coefficient
μ'_{rs}	residual static friction coefficient
μ'_{rd}	residual dynamic friction coefficient
μ'_p	initial or peak friction coefficient
v	Poisson's ratio
ρ	density
$\boldsymbol{\sigma}$	stress vector
σ_{ij}	stress components
$\sigma_1, \sigma_2, \sigma_3$	principal stress components
σ'_c	apparent isotropic preconsolidation stress
σ'_n	normal effective stress

σ'_m	isothermal value of apparent preconsolidation stress
τ	pseudo-time for thermo-elasto-plasticity integration
τ_{ij}	shear stress components
ϕ'_{cs}	critical state friction angle
ϕ'_{rs}	residual static friction angle
ϕ'_{rd}	residual dynamic friction angle
ϕ'_{mob}	friction angle at limit equilibrium
ϕ'_p	initial or peak friction angle
ω_0	constant with dimensions of angular velocity

Abbreviations

ATS	absent thermal-friction softening
CS	critical state
CSL	critical state line
FFS	full friction softening
LHS	left hand side
MCC	modified Cam Clay
NC	normally-consolidated
NCL	normal-consolidation line
OC	over-consolidated
OCC	original Cam Clay
OCR	over-consolidation ratio
RHS	right hand side
TFS	thermal-friction softening
URL	unloading-reloading line

Subscripts

0	at initial state
crit	critical
cs	at critical state

d	at the shearband-block interface
f	relative to the pore fluid
int	at intersection
max	maximum
n	relative to the pore volume
q	deviatoric
ref	at reference state
s	relative to the soil
sk	relative to the soil skeleton
v	volumetric
vap	vaporisation
w	relative to the water

Superscripts

d	deviatoric
e	elastic
ep	elasto-plastic
me	mechanical-elastic
p	plastic
te	thermo-elastic
tep	thermo-elasto-plastic
tot	total
tp	thermo-plastic

Chapter 1. Introduction

1.1. Background

The mechanics of the final collapse of large slope failures are still poorly understood, and have constituted a challenge to physicists, engineers and geologists over the last 40 years. The reasons why some observed catastrophic landslides moved so fast and so far cannot always be explained using standard analyses. Recent examples of such slope failures include the disastrous 1963 Vajont slide that occurred in northern Italy and claimed more than 2,000 victims, and the 1999 Jiufengershan slide, triggered by the Chi-Chi earthquake in Taiwan which killed 2,400 people in total.

Much better understanding is needed to facilitate risk assessment for existing slopes and the design of appropriate hazard mitigation measures. This need will keep growing, as the climatic changes and extreme weather conditions of recent years will exacerbate any tendency of existing slopes towards instability and the search for new oil and gas reserves spreads into deeper and more difficult ocean environments.

Frictional heating of the slip zone has long been considered a possible explanation for the unusually high velocities and long run-outs of some large-scale landslides (Habib, 1975, Anderson, 1980, Voight and Faust, 1982). Pore pressure in soils increases with temperature due to thermal expansion, but also because water adsorbed on clay particles is released as free pore water, eventually leading to thermal collapse of the skeleton (Hueckel and Pellegrini, 1991, Modaressi and Laloui, 1997). Under conditions of slow or no drainage, like the ones occurring in the rapidly deforming slip zone of a landslide, thermal collapse leads to pore pressure buildup (Hueckel and Baldi, 1990, Hueckel and Pellegrini, 1991). Furthermore, heating reduces the soil's apparent overconsolidation ratio, shrinks its elastic domain and lowers its peak stress ratio (Hueckel and Baldi, 1990, Laloui and Cekerevac, 2003). Thermoplastic friction-softening (i.e. decrease of the friction angle with temperature) may also take place, depending on the mineralogical composition of the soil (Modaressi and Laloui, 1997, Laloui, 2001). The importance of increased pore pressure and thermoplastic softening at the slip zone of a landslide is that they lead to decreased effective stress and declining soil strength, causing the sliding mass to accelerate and potentially making the difference between a relatively small-scale event and a catastrophic one.

For any particular site, the impact of frictional heating in the development of a landslide will depend on the in-situ conditions (i.e. the geometry of the slope, the thermo-mechanical properties of the soil and the pore pressure regime). Currently there is limited understanding regarding the combinations of these parameters that are critical, hence it is difficult to assess the associated risk and design prevention or mitigation measures for particular areas. However, insight can be gained by means of a systematic parametric study, using an appropriate model.

Such a model was presented by Vardoulakis (2000, 2002a). This was a one-dimensional model for a uniform slope, and was validated by back-analysing the Vajont landslide. However, the specialised constitutive law used for the soil restricts its applicability. In particular:

- It cannot capture the full range of temperature-dependent soil behaviour observed experimentally.
- It cannot be easily generalised to include the behaviour of the soil prior to failure, or to two- or three-dimensional problems. So the existing model cannot form the basis of a general predictive tool, for assessing the risk that specific initiation events pose to existing slopes.

In this work, we will improve the above model by adopting a more general and more realistic constitutive assumption for the soil, applicable to a wider range of soils. As a first approximation, uniform slopes will be considered. The model will take into account:

- Heat generation due to friction, and heat diffusion.
- Pore pressure generation due to heating, and pore pressure dissipation due to flow.
- The temperature dependence of the mechanical behaviour of soil.

The modified landslide model will be employed to simulate the dynamic evolution of landslides occurring in slopes of different geometry, soil properties and in-situ pore pressure regimes, to gain insight into the relative importance of these parameters, and combinations that are potentially critical in promoting catastrophic failure.

1.2. Aims and objectives

The general aims of our research are to:

- Investigate the role of frictional heating in the development of catastrophic landslides, in uniform slopes, for different slope inclinations and soil properties.

- Determine combinations of relevant soil parameters and in-situ conditions which can make a slope prone to catastrophic failure.

The objectives through which the aims will be achieved are:

- A review of published data on large-scale landslides and the thermo-mechanical behaviour of soils, to determine the range of relevant in-situ conditions and soil parameters.
- The development of a landslide model which accounts for thermal pressurisation, and includes a general thermo-elasto-plastic constitutive law for the soil.
- The development and implementation of a numerical discretisation of the above model, followed by a validation stage by back-analysing any sufficiently documented catastrophic landslide case histories.
- A parametric numerical study, using the discretised model, to systematically investigate the development of catastrophic failure in uniform slopes of various soil properties and in-situ conditions.

1.3. Structure of thesis

In Chapter 2 of this work, large-scale landslides occurring on land are analysed. Available classification methods are reviewed, catastrophic sliding cases are identified and available data from published case studies are critically reviewed and collated, with the aim of gathering information on the typical ranges of the slope properties involved. A review of landslides occurring under sea follows, and their similarities and differences with their terrestrial counterparts are analysed. Finally, insight on existing 'non-standard' theories to interpret catastrophic landslides is provided and the mechanisms of frictional heating and thermal pressurisation are discussed, with special attention given to the landslide model adopted in this work.

The third Chapter consists of a critical review of the available thermo-mechanical models for soils, which have been developed mainly in the context of nuclear repository design. The suitability of these models for implementation in our subsequent work is discussed, in order to identify an appropriate constitutive framework where the landslide model equations can be developed.

Chapter 4 deals with the mathematical generalisation of a thermoplastic constitutive model chosen among those mentioned in Chapter 3, so that it can be subsequently incorporated into the landslide model and applied in the future in 2- and 3-D analyses.

The model is then discretised, integrated numerically and validated by simulating some experimentally observed thermo-mechanical loading paths.

In Chapter 5 we describe in detail the mathematical development of a new landslide model, consisting of a set of three equations describing the time evolution of three quantities: the temperature and the excess pore pressure developing within the slip zone, and the velocity of the slide. The modified equations are then discretised numerically and the model is applied for predicting the dynamic evolution of rotational landslides. As an example the Vajont slide is treated, and it is shown that, using relevant data available in the literature, realistic values for the observed final velocity are obtained.

In Chapter 6, the above described model is generalised to the infinite slope geometry, in order to provide a simple enough tool that will allow us to explore the impact of frictional heating and the role of different parameters. A new form of dynamical equation is derived and numerically implemented. The infinite slope model is then validated by back-analysing the catastrophic evolution of the Jiufengershan rockslide case history.

In Chapter 7 a parametric analysis is carried out, with the aim of identifying the most important parameters in making a slope prone to catastrophic failure. This is done by carrying out a number of simulations using the infinite slope model while exploring all significant combinations of the relevant geometrical and geomechanical properties of the slope. The properties are then ranked in order of importance according to their influence in catastrophic sliding, and the significance of this outcome in the landslide prevention practice is discussed.

In Chapter 8 the conclusions are outlined, alongside with suggestions for further work on this subject.

Chapter 2. A review of landslide case studies and modelling

In the first part of this chapter, we will present a literature review of landslide case studies, both occurring on land and under sea, with the aim of gathering field data on catastrophic cases. An overview of all landslide types is provided first, to then focus on the study of those kinds which are more likely to evolve catastrophically. Then the most relevant documented case histories are discussed and categorised (The full list of the examined cases can be found in the Appendix, alongside with the relevant field data and references).

The second part of this chapter deals with a review of the available models in the literature to interpret catastrophic landsliding, with particular attention to those invoking the mechanisms of frictional heating and thermal pressurisation.

2.1. Sub-aerial landslide cases

2.1.1. Classification of sub-aerial slope movements

Sub-aerial (or terrestrial) landslides are widespread throughout the world and constitute a major natural hazard. Hundreds of documented cases can be found in literature, but several different phenomena lie under the general term 'landslide'. Here follows an overview of the main existing types and classification criteria of landslides, in order to be able to discern, among the many available case studies, the most relevant phenomena to our research.

As a first, classic categorization outline, we introduce the one proposed by Hutchinson (1988), which applies to mass movements on natural or man-made slopes and excludes very large-scale gravity tectonic movements and subsidence. This classification, which draws particularly on the work of Varnes (1978), is based principally on morphology.

- *Rebound.*

  When ground is unloaded, either artificially or naturally, the unloaded area responds with upwards movements of its base and inward movements of its sides. These displacements lead to fractures and other fabric changes.

- *Creep.*

Extremely slow movements which are imperceptible except through long-period measurements. The resulting displacements tend to be diffuse rather than concentrated upon distinct slip-surfaces. ‘Superficial creep’ is a predominantly seasonal phenomenon due to ground changes in volume, unlike ‘deep-seated creep’, which occurs at an essentially constant stress below the ultimate strength of the material involved. ‘Progressive’ or ‘pre-failure’ creep is an accelerating form of creep which normally presages overall shear failure.

- *Sagging of mountain slopes*.

  ‘Sagging’ is a general term for deep-seated deformations of mountain slopes which, in their present state of development, do not justify classification as landslides. The features of these phenomena represent either an early stage of landsliding or an expression of multiple toppling.

- *Landslides*.

  Relatively rapid downslope movements of soil and/or rock, taking place in one or more slip surfaces which define the moving mass. An initial failure stage is followed by a run-out.

  ‘Confined failures’ are those exhibiting a rear scarp and a slip surface, but the displacements do not develop sufficiently to produce a continuous failure surface emerging at the toe.

  ‘Rotational slips’ occur principally in slopes incorporating a rather thick deposit of clay or shale, but also in slopes of granular material and jointed rock. These slips can be single, successive or multiple. Failure takes place usually at a moderate speed. ‘Compound slides’ are intermediate in overall proportions and characterised by slip surfaces formed of a combination steep rearward part and a flatter sole. They are normally locked in place as a result of their slip surface geometry, and can move only when the slip mass is transformed into a cinematically admissible mechanism. Compound slides can be released by internal shearing towards the rear of slide mass, which normally takes place as a single event, or they can be progressive.

  ‘Translational slides’ represent a very large family. They involve shear failure on a fairly planar surface, and can be divided into a series of sub-types. ‘Sheet slides’ are very shallow failures affecting slopes of dry, cohesionless material. ‘Slab slides’ involve coherent but unlithified soils, while ‘rock slides’ involve relatively monolithic masses of soil, slipping on approximately planar slip surfaces formed by discontinuities which are frequently occupied by argillaceous fillings.

'Slides of debris' are translational slides affecting debris mantling a slope. The slipping mass has generally low cohesion, they are divided into 'non-periglacial' and 'periglacial' type.

- *Flow-like movements*.

  'Mudslides' are rather slow-moving masses of debris in a softened clayey matrix, sliding on distinct bounding shear surfaces, while 'periglacial mudslides' arise through a process of periglacial solifluction, involving repeated freezing and melting of clayey materials.

  'Flow slides' involve the sudden collapse and rapid run-out of a mass of granular material following some disturbance. The sudden loss of strength gives the failing material a semi-fluid character and allows a flow-slide to develop. They can occur, with different features, in loose materials, lightly cemented silts or weak rocks.

  'Debris flows' are very rapid flows of wet debris, and are normally associated with sudden access of water which mobilises debris mantling the slopes in mountainous areas; they involve rock debris and/or peat.

  'Sturzstroms' are extremely rapid flows of dry debris, and take sometimes origin from the evolution of some large rockslides or rockfalls.

- *Toppling failures*.

  Topplings are common in rock masses with steeply inclined discontinuities, and can be bounded by pre-existing discontinuities or released by tension failure in previously intact material.

- *Falls*.

  Rapid descent of masses of soil or rock of any size from steep slopes.

- *Complex slope movements*.

  Any combination of two or more of the above described slope movements is called a complex movement. It is worth mentioning the case of landslides breaking down into mudslides of flows at the toe. In the case of 'slump-earthflows', for example, the toes of landslides, disrupted by the slide movements, break down to form a mudslide or earthflow under the influence of the weather.

One of the key features to be considered when landslide hazard assessment is concerned is the run-out of the sliding mass. A much simpler classification, based on the manner of progression of movement rather than on the failure mechanism can be more useful on this matter. It was presented by Corominas (1996), based again on a rearrangement of the classification of Varnes (1978), and it comprises four categories:

- *Rockfalls* and *rockfall avalanches*, where at least part of the run-out path shows free fall;
- *Translational slides*, in which the mass is principally displaced by basal shearing and the translated materials maintain their stratigraphic order in the landslide deposit;
- *Earthflows*, *mudflows* and *mudslides*, of lobate shape and mostly composed of clayey material or heavily fractured claystones, shales, schists or flysch; in which the movement involves flowing.
- *Debris flows, debris slides and debris avalanches*, in which cohesionless material flows through a channel, or moves as a debris sheet.

This kind of grouping, in which the categories include one or more mechanisms of motion, has the purpose of providing explanation for the run-out distance of landslides. The author proposed attributes regarding the sliding path and its topographic constraints that can be used to refine this landslide categorization. For example, 'Unobstructed landslides' are movements of any type progressing downslope without obstacles or restrictions, while 'bends' and 'deflections' are obstacles on the path causing a change in former direction of progression of respectively less than 60° and more than 60°. 'Channelling' involves debris confinement into a channel, and the presence of an 'opposite wall obstruction' causes over-thickening or splitting of the sliding mass.

When repeated landsliding phenomena are to be considered, Shuzui (2000) proposed a classification method based on the history of landslide movements and the properties of the slip surface. This classification is restricted to cases of rock or earth slides moving downslope coherently, and is focused on the study of sliding surfaces. Based on field investigations on landslides of different movement history, the author suggests that the amount of displacement of the landslide reflects the properties of the slip surface, ranging from the shortest-reaching 'striation' type to 'brecciated' type, followed by the 'mylonite' type and finally by the farthest-reaching 'clay' type. The author also suggests that the content of smectite within the clayey slip surface increases as the sliding proceeds with larger displacements, while the content of siliceous minerals decreases.

Although extremely simplified and of rather restricted applicability, this schematic categorization (based on field surveys on some Japanese landslides) is interesting for its focusing on the sliding surface. It is summarised in Table 1 (Shuzui, 2000).

Table 1. From Shuzui (2000). Classification method based on the history of landslide movements and the properties of the slip surface.

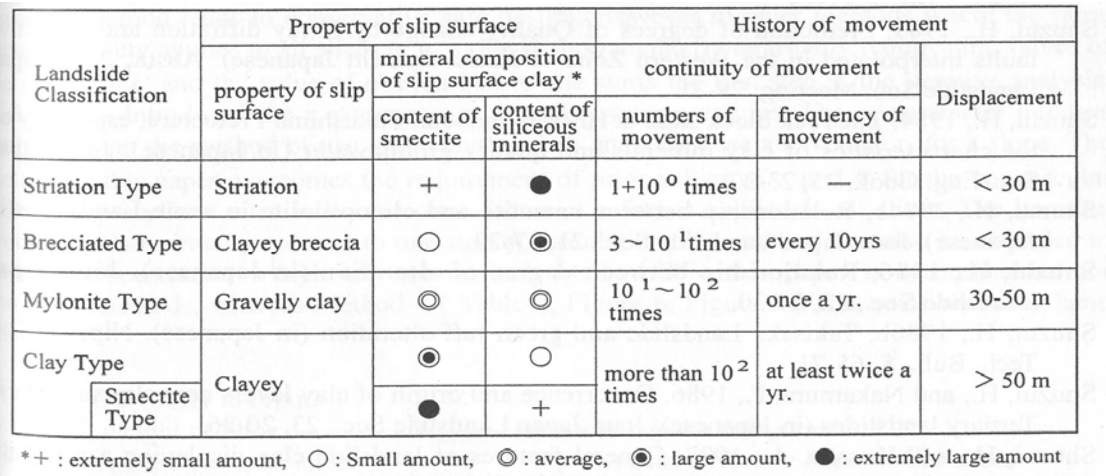

Landslide Classification	Property of slip surface			History of movement		
	property of slip surface	mineral composition of slip surface clay *		continuity of movement		Displacement
		content of smectite	content of siliceous minerals	numbers of movement	frequency of movement	
Striation Type	Striation	+	●	$1+10^{0}$ times	—	< 30 m
Brecciated Type	Clayey breccia	○	◉	$3\sim10^{1}$times	every 10yrs	< 30 m
Mylonite Type	Gravelly clay	◎	◎	$10^{1}\sim10^{2}$ times	once a yr.	30-50 m
Clay Type	Clayey	◉	○	more than 10^{2} times	at least twice a yr.	> 50 m
Smectite Type		●	+			

*+ : extremely small amount, ○ : Small amount, ◎ : average, ◉ : large amount, ● : extremely large amount

The last landslide classification that we are going to review is one focused on categorising large-scale cases only, hence of particular interest to our research. It was proposed by Wen et al. (2004) for the purpose of differentiating rapid giant landslides in terms of their dynamical behaviour. Three landslide types are individuated:

1. Slide, in which the mass moves as a block without disaggregation;
2. Slide-flow, in which the mass moves partially as a block and is partially destroyed whilst travelling, thus exhibiting flow-like motion;
3. Flow, where the mass fully disaggregates into debris and moves as granular flow.

The authors based their classification on the study of 70 recent cases of catastrophic landslides, and claim that the landslide type n. 1 constitutes “the overwhelming percentage of rapid giant landslides in China” (Wen et al., 2004).

2.1.2. From generic ‘slope movements’ to ‘catastrophic landslides’

Landslides that in literature have been referred to as ‘catastrophic’ occur in a wide variety of geotechnical contexts and geological settings, they are triggered by diverse processes and they do not all have comparable impacts on the environment.

Nevertheless, it is possible to outline a series of features that characterise catastrophic slope failures and may cause extensive damage, including loss of human life and property:

- Large masses and volumes involved in sliding
- Long travel distances
- High sliding speed
- Sudden acceleration

Case studies in which one or more of the above attributes are present, but no destruction occurs (e.g. when they take place in deserted areas) are often not referred to as catastrophic phenomena, although they often embody the same sliding mechanisms as destructive cases. Thus, any available field data from such cases is equally important to the study of catastrophic landslides.

Of the reported characteristics, the primary factors on which the dangerousness of a slope failure depends are probably the post-failure velocity and acceleration. Rapid landslides, even those not involving large masses, have the greatest potential to cause loss of life, because of the lack of time for the population to evacuate. A high speed (thus corresponding to a high kinetic energy) will increase the destructive potential of the slide, as well as the likelihood to trigger secondary and possibly more catastrophic events. Sadly famous are the cases when slides occurred in mountainous, almost uninhabited areas but nevertheless killed hundreds of people indirectly, by quickly plunging into a lake and triggering devastating surge waves (Hendron and Patton, 1985, Wieczorek et al., 2003, Yueping, 2008). If occurring underwater, the suddenness of a landslide might trigger a violent tsunami (e.g. see Tinti et al., 2007).

Long travel distance is another dangerous characteristic, and it is very often associated with rapid sliding. Moreover, there is a documented higher tendency for larger volumes to reach further than expected from their energy of mass (Corominas, 1996, De Blasio et al., 2008). On the other hand, a massive volume of soil or rock which is creeping or sagging does not necessarily constitute a major natural hazard: certain deep-seated alpine slides have crept for centuries before coming to a final rest, stopped for example by topographical constraints.

It is now useful to discuss typical ranges of velocity, volume and run-out of landslides, in an attempt to possibly establish threshold values between catastrophic and non-catastrophic cases that may guide us in choosing the most relevant case studies.

Regarding the range of sliding velocities within the definition of 'rapid', there is no unanimous agreement in literature. As a guidance, we can refer to the IUGS (1995) velocity classification, reported in Table 2. While the post-failure sliding velocity, for fast landslides, is normally measured or back-calculated as a unique average value, great attention is given to the changes shown in slow sliding regimes, especially if intermittent sliding (Van Genuchten, 1988) and/or accelerating displacements (Sornette et al., 2004, Chihara et al., 1994) are observed.

Concerning the volume of the sliding mass, it is not possible to decide a critical value enabling us to discern between catastrophic and non-catastrophic landslides, but in line with the experience gained in reviewing several case studies (Section 2.1.4), we propose here to consider 'large' any sliding mass whose volume is $\geq 10^6$ m^3.

At last, regarding the landslide run-out, it seems to us rather arbitrary to establish a general threshold distinguishing between short-reach and long-reach phenomena: the maximum 'safe' sliding distance will depend on the characteristics of the region (e.g. location of inhabited areas). As a general rule, this attribute will depend on the landslide's volume and its vertical drop. A useful index to describe the mobility of landslides is the angle of reach, expressed as the angle of the line connecting the head of the landslide source to the distal margin of the displaced mass (Corominas, 1996). As mentioned above, larger landslides usually show lower angles of reach, and because of this they are considered more mobile. However, due to the heterogeneity of the landslide data available in the literature it will not be possible to calculate the angle of reach for all the case studies reviewed in Section 2.1.4.

Table 2. IUGS (1995) landslide velocity classification.

Description of velocity	Velocity limits
7. Extremely rapid	> 5 m/sec
6. Very rapid	3 m/min to 5 m/sec
5. Rapid	1.8 m/hour to 3 m/min
4. Moderate	13 m/month to 1.8 m/hour
3. Slow	1.6 m/year to 13 m/month
2. Very slow	16 mm/year to 1.6 m/year
1. Extremely slow	≤ 16 mm/year

2.1.3. Two important sub-cases: Deep-seated and flow-like movements

“In spite of their apparent diversity, deep-seated and flow-like movements may be studied jointly. The basic impressions suggest that the two mass movement types occupy end members of the classification spectrum , but there is a reasonable possibility that many deep-seated landslides, now slowly moving, may represent only the initial stage of slope movements that eventually may be transformed into accelerated sliding and finally into large-scale, devastating rock avalanches” (Oyagi et al., 1994). Hence, every case study in which an initial stage of coherent sliding is present, regardless of the possible final evolution into a flow-like phenomenon, will be relevant to our landslide data collection.

According to the literature, not exclusive diagnostic features of deep-seated slope deformations are (Agliardi et al., 2001):

- Morpho-structures (ridges, scarps etc.) similar to those observed, at a smaller scale, landslides occurring in cohesive soils;
- Scale of the phenomenon comparable to the size of the slope;
- Present very low rate of displacement (mm/year);
- Presence of minor landslides inside the deformed mass and ancient collapses of the lower part of the slope.

Most of these slides do not have a macroscopically clear sliding surface, but many of them just do not show it until final collapse. On the other hand, many observed deep-seated slides in the Alps are in fact characterised by a basal sliding surface (Agliardi et al., 2001), which is normally very difficult to reach.

The model that will be developed in the forthcoming chapters aims to interpret the dynamics of sliding phenomena whilst displacing in a coherent manner, which can be schematised by a rigid mass sliding on a basal shear localisation zone. This type of behaviour is best represented by the early sliding stages (i.e. before breaking up into pieces) of earth and rock slides, but our analysis will also be relevant to large landslides whose mass, despite disintegrated, is displaced downslope for long distances whilst preserving its stratigraphic order. For example, in sturzstroms (Section 2.1) the upper part (often called “cap”) is “capable of travelling unmixed on top of a relatively thin shear region, where the shear rate must become very large to account for the high velocity of the sturzstrom” (De blasio and Elverhoi, 2008).

It does not appear an easy task to gather quantitative data about the coherent sliding stage of long run-out landslides, since in most case histories geotechnical data are available, if at all, for the final debris; i.e. after the slide has disaggregated. Nevertheless, not only will we focus our attention on coherent sliding phenomena in our search for data, but also on flow-like movements resulting from the transformation of an initially coherent landslide/rockslide.

2.1.4. Landslide case studies

In this section we identify and discuss a number of terrestrial landslide case studies found in the literature, with the aim of determining, wherever possible, relevant soil parameter ranges that may be useful in the parametric analysis that will be developed in Chapter 7. In the Appendix, each landslide case is summarised in a table and is assigned a number for convenience of reference in this section. The accuracy of the cited data relies on the quality of the drawings, plots and numbers furnished by the referenced authors.

The examples reported in the Appendix show the extremely wide range of different morphologies, sliding mechanisms and materials involved in fast and long run-out landsliding, hence the difficulty in finding characteristic trends of behaviour. The mobilisation of large rock and soil masses ($>10^6$ m^3) is usually crucial to achieving coherent long-reach sliding (in a fashion analogous to the Vajont case, n. 29, or the Jiufengershan case, n. 1), while smaller volumes can have extended run-outs, even on gently inclined slopes, only after transforming into flow-like slides.

Regarding sliding velocity, little data is available for the reported case studies, but the travel classification of the majority of fast slides (i.e. belonging to categories 5, 6 or 7 of Table 2) is ‘debris flow’ or ‘flow slide’. In fact, this is a typical evolution of large slope movements, and it appears easier to calculate the final average sliding velocity rather than to infer the velocity evolution during the early and intermediate sliding phases, when the masses may still retain their original integrity. As a trend we may indicate that for all types of landslides, all other things being equal, increasing velocities are obtained for higher slope angles, which as common sense suggests is due to greater gravity-dependent driving forces. On this matter Wen et al. (2004) proposed a first-approximation power function correlating velocity and slope angle of giant landslides occurring in China, most of which according to the authors take place on slopes dipping between 20° and 30°.

On the topic of shear strength determination for the geomaterial in the slip surface, we will focus our attention on the residual friction angle. If the material involved is clayey, a drop in shear resistance is likely to occur after large displacements, due to the reorientation of platy clay particles parallel to the direction of shearing. As guidance, we refer to the experimental findings outlined by Skempton (1985) (Figure 1). If the clay fraction (percentage in weigth of particles smaller than 0.002 mm) in the shear plane is less than about 25%, the soil does not show significant strength drop and it behaves much like a sand or silt, with a friction angle larger than 20°. On the contrary, when the clay fraction is about 50%, residual strength is controlled almost entirely by sliding friction of clay minerals. When the clay fraction is 25%-50% there is a ‘transitional’ type of behaviour, residual strength being dependent on the percentage of clay particles as well as on their nature.

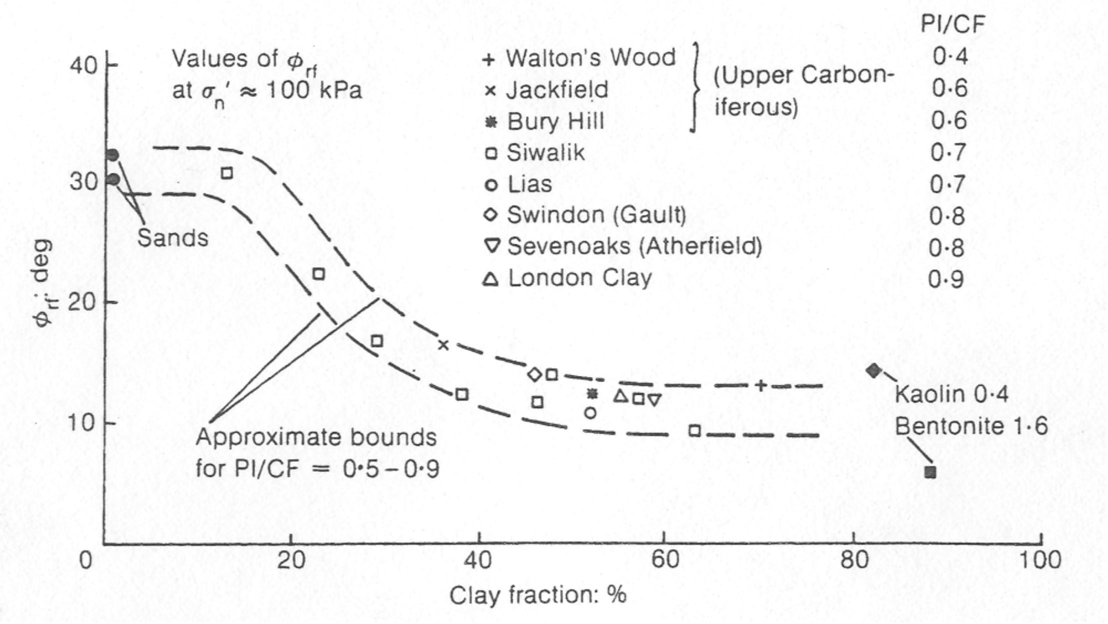

Figure 1. Residual friction angles from ring shear tests on different soils (Skempton 1985).

It is convenient to divide the treated case histories into four sub-categories, in order to discuss them separately (the numbering adopted below refers to the landslide case studies listed in the Appendix):

- Large masses sliding in a coherent state with long run-out
- Large masses with short run-out
- Large masses achieving a long run-out after evolving into a flow-like phenomenon

- Smaller masses with high destructive potential.

2.1.4.1. Large masses sliding in a coherent state with long run-out

Erismann (1979) reports as an enigmatic feature the fact that “in many large landslides the displaced mass, although sometimes disintegrated into small fragments, shows a surprising congruence of its sequential order before and after the event”. This behaviour can be mainly observed in deep-seated rotational or translational slides, especially when the slip plane occurs in a weaker clayey layer; but also in large scale dry debris slides (sturzstroms, cf. De Blasio et al., 2008). Such cases need to be studied with particular concern on the frictional heat production within the slip surface, and are listed below.

In addition to Vajont (landslide n.29), in seven more cases (landslides n. 1, 10, 24, 30, 31, 32, 33) frictional heating has been proposed as the main mechanism behind the observed loss of shear strength, and other non-standard hypotheses have been formulated to explain the long run-out have been formulated in 3 further cases (n. 12, 13, 26). The materials involved in these landslides are mainly sedimentary rocks (apart from n. 10), and sliding occurs on either joint sets of unknown mineralogy (n.10, 12, 13) or on weaker clayey layers (n. 1, 9, 11, 24). The volumes involved are all large, ranging from 10^6 to 10^9 m^3. The range of residual friction angle when slip occurs on rock joints is 27°-32°, while it can be as low as 5-10° when sliding occurs on thin clay layers (n. 6, 9, 11, 29).

It has been widely observed in the literature (Hunter and Fell, 2003, Skempton, 1985) that rapid sliding often occurs in strain-softening soils, such as over-consolidated clays. Most soils with clay fraction percentage greater than 30-40% have their peak friction angle (φ_p’) in the range of 22° to 30°, but they may experience a significant loss of strength in shearing as static and dynamic friction softening occur (Tika and Hutchinson, 1999). Skempton (1985) observed that the angles of (static) residual shearing resistance of the three most commonly occurring clay materials are approximately 15° for kaolinite, 10° for illite or clay mica and 5° for montmorillonite. The special case is also contemplated where the particles smaller than 0.002 mm are non-platy clay minerals (such as halloysite, gibbsite, bauxite, brucite, or rock flour consisting of finely divided quartz etc.) which have high residual friction angles (>25°) and therefore do not experience significant strain weakening (Hunter and Fell, 2003).

For a few case histories (n. 1, 9, 11, 29) some information about the slip surface is given. In general in this type of slides, shear localisation occurs (e.g. see Vardoulakis, 2002a, Puzrin and Germanovich, 2005, Troncone, 2005): all deformation takes place within a thin band of thickness of the order of some millimetres, embedded in an otherwise thicker clay layer of homogeneous characteristics. Such clay layers where the shearbands are localised have thicknesses of 1-10 cm, and the prevalent minerals are chlorite, illite (n. 1, 11, 29) and montmorillonite (n. 9).

Unfortunately, little information is available on the permeability, the dynamic residual angle and the friction-softening behaviour of the shearband materials, except for case n. 29 which appears to be the best documented one in the literature.

2.1.4.2. Large masses with short run-out

Other case histories, mostly consisting of large scale and deep seated slides, have similar characteristics to the above type of slides; but rather than collapsing catastrophically with sudden acceleration they exhibit a slow, creeping movement for decades, or even centuries, before completely stopping their movement. Their final rest, when artificial stabilisation is not carried out, can be often brought about by topographic and morphological constraints, such as the presence of obstacles and specific shear surface dipping conditions. On the other hand, sometimes a creeping slide is no other than the (possibly extremely protracted in time) initial stage of a catastrophic landslide of the type described in Section 2.1.4.1, hence deserving more consideration.

A few quantitative studies have been proposed to interpret the creeping movement of certain deep-seated landslides such as La Clapiére (n. 2): Sornette et al. (2004) and Helmstetter et al. (2004) proposed a “velocity law” to estimate the lifetime of the slide, i.e. the time at which the slide will eventually collapse. Vardoulakis (2002b) and Veveakis et al. (2007) interpreted the initial, creeping phase of Vajont (n. 1) with a thermal-softening and velocity-strengthening law, leading to an estimation of the collapse time of the slide. For La Frasse landslide (n. 36), Tacher et al. (2005) developed a model able to reproduce the creeping movements during some recent acceleration phases brought about by groundwater movement. A similar analysis was also employed to model the mechanical behaviour of the creeping Triesenberg slide (n. 37), by Francois et al. (2007).

Due to the economical inconveniency of drilling deep core samples, less data are available for the shear plane characteristics of deep-seated creeping slides; the attention of researchers is usually more focused on sliding velocity and its changes over time.

The measured sliding velocities range from some mm/day (case n.2) to 5 m/h (case n.3). The geometry of the failure surface assumes often a rotational shape. When the rupture surface is detected, it is often found to be rich in clay, especially marly clay (n. 7, 28), with residual friction angle $\phi'_{rs} = 16° - 19°$, or silty clay (n. 3) with $\phi'_{rs} = 16°$. The same general considerations on the typical friction angles for clays hold (Section 2.1.4.1), although we are unable to extract any specific trend for this type of slides due to the scarcity of direct field data.

2.1.4.3. Large masses achieving a long run-out after evolving into a flow-like phenomenon

Initially constrained movements may achieve long run-outs once they transform into a flow-like movement, which largely increases their mobility. This is probably the largest category among the landslides reported in the literature as “catastrophic”, involving a broad range of geomaterial types and achieving the largest velocities and run-outs. Hunter and Fell (2003) assert that slides of debris that undergo significant break-up and remoulding transforming into debris flows range from clayey silty sands to coarse grained granular soils, with low fine contents, and travel velocities are in the range of ‘rapid’ to ‘very rapid’ (Table 2). Slides of debris that, instead, remain intact during travel, generally encompass the higher clay content soil types and reach maximum velocities in the order of metres/minute. Some observations are also made by Hunter and Fell (2003) on velocity in relation to the slope inclination β, stating that for landslides in dilative soils (i.e. mainly sandy clays, clayey sands to coarse granular soils), rapid sliding predominantly occurs where the source area and immediate downslope angle is greater than β ~25°, but can also occur for angles down to β ~20°. For β >35° rapid sliding is likely to be experienced in spite of the soil type, excluding deep-seated slopes where the rupture surface extends below the toe.

Unfortunately, little data are available for the coherent sliding phase of these phenomena prior to transforming into a flow, as post-sliding investigations are normally carried out on the final landslide ‘deposit’. The volumes involved range from 1 to 40×10^6 m^3, the soils involved in the flow range from volcanic regolith (n.4) and moranic material (n. 8) to volcanic and sedimentary rock. Residual friction angles on shear surfaces range from $\phi'_{rs} = 9°$ on bentonitic claystone (n.25) to $\phi'_{rs} = 24°$ on moranic “terres noires” (n.8).

2.1.4.4. Smaller masses with high destructive potential

Landslides involving volumes of 10^2-10^5 m^3 sometimes have equally destructive effects than larger ones, and are often triggered by extreme meteorological events. Debris avalanches on volcanic soils (n.14, 15) or earthflows (n. 21) achieve long run-outs, while translational landslips and rock-block slides (n. 5, 18, 20, 22) typically have limited reach. Slip surfaces, often silty-clayey (n. 5, 20, 22, 27) have $\phi'_{rs} = 10 - 18°$.

2.1.4.5. Some catastrophic landslide cases

An overview is given hereafter of the catastrophic landslide case studies, among those classified in the Appendix, which deserve most attention for their destructiveness and relevance to our research. These selected cases are summarised in Table 3 with details on the country, date of occurrence, volume involved and number of victims.

Table 3. Selected catastrophic landslide cases.

Name of slide	Country of location	Date occurred	Volume (m^3)	Casualties
Vajont	Italy	09/10/1963	$270x10^6$	2000
Jiufengershan	Taiwan	21/09/1999	$42x10^6$	50
Sale Mountain	China	07/03/1983	$30x10^6$	237
Goldau	Switzerland	02/09/1806	$40x10^6$	457
Qianjiangping	China	13/07/2003	$24x10^6$	24

Sadly famous, and best documented in the literature is the case of Vajont, occurred in the oriental Italian Alps in 1963. This catastrophe was not only a tragedy for the victims and their families, but also for the experts and engineers in charge (Erismann and Abele, 2001). The landslide moved approximately $2.7 \times 10^8 m^3$ of rock, whose lower part impounded an artificial water reservoir of about $1.5 \times 10^8 m^3$. An ‘M-shaped’ scar was left on the flank of Mount Toc (Figure 2). The compact rock mass moved downslope at a final velocity of approximately 25–30 m/s, for a total displacement of 450– 500 m (Anderson, 1980, Hendron and Patton, 1985). As the mass rapidly plunged into the water reservoir, it produced a giant surge wave ($4.8 \times 10^7 m^3$) that overtopped the dam by 200 m and violently flooded the underlying valley, destroying all the nearby villages (Figure 3). Legal and social implications were extremely serious, as the experts who had been carrying out *ante eventum* analyses failed to predict such a strikingly high velocity: had the slide been slower, probably the impact with the lake would not have been sufficient to cause the water to overflow the dam.

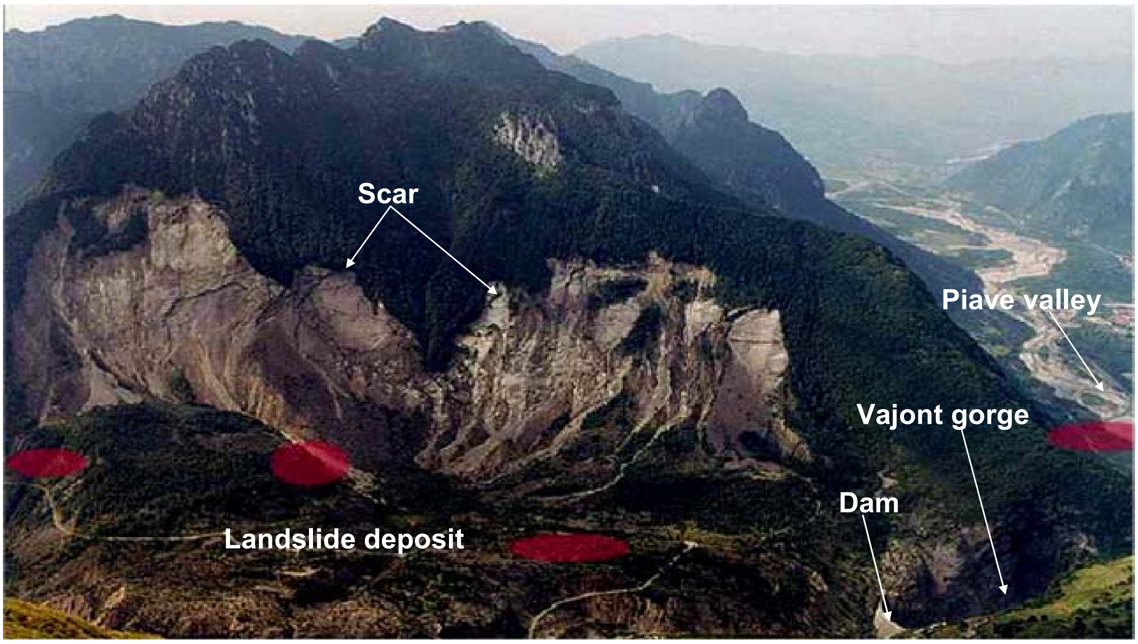

Figure 2. Overview of the Vajont valley after the disaster. Photo from Schrefler (2005).

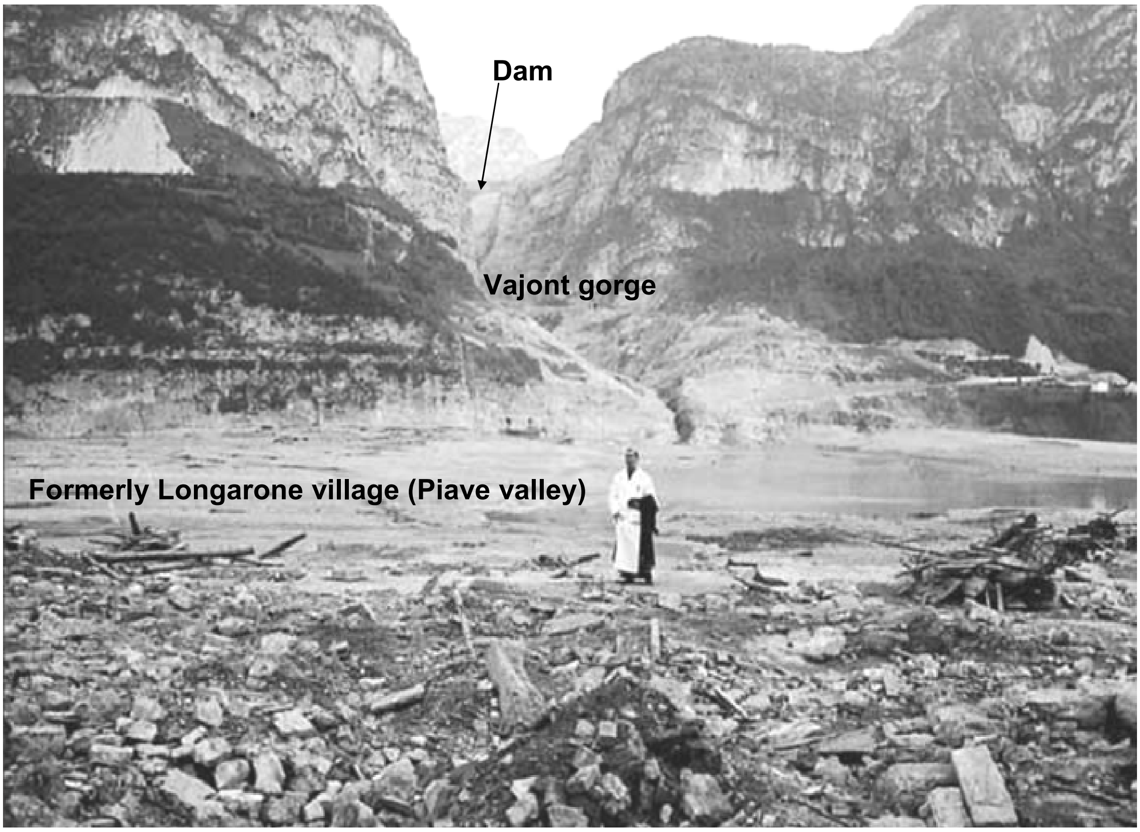

Figure 3. Historical photo of the location where the village of Longarone once stood, taken shortly after the disaster. Photo from Bojanowski (2007).

A similar case history to Vajont is the slide of Jiufengershan, triggered by the 1999 Chi-Chi earthquake in Taiwan. A 50×10^6 m^3 mass of sandstone and shale detached from a mountain flank (Figure 4) and travelled downslope at high velocity in a translational fashion for a total displacement of about 1 km. The debris deposit dammed two creeks and created three small lakes upstream (Chang et al., 2005). Several *post eventum* investigations were carried out on this slide, so that an adequate amount of data on the soil properties and in-situ conditions of the slope is available in the literature.

The Sale Mountain compound landslide, occurred in China in 1985, is yet another example of a giant rockslide that moved in a coherent fashion at an unexpectedly high velocity: in less than one minute the mass travelled 1 km (Zhang et al., 2002). Similarly to Vajont, deformation was found to be localised in a 2 mm thick shear band while the overburden moved as a rigid block, to the extent that an eyewitness of the event saved his life by hanging on to a tree and travelling with it for about 960m on the surface of the sliding mass. Even though a quantitative back-analysis of this event has been published (Miao et al., 2001), there is a certain lack of essential geotechnical data in the literature.

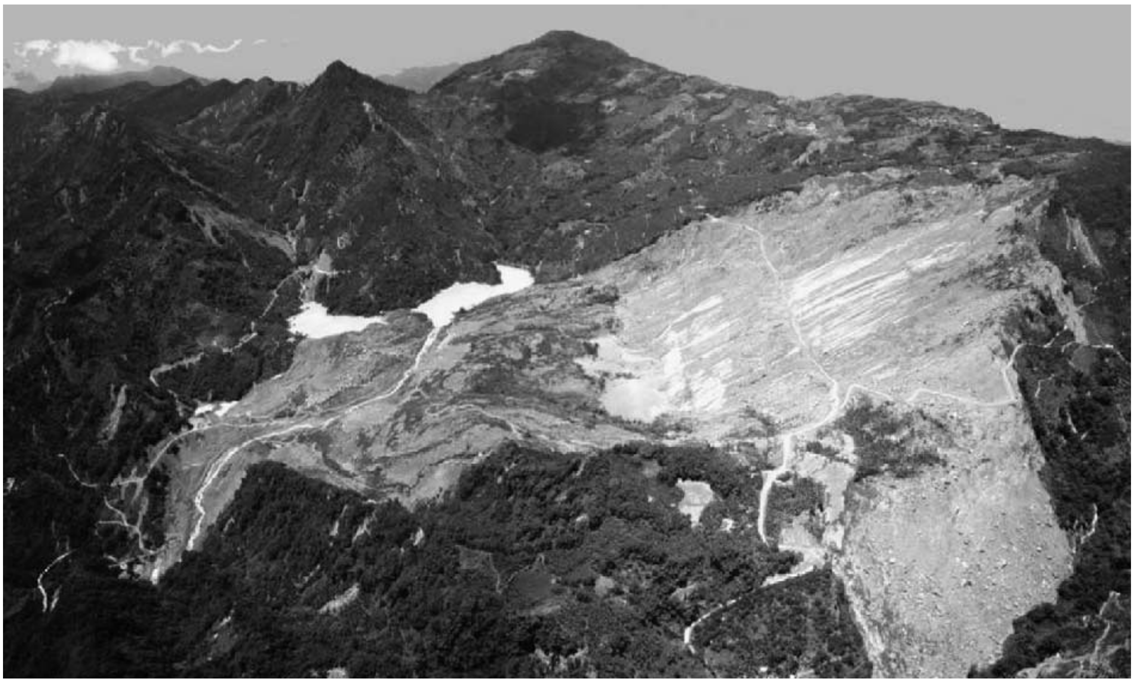

Figure 4. From Shou and Wang (2003). The planar slide of Jiufengershan, occurred in Taiwan in 1999.

Despite having happened two centuries ago, the Goldau landslide is one of the best known ones of the Swiss Alps (Figure 5). Historical documents report the suddenness and large size of the event, although the availability of quantitative data is very limited. Nevertheless, the sliding mode and conjectures of frictional heating in the slip plane (Erismann, 1979) make Goldau an interesting case to our research.

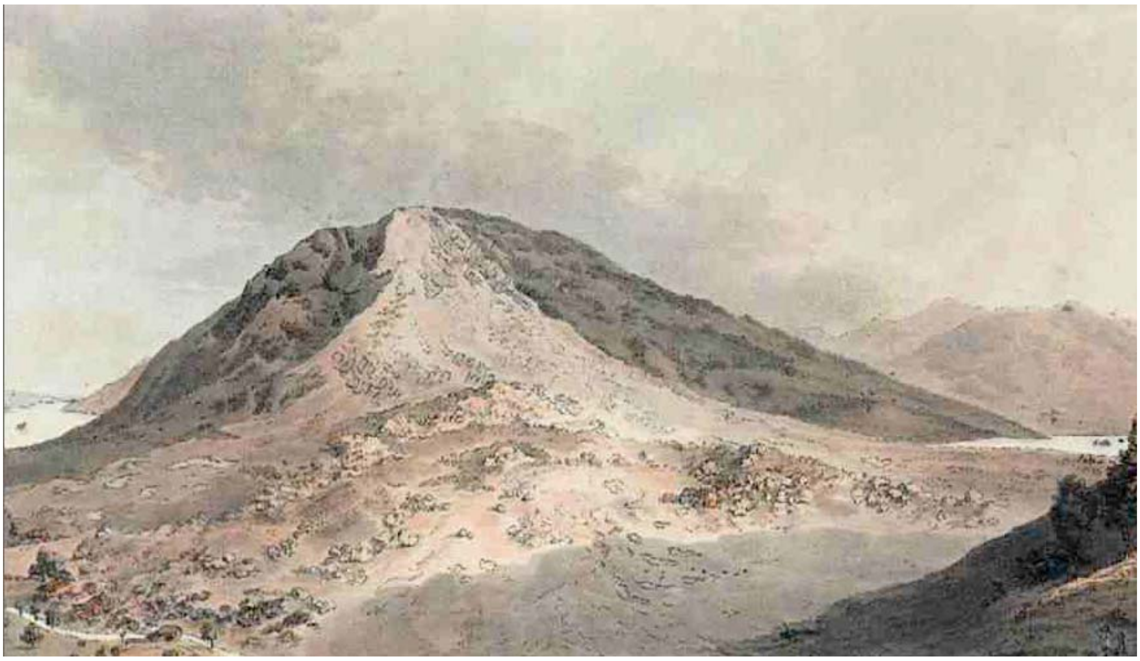

Figure 5. From Thuro et al. (2005). the Goldau landslide in a painting by H. Keller, 1806.

Figure 6. From Yueping (2008). Overview of Qiangjiangping slide, occurred in 2003 in China.

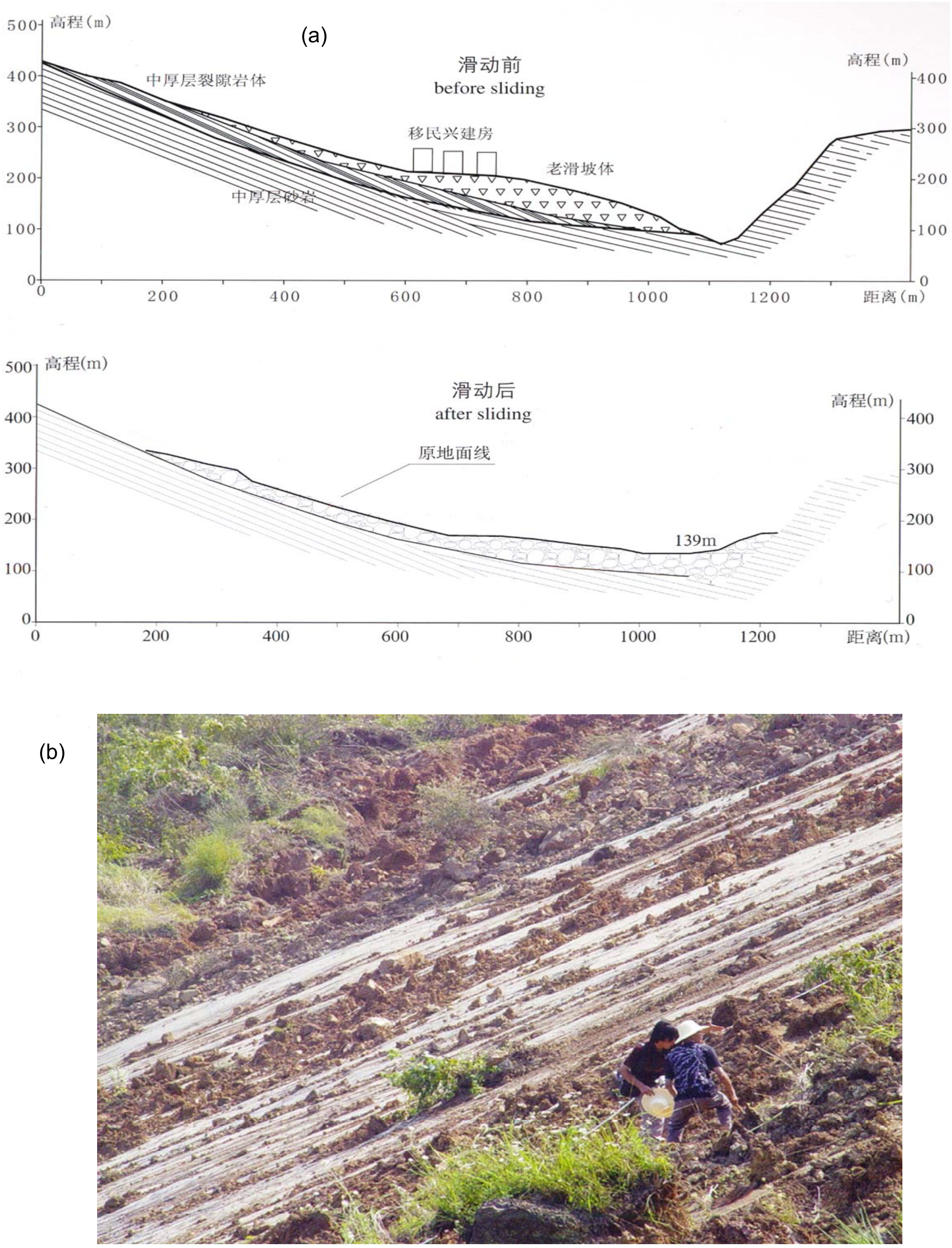

Figure 7. From Yueping (2008). Qiangjiangping landslide: (a) Sections of the slope before and after the slide and (b) photo of the slip surface.

It is finally worth mentioning the recent Qiangjiangping case (Figure 6), which analogously to Vajont was a reactivated slide, triggered by reservoir filling during the completion of the renowned Three Gorges hydro-electric project. A fast slip rate (1 m/s on average according to Wen et al., 2004) was reported for this event, which (unlike

Vajont) was not enough to generate significant waves by impacting the water. Unfortunately though, the debris rapidly dammed the underlying river, and a 30 m high surge was created subsequently upon dam breaching, killing 24 people in the surrounding shores. The geometry of this slide is clear (Figure 7), but no geotechnical data are available at the time of writing.

2.2. Submarine landslide cases

2.2.1. Classification of submarine landslides

Submarine landslides in the world are as frequent as their terrestrial counterparts. They are often cause of major disasters, involving loss of property and life, notably when they act as triggers of tsunamis or they impact on inhabited coastal areas. Many other submarine landslides go unnoticed, but the potential impact of these phenomena is increasing as Man is expanding in the oceans, building new oil and gas platforms and searching areas to dispose of nuclear waste. Moreover, undersea slope failures are of great interest to the scientific research community in understanding some still obscure mechanisms of movement, leading to substantial modification of continental margins.

Most of the terminology applied to submarine slides normally comes from that applied to terrestrial slides, but it is necessary to make distinctions to avoid confusion, as submarine phenomena are different in some aspects. Besides, it is difficult to provide an ad hoc classification as sub-oceanic movements have hardly ever been directly observed, thus it is extremely uncertain to infer deformational mechanisms and processes from the landslide geometry observed after the particular event. In fact, it may happen that many different deformational characteristics involved in the movement which are not preserved in the final configuration of the landslide.

Many authors, among which Canals et al. (2004), Lee et al. (1991) and Prior (1988) point out the aforementioned confusion in terms commonly used in underwater geology, for example in the overuse of the term ‘slump’, which should correctly only indicate the specific kind of sliding with rotational movement.

A brief and simple classification (Prior 1988), following concepts developed from terrestrial landslides is schematised in Figure 8, and comprises a continuum of slides and flows. The movement types can be described as follows.

- *Slides* consist of a mass sliding over one or more discrete basal shear planes, often occurring on slopes of less than 5 degrees. They often involve very large volumes, and can be subdivided according to the geometry of shear surfaces into translational and rotational. Within this category, the sliding mechanisms are essentially the same as in terrestrial landslides. In translational slides, blocks of rock or slabs of sediment translate downslope on a basal plane inclined approximately parallel to the slope surface. Rotational slides (slumps) involve the displacement of more or less intact blocks over curved slip surfaces. Intermediate sub-categories are successive slides, multiple retrogressive slides and bottleneck slides, the latter representing a transitional case between real slides and flows. More than one category can be represented at the same time inside a submarine landslide complex.

- *Flows*, believed to be the most diffused in the submarine environment and showing the most different features compared to terrestrial mass movements, are subdivided into debris flows, liquefaction flows, grain flows and turbidity flows. Debris flows are sediment movements in which clasts are often supported by a matrix made of a mixture of fluid and fine sediment. Liquefaction flows involve the collapse of loose and coarse sediment, as while the particles lose contact, the particle weight is transferred to the pore water. In grain flows, loose individual sediment grains move downslope. This is the case, for example, of sand flows occurring in the submarine canyon margins.

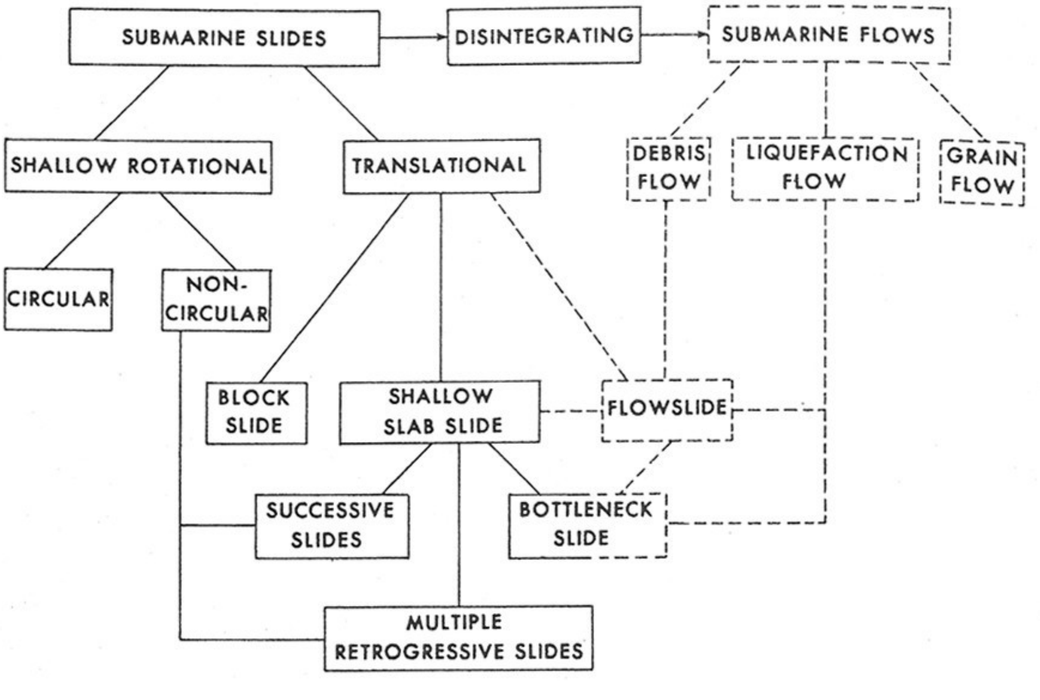

Figure 8. Classification of submarine slides by Prior (1988).

Another classification of subaqueous landslides was proposed by Lee et al. (1991), based on the modification of that by Varnes (1978), effectively synthesised in Figure 9. While the ‘slides’ part, which in turn mirrors the terrestrial slides case, is analogous to the previous classification, the ‘mass flows’ part contains more detailed observations. Slides can often transform into flows as the sliding mass progressively disintegrates while moving downslope. Mudflows are similar to debris flows, but they involve muddy sediments. Turbidity currents, represented in the last drawing on the right in Figure 9, involve the transport of a relatively diluted suspension of sediment grains supported by an upward component of fluid turbulence.

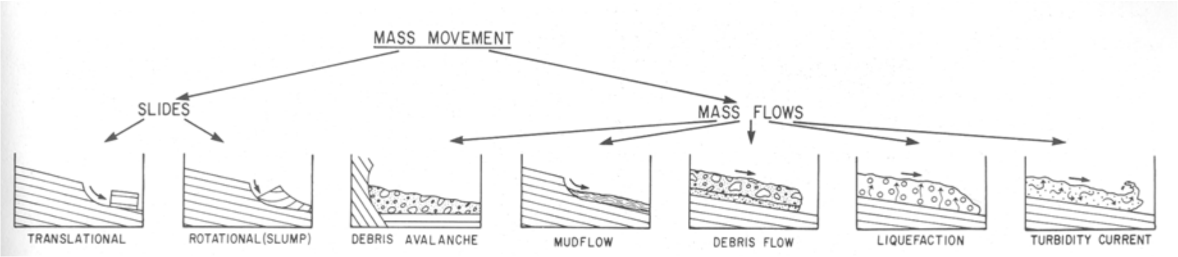

Figure 9. Classification of submarine slides by Lee et al. (1988).

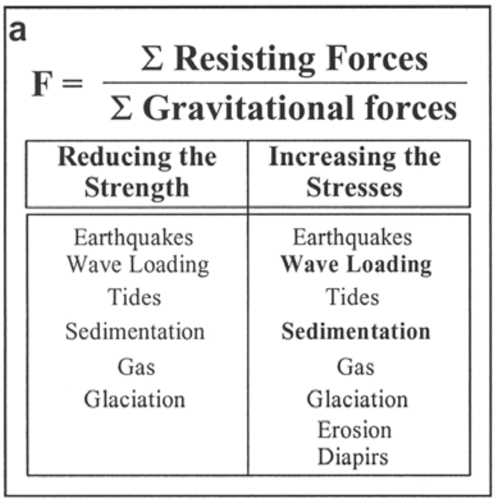

a

$$F = \frac{\Sigma \text{ Resisting Forces}}{\Sigma \text{ Gravitational forces}}$$

Reducing the Strength	**Increasing the Stresses**
Earthquakes	Earthquakes
Wave Loading	**Wave Loading**
Tides	Tides
Sedimentation	**Sedimentation**
Gas	Gas
Glaciation	Glaciation
	Erosion
	Diapirs

Figure 10. Events that are likely to trigger submarine slides by reducing their safety factor (Locat and Lee, 2000).

2.2.2. Typical environments and causes of submarine landslides

A schematic list of possible factors which are prone to initiate submarine landslides based on conventional stability analysis can be seen in Figure 10 (Locat and Lee, 2000).

It can be noted, first of all, that some of the causes, such as gas charging and wave loading, are peculiar to the subaqueous environment. In general, a landslide occurs when the downslope driving stress exceeds the resisting strength of the material. The action of gravity is obviously common to all environments, as the seafloor is always relatively inclined, but gravity is not the unique factor.

Hampton et al. (1996) proposed a comprehensive account of the typical "submarine landslide territory", consisting of five environments, listed below.

- *Fjords*. These submerged glacially eroded valleys usually have a sediment-laden river delta at the head. The sediment deposition rate on the delta can outpace the expulsion of pore water, which determines a low static shear strength due to under-consolidation. The typically rocky sediment is also predisposed to loss of strength under the load of waves and possible earthquakes.
- *River deltas on the continental margin*. Subaqueous slope failures are common in those areas of the continental margin where a river mouth provides a point source entry of sediment. Specific conditions are needed for slope failure to occur in deltas. High sedimentation rate is necessary in order to accumulate a sufficiently thick bed of sediment. The sediment is often fine-grained or plastic, so that the low permeability can allow to retain pore pressure and as a result to produce under-consolidation as in the above case. Key factors to trigger these processes are environmental loads, such as wave storms and earthquakes.
- *Submarine Canyons*. Canyons are very frequent underwater and their tall and steep side walls facilitate the insurgence of landslides, which in turn are responsible for the continuous shape evolution of canyons. Mass movements are caused by gravity and internally derived seepage forces.
- *Open continental margin*. Typical slopes of 3-6 degrees determine a tendency for gravity-driven mass movements in these areas, off the continents and larger islands. Apart from some areas of high tectonic steepening, gravity is not normally reputed to be great enough to cause failure. Causes can be earthquake shaking, effects of rapidly changing sea level and gas hydrate dissociation.
- *Oceanic volcanic islands and ridges*. Some of the biggest existing landslides occur on the flanks of volcanic islands, caused by still poorly understood factors. Earthquakes in this case are more a consequence than a cause of volcanic

landslides, and the mechanisms may be related to the inherently unstable structure of volcanic islands.

Other causes listed by Hampton et al. (1996) which have been proposed for the occurrence of submarine landslides are tectonic processes, such as faults and subduction, oversteepening of tall carbonate slopes and biologic weakening processes.

2.2.3. Similarities and differences between terrestrial and submarine landslides

The morphology and mechanics of the two kind of landslides have many similarities, but also important differences.

Firstly, subaqueous landslides can be much larger than their sub-aerial counterparts, the largest of which displace masses of the order of 20-25 cubic kilometres. By comparison, the largest submarine mass movements have involved volumes up to 20,000 km^3 as a single failure event (Hampton et al., 1996). As an example, the well-documented Storegga slide off the coast of Norway (Bugge et al. 1988) has a volume of 5000 km^3.

Secondly, the sliding run-out is also normally much larger for underwater events, often being of the order of hundredths of km.

Thirdly, gravity has a less significant role as a driving force, under water. Submarine landslides can originate on virtually flat surfaces. Examples of low slope angle failures include the Mississipi river delta slide and Klamath river delta slide, characterised by slope angles of 0.1-0.4° and 0.25° respectively (Leroueil, 1996 and Locat et al., 1996).

Legros (2002) compared terrestrial and submarine slides in graphs representing the ratio of the total drop height H_{max} and the runout distance L_{max} plotted against the mass volume V (Figure 11a). The difference is striking as subaqueous slides show a much lower ratio H_{max}/L_{max}. This is explained by Legros (2002) with the larger mobility of submarine landslides as a consequence of their mixing with large amounts of water. Plotting L_{max} against V (Figure 11b) shows, however, that the two types of landslides follow exactly the same trend. A possible interpretation of this is that L_{max} is essentially a function of V, with H_{max} only being of minor influence; which suggests the similarity in the emplacement mechanisms of the two types of landslides, despite the different environments. There is a documented higher tendency for underwater phenomena to transform into flows, hence the longer run-outs. Some submarine debris flows convert into turbidity currents by incorporating overlying sea water, so that the remoulded shear strength of the material in the starting zone can be much higher than the strength of the flowing debris flow (Leroueil et al 1996). In such cases, the surrounding water plays an important role in determining a peculiarly subaqueous phenomenon. However, the rapid transformation into debris flows as the mass slides downslope does not always occur (Legros, 2002), and many submarine landslide deposits have a morphology more typical of coherent landslides than of debris flows.

In general, we may conclude that except for the occurrence of turbidity currents, the aquatic environment experiences the same types of mass failure events as found on land (Locat and Lee, 2000).

2.2.4. Data availability and trends in submarine mass wasting phenomena

2.2.4.1. Observations from the available literature

According to Sangrey (1977), The state of the art in marine geotechnology can best be defined with reference to what is known about soils on land. Differences between these two states of knowledge are the significant problems for the marine environment. Urgeles et al (2006) observe that in the submarine environment there is a problem of accessibility, and complex acoustic techniques need to be applied only to detect the morphology of the relief of a determined area. Moreover, it is only possible to obtain a limited number of core samples, which are enormously expensive for academic standards, and their limited penetration does not always allow to detect the failure planes. Among the major problems quoted by Sangrey (1977) are the disturbances in core sampling resulting from uniquely marine factors, the excess in situ pore pressure caused by rapid sedimentation, the presence of gas in sediments and the presence of dynamic loading effects.

Slope stability analysis requires knowledge of the slope topography, the shape of the failure plane and a variety of engineering properties of the involved materials. These properties are very rarely available for submarine slides, apart from some areas of great economical interest related to the oil industry, where the presence of offshore platforms and the larger economical availability makes it possible to make extensive use of high-technology coring and mapping methods.

For all the aforementioned reasons, the difficulty in finding trends of behaviour and geomechanical data for subaqueous landslides is apparent.

Regarding the sliding mode trends, Booth et al. (1991) report a tendency towards disintegrative landsliding in the marine environment of the US economic zone (for which a large amount of data is available), claiming that this happens in two thirds of cases (Figure 12). After initial slope failure, which can be translational or rotational, landslide bodies tend to develop large strains, lose their internal structure and flow downslope. This concept is enforced in Figure 13, where the frequency distribution of the landslide types is shown in the histograms.

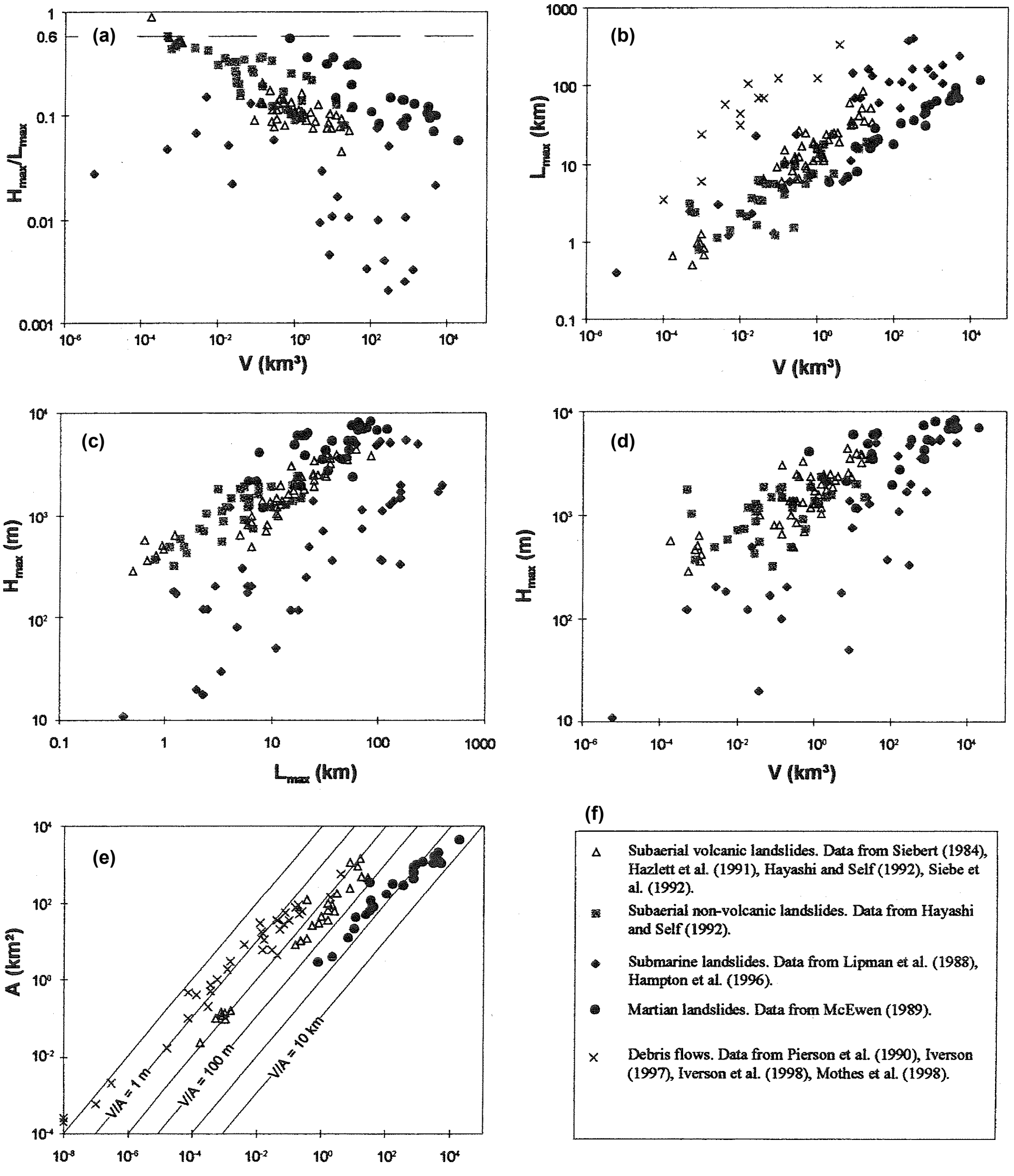

Figure 11. From Legros, 2002. Relationships between geometrical properties plotted for sub-aerial volcanic and non-volcanic slides, submarine slides and martian slides. (a) Ratio of total fall height/runout vs volume, (b) runout vs volume, (c) fall height vs runout, (d) fall height vs volume, (e) area covered by the landslide deposit vs volume, (f) Author's legend.

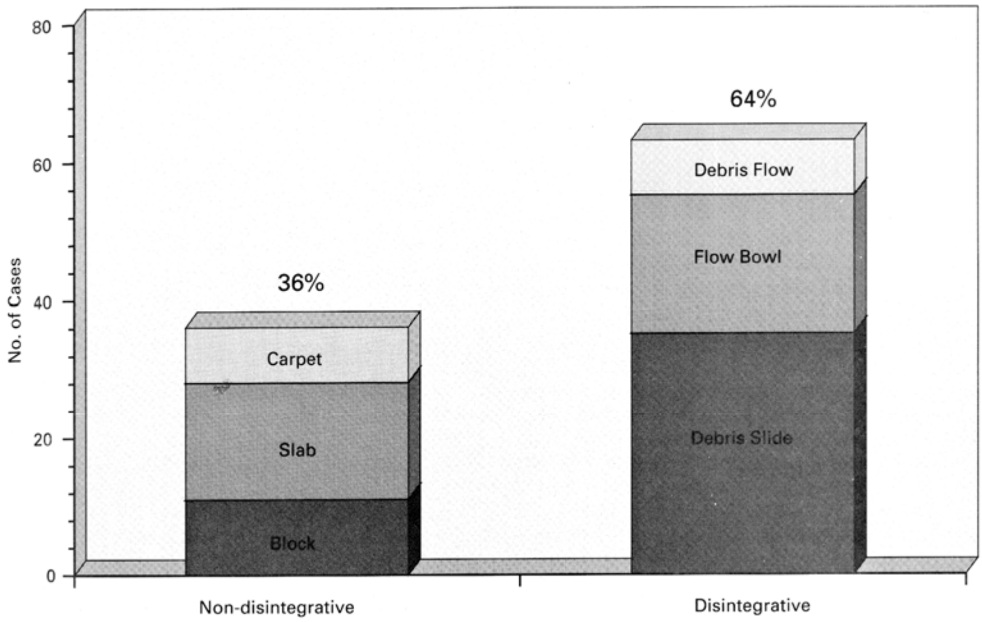

Figure 12. Percentages of disintegrative and non-disintegrative submarine landslides (Booth et al., 1991)

.

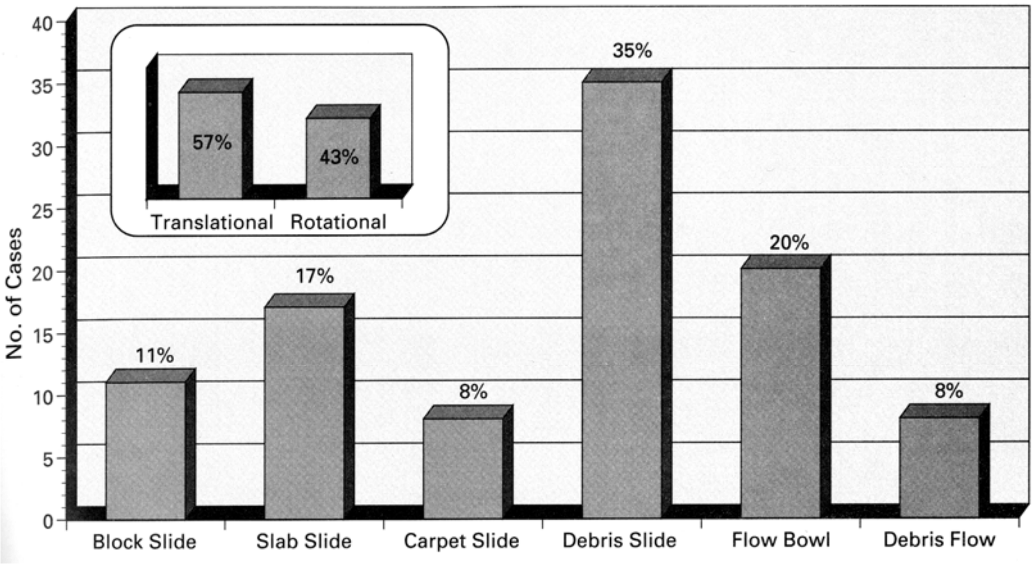

Figure 13. Frequency of occurrence of different types of submarine landslides.

It has also been observed (Booth et al., 1991) that the average-sized open-slope slide (about 100 km^2) tends to occur at lower slope angles and is an order of magnitude larger than the average canyon landslide, and large-scale slides tend to be associated with gentler slopes than small-scale ones.

Hünherbach and Masson (2004) reviewed 260 documented submarine slope failures, belonging to both the US and Northern European continental margins, asserting that the only parameters that are sufficiently available to be discussed in detail are (a) dimensions, (b) slope angle, (c) total height, (d) headwall height and (e) water depth. After a statistical analysis of not always complete database entries, the authors could conclude the following:

- The slope angle does not influence the occurrence of subaqueous landslides, also given that the largest ones appear to occur on the lowest slopes.
- On both sides of the Atlantic continental margin, there appears to be a peak in landslide headwall location at a depth of about 1000-1300 m, suggesting the presence of specific weak layers prone to failure.
- Landslides in fjords tend to be disintegrative.
- Geotechnical measurements and sediment rheology are seldom available.

It is finally worth reporting here the observation of Silva et al. (2004) that one of the most important differences between marine and terrestrial sediments is the generally less significant spatial variation of engineering properties in marine sediments, implying that soil properties of subaqueous deposits are often similar over large areas. This means that the need for systematic sampling can be smaller.

2.2.4.2. Data collection

We have collected as many case studies of submarine slides as possible in which geomechanical properties were measured or deducted, in an attempt to collate data and associate soil properties and mineralogy with landslide behaviour.

Some of the best documented case studies, among those occurring in deep-water, are the Storegga slide off the coast of Norway (Bugge et al., 1988, Kvalstad et al., 2005a, 2005b, Forsberg and Locat 2005), the Gebra, Finneidfjord and Afen slides (Canals et al., 2004), the Gulf of Mexico slides (Silva et al., 2004), the Canary slide (Roberts and Cramp, 1996, Canals et al., 2004), the Ebro Slope slide (Urgeles et al. 2006), the North Aegean trough slide (Lykousis et al. 2002) and the Hudson Apron flowslide (Desgagnes et al. 2000). Better documented, for obvious practical reasons, are the few case studies of landslides which initiated on the coast and terminated under water, or those involving parts of coast due to retrogressive behaviour of the submarine landslide (Cornforth and Lowell 1996). Some examples of the kind of available data follow below.

Mineralogy is known for the Hudson Apron slide (silty clay, clay fraction 37-60%, composed of illite, chlorite and little smectite), the undrained shear strength is measured (0.5 to 15 kPa) and a probable failure plane was detected at a depth of 20 metres;

although all investigations were carried out on the landslide deposit, which is hardly representative of the initial sliding behaviour. The 'North Aegean Through' slide is a typical translational one and the sediment stratigraphy was detected through a total of five gravity cores, the major slip plane being assumed to have developed within a muddy layer. Twelve Geo-borings (the highest number for a single landsliding area) were performed in the Storegga area, allowing Forsberg and Locat (2005) to detect the mineralogy and to conclude that fine grained hemipelagic/glacial marine deposits are present in all slip planes of the sliding area.

We observe that soil data are uniquely available, if at all, in the form of borehole log diagrams or core sample profiles. As an example, in Figure 14 data are reported from four sediment cores from the North Aegean Through slide and in Figure 15 measured parameters from three core logs of the Ebro slide are represented. The difficulty of deducing useful information on the key mechanical properties of a slide from data of this kind is apparent, hence the impossibility to find representative trends for submarine sliding phenomena.

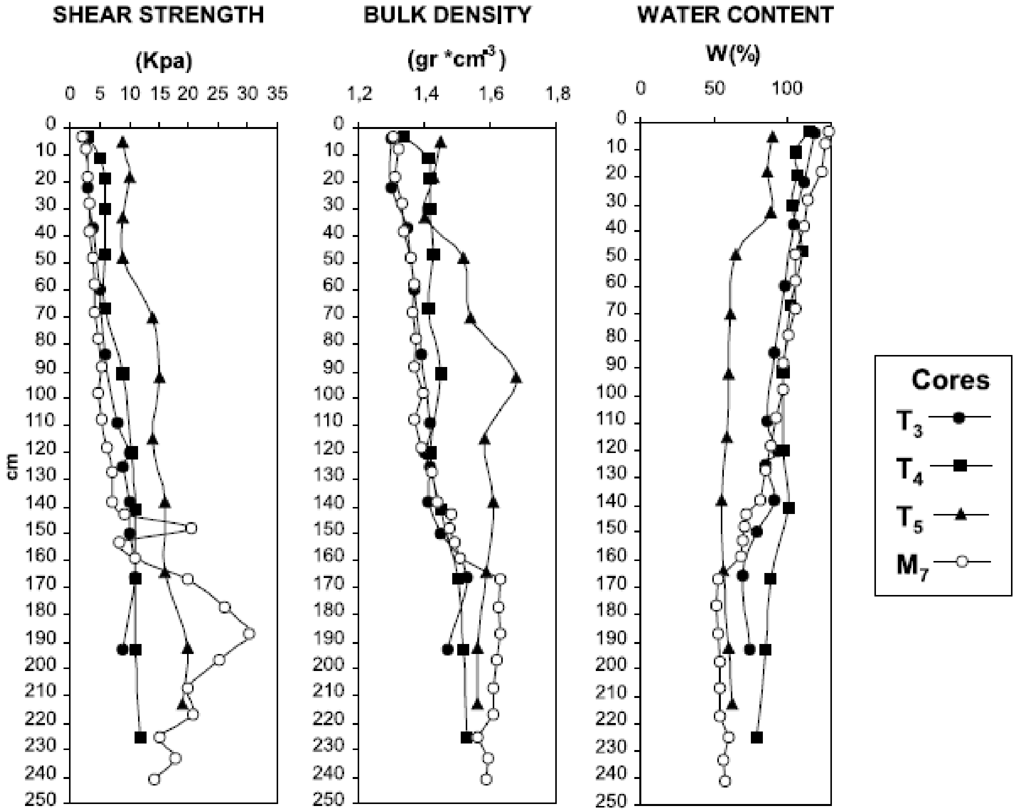

Figure 14. Soil properties deduced from four marine sediment cores (Lykousis et al., 2002)

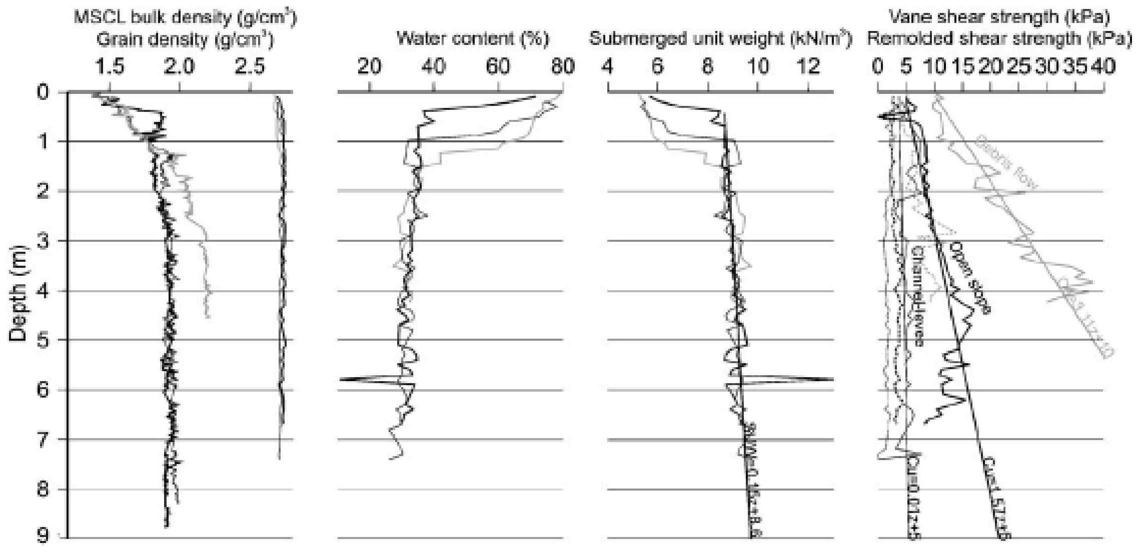

Figure 15. Example of submarine core logs data (Urgeles et al, 2006).

2.2.4.3. Relevance of submarine landslides to our research

For submarine landslides, unlike their sub-aerial counterparts, it has not been possible to find reasonable ranges of soil parameters which could be considered representative of particular submarine sliding modes and used for the calibration of the new landslide model (cf. Chapters 5, 6 and 7), as the available properties are scattered, uncertain and too small in number.

We have seen, however, some subaqueous mass displacement phenomena exhibiting coherent sliding, like submarine 'block slides' and 'slab slides' (Lee et al., 1991). Even flow-like phenomena and turbidity currents can have a relatively short phase, immediately after failure, of coherent sliding.

Regarding the most relevant phenomena to us, we would exclude river delta slides, and probably fjord landslides as well, as these are normally brought about by sediment underconsolidation which constitutes a unique marine mechanism. All other marine mass wasting phenomena on the contrary, especially slides occurring in the open continental margin, are to be considered of maximum significance to our research, as a dynamic landslide model accounting for frictional heating could in principle be employed interpret the initial (coherent) phase of their sliding.

2.3. Catastrophic landslides. Review of existing theories

A defining characteristic of some large landslides is that they travel further than what simple frictional models predict (Legros, 2002), and their destructive potential is due to their enormous energy released in a short time, one minute being a typical value (Erismann, 1979). Standard analyses have not always been able to interpret such extreme sliding events. Based on post-failure field observations and theoretical assumptions, some newer theories, which in most cases did not evolve into a comprehensive model, have been formulated in the literature to interpret the unusually high velocities and long run-outs of some large-scale landslides.

Habib (1975) was the first one to propose the vaporisation of pore water due to local frictional heating to justify the strength loss in deep-seated rockslides, notably for the case of Vajont. The "air-cushion layer" hypothesis was formulated by Shreve (1966), although without direct evidence, to interpret a massive rockslide in Alaska: landslides of this type are believed to slip on a layer of trapped and compressed air, provided there is no fluid leakage from beneath the flanks. A "self-lubrication" concept was described by Gaziev (1984) for rockslides, concerning crushing of the rock in the shear zone to a powdered state which causes the shear resistance to disappear. Self-lubrication caused by interface melting in rockslides was first proposed by Erismann (1979), and most recently by De Blasio and Elverhoi (2008) to interpret the loss of frictional resistance and consequent large run-outs occurring in sturzstroms (Section 2.1), in which the overburden travels coherently on top of a basal shear plane: a molten rock layer due to frictional heating could self-lubricate the base of the landslide under certain field conditions. Zhongyou (1984) conjectured the existence of a different self-lubrication process, due to the existence of a "special oily soil" present in semi-rock strata which reduces the slip surface strength. Legros (2002), as anticipated in Section 2.2.3, explains the excessively large run-outs observed for some submarine landslides by the presence of large amounts of water mixing with the soil.

Vardoulakis (2000, 2002a) developed a physically based landslide model which takes into account the evolution of frictionally generated heat and pore pressure build-up, thus justifying the exceptionally large slip rate due to the loss of shear strength documented for the Vajont landslide. Other authors (Voight and Faust, 1982) had hypothesised pore water pressurisation to explain the catastrophic evolution of large slope failures, and more recently Chang et al (2005) formulated a block-on-slope thermo-mechanical model to back-analyse the 1999 Jiufengershan earthquake-triggered catastrophic landslide in Taiwan.

2.3.1. Field evidence of frictional heating

It emerges from the above section that several authors have addressed the issue of frictional heating of the soil/rock in the shear zone of a slide. Some evidence of this phenomenon, in the form of molten rock generated by friction, has been observed both for prehistoric and for recent landslides.

Layers of fused rock, normally called ‘frictionites’ or ‘pseudotachylites’, are usually arranged in thin layers a few centimetres thick, which suggests not only the significant temperature rise locally caused by friction, but also the characteristic thinness of the shear surfaces in these localisation phenomena: if the shear layer were thick, heat would be dissipated over a larger volume and would not be enough to melt the rock (De Blasio and Elverhoi, 2008).

Molten rocks were first observed in the prehistoric Koefels landslide (Erismann, 1979, Erismann and Abele, 2001) in the form of porous, pumice-like (Figure 16) and glassy formations (Figure 17). Glassy and compact frictionite was also found in the main sliding surface of the ancient Langtang slide (Masch et al., 1985, Erismann and Abele, 2001). Similarly, the Arequipa volcanic landslide deposit in Peru shows glass-like formations at its basal contact with the bedrock (Legros et al., 2001). The observed thickness of molten layers in all the above cases ranges from a few mm up to a few cm.

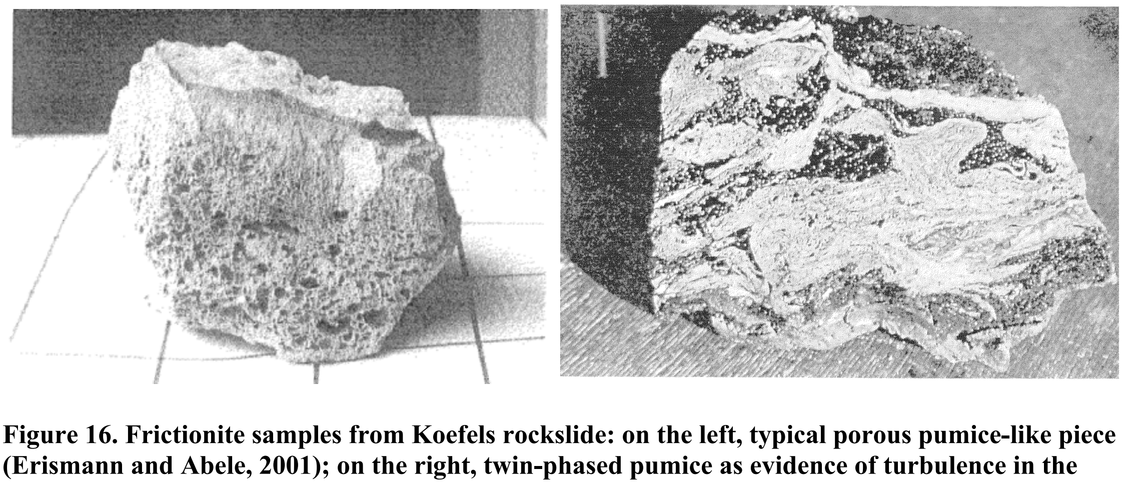

Figure 16. Frictionite samples from Koefels rockslide: on the left, typical porous pumice-like piece (Erismann and Abele, 2001); on the right, twin-phased pumice as evidence of turbulence in the liquid state of the rock (Erismann, 1979).

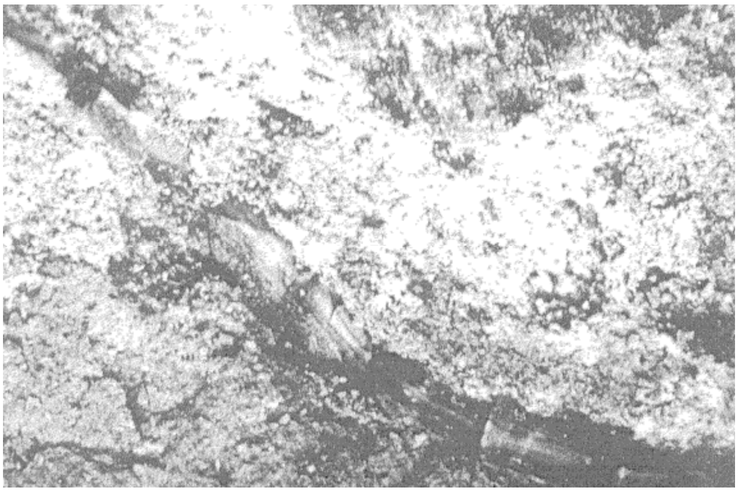

Figure 17. From Erismann and Abele (2001). Glassy frictionite (vein across the picture diagonal) from a secondary sliding surface in Koefels slide.

In the recent Jiufengershan landslide that occurred in Taiwan (1999), evidence of high-speed frictional slip within a short timeframe is given by the presence of glassy and vescicular pseudotachylites (Figure 18), found both on the glide plane as thin layers (1-10mm) and as veins injected into cracks in the host rocks (Lin et al., 2001). Such rock melting is estimated by the authors to require temperatures around 1500 °C to occur at the given depth. Most recently, Zhang et al. (2002) reported the presence of muscovite flakes (Figure 19) and glass beads in the 2 mm thick shear zone of the Sale Mountain landslide, occurred in China in 1983. At the estimated slip rate of 20 m/s, temperature must have locally reached 500-600 °C in order that kaolinite and montmorillonite minerals re-crystallised into muscovite and quartz grains were melted to form glass beads.

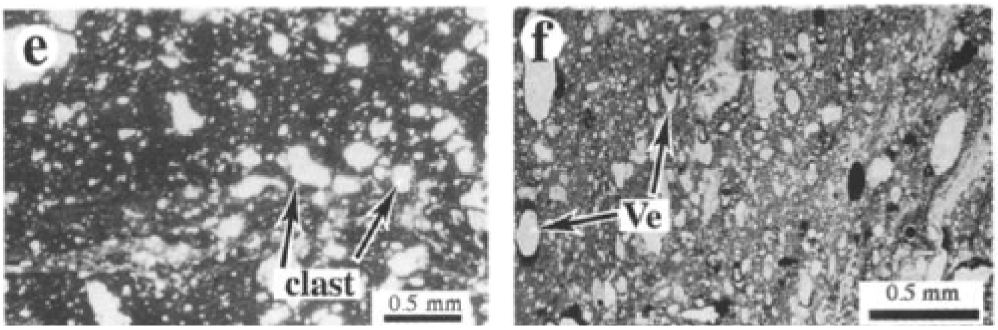

Figure 18. From Lin et al. (2001). Glass matrix with irregular shaped clasts (left) and vescicles (right) within the pseudotachylite found in the slip plane of Jiufengershan landslide.

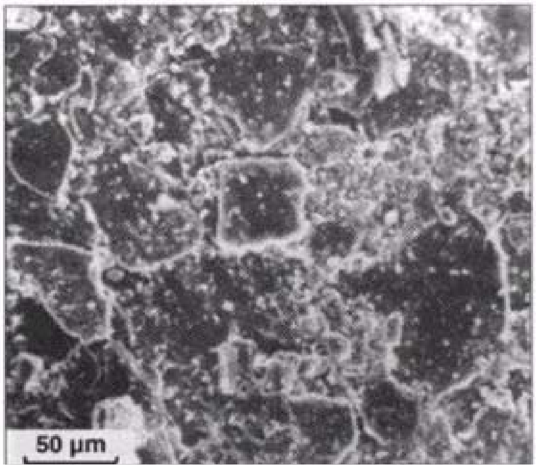

Figure 19. From Zhang et al. (2002). Muscovite flakes oriented parallel to shear direction taken from the rupture plane of Sale Mountain Landslide.

It emerges from the scattered examples reported above that evidence of frictional rock melting is rather infrequent compared to the abundance of large-scale landslides in the world. This may be due to a lack of dedicated site investigations, but also to the frequent occurrence of this type of landslides on weak clayey slip planes rather than rock: in such cases, the heat production is expected to be generally lower due to a smaller friction, which will tend to vanish as the slide progresses downslope due to the emergence of pore water pressurisation and material friction softening (cf. Section 2.3.4 and Chapter 5). This could be the case, for example, of the well-documented Vajont slide, and also for the Jiufengershan event. We observe that in all cases where the slide overburden is made of rock but the shear surface principally occurs in soil, it may still be possible to locally produce frictionites along the rupture plane, due to the occasional presence of rock-to-rock contact providing a higher friction coefficient, hence possibly raising the temperature up to the melting point.

2.3.2. Some theories on the thermal collapse of landslides

Of the theories mentioned in Section 2.3, only a few evolved from conjectures into some form of quantitative model for the prediction of the slide velocity and run-out. In order to model the behaviour of sub-aerial (or submarine) catastrophic landslides occurring in water-saturated soil and/or rock, theories proposing thermal pressurisation as the key mechanism to account for the loss of strength in the slip zone are of particular interest to this research.

Voight and Faust (1982) were the first authors to propose that “fluid pressure changes induced by heat liberated within the slip zone provide a reasonable explanation for dynamic problems implied by some high-speed landslides". While Habib (1967) had theorised vaporisation of pore water and subsequent creation of a gas cushion to justify the loss of shear strength in the slip plane, Voight and Faust (1982) proposed that substantial strength loss would happen due to a mere rise in pore water pressure, without the need for water to change phase. The authors presented a first-attempt model for evaluating the pore pressure changes and temperature rise during a rapid land sliding event. Under the substantially simplifying assumptions that due to high slip rate, heat and excess pore pressure do not have the time to diffuse away of the slip zone, the mathematical model was solved analytically and a parametric study was presented to qualitatively highlight the basic implications of frictional heating and pore pressure build-up:

- As the effective stress across the fault vanishes, so also does the increase in frictional heat, due to the concurrent reduction of friction.
- The temperature rise during sliding is greater for larger initial effective normal stresses.
- The temperature and pore pressure rise depend on the ratio between slide displacement and shear zone thickness.

Calculations were also made alongside the parametric study in an attempt to match the final velocity of the Vajont case, showing that despite the strong simplifications, a model involving pressurisation and frictional heating can provide a rational explanation for the observed extremely low values of apparent kinetic friction. Nevertheless, in the description of the strength loss mechanism no account was taken for displacement and velocity softening (i.e. the decrease in the soil friction coefficient with increasing displacement and velocity), while this phenomenon is widely acknowledged and was subsequently shown to occur in the clayey soil of Vajont (Tika and Hutchinson, 1999).

More recently, Chang et al. (2005) presented a quantitative analysis of earthquake-triggered landsliding by resorting to thermo-mechanics. Thermal pressurisation, whose occurrence is possible in low permeability shear zones (e.g. clayey materials), determines the evolution of the shear strength during the sliding process. Starting from some field evidence of high pore pressures developed within the sliding body (near the main shear zone, mud injections infilling pre-existing fractures and joints had been observed in the landslide material), the authors formulated a block-on-slope model to study both the triggering and the propagation phase of the Jiufengershan catastrophic landslide. The model accounts for the partial transformation of frictional energy into heat through a parameter called “thermal absorption coefficient”, and subsequent temperature rise within the shearing zone. A parametric analysis is then presented, in which the kinematical parameters of a sliding block are calculated and different scenarios are examined depending on selected values of pore pressure and thermal absorption coefficient. In the “avalanche regime” case, representing the catastrophic sliding scenario which matches the field observations for the Jiufengershan slide, the block acquires a maximum velocity of 80 m/s and the final fault plane temperature reaches 113 °C. The time evolution of pore pressures and shear stress within the slip plane is also calculated. These results confirm the importance of the thermal pressurisation mechanism in interpreting high-speed sliding, as emerged in the preceding literature. Nevertheless, the proposed model equations are not able to interpret in a self-consistent manner the landslide motion coupled with the equations for heat flow and pore pressure evolution across the shear zone, and do not therefore appear as suitable a basis for constitutive improvements and future generalisation as the governing equations of Vardoulakis (2002a), which will be presented with more detail in Section 2.3.4.

2.3.3. The mechanism of thermal pressurisation

Frictional heating and thermal pressurisation are believed to be responsible for the weakening of shear resistance in a variety of contexts, when the material under consideration is subjected to relatively rapid temperature changes: from the reservoir rock involved in petroleum drilling and deep geological formations destined to store radioactive waste to rapid fault slip events, either due to tectonic (seismic) forces within the Earth crust or driven by gravity (landsliding) on the Earth surface. While the reason for heat production due to friction in the slip plane is rather intuitive, the mechanism of pressurisation deserves more attention since it manifests itself in different forms depending on the geomaterial in question.

Thermal pressurisation has been largely studied, especially when it occurs in rock leading to shear failure or hydraulic fracturing. Thermal weakening of rock faults during co-seismic slip has been extensively reviewed by Rice (2006), while Wibberley and Shimamoto (2005) and Sulem et al. (2007) have dealt with the thermal collapse of clay materials in fault zones. Vardoulakis (2000, 2002a), as mentioned in Section 2.3, has studied thermal pressurisation in clayey gouges with application to the dynamic behaviour of rapid landslides. Some experimental evidence of thermal pressurisation in both rocks and soils has been collected, among others, by Campanella and Mitchell (1968), Baldi et al. (1988), Sultan (1997), Sultan et al. (2002), Ghabezloo and Sulem (2008).

Efforts have been made in the literature to measure or calculate an average value for the key parameter that governs thermal pressurisation, which is the pressurisation coefficient λ_m, defined as the pore pressure increase due to a unit temperature increase under undrained conditions (at constant specific volume). It has emerged that this coefficient is far from being constant but depends on the considered material, in addition to the temperature and the stress level. Different average values for λ_m have been proposed, ranging two of orders of magnitude. For clay, Campanella and Mitchell (1968) found λ_m=0.01 MPa/°C, Vardoulakis (2002a) proposed λ_m=0.06 MPa/°C while Sulem et al. (2007) suggested λ_m=0.1 MPa/°C. For sandstone, Campanella and Mitchell (1968) proposed λ_m=0.05 MPa/°C while Rice (2006) estimated λ_m=0.92 MPa/°C for a 7 km deep fault in rock with intact walls.

A substantial difference in the thermal pressurisation mechanisms emerges between clay and rock materials: while rocks essentially behave elastically and λ_m is found to depend on thermo-elastic coefficients only, clays may undergo plastic straining upon thermal loading, giving rise to an additional dependency for λ_m on the soil's thermo-plastic contraction coefficient.

For rocks, the coefficient λ_m can be expressed as

$$\lambda_m = \left(\alpha_f - \alpha_n\right) / \left(c_f + c_n\right) \tag{1.1}$$

(Rice, 2006), where the α's are thermo-elastic expansion coefficients, the c's compressibility coefficients and the subscripts f and n denote the pore fluid and the pore volume respectively. By looking at the numerator of Equation (1.1), the physics behind thermo-elastic pressurisation are evident: pore pressure increases due to the fluid exhibiting a higher thermal volume increase than the pore space, i.e. the pressurisation mechanism depends on the differential expansion of the fluid and the pore space.

Experimental results for granular rock (Ghabezloo and Sulem, 2008) draw attention to the dependency of the pressurisation coefficient on stress and temperature. The latter has an influence on λ_m mainly due to the thermal increase of expansion coefficients, the former is important due to the stress-dependent character of the pore volume compressibility c_n. As a consequence of this variability Ghabezloo and Sulem (2008) calculated for Rothbach sandstone, by using a non-linear elastic model, that λ_m increases with both temperature and confining effective stress, ranging from 0.02 to 0.72 MPa/°C.

In clayey soils, as opposed to rocks, drained isotropic thermal loading tests have shown that the material, when heated in normally consolidated state, exhibits an irreversible contraction representing a structural collapse, and the corresponding overall (elasto-plastic) contraction coefficient is negative. Such contraction appears to be due to the change in thickness of the clay particles' double layer, where the increase in temperature eventually causes a breakdown of the adsorbed water (Sulem et al., 2007). Under conditions of slow or no drainage, such as those practically occurring during the rapid deformation of a thin, low-permeability shear zone, pore water pressure may develop as a result of heating (Hueckel and Pellegrini, 1991). In fact, the collapse of adsorbed water promotes the rearrangement of the soil skeleton, whose volume would tend to contract but given the isochoric conditions, pressurisation occurs instead.

Based on standard poro-mechanics and relevant assumptions, Sulem et al. (2007) deduced the expression of pressurisation coefficient for a clayey gouge at relatively low depth:

$$\lambda_m = -\frac{\left(\alpha - \alpha^e\right)}{c} \tag{1.2}$$

where α is the (negative) soil's elasto-plastic contraction coefficient, α^e the thermo-elastic contraction coefficient and c the compressibility of the material.

The pressurisation phenomenon essentially consists in an increase of pore pressure while the confining stress is constant, thus inducing a decrease of the effective stress: this induces elastic unloading for the geomaterial, and prescribes the choice of the elastic 'swelling' (unloading) value for the compressibility modulus of the pore space (Vardoulakis 2002a, Sulem et al. 2007, Ghabezloo and Sulem 2008). The topic of pressurisation coefficient for clays is expanded in Section 5.3.2.

2.3.4. A comprehensive thermo-poro-mechanical model

Vardoulakis (2002a) presented a physically based 1-D dynamic analysis able to interpret the post-failure regime of large landslides and rockslides consisting of a coherent mass sliding on a thin clayey layer, by considering the soil as a two-phase mixture of solids and fluid, and deriving the equations that govern the motion of the deforming shear band from the conservation laws of mass, momentum and energy. The considered time window is that of catastrophic acceleration, which starts at incipient failure and ends a few seconds later, when the acquired displacement and velocity are such that the landslide begins to break up into pieces. The model takes into account frictional heating, pore pressure build-up and thermoplastic collapse of the soil skeleton, leading to the vanishing of shear resistance and unconstrained acceleration. The problem variables evolve over time and vary only along the landslide thickness, since the model is one-dimensional.

The problem geometry is schematically divided up into two sub-units:

- The failure plane consisting of a thin shearband, where all the deformation is concentrated and frictional heating takes place,
- The overlying soil and rock mass, which at early stages of the sliding process can be considered as a rigid block (Figure 20).

The thickness of the shearband cannot be calculated from the model parameters and needs to be imposed *a priori*. Based on studies on the microscopic structure of clay (Morgenstern and Tschalenko, 1967), it has been estimated that the shearband thickness has to be in the order of a few hundreds of micrometers. Vardoulakis (2002a) thus suggests to impose a factor of 200 between particle size and shearband thickness, leading to an estimated thickness of d=1.4mm for a clay soil with $d_{50\%}$=0.007mm. This value highlights the remarkable difference between the characteristic lengths of the two sub-structures. Considering an average height of h=150m for the Vajont slide (Hendron and Patton, 1985), the geometrical scaling factor between slide and shearband thickness is 10^5, which justifies the need of splitting the problem into two sub-problems. In fact, being the characteristic dimensions and weights so different, inertial forces will have a different relative importance in the dynamical evolution of the two structures.

The shearband equations, which are derived from first principles, are coupled with the dynamical equation, which is derived from moment balance considerations and describes the movement of the overlying rigid block. The coupling variable between the two sub-units is the velocity at the upper boundary of the shearband, which also represents the sliding velocity of the whole rigid mass.

The model consists of a set of coupled partial differential equations describing the time evolution of temperature, pore pressure and velocity within the shearband. As the rigid mass starts moving downslope, strain and strain-rate softening occur within the shearband. At the same time, temperature within the slip zone is increased due to the heat produced by friction. As soon as a critical value of temperature is reached, the soil skeleton experiences thermo-plastic collapse showing volumetric contraction, thus feeding pore water pressure build-up. This in turn drastically decreases the shear resistance, and allows the overlying mass to move downslope ever more freely.

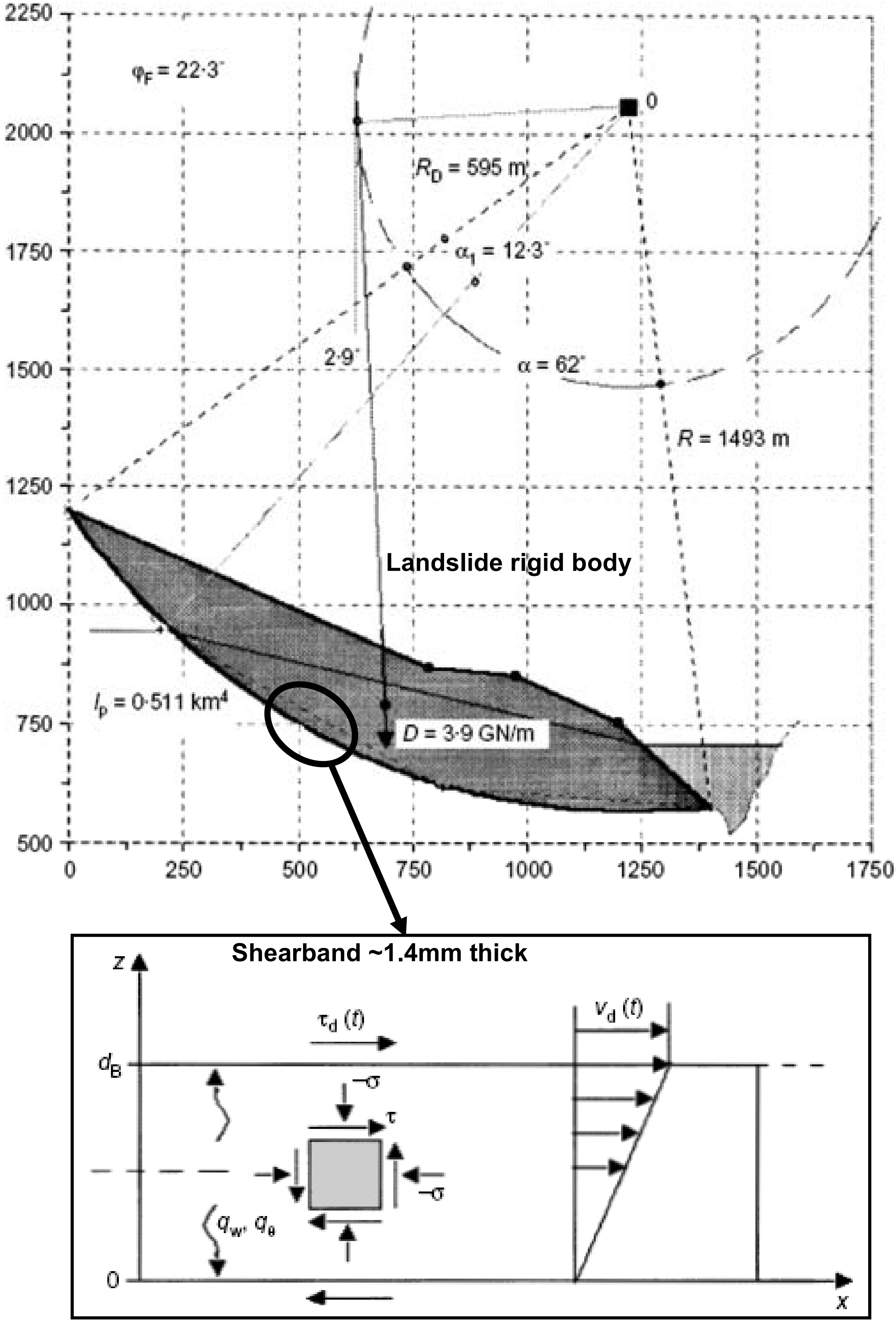

Figure 20. 'Section 5' of Vajont landslide and schematic enlargement of the shearband area, where all deformation is concentrated during sliding (after Vardoulakis, 2002a).

With regard to the constitutive model adopted, the soil is assumed to obey a simple Mohr-Coulomb law (see Figure 21): the stress state of a material point within the shearband lies on the linear yield locus and, as sliding progresses, moves along the envelope towards zero, as pressurisation takes place and reduces the normal effective stress. At the same time, the Mohr-Coulomb line decreases its slope due to reduction of the soil friction angle with increasing displacement and velocity (i.e., strain and strain-rate friction softening occurs). The material softening laws are derived from the experimental results reported by Tika and Hutchinson (1999), who performed ring shear experiments on the Vajont failure surface clay. The experimental data are interpolated with hyperbolas (see Figure 22 for displacement softening, and Figure 23 for velocity softening) and the corresponding mathematical laws are implemented in the landslide model.

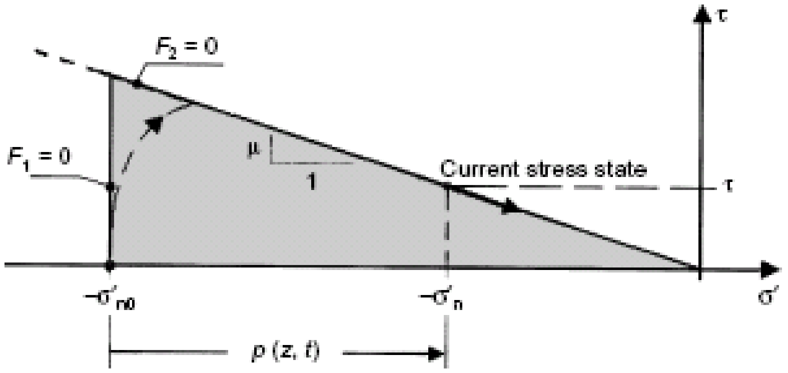

Figure 21. Scheme of the Mohr-Coulomb constitutive model from Vardoulakis (2002a). Compressive stress is taken negative in this plot.

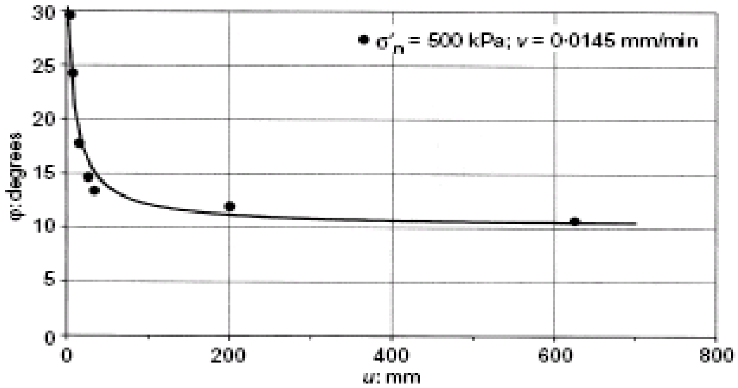

Figure 22. Displacement softening data from ring shear tests (Tika and Hutchinson, 1999) and hyperbolic interpolation law (Vardoulakis, 2002a).

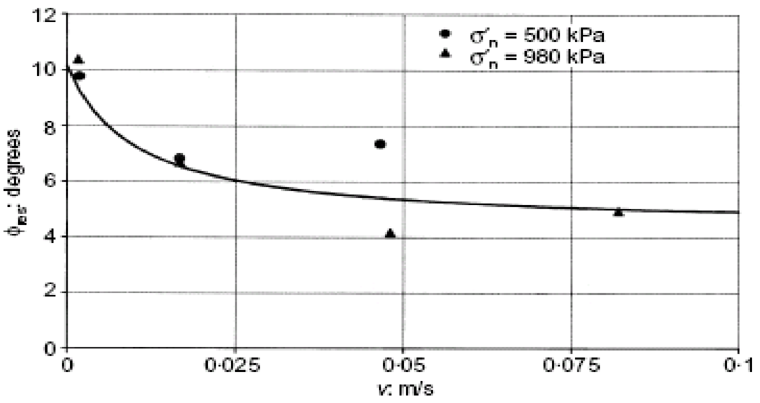

Figure 23. Velocity softening data from ring shear tests (Tika and Hutchinson, 1999) and hyperbolic interpolation law (Vardoulakis, 2002a).

2.3.4.1. The shearband equations

The first model equation, derived by Vardoulakis (2000) from the local form of the energy balance law within the shearband, describes the 1-D time evolution of temperature θ within the shearband:

$$\frac{\partial \theta}{\partial t} = k_m \frac{\partial^2 \theta}{\partial z^2} + \hat{\mu}(\gamma, \dot{\gamma}) \frac{|\sigma'_{n0} - u| \dot{\gamma}}{j(\rho C)_m}. \tag{2.1}$$

The first term on the right-hand side is a heat diffusion term, where k_m is a constant diffusivity coefficient, and the second one is a heat generation term, where $\hat{\mu}(\gamma, \dot{\gamma}) |\sigma'_{n0} - u| \dot{\gamma} = D$ is the dissipation term, taken equal to the plastic work. Dissipation depends on the plastic shear strain rate $\dot{\gamma}$ (conditions of simple shear inside the shearband are assumed), the initial effective stress σ'_{n0}, the excess pore pressure u and the strain- and strain rate-dependent friction coefficient $\hat{\mu}$. The expression $|\sigma'_{n0} - u|$ reflects the effective stress principle: any generated excess pore pressures need to be subtracted from σ'_{n0}, the initial vertical effective stress (i.e., the effective stress acting on the shearband in static conditions). Finally, $j(\rho C)_m = C_f$ is a thermal constant that derives from the energy balance (Vardoulakis, 2000), where j is the mechanical equivalent of heat, $(\rho C)_m$ the product of the density and the specific heat of the soil-water mixture.

The second equation describes the time evolution of excess pore pressure u generated within the shearband:

$$\frac{\partial u}{\partial t} = \frac{\partial}{\partial z}\left(c_v \frac{\partial u}{\partial z} \right) + \lambda_m \frac{\partial \theta}{\partial t}. \tag{2.2}$$

The first term on the right-hand side is a diffusion term, where c_v is a temperature-dependent consolidation coefficient. If this was the only nonzero term on the right hand side, Equation (2.2) would correspond to a classic one-dimensional consolidation equation (e.g. see Powrie, 1997) describing the dissipation of excess pore water pressures in a porous medium. The second term describes pore pressure generation, which depends on the heat produced, thus providing the cause of the occurrence of excess pore pressures. The term λ_m is the temperature- and pore pressure-dependent pressurisation coefficient (cf. sections 2.3.3 and 5.3.2), equal to the ratio between the thermoplastic contraction coefficient and the compressibility of the soil. Coefficient λ_m is set to zero until the temperature reaches the critical value for thermal collapse of the soil skeleton, which in turn is determined from experimental data collected by Sultan (1997). The determination of pressurisation coefficient nevertheless remains for the author rather uncertain, due to a lack of direct experimental data (Vardoulakis, 2002a).

The third equation, derived from momentum balance inside the shear band, describes the velocity profile therein:

$$\frac{\partial v}{\partial t}=\frac{1}{\rho}\left[-\hat{\mu}\left(\gamma,\dot{\gamma}\right)\frac{\partial u}{\partial z}+H\left|\sigma'_{n0}-u\right|\left(\frac{\partial^2 v}{\partial z^2}\right)\right], \tag{2.3}$$

where $H=\dfrac{\partial\hat{\mu}}{\partial\dot{\gamma}}$ is the "frictional rate sensitivity". Since the structure of this equation would lead to mathematical ill-posedness in the case $H\leq 0$ (Vardoulakis, 2001 and 2002a), a "second-gradient regularisation" (Vardoulakis and Sulem, 1995) of the softening law was applied, leading to express (2.3) as a function of the fourth-order spatial derivative of velocity. On the other hand, since after integration of the momentum equation the resulting spatial profile of velocity within the shearband is very close to a linear one (Vardoulakis 2001), the author suggests that a "linear approximation" for the shearband velocity could be adopted instead of Equation (2.3). This enables us to replace (2.3) with the expression

$$v=v_d\left(t\right)\frac{z}{d} \tag{2.4}$$

(Vardoulakis 2000), where z is the coordinate defining the spatial position along the domain thickness, d the (imposed) shearband thickness and $v_d\left(t\right)$ is the time evolution law for the velocity of the landslide, which coincides with the shearband velocity at its upper boundary (cf. Figure 20). The governing equations for the shearband are therefore reduced to the first two, and (2.4) can be expressed in function of the landslide velocity, as soon as we proceed to consider the second sub-structure, constituted by the landslide overburden.

2.3.4.2. The dynamical equation

Vardoulakis (2002a) presented a dynamic slip-circle analysis in order to apply the above shearband model to the case history of Vajont, of which many field data are available (Muller, 1964, Hendron and Patton, 1985, Tikka and Hutchinson 1999). Assuming a rigid-body rotational failure mechanism, as can be seen from the drawings of 'section 5' of the Vajont slide (cf. Hendron and Patton, 1985 and Figure 20), the dynamical equation is obtained from the moment balance of the involved driving and resisting forces:

$$\frac{dv_d}{dt} = R\omega_0^2 \left(A(\mu_m) + \frac{u_d(t)}{p_c(\mu_m)} \right) \tag{2.5}$$

where ω_0 is a constant depending on the landslide geometry, A and p_c two functions of both the mobilised friction coefficient and the friction coefficient for incipient failure for the considered critical failure circle. The variable u_d is the excess pore pressure at $z = d$, i.e. at the shearband-rigid block interface, whose evolution law is described by Equation (2.2). Equation (2.5) was derived with the fundamental assumption that the normal effective stress is constant along the whole failure circle, and set equal to a mean value.

2.3.4.3. The landslide equations

The above governing equations form a system whose solution yields the time evolution of temperature, pore pressure and slide velocity:

$$\begin{cases} \text{(I)} & \dfrac{\partial \theta}{\partial t} = k_m \dfrac{\partial^2 \theta}{\partial z^2} + \dfrac{D(u, \dot{\gamma})}{C_f} \\ \text{(II)} & \dfrac{\partial u}{\partial t} = \dfrac{\partial}{\partial z}\left(c_v(\theta) \dfrac{\partial u}{\partial z} \right) + \lambda_m(\theta, u) \dfrac{\partial \theta}{\partial t} . \\ \text{(III)} & \dfrac{dv_d}{dt} = R\omega_0^2 \left(A(\mu_m) + \dfrac{u_d}{p_c(\mu_m)} \right) \end{cases} \tag{2.6}$$

Several couplings (i.e. interdependencies between variables) appear in the above equations: Equation (2.6)-(I) contains pore pressure-, displacement- and velocity-dependency through the dissipation term, Equation (2.6)-(II) includes temperature-dependency in the nonlinear coefficients and the second addend and Equation (2.6)-(III) is coupled to the other two through excess pore pressure and the displacement- and velocity-dependent mobilised friction coefficient.

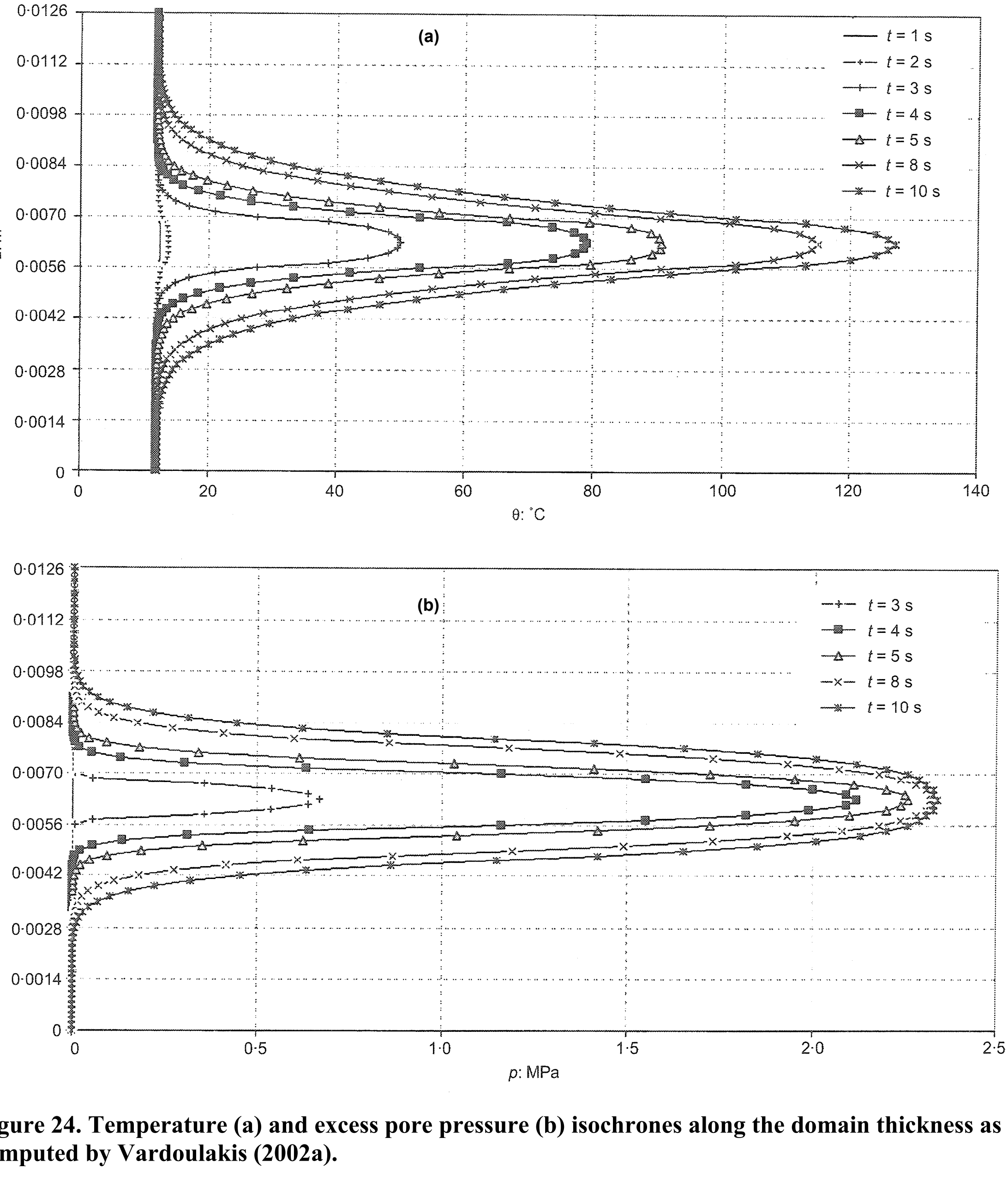

Figure 24. Temperature (a) and excess pore pressure (b) isochrones along the domain thickness as computed by Vardoulakis (2002a).

2.3.4.4. Vardoulakis' computational results and discussion

After being made dimensionless, equations (2.6) were integrated numerically over a thickness domain comprising the shearband and a portion of the surrounding soil (in both directions of z). The thickness domain was chosen to be large enough to be able to assume that at the boundaries, the excess pore pressure is zero and the temperature is equal to the ambient temperature. On the other hand, at the shearband lower boundary (and in the underlying domain, for $z \leq 0$) the velocity is zero, while at the shearband upper boundary (as well as the overlying thickness domain, for $z \geq d$) the velocity is equal to the slide velocity v_d (Figure 20).

The computational results of Vardoulakis (2002a) for the temperature and pore pressure isochrones over the thickness domain, concerning a time window of 10 seconds after initiation of the Vajont landslide can be seen in Figure 24. The considered time window was chosen so that the corresponding displacement of the rotating body was not "exceedingly large" (Vardoulakis, 2002a) and thus the hypothesis of rigid body could remain valid. Furthermore, possibly more significant are the computed values of the slide velocity (Figure 25) and displacement (Figure 26) over time. At t=8s after slide activation, v_d=20m/s and displacement x_d=74m. These values are consistent with those observed in the Vajont landslide, highlighting the usefulness of this model towards the development of a predictive tool.

However, it may be observed that the constitutive law adopted for the soil restricts the applicability of the model, as it cannot capture the full range of temperature-dependent soil behaviour, including thermal hardening and the possible decrease of the friction coefficient alongside temperature (cf. Chapters 3 and 4), and it cannot be easily generalised in 2- and 3-D in the future. Furthermore, there are uncertainties in the structure and values of the pressurisation coefficient λ_m. In the forthcoming chapters, this landslide model will be improved by resorting to a more representative constitutive law.

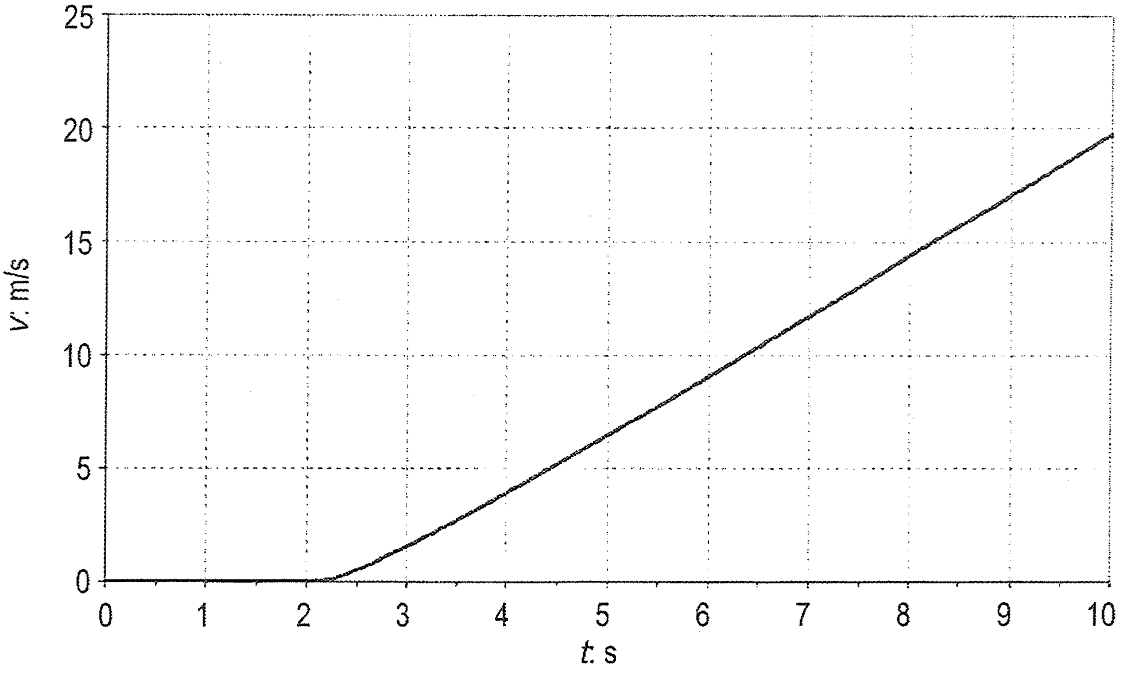

Figure 25. Computed landslide velocity over time, for the Vajont case (Vardoulakis, 2002a).

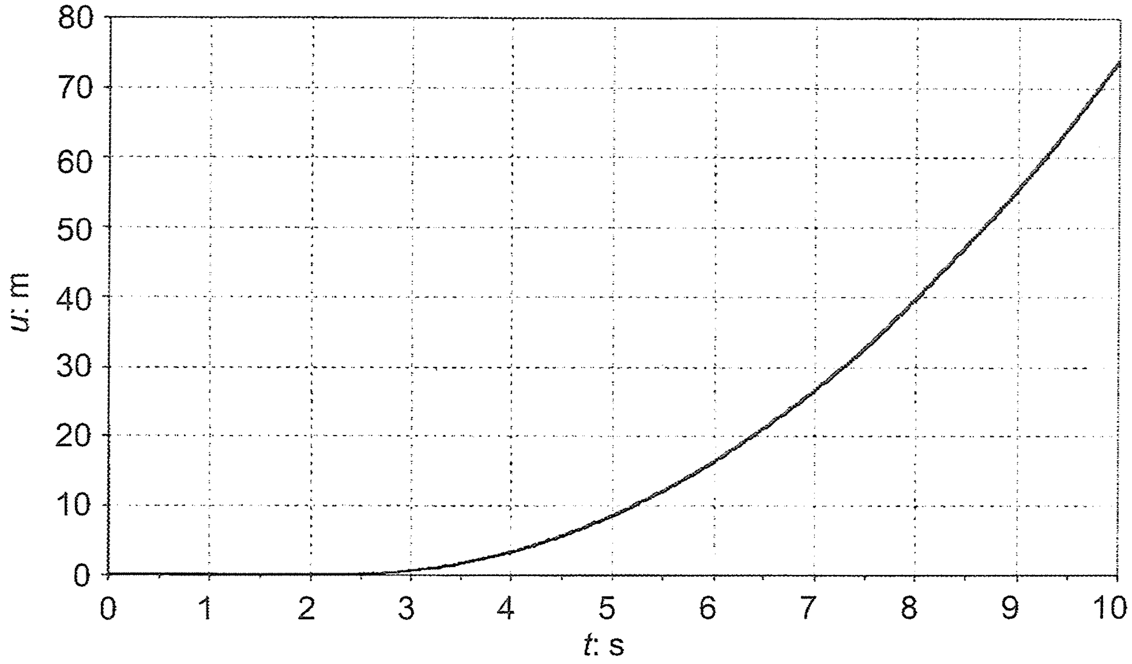

Figure 26. Computed landslide displacement over time, for the Vajont case (Vardoulakis, 2002a).

Chapter 3. Thermo-plasticity in clays. Review of existing models

3.1. The need for thermoplastic constitutive modelling

In Chapter 1, we have examined landslide case histories and existing models which have been proposed in the literature to explain the unexpected loss in shear strength observed in some catastrophic landslide cases. It emerged that a possible explanation to these phenomena can be given by taking into account frictional heating and thermal pressurisation. Vardoulakis (2002a) presented a comprehensive thermo-poro-mechanical model, able to provide an effective back-analysis of the final collapse phase of the Vajont slide. Nevertheless, the specialised constitutive law used for the soil restricts the model's applicability. In particular, it cannot capture the full range of temperature-dependent soil behaviour observed experimentally, and it cannot be easily generalised to two- or three-dimensional problems. In order to improve the model, account should be taken for the temperature dependence of the mechanical behaviour of soil, since whenever heat production is involved, different mechanisms may arise that lead the soil-water mixture to alter its volumetric behaviour and show plastic yield in unexpected conditions. As a first step towards the development of a more realistic constitutive law, it is necessary to gather data and insight into the existing theories on the thermoplastic behaviour of soils.

3.2. The 'ingredients' of soil elasto-plasticity

The main notions of soil elasto-plasticity are briefly recalled hereafter, for ease of reference in the forthcoming sections.

The yield locus defines the combinations of mean effective stress and deviatoric stress at which plastic yield begins to occur in the soil (e.g. see Muir Wood, 1990). When a plastic loading state is attained, irrecoverable deformations develop (plastic flow occurs), alongside a change in size of the yield curve itself. Consistently with the Modified Cam-Clay theory (MCC) of Roscoe and Burland (1968), in isothermal conditions the size of the yield locus

$$f = f\left(p', q, \sigma'_c\left(\varepsilon_v^p\right)\right) \tag{3.1}$$

is a function of plastic volumetric strain through the 'hardening relationship', defining the variation of apparent preconsolidation stress σ'_c with volumetric strain ε_v^p. When plastic loading occurs, the elastic domain, enclosed within the yield surface, expands in case of hardening, at positive (compactive) volumetric strain rates; and shrinks in case of softening, at negative (dilative) volumetric strain rates. When temperature variations $\Delta\theta$ occur, experimental evidence indicates that the elastic domain contracts with $\Delta\theta > 0$ and enlarges with $\Delta\theta < 0$.

The generalisation of the Critical State model to introduce explicit dependency on temperature consists of rewriting of the following classic "ingredients of elasto-plasticity" (Muir Wood, 1990):

- *Elasticity law*, describing the recoverable deformations;
- *Yield condition*, describing the boundary of the stress region within which it is possible to describe the deformation as elastic and recoverable;
- *Hardening rule*, describing the way in which the absolute magnitude of the plastic deformation is linked with the changing size of the yield locus.
- *Plastic potential (flow rule)*, to specify the relative magnitudes of various components of plastic deformation that occurs when the soil is yielding.

3.3. Hueckel's constitutive model

A thermo-elasto-plastic constitutive model for saturated soils was developed by Hueckel and co-workers, based on experimental evidence, modification of the well-known Critical State Soil Mechanics elasto-plastic theory (Roscoe and Schofield 1963, Schofield and Wroth 1968, Roscoe and Burland 1968) and on Prager's thermoplasticity theory (Prager, 1958). The original model interprets the thermoplastic behaviour of the soil skeleton and is used to describe drained failure (Hueckel and Baldi, 1990 and Hueckel and Borsetto, 1990), while a second model for thermal volume change of pore water (Baldi et al., 1988, Hueckel and Pellegrini, 1991) is used in combination with the former to interpret undrained failure.

Hueckel's model is described hereafter in terms of the four components of elasto-plasticity described in Section 3.2.

3.3.1. Thermoelasticity

It has been experimentally shown (Hueckel and Peano, 1987), mainly from carrying out temperature-controlled triaxial tests, that elastic thermal expansion tends to occur at low effective confining stress (i.e., mainly in overconsolidated samples), and elasto-plastic thermal compaction tends to occur at higher effective confining stress (i.e., mainly in normally-consolidated samples).

Thermoelastic volumetric strains, ε_v^{te}, in thermal conditions at constant isotropic stress, are non-linearly dependent on the mean effective stress *p'* and the temperature θ.

The thermoelastic deviatoric strain, ε_q^{te}, is on the contrary purely mechanical (despite its name, due to reasons of consistency of notation in a model that accounts for temperature effects), and proportional to deviatoric stress. The elastic constitutive laws, expressed in 'triaxial' notation (i.e., in terms of isotropic and deviatoric stress), are

$$\varepsilon_v^{te} = \frac{K}{1+e_0} \ln \frac{p'}{p'_0} - \alpha \Delta\theta \tag{3.2}$$

$$\varepsilon_q^{te} = \frac{1}{3G}\left(q - q_0\right) \tag{3.3}$$

where:

$$p' = \frac{\sigma_1' + 2\sigma_3'}{3}$$

$$q = \sigma_1' - \sigma_3'$$

K = bulk modulus at reference temperature,

G = shear modulus at reference temperature,

p_0', q_0 = values of *p'* and *q* at initial state,

α = coefficient of thermal expansion of clay, which includes the coefficient of expansion of the clay solid mineral and that of porous skeleton, for an overall dependency on four coefficients of "thermoplastic sensitivity" (Hueckel and Pellegrini, 1991).

3.3.2. Yield surface

The elliptical yield locus, derived from that of MCC, is expressed as:

$$f = \left(\frac{2p'}{\sigma'_c\left(\varepsilon_v^{tp}, \Delta\theta\right)} - 1 \right)^2 + \frac{4q^2}{\left[M\sigma'_c\left(\varepsilon_v^{tp}, \Delta\theta\right)\right]^2} - 1 \tag{3.4}$$

In the above, the change in size of the yield surface is expressed through the change of the temperature-dependent apparent preconsolidation stress σ'_c, i.e. by the hardening rule. The critical state parameter M is here considered to be independent of temperature.

3.3.3. Hardening relationship

The evolution law of the apparent preconsolidation isotropic stress is given by

$$\sigma'_c = 2\left(\bar{a}\exp\left\{\frac{1}{\lambda - K_T}\left[e_1 + (1+e_0)\varepsilon_v^{tp}\right]\right\} + a_1\Delta\theta + a_2\,\mathrm{sign}(\Delta\theta)\Delta\theta^2\right) \tag{3.5}$$

where:

$K_T = \dfrac{K}{1+e_0} + (\alpha_1 + \alpha_3\Delta\theta)\Delta\theta$ is a temperature dependent bulk modulus,

λ is the slope of the isotropic normal-compression line,

$\bar{a}$ = coefficient with the dimensions of a pressure,

e_0, e_1 = reference void ratio values,

a_1, a_2 = coefficients of thermal sensitivity of the yield surface.

3.3.4. Flow rule

The flow rule defines the mode of plastic deformation through the plastic potential function, which specifies the relative magnitudes of shear and volumetric strain. Both elastic and plastic strains occur at yielding, and their rates follow the additivity principle (Hueckel and Pellegrini, 1991):

$$\begin{aligned}\dot{\varepsilon}_v &= \dot{\varepsilon}_v^{te} + \dot{\varepsilon}_v^{tp}\\ \dot{\varepsilon}_q &= \dot{\varepsilon}_q^{te} + \dot{\varepsilon}_q^{tp}\end{aligned} \tag{3.6}$$

In general plasticity, the flow rule has the form $\dot{\varepsilon}^p = \dot{\lambda}\dfrac{\partial g}{\partial \boldsymbol{\sigma}}$, where $\dot{\varepsilon}^p$ is the plastic strain rate, g the plastic potential, $\boldsymbol{\sigma}$ the stress tensor and $\dot{\lambda}$ the scalar-valued plastic multiplier, whose expression needs to be determined by the conditions which exist when plastic loading continues (Section 3.3.5).

Hueckel and Borsetto (1990) proposed a non-associative flow rule, consisting of a single plastic potential function g, but two distinct plastic multipliers, a 'volumetric' one, $\dot{\lambda}_v$, and a 'deviatoric' one, $\dot{\lambda}_q$ so that:

$$\dot{\varepsilon}_v^{tp} = \dot{\lambda}_v\frac{\partial g}{\partial p'} \tag{3.7}$$

$$\dot{\varepsilon}_q^{tp} = \dot{\lambda}_q \frac{\partial g}{\partial q} \tag{3.8}$$

where the multipliers, postulated by to be positive at plastic yielding and zero otherwise, are functions of the stress and temperature rates.

3.3.5. Consistency condition and plastic multiplier

The multiplier $\dot{\lambda}_v$ is obtained through the so-called consistency condition. This equation expresses an important postulate of theoretical plasticity, stating that if a stress increment causes plastic loading and a corresponding change of plastic volumetric strains, it must lie again on the new updated yield surface, which obeys the yield locus equation expressed now in terms of the updated values of stress and plastic strain. Analytically, the consistency condition can be expressed as

$$\dot{f} = \frac{\partial f}{\partial p'}\dot{p}' + \frac{\partial f}{\partial q}\dot{q} + \frac{\partial f}{\partial \theta}\dot{\theta} + \frac{\partial f}{\partial \varepsilon_v^{tp}}\dot{\varepsilon}_v^{tp} = 0 \tag{3.9}$$

(Hueckel and Borsetto, 1990), where *f* is the yield locus expressed in this case by (3.4). The plastic multiplier can be calculated by substituting (3.7) in the above (3.9), thus obtaining

$$\dot{\lambda}_v = \frac{\frac{\partial f}{\partial q}\dot{q} + \frac{\partial f}{\partial p}\dot{p} + \frac{\partial f}{\partial \theta}\dot{\theta}}{\tilde{H}} \tag{3.10}$$

where the ‘hardening modulus’ $\tilde{H}$ has expression

$$\tilde{H} = -\frac{\partial f}{\partial \varepsilon_v^p}\frac{\partial g}{\partial p'}. \tag{3.11}$$

Experimental observations led the authors to decide a different general form for the multiplier Λ_q, which reflects the “deviation of thermoplastic strain rate from the normal to mechanical plastic potential” (Hueckel and Borsetto, 1990):

$$\dot{\lambda}_q = \dot{\lambda}_v + \frac{f_1}{\tilde{H}}\dot{\theta} \tag{3.12}$$

where f_1 is a function of stress, temperature and plastic strain.

3.3.6. Loading/unloading and hardening/softening conditions

To complete the description of their constitutive model, Hueckel and Borsetto (1990) specified the loading and unloading criteria, as these will differ from classic ‘isothermal’ plasticity due to the presence of temperature as an additional variable featuring in the yield locus expression.

The condition of elastic unloading requires that $f < 0$, or $f = 0$ and $\frac{\partial f}{\partial q}\dot{q} + \frac{\partial f}{\partial p'}\dot{p}' + \frac{\partial f}{\partial \theta}\dot{\theta} < 0$ (or equivalently, $\dot{f} < 0$ from the consistency condition (3.9), since at elastic states $\dot{\varepsilon}_v^{tp} = 0$), at $\dot{\lambda}_v = 0$.

Plastic loading, instead, requires $f = 0$ and $\dot{f} = \frac{\partial f}{\partial p'}\dot{p}' + \frac{\partial f}{\partial q}\dot{q} + \frac{\partial f}{\partial \theta}\dot{\theta} + \frac{\partial f}{\partial \varepsilon_v^{tp}}\dot{\varepsilon}_v^{tp} = 0$, at $\dot{\lambda}_v > 0$. At plastic loading we can have the two cases of hardening (increase of elastic domain) and softening (decrease of elastic domain).

The condition of hardening is

$$\frac{\partial f}{\partial q}\dot{q} + \frac{\partial f}{\partial p'}\dot{p}' + \frac{\partial f}{\partial \theta}\dot{\theta} > 0 \text{, at } \tilde{H} > 0 \text{, } \frac{\partial g}{\partial p'} > 0$$

while the condition for softening is

$$\frac{\partial f}{\partial q}\dot{q} + \frac{\partial f}{\partial p'}\dot{p}' + \frac{\partial f}{\partial \theta}\dot{\theta} < 0 \text{, at } \tilde{H} < 0 \text{, } \frac{\partial g}{\partial p'} < 0 .$$

It can be seen above that the same condition, $\frac{\partial f}{\partial q}\dot{q} + \frac{\partial f}{\partial p'}\dot{p}' + \frac{\partial f}{\partial \theta}\dot{\theta} < 0$, represents both the situation of elastic unloading and that of thermoplastic loading at softening. To distinguish between the two cases, it is sufficient to look at the plastic multiplier $\dot{\lambda}_v$ and check whether this is positive or zero, as specified in the conditions above.

We observe that in order to gain a better understanding of the relationship between the sign of the expression $\tilde{p} = \left(\frac{\partial f}{\partial q}\dot{q} + \frac{\partial f}{\partial p'}\dot{p}' + \frac{\partial f}{\partial \theta}\dot{\theta} \right)$ and the loading/unloading condition, it is perhaps more convenient to look at its geometrical meaning. The sign of $\tilde{p}$ determines the direction of the 'stress-temperature rate' vector $\left(\dot{p}', \dot{q}, \dot{\theta}\right)$ by revealing the angle formed between the direction of loading increment and the normal to the yield surface. In fact, in contrast with isothermal plasticity, the yield function now depends on three variables $\left(p', q, \theta\right)$ and may be visualised in three dimensions. In this framework, $\tilde{p} > 0$ is the mathematical condition for which the stress-temperature rate vector points outside the yield locus, while the condition $\tilde{p} < 0$ means an inward orientation of the stress-temperature rate vector with respect to the yield surface. We can now understand why in thermal plasticity the distinction between hardening and softening cannot be uniquely defined by the orientation of the two-dimensional 'stress rate' vector ($\dot{p}', \dot{q}$)

(Hueckel and Borsetto 1990): the stress rate vector $\left(\dot{p}',\dot{q}\right)$ is no other than the projection of the stress-temperature rate vector $\left(\dot{p}',\dot{q},\dot{\theta}\right)$ into the $\left(p',q\right)$ plane. Thus, the stress rate vector (in two dimensions) can point inwards at hardening, while the stress-temperature rate vector (in three dimensions) still points outwards. As an example, in Figure 27 this situation is visualized in three dimensions, where the modified Cam-Clay ellipse shrinking with increasing temperature describes a 'saddle-shaped' function in (p,q,θ) space. A sample stress-temperature increment vector $\Delta\mathrm{v}=\left(\Delta p',\Delta q,\Delta\theta\right)$ has been drawn in Figure 27, which can be shown to represent a case of hardening by projecting it both in the (q, θ) plane (2-D section at p'=constant) and in the $\left(p',q\right)$ plane (2-D section at θ=constant), in Figure 28: despite its projection on the $\left(p',q\right)$ plane points inwards, the $\left(q,\theta\right)$ projection reveals that the stress-temperature rate vector $\left(\dot{p}',\dot{q},\dot{\theta}\right)$ actually points outwards.

The above depicted situation is illustrated analytically by Hueckel and Borsetto (1990), together with the opposite and symmetric situation of having an outward stress rate at softening.

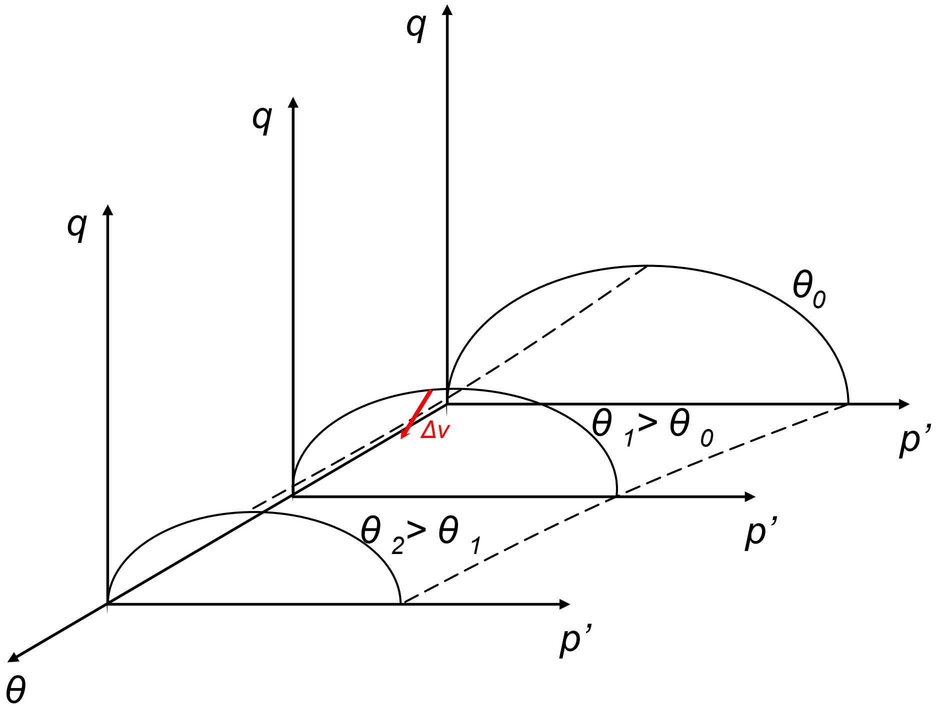

Figure 27. Sample thermo-plastic yield locus in three dimensions, with sample stress-temperature rate vector Δv.

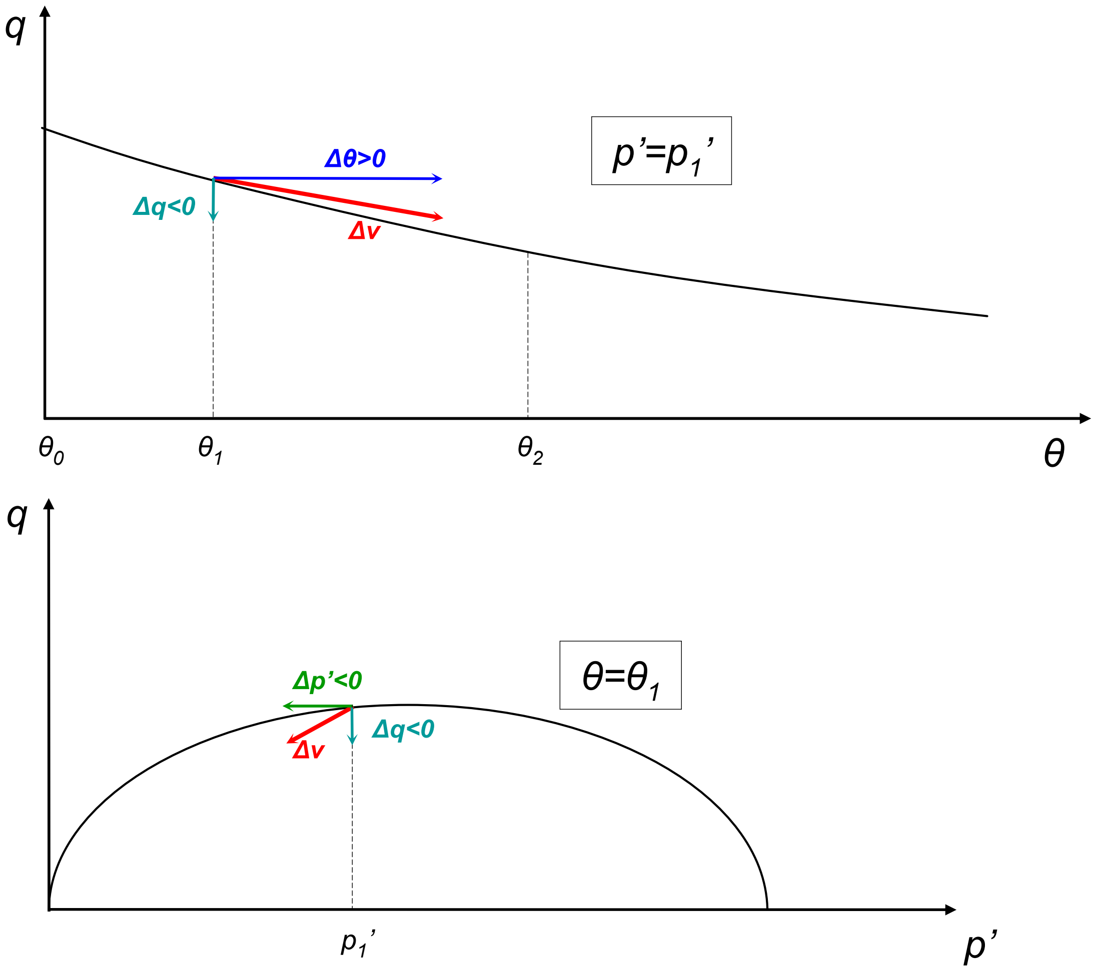

Figure 28. Projections of the stress-temperature rate vector Δv (Figure 27) on the deviatoric stress vs. temperature plane and on the deviatoric stress vs. mean effective stress plane.

3.3.7. Associative flow rule

Despite the non-associative flow rule assumed in the formulation of the constitutive model by Hueckel and Borsetto (1990), and despite the experimental evidence of some non-associative behaviour (Hueckel and Baldi, 1990), the model adopted by the authors for carrying out numerical simulations (Hueckel and Pellegrini, 1991) is associative. Furthermore, to our knowledge no explicit formulation is given for the plastic potential g in any of the authors' publications on the subject. Adopted for simplicity, the associative rule prescribes that the yield and plastic potential functions coincide, i.e. $g = f$, and also $\dot{\lambda}_v = \dot{\lambda}_q$. The flow rule (Section 3.3.4) may be thus simplified as

$$\begin{aligned} \dot{\varepsilon}_v^{tp} &= \dot{\lambda}\frac{\partial f}{\partial p'} \\ \dot{\varepsilon}_q^{tp} &= \dot{\lambda}\frac{\partial f}{\partial q} \end{aligned} \qquad (3.13)$$

where $\dot{\lambda}$ is expressed in the same way as $\dot{\lambda}_v$ in Equation (3.10).

3.4. Laloui's constitutive model

3.4.1. Introduction

The second thermoplastic model that we are going to review was developed by Laloui et al. (2002, 2005) and Laloui and Cekerevac (2003) and includes the description of an isotropic and a deviatoric yield mechanism. Laloui and co-workers also proposed more sophisticated cyclic thermoplastic and thermo-viscoplastic orthotropic models in order to take soil anisotropy into account (Modaressi and Laloui 1997, Laloui 2001); however, we will not extend our review to these models since treating anisotropic soils is outside the scope of this work.

Laloui's thermo-mechanical model, similarly to Hueckel's model, mainly explores the volumetric behaviour and the isotropic yield mechanism of clays subjected to temperature changes. In a more recent paper, a theoretical formulation including a separate deviatoric mechanism was added to complete the constitutive framework (Laloui et al., 2005). Experiments were performed by the authors using a standard triaxial apparatus, modified to enable temperature control. Laboratory tests involved either thermal loading of clay samples at constant confining stress, or isothermal isotropic compression tests carried out at different (constant) temperatures.

The structure of this model is similar to that of Hueckel's model, but appears simpler in that it involves fewer material parameters and the yield locus is assumed to coincide with the plastic potential (associative flow rule). On the other hand, the authors resort to concepts from the theory of 'multi-mechanism plasticity' (Koiter 1960, Mandel 1965) to formulate the equations describing the deviatoric thermoplastic behaviour, resulting in the need for two separate plastic multipliers, despite the assumption of associative flow rule.

The total strain rate tensor due to thermo-mechanical loading is composed of a thermo-elastic part, $\dot{\varepsilon}^{te}$, and thermo-plastic part, $\dot{\varepsilon}^{tp}$:

$$\dot{\varepsilon}_{ij} = \dot{\varepsilon}_{ij}^{te} + \dot{\varepsilon}_{ij}^{tp} . \tag{3.14}$$

the elastic and plastic contributions to the total strain rate are discussed separately hereafter.

3.4.2. Thermoelasticity

The volumetric thermoelastic strain rate is the sum of a reversible thermal strain and a mechanical strain component:

$$\dot{\varepsilon}_v^{te} = \frac{\dot{p}'}{K} + \beta_s \dot{\theta} \tag{3.15}$$

where β_s is the elastic thermal expansion coefficient of the solid skeleton, which is allowed to vary non-linearly with temperature and pressure (Laloui and Cekerevac, 2003). The elastic bulk modulus depends on the stress value according to

$$K = K_{ref} \left(\frac{p'}{p_{ref}} \right)^n \tag{3.16}$$

where n is a material constant.

The (purely mechanical) deviatoric elastic strain rate is written as

$$\dot{\varepsilon}_d^e = \frac{\dot{\sigma}^d}{G} \tag{3.17}$$

where $\dot{\sigma}^d$ is the deviatoric effective stress tensor, and the shear elastic modulus is given by

$$G = G_{ref} \left(\frac{p'}{p_{ref}} \right)^n . \tag{3.18}$$

3.4.3. Multi-mechanism thermoplasticity

Laloui et al. (2005) propose to formally sub-divide their plastic framework into an isotropic and a deviatoric mechanism, giving rise to two different flow relationships and two consistency conditions. The total plastic strain rate is presented as the sum of two partial strain rates:

$$\dot{\varepsilon}_{ij}^{tp} = \sum_{k=1}^{2} \dot{\varepsilon}_{ij,k}^{tp} = \dot{\varepsilon}_{ij,iso}^{tp} + \dot{\varepsilon}_{ij,dev}^{tp} \tag{3.19}$$

(Laloui et al., 2005), where each strain rate occurs if the stress state reaches the corresponding yield function. The isotropic yield surface f_{Ti} is identified with the curve describing the temperature dependency of apparent preconsolidation stress in the (p', θ) plane, while the deviatoric yield surface f_{Td} coincides with the original Cam Clay (OCC) yield envelope (Roscoe and Schofield, 1963) in the (p', q) plane. In this multi-mechanism framework, a general form of flow rule can be written as:

$$\dot{\varepsilon}_{ij}^{tp} = \sum_{k=1}^{2} \dot{\lambda}_k \frac{\partial g_k}{\partial \sigma'_{ij}} \tag{3.20}$$

where one plastic potential and one plastic multiplier per mechanism are employed.
The two yield functions can be represented together, in a 3-dimensional space in order to define a closed domain representing the elastic region (Figure 32).

3.4.3.1. Isotropic yield mechanism and flow rule

The expression of the isotropic yield limit is

$$f_{Ti} = p' - \sigma'_c\left(\varepsilon_v^p, \theta\right) r \tag{3.21}$$

(Laloui et al., 2005). In the above, σ'_c is the apparent isotropic preconsolidation stress and r represents the “degree of plastification” to account for “progressive evolution of the yield limit during loading” (Laloui et al., 2005).

The apparent preconsolidation stress is expressed as a function of volumetric plastic strain and temperature (Laloui and Cekerevac, 2003):

$$\sigma'_c = \sigma'_{c0}\left(\theta_0\right)\left[1 - \gamma \log\left(\theta/\theta_0\right)\right] \exp\left(\tilde{\beta}\varepsilon_v^p\right). \tag{3.22}$$

In the above, $\sigma'_{c0}\left(\theta_0\right)$ is the preconsolidation stress at reference temperature, γ is a material parameter defining the rate of decrease of σ'_c with θ and $\tilde{\beta}$ is the plastic compressibility modulus.

By substituting expression (3.22) into the yield locus expression, we obtain the final form of the isotropic thermoplastic yield locus:

$$f_{Ti} = p' - \sigma'_{c0}\left(\theta_0\right)\left[1 - \gamma \log\left(\theta/\theta_0\right)\right] \exp\left(\tilde{\beta}\varepsilon_v^p\right) r. \tag{3.23}$$

Laloui’s isotropic yield limit is represented in Figure 29 along with some experimental data points. At the left of the curve, any stress or temperature change causes reversible strains. As soon as the curve is attained by an increase in mean stress and/or temperature, plastic strains occur.

The flow rule proposed by the authors is associated. The ‘isotropic contribution’ to the total strain rate (Laloui et al., 2005) is:

$$\dot{\varepsilon}_v^p = \dot{\lambda}_i \frac{\partial g_{Ti}}{\partial p'} = \dot{\lambda}_i \frac{\partial f_{Ti}}{\partial p'} = \dot{\lambda}_i. \tag{3.24}$$

3.4.3.2. Deviatoric yield mechanism and flow rule

The deviatoric yield surface proposed by Laloui et al. (2005) is based on the OCC yield locus:

$$f_{Td} = \frac{q}{Mp'} + \log\frac{d\,p'}{\sigma'_{c}} - 1 = 0 \tag{3.25}$$

where *M* is the critical state parameter and *d* represents the distance between the critical state line at ambient temperature and the isotropic consolidation curve for a given temperature.

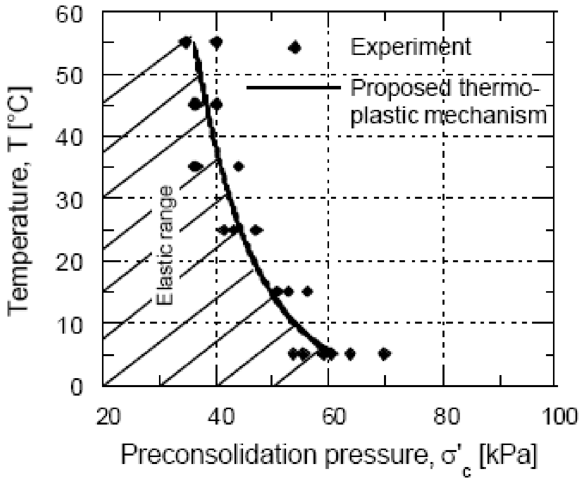

Figure 29. Isotropic yield locus (Laloui et al., 2002).

The deviatoric flow rule, following the multi-mechanism plasticity framework, here represents only a partial, 'deviatoric contribution' to the total plastic strain rate (Laloui et al., 2005):

$$\begin{aligned} \dot{\varepsilon}_v^p &= \dot{\lambda}_d \frac{\partial g_{Td}}{\partial p'} = \dot{\lambda}_d \frac{\partial f_{Td}}{\partial p'} = \dot{\lambda}_d \frac{1}{Mp'}\left(M - \frac{q}{p'}\right) \\ \dot{\varepsilon}_d^p &= \dot{\lambda}_d \frac{\partial g_{Td}}{\partial q} = \dot{\lambda}_d \frac{\partial f_{Td}}{\partial q} = \dot{\lambda}_d \frac{1}{Mp'} \end{aligned} \tag{3.26}$$

3.4.3.3. Thermal dependency of the soil's friction angle

A dependency law with temperature for the critical state soil parameter *M* is proposed for this constitutive model, based on some experimental evidence summarised by Laloui (2001) suggesting that in some clays the friction angle at critical state ϕ'_{cs} might decrease with increasing temperature (cf. Hicher, 1974 and Despax, 1976). In fact, results gathered from experiments on diverse soils seem to show that friction angle can be constant, slightly increase or decrease with increasing temperature, depending on the nature of the clay (Figure 30). Thermal dependency can be quite pronounced for kaolin clay (Laloui et al., 2002), showing a linear decrease of ϕ'_{cs} for increasing temperature

(Figure 30). On the other hand, tests carried out by Marques et al. (2004) on a Canadian marine clay show the virtual absence of thermal effects on the friction angle at critical state (Figure 31). Moreover, Sulem et al. (2007) report a tendency for ϕ'_{cs} to slightly increase with temperature, for a clayey gouge extracted at a 760 m depth from an active fault.

In order to take into account potential thermal-friction softening, Laloui et al. (2005) proposed a linear decreasing law of parameter M with temperature:

$$M = M_0 - \tilde{g}\left(\theta - \theta_0\right) \tag{3.27}$$

where M_0 is the slope of the critical state line at reference temperature and $\tilde{g}$ the experimentally measured slope of variation of M with temperature. This expression can be substituted in (3.25), to obtain the final expression of the deviatoric thermoplastic yield locus:

$$f_d = \frac{q}{M_0 - \tilde{g}\left(\theta - \theta_0\right) p'} + \log \frac{d\, p'}{\sigma'_c} - 1 = 0 \tag{3.28}$$

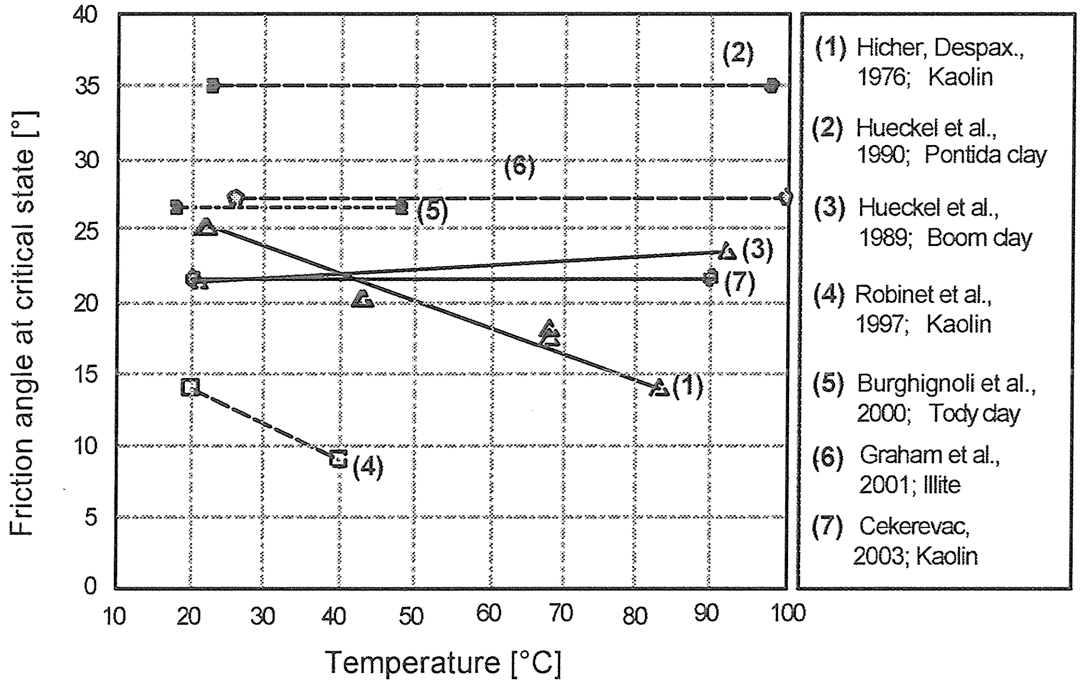

Figure 30. Experimental data on the influence of temperature on the friction angle at critical state of some clays (Laloui et al., 2001).

3.4.3.4. Volumetric strain coupling and consistency conditions

The two above presented mechanisms are coupled through the hardening relationship (3.22), since both yield loci depend on the apparent overconsolidation stress. The total volumetric strain rate results from the sum of the two 'partial' contributions:

$$\dot{\varepsilon}_v^p = \dot{\lambda}_d \frac{\partial f_{Td}}{\partial p'} + \dot{\lambda}_i \frac{\partial f_{Ti}}{\partial p'} . \tag{3.29}$$

It is finally worth mentioning the expressions of the consistency conditions, determined by two distinct equations as required by the multi-mechanism approach, allowing us to calculate the two plastic multipliers:

$$\dot{f}_{Ti} = \frac{\partial f_{Ti}}{\partial p'} \dot{p}' + \frac{\partial f_{Ti}}{\partial \theta} \dot{\theta} + \frac{\partial f_{Ti}}{\partial r} \dot{r} + \frac{\partial f_{Ti}}{\partial \varepsilon_v^p} \dot{\varepsilon}_v^p = 0 \tag{3.30}$$

$$\dot{f}_{Td} = \frac{\partial f_{Td}}{\partial p'} \dot{p}' + \frac{\partial f_{Td}}{\partial \theta} \dot{\theta} + \frac{\partial f_{Td}}{\partial q} \dot{q} + \frac{\partial f_{Td}}{\partial \varepsilon_v^p} \dot{\varepsilon}_v^p = 0 . \tag{3.31}$$

As a summary of Laloui's model, the coupled isotropic and deviatoric yield loci are visualised a three-dimensional space in Figure 32.

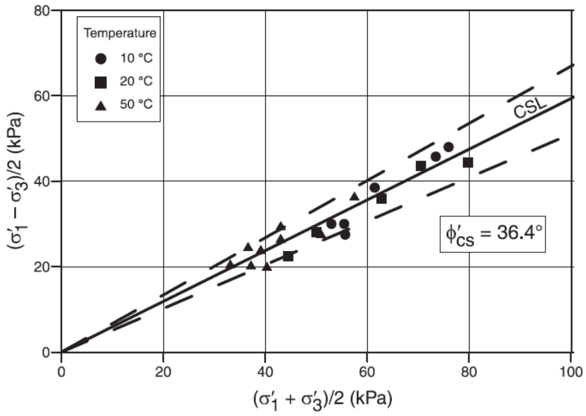

Figure 31. From Marques et al. (2004). Temperature effect on the critical state line for the St-Roch-de-l'Achigan Canadian clay.

3.5. Other authors' contributions to thermo-mechanical soil modelling

We are now going to briefly present two further constitutive thermo-mechanical models which have been recently presented, both based on the modification of Hueckel's model, in an attempt to better represent the volumetric behaviour of soils, especially focusing on the thermal behaviour of overconsolidated clays.

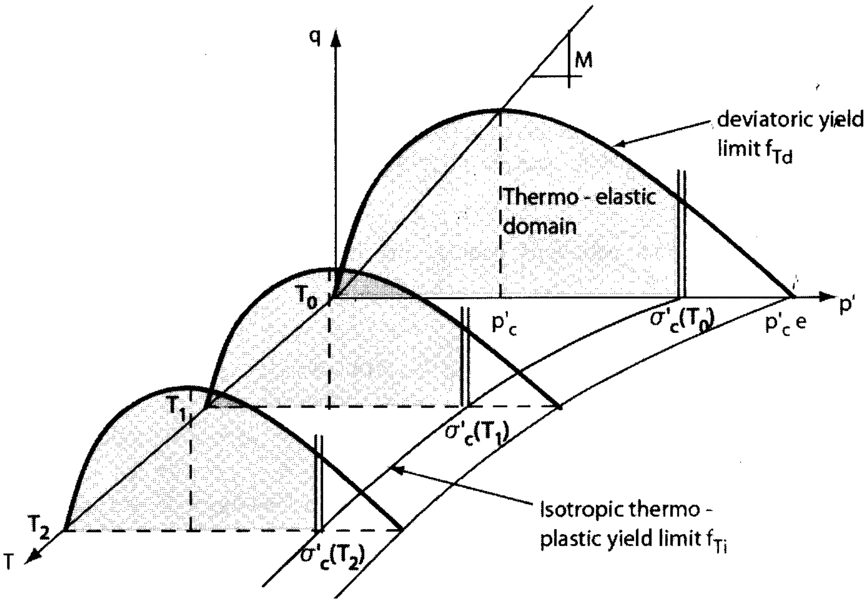

Figure 32. From Laloui et al., 2005. Coupled yield loci enclosing the thermo-elastic domain in terms of mean isotropic stress (*p'*), deviatoric stress (*q*) and temperature (T).

3.5.1. Sultan's model

Sultan et al. (2002, 2004) and Cui et al. (2000) presented a thermo-mechanical model for saturated clays based on Hueckel's model and on further experimental results, mainly focusing on investigating the response to heating of Belgian Boom Clay as a potential host for nuclear waste disposal.

Great importance is given by the authors to the effect of over-consolidation ratio (OCR) on the volumetric behaviour of Boom Clay. As observed in Section 3.3.1, depending on whether OCR=1 or OCR>1, the soil respectively will tend to contract plastically or dilate elastically.

Hueckel's model in case of highly overconsolidated soils predicts the occurrence of elastic thermal expansion only, at least for the initial stages of thermal loading (i.e., before the yield locus is attained). The authors claim that this behaviour should be better modelled as some irreversible thermal contraction is experimentally observed at all OCR values. Thus, an additional plastic volumetric mechanism (in the θ vs. p' plane) called "thermal yield" (TY) is proposed (Cui et al., 2000), within the framework of a multi-mechanism approach similar to the one adopted by Laloui et al. (2005). The TY curve allows for the occurrence of plastic strains from the very beginning of thermal loading. By coupling the TY curve with the hardening law of Hueckel's model (3.5), thermal hardening behaviour is believed to be better represented.

Deviatoric effects, in analogy with Hueckel, are described by Cui et al. (2000) following the Modified Cam-Clay framework, adopting an associated flow rule and assuming the critical state friction parameter *M* as constant, due to the scarce availability of experimental evidence able to show differently. The 3-D visualization of the yield locus is shown in Figure 33.

3.5.2. Robinet's model

Robinet et al. (1996) also proposed a modification of Hueckel's model with the introduction of a further thermo-plastic mechanism to better interpret thermal softening. An additional isotropic yield surface is proposed, associated with a threshold temperature, beyond which both reversible and irreversible thermal strains may develop. Furthermore, a different hardening rule to those described so far is proposed, in the form of product of two exponential functions, with the purpose of not allowing the yield surface size to change at cooling (in contrast with Hueckel's and Laloui's models), when the temperature is below a threshold value.

Regarding the deviatoric part, modified Cam-Clay is adopted, in analogy with the models of Hueckel and Sultan. However, a non-associative flow rule is proposed here, with the plastic potential implicitly dependent on temperature changes.

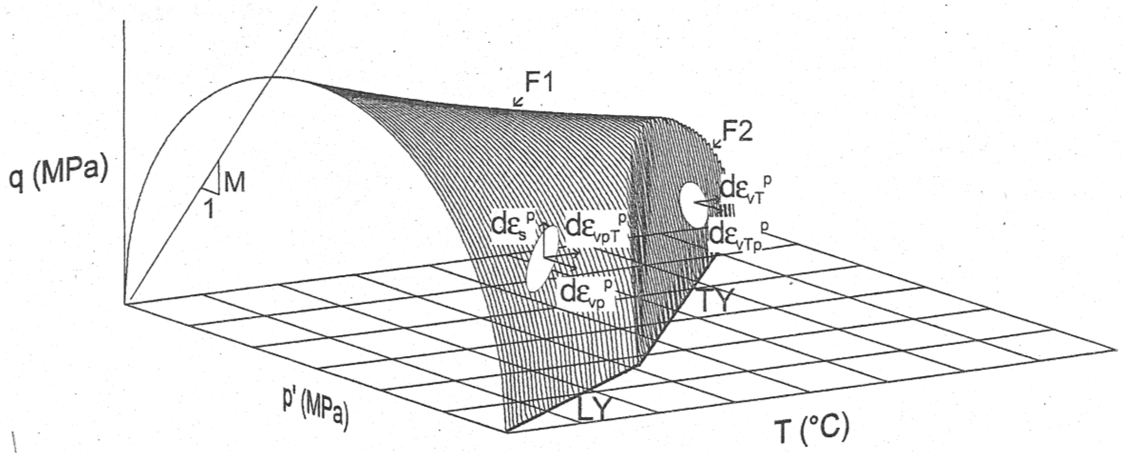

Figure 33. From Cui et al. (2000). Yield surface in 3 dimensions. On the temperature (T) vs. isotropic stress (p') plane, TY represents the newly introduced thermal yield curve, while LY corresponds to Hueckel's hardening law.

3.6. Discussion

The constitutive models reviewed in this chapter depict a fairly comprehensive view of the thermo-mechanical behaviour of clays, and despite they have all been primarily developed in the framework of nuclear waste disposal in deep geological formations, it is reasonable to employ them in other fields, after the necessary modifications.

The first comprehensive thermo-mechanical model suitable for numerical implementations was developed by Hueckel and co-workers. After them, Sultan, Robinet and co-workers aimed to improve on the volumetric thermo-plastic mechanism in response to specific problems arising in the context of nuclear waste repository design, where the soil undergoes relatively slow temperature changes whilst remaining at constant confining stress. Laloui and co-workers independently developed a thermo-mechanical constitutive framework which appears simpler, yet able to realistically describe the main features of the soil's deformational response to heating.

Our aim is to incorporate one of the above described constitutive laws into the governing equations of a model describing the production of heat and excess pore pressure in a rapidly deforming shearband (Chapter 5). Given the extreme overall complexity of such model, and the presence of some uncertainties in the determination of its parameters, the thermo-plastic constitutive model for the soil should be as simple as possible, i.e. it should contain the least possible number of material parameters and should be easy to generalise. Among the above reviewed models, Laloui's one appears to be the most suitable for the purpose, since its formulation is simpler, there are fewer material parameters and the elastic law can be easily inverted leading to a strain-controlled problem, which will more easily allow future generalisations. Nevertheless, the model will need modifications since adopting a multi-mechanism framework implying the use of two separate plastic multipliers does not appear necessary to our purposes, and the OCC yield locus is notoriously awkward for numerical implementations as compared to MCC, due to the uncertainties in the direction of the plastic strain increment vector at the tip of the yield envelope (e.g. see Muir Wood, 1990). Furthermore, the stress-strain formulation adopted by Laloui and co-workers is the classic 'triaxial' one, which is appropriate to interpret triaxial testing, but not general enough for other contexts and for potential Finite Element implementations.

In the next chapter, we will focus on improving and generalising Laloui's model in order to make it suitable for the implementation into a thermo-mechanical landslide model.

Chapter 4. An improved thermo-mechanical constitutive model

4.1. Introduction

In this chapter a new generalised thermoplastic model is developed, based on the isotropic hardening law describing the evolution of apparent preconsolidation stress with temperature of Laloui & Cekerevac (2003) and adopting the linear thermal-friction softening law of Laloui et al. (2005). With these ingredients we can re-derive the constitutive equations from a standard plasticity framework, with a general stress space formulation in order to facilitate future generalisation of the model in 2- and 3-D. Furthermore Modified Cam-Clay will be adopted for the deviatoric behaviour, as this is a widely used model with clear advantages when it comes to numerical implementation (cf. Section 3.6). The resulting qualitative shape of the yield surface in 3 dimensions is shown in Figure 34. It can be noticed that the tip of the yield locus, i.e. the apparent preconsolidation stress, varies with temperature in the (*p*',θ) plane (cf. Section 3.4.3.1) according to the following exponential law (Laloui & Cekerevac 2003):

$$\sigma'_c = \sigma'_{c0} \exp(\tilde{\beta}\varepsilon_v^p)\left[1-\gamma \log\left(\theta/\theta_0\right)\right] \tag{4.1}$$

At the same time, if the considered soil shows some thermal-friction sensitivity (i.e. $\tilde{g} \neq 0$, cf. Section 3.4.3.3), the critical state parameter *M* may linearly vary as (Laloui et al., 2005)

$$M = M_0 - \tilde{g}\left(\theta - \theta_0\right). \tag{4.2}$$

Starting from a classic plasticity formulation, we will hereafter derive the stress-strain rate equations including the above thermo-mechanical laws in the framework of Modified Cam Clay (MCC).

4.2. Problem formulation

Within the range of small deformations and rotations, from standard kinematics we can assume the validity of additive decomposition of total strain into elastic and plastic part, as well as the corresponding decomposition of their rates:

$$\dot{\boldsymbol{\varepsilon}} = \dot{\boldsymbol{\varepsilon}}^e + \dot{\boldsymbol{\varepsilon}}^p \tag{4.3}$$

In presence of thermal loading, elastic strain can be separated into two contributions: a mechanical-elastic and a thermo-elastic part, $\dot{\boldsymbol{\varepsilon}}^e = \dot{\boldsymbol{\varepsilon}}^{me} + \dot{\boldsymbol{\varepsilon}}^{te}$ so that from (4.3),

$$\dot{\boldsymbol{\varepsilon}} = \dot{\boldsymbol{\varepsilon}}^{me} + \dot{\boldsymbol{\varepsilon}}^{te} + \dot{\boldsymbol{\varepsilon}}^{p} \,. \tag{4.4}$$

The basic stress-strain relationship

$$\dot{\boldsymbol{\sigma}} = \mathbf{D}^{me} \dot{\boldsymbol{\varepsilon}}^{e} \tag{4.5}$$

where $\mathbf{D}^{me}$ is the standard fourth-order tensor of elastic moduli, in thermal conditions is equivalent to

$$\dot{\boldsymbol{\sigma}} = \mathbf{D}^{me} \dot{\boldsymbol{\varepsilon}}^{me} + \mathbf{D}^{me} \dot{\boldsymbol{\varepsilon}}^{te} \tag{4.6}$$

which, since thermal elastic strain rates are proportional to the temperature rate, can be rewritten as

$$\dot{\boldsymbol{\sigma}} = \mathbf{D}^{me} \dot{\boldsymbol{\varepsilon}}^{me} + \mathbf{D}^{te} \dot{\theta} \tag{4.7}$$

where $\dot{\theta}$ is the temperature rate and the thermoelasticity tensor $\mathbf{D}^{te}$ will be specified shortly hereafter.

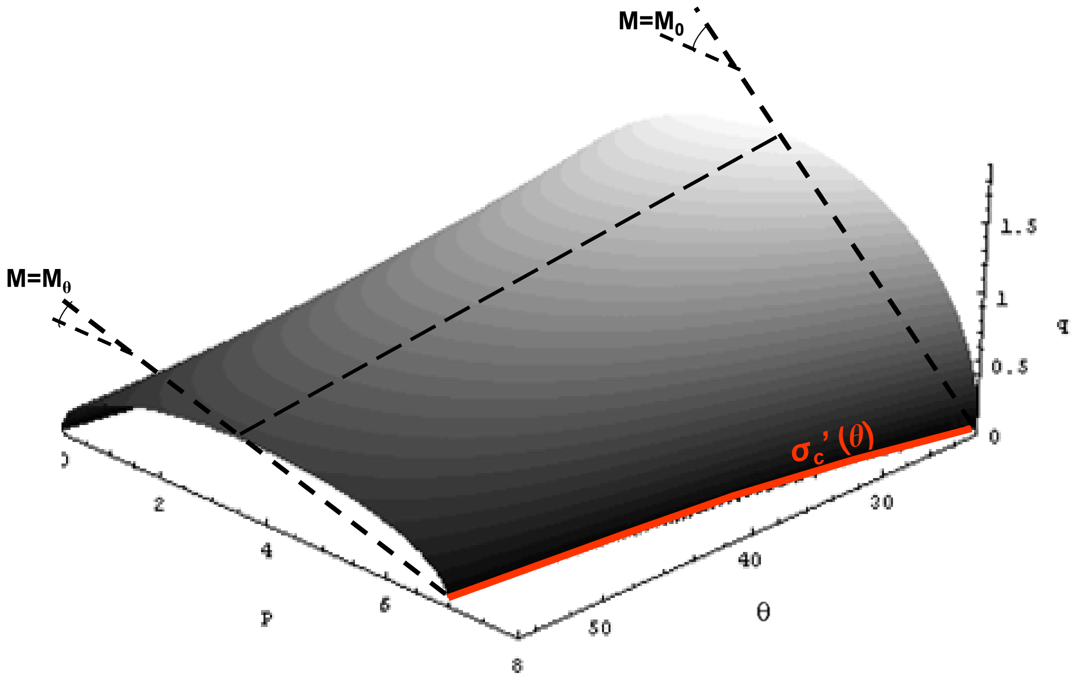

Figure 34. Qualitative shape of the thermo-plastic yield locus at critical state, demonstrating temperature dependence of the apparent preconsolidation stress and thermal-friction softening.

In the following, we will implement thermal dependency upon the above mechanics framework, resorting to an existing thermoelastic law, a temperature dependency law for the apparent preconsolidation stress $\sigma_c(\varepsilon_v^p, \theta)$ and a temperature dependency law for the critical state parameter $M(\theta)$. More specifically, the isotropic thermal hardening law (4.1), prescribing dependency of the apparent preconsolidation stress on temperature as well as on cumulated plastic volumetric strain will be incorporated into the MCC yield locus equation (see Equation (4.31)), alongside with the linear thermal-friction softening law (4.2). As a result, the new form of yield function f will depend on temperature θ, in addition to stress $\boldsymbol{\sigma}$ and hardening parameter ε_v^p:

$$f(\boldsymbol{\sigma}, \varepsilon_v^p, \theta) = 0 . \tag{4.8}$$

The consistency condition $\dot{f} = 0$, expressing the plasticity postulate that at plastic yield the stress state must always lie on the yield locus (Section 3.3.5) must now account for thermal dependency:

$$\dot{f} = f_{\boldsymbol{\sigma}} \dot{\boldsymbol{\sigma}} + f_{\varepsilon_v^p} \dot{\varepsilon}_v^p + f_\theta \dot{\theta} = 0 . \tag{4.9}$$

In the above, the subscripts denote the partial derivatives of the yield function with respect to other model variables, more specifically:

$$f_{\boldsymbol{\sigma}} = \frac{\partial f}{\partial \boldsymbol{\sigma}} = \frac{\partial f}{\partial p'} \frac{\partial p'}{\partial \sigma_{ij}} + \frac{\partial f}{\partial q} \frac{\partial q}{\partial \sigma_{ij}}$$

$$f_{\varepsilon_v^p} = \frac{\partial f}{\partial \varepsilon_v^p} = \frac{\partial f}{\partial \sigma_c} \frac{\partial \sigma_c}{\partial \varepsilon_v^p}$$

$$f_\theta = \frac{\partial f}{\partial \theta} = \frac{\partial f}{\partial \sigma_c} \frac{\partial \sigma_c}{\partial \theta} + \frac{\partial f}{\partial M} \frac{\partial M}{\partial \theta} .$$

Another essential ingredient of plasticity (Section 3.2) is the flow rule, defining the relative magnitudes of various components of plastic deformation (Section 3.3.4). A general form of flow rule is

$$\dot{\boldsymbol{\varepsilon}}^p = \dot{\lambda} \frac{\partial g}{\partial \boldsymbol{\sigma}} = \dot{\lambda} g_{\boldsymbol{\sigma}} . \tag{4.10}$$

where g is the plastic potential, defined as the curve to which the plastic strain increment vectors are orthogonal, and $\dot{\lambda}$ is the plastic multiplier, a scalar-valued parameter whose expression will be determined in Section 4.4.1 from the consistency condition. In the framework of MCC, *g* coincides with the yield locus *f* (associativity is assumed). From Equation (4.10), substituting *g=f* we can express the isotropic plastic strain rate as

$$\dot{\varepsilon}_v^p = \dot{\lambda} \frac{\partial f}{\partial \sigma_{kk}} = \dot{\lambda} \left(\frac{\partial f}{\partial \sigma_{11}} + \frac{\partial f}{\partial \sigma_{22}} + \frac{\partial f}{\partial \sigma_{33}} \right) = \dot{\lambda} \frac{\partial f}{\partial p'} . \tag{4.11}$$

Based on the above outlined framework, we will now derive the equations of the thermo-elasto-plastic model. It is necessary to start the description from the constitutive law of elasticity, which forms the basis of all stress-strain relationships, to which a description of plasticity will follow. In fact, elastic (i.e., recoverable) strains are always present when soil is deformed, while plastic (i.e., irrecoverable) strains occur only if the yield locus is attained by the stress state.

4.3. Thermoelasticity

The thermoelastic relationships imply recoverable volumetric dilation with increased temperature, and can be obtained from standard continuum mechanics (e.g. Mase, 1970, Section 6.10). The strain rate components of an isotropic body subjected to thermal loading are expressed by

$$\dot{\boldsymbol{\varepsilon}}^{te} = \alpha \boldsymbol{\delta}_{ij} \dot{\theta} \tag{4.12}$$

where α is the thermal elastic expansion coefficient and $\boldsymbol{\delta}_{ij}$ is the *Kronecker delta*, a function of the variables *i,j* defined as

$$\delta_{ij} = \begin{cases} 1 & \text{for} \quad i = j \\ 0 & \text{for} \quad i \neq j \end{cases} \tag{4.13}$$

which practically, in Equation (4.12) zeroes all the deviatoric components of strain. Adding up the mechanical-elastic part (standard *Hooke's* law) yields the so-called *Duhamel-Neumann* relations, which in turn can be inverted to give the thermoelastic constitutive equations:

$$\dot{\boldsymbol{\sigma}} = \lambda \boldsymbol{\delta}_{ij} \dot{\boldsymbol{\varepsilon}}_{kk}^{me} + 2\mu \dot{\boldsymbol{\varepsilon}}_{ij}^{me} - \left(3\lambda + 2\mu\right) \alpha \boldsymbol{\delta}_{ij} \dot{\theta} \tag{4.14}$$

where λ and μ are the *Lamè* constants (Mase, 1970).

On the other hand, Laloui et al. (2005) provided the thermoelastic relations

$$\dot{\varepsilon}_v^{te} = \beta_s \dot{\theta}; \tag{4.15}$$

in terms of volumetric strain, which can be equivalently written in vector form as

$$\dot{\boldsymbol{\varepsilon}}^{te} = \mathbf{C}^{Te} \dot{\theta} \tag{4.16}$$

where $\mathbf{C}^{Te} = \frac{1}{3} \beta_s \boldsymbol{\delta}_{ij}$. By comparing (4.12) and (4.16) we deduce

$$\alpha = \frac{1}{3} \beta_s , \tag{4.17}$$

which allows us to write, from (4.15),

$$\dot{\varepsilon}_v^{te} = 3\alpha \dot{\theta} . \tag{4.18}$$

Substituting the definitions of the *Lamè* constants in (4.14) yields

$$\dot{\boldsymbol{\sigma}} = (K - \frac{2}{3}G)\boldsymbol{\delta}_{ij}\dot{\boldsymbol{\varepsilon}}_{kk}^{me} + 2G\dot{\boldsymbol{\varepsilon}}_{ij}^{me} - \beta_s K\boldsymbol{\delta}_{ij}\dot{\theta} \tag{4.19}$$

where *K*, *G* are the (mean stress-dependent) elastic moduli of the soil, also known as bulk modulus and shear modulus respectively:

$$K = \frac{\partial p'}{\partial \varepsilon_v^e} = \frac{\mathrm{v}p'}{\kappa}; \quad G = \frac{3(1-2\nu)}{2(1+\nu)}K. \tag{4.20}$$

in the above, κ is the slope of the elastic compression line, or unloading-reloading line (URL), v the specific volume and ν the soil's Poisson ratio.

Equation (4.19) can be rewritten as

$$\dot{\boldsymbol{\sigma}} = \mathbf{D}^{me}\dot{\boldsymbol{\varepsilon}}^{me} + \mathbf{D}^{te}\dot{\theta}, \tag{4.21}$$

where $\mathbf{D}^{me}$ is the standard tensor of elastic moduli, which has the form

$$\mathbf{D}^{me} = \begin{bmatrix} K+\frac{4}{3}G & K-\frac{2}{3}G & K-\frac{2}{3}G & 0 & 0 & 0 \\ K-\frac{2}{3}G & K+\frac{4}{3}G & K-\frac{2}{3}G & 0 & 0 & 0 \\ K-\frac{2}{3}G & K-\frac{2}{3}G & K+\frac{4}{3}G & 0 & 0 & 0 \\ 0 & 0 & 0 & G & 0 & 0 \\ 0 & 0 & 0 & 0 & G & 0 \\ 0 & 0 & 0 & 0 & 0 & G \end{bmatrix} \tag{4.22}$$

and the thermal tensor is

$$\mathbf{D}^{te} = -\beta_s K\boldsymbol{\delta}_{ij}, \tag{4.23}$$

so that (4.21) can be finally written (in terms of effective stress) as:

$$\begin{Bmatrix} \dot{\sigma}'_{11} \\ \dot{\sigma}'_{22} \\ \dot{\sigma}'_{33} \\ \dot{\tau}_{12} \\ \dot{\tau}_{12} \\ \dot{\tau}_{23} \end{Bmatrix} = \mathbf{D}^{me} \begin{bmatrix} \dot{\varepsilon}_{11} \\ \dot{\varepsilon}_{22} \\ \dot{\varepsilon}_{33} \\ \dot{\gamma}_{12} \\ \dot{\gamma}_{13} \\ \dot{\gamma}_{23} \end{bmatrix} + \mathbf{D}^{te}\dot{\theta}. \tag{4.24}$$

4.4. Thermoplasticity

4.4.1. Calculation of the plastic multiplier

Substituting (4.4) into (4.21) yields

$$\dot{\boldsymbol{\sigma}} = \mathbf{D}^{me}(\dot{\boldsymbol{\varepsilon}} - \dot{\boldsymbol{\varepsilon}}^{te} - \dot{\boldsymbol{\varepsilon}}^{p}) + \mathbf{D}^{te}\dot{\theta} \tag{4.25}$$

or equivalently, by substituting (4.10) and (4.16),

$$\dot{\boldsymbol{\sigma}} = \mathbf{D}^{me}\dot{\boldsymbol{\varepsilon}} - \left(\mathbf{D}^{me}\mathbf{C}^{te} - \mathbf{D}^{te}\right)\dot{\theta} - \mathbf{D}^{me}\dot{\lambda} g_{\boldsymbol{\sigma}} . \tag{4.26}$$

Equation (4.26) can be substituted into the consistency Equation (4.9)

$$f_{\boldsymbol{\sigma}}\mathbf{D}^{me}\dot{\boldsymbol{\varepsilon}} - f_{\boldsymbol{\sigma}}\left(\mathbf{D}^{me}\mathbf{C}^{te} - \mathbf{D}^{te}\right)\dot{\theta} - f_{\boldsymbol{\sigma}}\mathbf{D}^{me}\dot{\lambda} g_{\boldsymbol{\sigma}} + f_{\varepsilon_v^p}\dot{\lambda} g_p + f_{\theta}\dot{\theta} = 0 . \tag{4.27}$$

Solving this equation for the plastic multiplier yields

$$\dot{\lambda} = \frac{f_{\boldsymbol{\sigma}}\mathbf{D}^{me}\dot{\boldsymbol{\varepsilon}} + \left(f_{\theta} - f_{\boldsymbol{\sigma}}\mathbf{D}^{me}\mathbf{C}^{te} + f_{\boldsymbol{\sigma}}\mathbf{D}^{te}\right)\dot{\theta}}{f_{\boldsymbol{\sigma}}\mathbf{D}^{me} g_{\boldsymbol{\sigma}} - f_{\varepsilon_v^p} g_{p'}} . \tag{4.28}$$

In the above, expression $-f_{\boldsymbol{\sigma}}\mathbf{D}^{me}\mathbf{C}^{te} + f_{\boldsymbol{\sigma}}\mathbf{D}^{te}$ can be algebraically manipulated as:

$$\begin{aligned} f_{\boldsymbol{\sigma}}\left(\mathbf{D}^{te} - \mathbf{D}^{me}\mathbf{C}^{te}\right) &= f_{\boldsymbol{\sigma}}\left(\mathbf{D}^{te} - \mathbf{D}^{me}\frac{1}{3}\beta_s\boldsymbol{\delta}_{kl}\right) \\ &= f_{\boldsymbol{\sigma}}\left\{\mathbf{D}^{te} - \frac{1}{3}\beta_s\left[\left(K - \frac{2}{3}G\right)\boldsymbol{\delta}_{ij}\boldsymbol{\delta}_{kk} + 2G\boldsymbol{\delta}_{ij}\right]\right\} = \\ &= f_{\boldsymbol{\sigma}}\left[-\beta_s K\boldsymbol{\delta}_{ij} - \frac{1}{3}\beta_s\left(3K - 2G + 2G\right)\boldsymbol{\delta}_{ij}\right] = \\ &= -2K\beta_s f_{\boldsymbol{\sigma}}\boldsymbol{\delta}_{ij} = 2\mathbf{D}^{te} f_{\boldsymbol{\sigma}} \end{aligned} \tag{4.29}$$

which leads to the final expression:

$$\dot{\lambda} = \frac{f_{\boldsymbol{\sigma}}\mathbf{D}^{me}\dot{\boldsymbol{\varepsilon}} + \left(f_{\theta} + 2\mathbf{D}^{te} f_{\boldsymbol{\sigma}}\right)\dot{\theta}}{f_{\boldsymbol{\sigma}}\mathbf{D}^{me} g_{\boldsymbol{\sigma}} - f_{\varepsilon_v^p} g_{p'}} = \frac{1}{\tilde{H}}\left[f_{\boldsymbol{\sigma}}\mathbf{D}^{me}\dot{\boldsymbol{\varepsilon}} + \left(f_{\theta} + 2\mathbf{D}^{te} f_{\boldsymbol{\sigma}}\right)\dot{\theta}\right] . \tag{4.30}$$

We may recall here that the MCC yield surface has expression

$$f = q^2 - M^2 p'\left(\sigma'_c - p'\right) \tag{4.31}$$

and its derivatives, featuring in Equation (4.30), are described in Section 4.2. In thermal conditions, we may employ expression (4.1) to describe thermal dependency of the preconsolidation stress. The critical state parameter M may be allowed to vary according to the linear thermal-friction softening law (4.2). Substituting equations (4.2) and (4.1) into (4.31) yields

$$f = q^2 - \left[M_0 - \tilde{g}\left(\theta - \theta_0\right)\right]^2 p'\left\{\sigma'_{c0}\exp\left(\beta\varepsilon_v^p\right)\left[1 - \gamma\log\left(\frac{\theta}{\theta_0}\right)\right] - p'\right\} . \tag{4.32}$$

The partial derivatives of the yield function outlined in Section 4.2 can finally be calculated, as follows:

$$\begin{aligned}
&f_\theta = \frac{\sigma'_m \lambda p' \left[M_0 - \tilde{g}\left(\theta - \theta_0\right)\right]^2}{\theta} + 2\tilde{g}p'\left[M_0 - \tilde{g}\left(\theta - \theta_0\right)\right]\left\{\sigma'_m\left[1-\gamma\log\left(\theta/\theta_0\right)\right] - p'\right\} \\
&f_{\varepsilon_v^p} = -\sigma'_m p' \tilde{\beta}\left[1-\gamma\log\left(\theta/\theta_0\right)\right]\left[M_0 - \tilde{g}\left(\theta - \theta_0\right)\right]^2 \\
&f_{p'} = g_{p'} = \left[M_0 - \tilde{g}\left(\theta - \theta_0\right)\right]^2\left\{2p' - \sigma'_m\left[1-\gamma\log\left(\theta/\theta_0\right)\right]\right\} \\
&f_q = 2q
\end{aligned} \tag{4.33}$$

In the above equations,

$$\sigma'_m = \sigma'_{c0}\exp\left(\tilde{\beta}\varepsilon_v^p\right) \tag{4.34}$$

is the 'isothermal' value of apparent preconsolidation stress (Laloui and Cekerevac 2003). Equation (4.34) corresponds to the classic MCC hardening law, where thermal loading is not expected and preconsolidation stress depends on the volumetric plastic strains developed during the loading history of the considered soil.

4.4.2. Thermo-elasto-plastic stress-strain rate equations

Employing (4.4) into (4.7) yields

$$\dot{\boldsymbol{\sigma}} = \mathbf{D}^{me}\left(\dot{\boldsymbol{\varepsilon}} - \dot{\boldsymbol{\varepsilon}}^{te} - \dot{\boldsymbol{\varepsilon}}^{p}\right) + \mathbf{D}^{te}\dot{\theta} \tag{4.35}$$

which, by substituting (4.16) leads to

$$\dot{\boldsymbol{\sigma}} = \mathbf{D}^{me}\left(\dot{\boldsymbol{\varepsilon}} - \dot{\boldsymbol{\varepsilon}}^{p}\right) + \left(\mathbf{D}^{te} - \mathbf{C}^{te}\mathbf{D}^{me}\right)\dot{\theta}\,. \tag{4.36}$$

Substituting (4.10) and (4.30) yields

$$\dot{\boldsymbol{\sigma}} = \mathbf{D}^{me}\left\{\dot{\boldsymbol{\varepsilon}} - \frac{1}{\tilde{H}}\left[f_{\boldsymbol{\sigma}}\mathbf{D}^{me}\dot{\boldsymbol{\varepsilon}} + \left(f_T + 2\mathbf{D}^{te}f_{\boldsymbol{\sigma}}\right)\dot{\theta}\right]g_{\boldsymbol{\sigma}}\right\} + \left(\mathbf{D}^{te} - \mathbf{C}^{te}\mathbf{D}^{me}\right)\dot{\theta} \tag{4.37}$$

By regrouping the terms, the above becomes

$$\dot{\boldsymbol{\sigma}} = \dot{\boldsymbol{\sigma}}^{e} - \dot{\lambda}\mathbf{D}^{me}g_{\boldsymbol{\sigma}} + \left(\mathbf{D}^{te} - \mathbf{C}^{te}\mathbf{D}^{me}\right)\dot{\theta} = \mathbf{D}^{mep}\dot{\boldsymbol{\varepsilon}} + \mathbf{D}^{tep}\dot{\theta} \tag{4.38}$$

which represents the stress-strain rate equation in the general case of thermo-mechanical loading.

4.4.3. Hardening law and final thermoplastic equations

The hardening rule describes the way in which plastic deformation is linked with the change in size of the yield locus, through the value of apparent preconsolidation stress located at the 'tip' of the envelope (i.e. at the intersection of the yield locus with the isotropic axis), according to modified Cam Clay (e.g. see Muir Wood, 1990). The MCC hardening law (not accounting for thermal effects) is

$$\dot{\varepsilon}_v^p = \frac{\lambda - \kappa}{\mathrm{v}}\frac{\dot{\sigma}_c}{\sigma_c} \tag{4.39}$$

where v=current specific volume, λ and κ respectively the slopes of the normal compression line (NCL) and of the unloading-reloading line (URL).

Alternatively, we can express the dependency of apparent preconsolidation stress on accumulated plastic volumetric strains (in isothermal conditions) by using Equation (4.34):

$$\sigma'_c\left(\varepsilon_v^p\right) = \sigma'_{c0}\exp\left(\tilde{\beta}\varepsilon_v^p\right) \tag{4.40}$$

which by differentiation yields

$$\dot{\varepsilon}_v^p = \frac{1}{\tilde{\beta}}\frac{\dot{\sigma}_c}{\sigma_c}. \tag{4.41}$$

The above coincides with (4.39), providing that the compressibility parameter $\tilde{\beta}$ has the form

$$\tilde{\beta} = \frac{\mathrm{v}}{\lambda - k}. \tag{4.42}$$

In thermal conditions, the hardening relationship corresponding to (4.41) is obtained by taking the rate of (4.1):

$$\dot{\sigma}'_c\left(\dot{\varepsilon}_v^p,\dot{\theta}\right) = \sigma'_{c0}\exp\left(\tilde{\beta}\varepsilon_v^p\right)\left\{\beta\left[1-\gamma\log\left(\frac{\theta}{\theta_0}\right)\right]\dot{\varepsilon}_v^p - \gamma\frac{\dot{\theta}}{\theta}\right\}. \tag{4.43}$$

which, by subsituting (4.34) and (4.10) may be rewritten as

$$\dot{\sigma}'_c\left(\dot{\varepsilon}_v^p,\dot{\theta}\right) = \sigma'_m\left\{\tilde{\beta}\left[1-\gamma\log\left(\frac{\theta}{\theta_0}\right)\right]\dot{\lambda}f_p - \gamma\frac{\dot{\theta}}{\theta}\right\} \tag{4.44}$$

or, more synthetically,

$$\dot{\sigma}'_c\left(\dot{\varepsilon}_v^p,\dot{\theta}\right) = A\dot{\theta} + B\dot{\lambda} \tag{4.45}$$

where

$$\begin{aligned} A &= -\gamma\sigma'_m/\theta \\ B &= \tilde{\beta}\sigma'_m\left[1-\gamma\log\left(\theta/\theta_0\right)\right]f_p \end{aligned}. \tag{4.46}$$

Therefore at plastic yielding, for given total strain and temperature rates it is necessary to solve the following system of ordinary differential equations (ODEs), composed by (4.38) and (4.45):

$$\begin{cases} \dot{\boldsymbol{\sigma}} = \mathbf{D}^{mep}\dot{\boldsymbol{\varepsilon}} + \mathbf{D}^{Tep}\dot{\theta} \\ \dot{\sigma}'_c = A\cdot\dot{\theta} + B\cdot\dot{\lambda} \end{cases} \tag{4.47}$$

4.5. Numerical integration scheme

We have so far described the mathematical laws that control the stress-strain relationship for an element of soil subjected to mechanical and thermal loading. In order to apply the constitutive equations to the solution of a real case, they need to be integrated with the relevant initial and boundary conditions. The complexity of the problem requires the computation of an approximate solution, thus a discretisation of the constitutive equations is needed, in which the initial continuous problem is replaced by a discrete problem whose solution is known to approximate that of the continuous problem. The solution is then found numerically, resorting to a computational scheme which is chosen among the many available in the literature for its suitability to the specific problem.

The two ODEs (4.47) contain time derivatives, of general form $\left(dy_i/dt\right)=f_i$. The underlying idea of discretisation is rewriting the exact differentials dy_i, dt as finite steps Δy_i, Δt. In the limit of making the step-size very small, a satisfactory approximation to the original differential equation is obtained.

4.5.1. Overview of integration algorithms

The differential equations (4.47) outlined above, after discretisation need to be integrated to obtain the unknown increment in the stresses. There are several methods available to perform the task, but they all fall into the two wide sub-categories of explicit and implicit methods.

As a basis to decide which integration method is more suitable, accuracy, stability and computational expense are the main criteria. Accuracy is related to the ‘truncation error’, i.e. to the discrepancy between the true (analytical) answer and the answer obtained in the calculation, and can be exactly estimated in terms of Taylor expansion term truncation. Accuracy depends on the specific algorithm used and is therefore known in advance by the modeller. However, sometimes very accurate schemes can be numerically unstable. Numerical stability is related to the experienced capability of the method to perform well in a computer, since due to accumulated round-off errors (intrinsic errors in the computer representation of real numbers) some algorithms do not lead to the right answer if some parameters are not carefully controlled. While some methods are known to be unconditionally stable, some others are not and might not converge if, for example, the size of the time-step is chosen to be too large. Finally, computational expense reflects the time taken by the computer's CPU to perform the calculations, and depends on several factors such as the dimensions of the time and spatial domains.

In the following, we will briefly review the available integration methods.

4.5.1.1. Explicit methods

Explicit methods calculate the state of a system at a later time from the state of the system at the current time.

The simplest explicit scheme is the first-order Forward Euler method, which starting from the discretised derivative

$$y'(t) = f\left(t, y(t)\right) = \frac{y(t+\Delta t) - y(t)}{\Delta t} \tag{4.48}$$

yields the formula

$$y(t+\Delta t) = y(t) + f\left(t, y(t)\right)\Delta t \tag{4.49}$$

which implies the computation, at each time-step, of the recursive formula

$$y_{t+\Delta t} = y_t + \Delta t \cdot f\left(t, y_t\right). \tag{4.50}$$

This method is not normally recommended since it is unsymmetrical, in that the solution given through the interval Δt is based only on derivative information at the beginning of the interval (Figure 35). This implies the accumulation of errors alongside time integration, leading to generally unacceptable accuracies.

Based on the Euler method, several more accurate explicit schemes have been developed (e.g. see Press, 1988), all belonging to the family of Runge-Kutta (RK) methods, the most widespread of which being the fourth-order RK formula (Figure 36): at each step the derivative is evaluated four times by reproducing the terms in the Taylor series (up to the fourth order term), once at the initial point, twice at trial points in the middle of the time interval, and once at a trial endpoint. Despite being old, this method is not obsolete, since it is stable and robust. In most practical cases though, RK and other explicit, Euler-based methods should be improved with the adoption of 'adaptive step-size control'. In fact, inevitable numerical errors are produced, which need to be controlled (to remain within a prescribed accuracy) by iterative changing of the time-step size.

For applications to plasticity problems, explicit methods are straightforward, in that they imply the evaluation of the relevant unknown quantities (hardening parameter, yield surface and plastic potential) at known stress states. On the other hand, the integration process has some drawbacks:

A. Iterative forms of correction are essential for the calculated stresses after each applied strain increment, since the 'consistency condition' for the stress state to lie on the yield surface is not enforced by the integration method. In other words, at the end of each increment in the explicit integration process, the stresses may diverge from the yield condition. This represents the so-called 'yield surface drift', and its extent depends on the nonlinearity of the involved equations (Sloan at al., 2001).
B. When the stress state passes from elastic to plastic state, the intermediate point of intersection of the stress path with the yield surface needs to be found separately, through the solution of an additional nonlinear equation. This defines an additional 'intersection problem' that needs to be included in an explicit elasto-plastic integration algorithm.

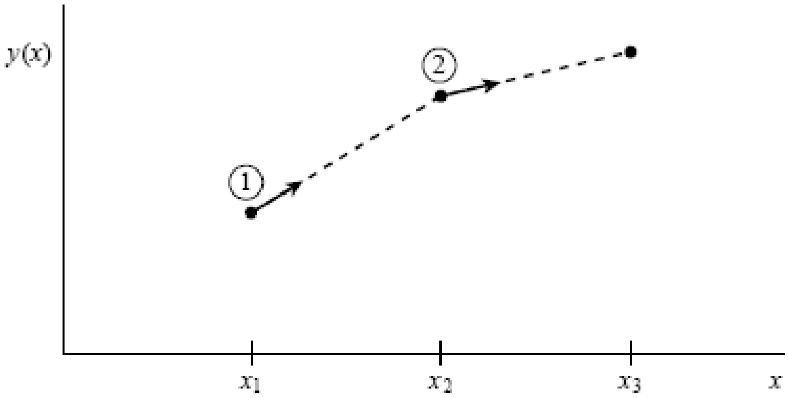

Figure 35. Scheme of the Forward Euler method. This is the simplest and least accurate method for the integration of an ODE. To find the next function value (2), the derivative at the start of the interval (1) is used. After Press at al., 1988.

4.5.1.2. Implicit methods

The simplest implicit integration scheme is the Backward Euler scheme, according to which, instead of (4.48) the time derivative is discretised as

$$y'(t)=f\left(t,y(t)\right)=\frac{y(t)-y(t-\Delta t)}{\Delta t}, \tag{4.51}$$

Which eventually yields the recursive formula

$$y_{t+\Delta t}=y_t+\Delta t\cdot f\left(t+\Delta t,y_{t+\Delta t}\right) \tag{4.52}$$

where the function needs to be evaluated at the unknown time-step $(t+\Delta t)$. The dependence of the right-hand side on the variables at $(t+\Delta t)$ rather than t implies the inability to solve the equation directly for $y_{t+\Delta t}$.

Implicit methods in plasticity do not require the computation of either the stress correction (described above, at point A), or the intersection with the yield surface (point B above), but since the unknown quantities are evaluated at unknown stress states, integration requires solving iteratively a system of non-linear equations. A well-known implicit method is the Backward Euler Return scheme, which has been effectively applied to metal plasticity problems as well as critical state soil mechanics (Borja and Lee, 1990). Nevertheless, In order to apply an implicit iteration scheme, second derivatives of the yield function ad plastic potential are required, which is a particularly difficult and time-consuming task for complex constitutive relations such as those belonging to the Cam Clay family, especially when thermal effects are included.

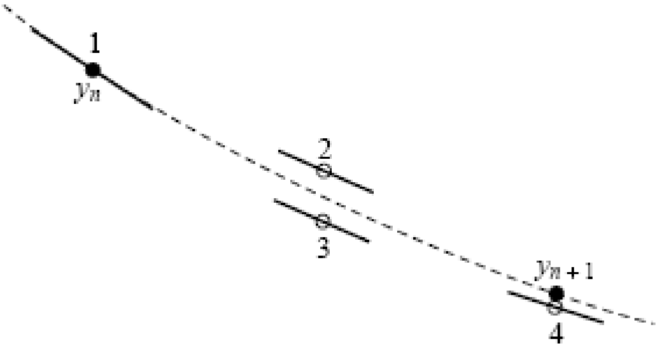

Figure 36. Fourth-order Runge-Kutta method. The derivative at point n+1 is calculated from the known value at 1 (filled-in dot) and three trial values at 2,3,4 (open dots). After Press at al., 1988.

4.5.1.3. A refined explicit scheme

We can observe that explicit methods are more suitable to our purpose, since they require only first derivatives of the involved quantities and are therefore more reliable and efficient for complex constitutive laws like the ones featuring the thermoplasticity problem at hand.

A particularly suitable 'refined explicit' integration scheme with 'automatic error control' is that proposed by Sloan et al. (2001), which has been shown to be robust and efficient to integrate constitutive models of the Cam-Clay family. This method is ‘refined’ in that the drawbacks of basic explicit schemes are overcome by implementing additional improvement schemes specifically aimed to the solution of complex soil elasto-plastic constitutive relationships. Sloan’s scheme is able to deal with non-linear elasticity, and is easy to generalise since most of the algorithm is independent of the precise form of the stress-strain relationship.

Key features of this algorithm are:

- Correction of ‘yield surface drift’ (Section 4.5.1.1): stresses are restored to the yield surface after each integration step, by solving a single nonlinear equation.
- Automatic error control: a local measure of the error in the computed stresses is estimated with a modified Euler scheme, and used to automatically sub-increment the imposed strain increment.
- Automatic step-size control (Section 4.5.1.1): The size of each sub-increment varies throughout the integration process, depending on the non-linearity of the constitutive relations.

4.5.2. Strain-controlled integration scheme

We hereby propose a general thermoplastic integration scheme for a soil element. Unlike Laloui et al (2005), we formulate the equations so that we control the strains (instead of the stresses), to make it easier in the future to generalise the model to 2- and 3-D analyses and to have it ready for a prospective Finite Element implementation.

In order to integrate equations (4.47), it is convenient to define a ‘pseudo-time’ τ:

$$\tau = \left(t - t_0\right) / \Delta t \tag{4.53}$$

where t_0 is the time at the start of load increment, $t_0 + \Delta t$ the time at the end of load increment, and $\tau \in \left[0,1\right]$. Applying the chain rule of differentiation to the equations (4.47) yields

$$\frac{d\boldsymbol{\sigma}}{d\tau} = \mathbf{D}^{mep}\dot{\boldsymbol{\varepsilon}} + \mathbf{D}^{tep}\dot{\theta} = \Delta\boldsymbol{\sigma}_e - \Delta\lambda\mathbf{D}^{me}g_{\boldsymbol{\sigma}} + \left(\mathbf{D}^{te} - \mathbf{C}^{te}\mathbf{D}^{me}\right)\Delta\theta\,, \tag{4.54}$$

$$\frac{d\sigma_c}{d\tau} = A \cdot \Delta\theta + B \cdot \Delta\lambda\,, \tag{4.55}$$

where

$$\Delta\lambda = \frac{1}{\tilde{H}}\left[f_{\boldsymbol{\sigma}}\mathbf{D}^{me}\Delta\boldsymbol{\varepsilon} + \left(f_\theta + 2\mathbf{D}^{te}f_{\boldsymbol{\sigma}}\right)\Delta\theta\right]. \tag{4.56}$$

Equations (4.54) and (4.55) can be integrated over the pseudo-time interval $\tau \in \left[0,1\right]$.

The known values are the imposed total strain and temperature increments, $\Delta\boldsymbol{\varepsilon}$, $\Delta\theta$, together with the initial values of the stresses ($\boldsymbol{\sigma}_0$), temperature (θ_0), apparent preconsolidation stress (σ'_{c0}) and critical state parameter (M_0) at the start of the pseudo-time increment. The unknown value is the stress increment, to be found once the increment in preconsolidation pressure (our 'hardening parameter') has been computed. In the following, we will modify Sloan's (2001) integration scheme to include thermal effects according to the above presented modified thermo-mechanical constitutive relations, starting from the above listed initial conditions of our problem.

4.5.3. Elasticity domain and yield surface intersection

Given a vector of externally imposed total strain increment $\Delta\boldsymbol{\varepsilon}^{tot}$, a 'trial' stress increment in the elastic domain can be calculated as

$$\Delta\boldsymbol{\sigma} = \mathbf{D}^{me}\Delta\boldsymbol{\varepsilon}^{me} + \mathbf{D}^{te}\Delta\theta \tag{4.57}$$

where

$$\Delta\boldsymbol{\varepsilon}^{me} = \Delta\boldsymbol{\varepsilon}^{tot} - \Delta\boldsymbol{\varepsilon}^{te} \tag{4.58}$$

and $\Delta\boldsymbol{\varepsilon}^{te} = \mathbf{C}^{te}\Delta\theta$, from Equation (4.16). Nevertheless, since in our case elasticity is nonlinear, the stress-dependent moduli *K* and *G* should be integrated for p' and ε_v to give the secant elastic moduli $\overline{K}(\boldsymbol{\sigma},\Delta\varepsilon_v)$ and $\overline{G}(\boldsymbol{\sigma},\Delta\varepsilon_v)$ (Sloan, 2001) featuring in the secant elasticity matrix $\overline{\mathbf{D}}^{me}(\boldsymbol{\sigma}_0,\Delta\varepsilon_v)$, derived from (4.22), where

$$\Delta\varepsilon_v = \sum_{k=1}^{3}\Delta\varepsilon_{kk}^{tot} . \tag{4.59}$$

In the same way, the secant bulk modulus $\overline{K}(\boldsymbol{\sigma},\Delta\varepsilon_v)$ also features in the secant thermo-elasticity matrix $\overline{\mathbf{D}}^{te}(\boldsymbol{\sigma}_0,\Delta\varepsilon_v)$, derived from (4.23).

By employing the secant elasticity matrices, Equation (4.57) becomes

$$\Delta\overline{\boldsymbol{\sigma}} = \overline{\mathbf{D}}^{me}\Delta\boldsymbol{\varepsilon}^{me} + \overline{\mathbf{D}}^{te}\Delta\theta . \tag{4.60}$$

This stress increment $\Delta\overline{\boldsymbol{\sigma}}$ is used as a check on whether the stress state has changed from elastic to plastic due to the current strain and temperature increments. If by applying $\Delta\overline{\boldsymbol{\sigma}}$ the stress state remains within the elastic domain, the new stress state will be calculated as $\boldsymbol{\sigma}_0 + \Delta\overline{\boldsymbol{\sigma}}$, as described in Section 4.5.4 at point (2). If instead the yield surface is met, it is necessary to calculate the fraction of applied (mechanical and thermal) strains responsible for the 'elastic part' of the stress increment, i.e. the path from initial stress $\boldsymbol{\sigma}_0$ to intersection stress $\boldsymbol{\sigma}_{\text{int}}$. This problem corresponds to finding the scalar quantity r satisfying the equation

$$f\left(\boldsymbol{\sigma}_0 + r\left(\overline{\mathbf{D}}^{me}\Delta\boldsymbol{\varepsilon}^{me}\right), \theta_0 + r\mathbf{D}^{te}\Delta\theta\right) = f\left(\boldsymbol{\sigma}_{\text{int}}, \theta_{\text{int}}\right). \qquad (4.61)$$

A value of r=1 indicates purely elastic deformation, r=0 purely plastic deformation. If $r \in \left]0,1\right[$ the elastic part of stress increment is given by $\left(\overline{\mathbf{D}}^{me}\Delta\boldsymbol{\varepsilon}^{me} + \mathbf{D}^{te}\Delta\theta\right)r$, after which plastic yielding occurs. The problem is now more complicated compared to that described by Sloan (2001), since in presence of a temperature increase the yield surface changes in size also when the stress state lies within the elastic domain, due to the thermal hardening law (Figure 37).

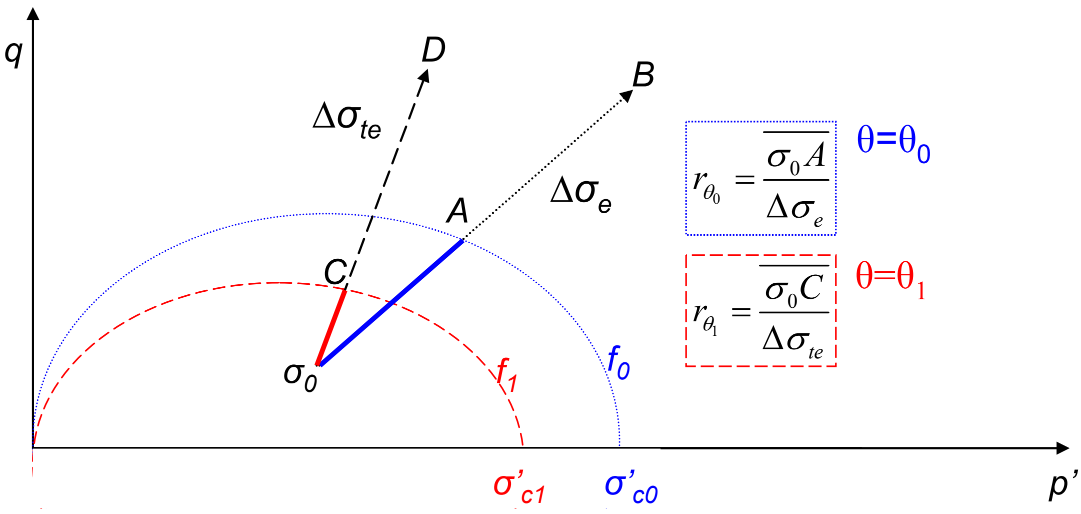

Figure 37. Geometry of the yield surface intersection problem. Comparison between isothermal case (dotted lines) and the more complicated case of thermo-mechanical loading (dashed lines): segments σ_0B and σ_0D represent the total 'secant' stress increment, OA and OC the 'elastic portion' to be calculated.

The numerical solution of (4.61) is found following the 'Pegasus' algorithm (Dowell and Jarratt, 1972). The algorithm was modified to account for the thermal component of the strain increment vector and for the thermal dependency of the apparent preconsolidation stress and of the critical state parameter. The main changes compared to the standard elasto-plasticity procedure arise in steps (2) and (3) of the algorithm, described in detail hereafter:

(1) Enter with initial (current) values of the stresses ($\boldsymbol{\sigma}_0$), temperature (θ_0), apparent preconsolidation stress (σ'_{c0}), initial values of r-factor r_0, r_1

(respectively set to 0 and 1), reference values of critical state parameter (M_{ref}) and temperature (θ_{ref}), the maximum number of iterations *max* (usually 10) and the tolerance for the yield surface value *ftol* (usually of the order of 10^{-6}).

(2) Calculate:

$$\overline{\mathbf{D}}^{me0} = \overline{\mathbf{D}}^{me}\left(\boldsymbol{\sigma}_0, r_0\Delta\varepsilon_v\right),$$

$$\overline{\mathbf{D}}^{te0} = \overline{\mathbf{D}}^{te}\left(\boldsymbol{\sigma}_0, r_0\Delta\varepsilon_v\right),$$

$$\Delta\overline{\boldsymbol{\sigma}}_{e0} = r_0\left(\overline{\mathbf{D}}^{me0}\Delta\varepsilon + \overline{\mathbf{D}}^{te0}\Delta\theta\right),$$

$$\overline{\mathbf{D}}^{me1} = \overline{\mathbf{D}}^{me}\left(\boldsymbol{\sigma}_0, r_1\Delta\varepsilon_v\right),$$

$$\overline{\mathbf{D}}^{te1} = \overline{\mathbf{D}}^{te}\left(\boldsymbol{\sigma}_0, r_1\Delta\varepsilon_v\right),$$

$$\Delta\overline{\boldsymbol{\sigma}}_{e1} = r_1\left(\overline{\mathbf{D}}^{me1}\Delta\varepsilon + \overline{\mathbf{D}}^{te1}\Delta\theta\right),$$

where $\overline{\mathbf{D}}^{me}$ is the above mentioned secant elasticity matrix and $\overline{\mathbf{D}}^{te} = -\beta_s\boldsymbol{\delta}_{ij}\overline{K}$.

(3) Calculate:

$\left(p'_a, q_a\right)$ from stress state $\left(\boldsymbol{\sigma}_0 + \Delta\overline{\boldsymbol{\sigma}}_{e0}\right)$,

$$\sigma'_{ca} = \sigma'_{c0} + \Delta\sigma'_{ca} = \sigma'_{c0}\left\{1 - r_0\frac{\gamma\Delta\theta}{\theta_0\left[1-\gamma\log\left(\theta_0/\theta_{ref}\right)\right]}\right\},$$

$$M_a = M_0 + \Delta M_a = M_0 - g\left(\theta_{ref} - \theta_0 - r_0\Delta\theta\right),$$

$$F_0 = {q_a}^2 - {M_a}^2 p'_a\left(\sigma'_{ca} - p'_a\right),$$

$\left(p'_b, q_b\right)$ from stress state $\left(\boldsymbol{\sigma}_0 + \Delta\overline{\boldsymbol{\sigma}}_{e1}\right)$,

$$\sigma'_{cb} = \sigma'_{c0} + \Delta\sigma'_{cb} = \sigma'_{c0}\left\{1 - r_1\frac{\gamma\Delta\theta}{\theta_0\left[1-\gamma\log\left(\theta_0/\theta_{ref}\right)\right]}\right\},$$

$$M_b = M_0 + \Delta M_b = M_0 - g\left(\theta_{ref} - \theta_0 - r_1\Delta\theta\right),$$

$$F_1 = {q_b}^2 - {M_b}^2 p'_b\left(\sigma'_{cb} - p'_b\right).$$

(4) Execute steps (5)-(8) *max* times.

(5) Calculate:

$$r = r_1 - F_1\left(r_1 - r_0\right)/\left(F_1 - F_0\right),$$

$$\overline{\mathbf{D}}^{me2} = \overline{\mathbf{D}}^{me}\left(\boldsymbol{\sigma}_0, r\Delta\varepsilon_v\right),$$

$$\overline{\mathbf{D}}^{te2} = \overline{\mathbf{D}}^{te}\left(\boldsymbol{\sigma}_0, r\Delta\varepsilon_v\right),$$

$$\Delta\overline{\boldsymbol{\sigma}}_{e2} = r\left(\overline{\mathbf{D}}^{me2}\Delta\varepsilon + \overline{\mathbf{D}}^{te2}\Delta\theta\right),$$

$\left(p'_c, q_c\right)$ from stress state $\left(\boldsymbol{\sigma}_0 + \Delta\overline{\boldsymbol{\sigma}}_{e2}\right)$,

$$\sigma'_{cc} = \sigma'_{c0} + \Delta\sigma'_{cc} = \sigma'_{c0}\left\{1 - r\frac{\gamma\Delta\theta}{\theta_0\left[1-\gamma\log\left(\theta_0/\theta_{ref}\right)\right]}\right\},$$

$$M_c = M_0 + \Delta M_c = M_0 - g\left(\theta_{ref} - \theta_0 - r\Delta\theta\right),$$

$$F_{new} = q_c^{\,2} - M_c^{\,2} p'_c\left(\sigma'_{cc} - p'_c\right).$$

(6) If $ftol \geq |F_{new}|$ go to (10).

(7) If F_{new} has opposite sign to F_0:

$r_1 = r_0,\ F_1 = F_0.$

Otherwise:

$F_1 = F_1F_0/\left(F_0 + F_{new}\right).$

(8) $r_0 = r\ ,\ F_0 = F_{new}.$

(9) If convergence has not been achieved after *max* iterations, the simulation is stopped and an error message is printed, as the algorithm cannot proceed without computing the yield surface intersection.

(10) Output the value of *r*.

4.5.4. Elasto-plasticity domain

It is now needed to describe the integration of the model equations at plastic yielding. The yield surface ‘drift’ correction does not need any description here, since the relevant algorithm proposed by Sloan et al. (2001, Section 3.3) may be employed unchanged in our model as well.

At plastic yielding, we need to integrate the constitutive equations (4.54) and (4.55) starting from the relevant initial conditions specified in Section 4.5.2 and an initial pseudo time $\Delta\tau_1$, initially set to unity to allow for the case where sub-stepping is not needed. The resulting solution is then analysed with a relative error estimation. If such error is smaller than the prescribed tolerance, the current strain and temperature increments are accepted and the stresses and apparent preconsolidation stress are updated. Otherwise, the solution is rejected and a smaller step size is computed. The procedure is then repeated. Subsequent steps may vary in size depending on the computed error. The integration procedure finishes when the sum of all applied sub-steps equals the initially imposed strain and temperature increments, at $\sum\Delta\tau_i = T = 1$ since $\Delta\boldsymbol{\varepsilon} = \sum\Delta\boldsymbol{\varepsilon}_i$, $\Delta\boldsymbol{\varepsilon}_i = \Delta\tau_i\Delta\boldsymbol{\varepsilon}$ and $\Delta\theta = \sum\Delta\theta_i$, $\Delta\theta_i = \Delta\tau_i\Delta\theta$. This integration scheme is based on that proposed by Sloan et al. (2001, Section 3.4), where further details and the theoretical background can be found. However, our case is more complex, due to the temperature-dependency of the yield surface. In the following, we will briefly outline the algorithm to be used to integrate the thermo-elasto-plastic model equations:

(1) Enter with initial (current) values of the stresses ($\boldsymbol{\sigma}_0$), temperature (θ_0), apparent preconsolidation stress (σ'_{c0}), reference values of critical state parameter (M_{ref}) and temperature (θ_{ref}) and the tolerance for the yield stress values *stol.*

(2) Calculate the stress increment and the trial elastic stress state as:

$$\Delta\bar{\boldsymbol{\sigma}}_e = \bar{\mathbf{D}}^{me}\left(\boldsymbol{\sigma}_0,\Delta\varepsilon_v\right)\Delta\varepsilon + \bar{\mathbf{D}}^{te}\left(\boldsymbol{\sigma}_0,\Delta\varepsilon_v\right)\Delta\theta,$$
$$\bar{\boldsymbol{\sigma}}_e = \boldsymbol{\sigma}_0 + \Delta\bar{\boldsymbol{\sigma}}_e.$$

If $f\left(\bar{\boldsymbol{\sigma}}_e,\theta_0+\Delta\theta\right)\le ftol$, the increment is elastic, then $\boldsymbol{\sigma}_0 = \bar{\boldsymbol{\sigma}}_e$ and $\sigma'_{c1} = \sigma'_c\left(\theta_0+\Delta\theta\right)$, go to step (16).

(3) If $f\left(\boldsymbol{\sigma}_0,\theta_0\right) < -ftol$ and $f\left(\bar{\boldsymbol{\sigma}}_e,\theta_0+\Delta\theta\right) > ftol$ a transition from elastic to plastic state is taking place. Call Pegasus algorithm (described in Section 4.5.3) to compute coefficient *r*. Go to (5).

(4) If $\left|f\left(\boldsymbol{\sigma}_0,\theta_0\right)\right| \le ftol$ and $f\left(\bar{\boldsymbol{\sigma}}_e,\theta_0+\Delta\theta\right) > ftol$ then check for elastic unloading by calculating the angle ϑ between the yield surface gradient and the tangential elastic stress increment:

$$\cos\vartheta = \frac{\dfrac{\partial f}{\partial \boldsymbol{\sigma}}\Delta\boldsymbol{\sigma}_e}{\left\|\dfrac{\partial f}{\partial \boldsymbol{\sigma}}\right\|_2 \left\|\Delta\boldsymbol{\sigma}_e\right\|_2}.$$

If $\cos\vartheta \ge ltol$ where *ltol* is a suitable tolerance, then the stress increment is purely plastic, set *r*=0.

Otherwise, stop the program as elastic unloading occurs (this is an unlikely case in our problem, so the intersection scheme developed by Sloan et al. (2001) to compute ‘elasto-plastic unloading’ is not implemented in our code).

(5) Determine the value of stress at the beginning of plastic flow, and compute the ‘plastic portions’ of strain and temperature as:

$$\boldsymbol{\sigma}_0 \leftarrow \boldsymbol{\sigma}_0 + r\left[\bar{\mathbf{D}}^{me}\left(\boldsymbol{\sigma}_0,r\Delta\varepsilon\right)\Delta\varepsilon + \bar{\mathbf{D}}^{te}\left(\boldsymbol{\sigma}_0,r\Delta\varepsilon\right)\Delta\theta\right]$$
$$\Delta\varepsilon \leftarrow \left(1-r\right)\Delta\varepsilon$$
$$\Delta\theta \leftarrow \left(1-r\right)\Delta\theta.$$

(6) Set $\tau = 0$, $\Delta\tau = 1$.

(7) Perform steps (8)-(15) while $\tau < 1$.

(8) Compute $\Delta\boldsymbol{\sigma}_i$, $\Delta\sigma'_{ci}$ for i=1,2 (with reference to Equations (4.54) and (4.55) of Section 4.5.2):

$$\Delta\boldsymbol{\sigma}_{ei} = \Delta\tau\left(\mathbf{D}_i^{me}\Delta\boldsymbol{\varepsilon} + \mathbf{D}_i^{te}\Delta\theta\right),$$

$$\Delta\boldsymbol{\sigma}_i = \Delta\boldsymbol{\sigma}_{ei} - \Delta\lambda_i\mathbf{D}_i^{me}g_{\boldsymbol{\sigma}i} + \left(\mathbf{D}_i^{te} - \mathbf{C}^{te}\mathbf{D}_i^{me}\right)\Delta\theta$$

$$\Delta\sigma_{ci} = A_i\cdot\Delta\theta + B_i\cdot\Delta\lambda_i,$$

where:

$$\Delta\lambda_i = \max\left\{\frac{1}{\tilde{H}_i}\left[f_{\boldsymbol{\sigma}i}\mathbf{D}_i^{me}\Delta\boldsymbol{\varepsilon} + \left(f_{\theta i} + 2\mathbf{D}_i^{te}f_{\boldsymbol{\sigma}i}\right)\Delta\theta\right], 0\right\},$$

$$B_i = \sigma'_{c0}\exp\left(\beta\varepsilon_{vi}^{p}\right)\tilde{\beta}\left[1 - \gamma\log\left(\frac{\theta_i}{\theta_0}\right)\right]g_{pi},$$

$$A_i = -\frac{\sigma'_{c0}\exp\left(\tilde{\beta}\varepsilon_{vi}^{p}\right)\gamma}{\theta_i},$$

$$\mathbf{D}_i^{me} = \mathbf{D}^{me}\left(\boldsymbol{\sigma}_i\right),$$

$$\mathbf{D}_i^{te} = \mathbf{D}^{te}\left(\boldsymbol{\sigma}_i\right)$$

are evaluated at $\left(\tilde{\boldsymbol{\sigma}}_i, \tilde{\sigma}'_{ci}\right)$ and:

$$\tilde{\boldsymbol{\sigma}}_i = \boldsymbol{\sigma}_\tau, \quad \tilde{\boldsymbol{\sigma}}_2 = \boldsymbol{\sigma}_\tau + \Delta\boldsymbol{\sigma}_1$$

$$\tilde{\sigma}'_{ci} = \sigma'_{c\tau}, \quad \tilde{\sigma}'_{c2} = \sigma'_{c\tau} + \Delta\sigma'_{c1}$$

(9) Compute the new stresses and preconsolidation stress as:

$$\tilde{\boldsymbol{\sigma}}_{\tau+\Delta\tau} = \boldsymbol{\sigma}_\tau + \frac{1}{2}\left(\Delta\boldsymbol{\sigma}_1 + \Delta\boldsymbol{\sigma}_2\right),$$

$$\tilde{\sigma}'_{c(\tau+\Delta\tau)} = \sigma'_{c(\tau)} + \frac{1}{2}\left(\Delta\sigma'_{c1} + \Delta\sigma'_{c2}\right)$$

(10) Determine the relative error from:

$$R_{\tau+\Delta\tau} = \max\left\{\frac{\left\|\Delta\boldsymbol{\sigma}_2 - \Delta\boldsymbol{\sigma}_1\right\|}{2\left\|\tilde{\boldsymbol{\sigma}}_{\tau+\Delta\tau}\right\|}, \frac{\Delta\sigma'_{c2} - \Delta\sigma'_{c1}}{2\tilde{\sigma}'_{c(\tau+\Delta\tau)}}, eps\right\},$$

where *eps* is the smallest relative error which can be calculated.

(11) If $R_{\tau+\Delta\tau} > stol$, we need to find a smaller pseudo-time step by computing:

$$q = \max\left\{0.9\sqrt{\frac{stol}{R_{\tau+\Delta\tau}}}, 0.1\right\},$$

and setting

$\Delta\tau \leftarrow \max\left\{q\Delta\tau, \Delta\tau_{\min}\right\}$.

Return to (8).

(12) Update stress and apparent preconsolidation stress:

$$\boldsymbol{\sigma}_{\tau+\Delta\tau} = \tilde{\boldsymbol{\sigma}}_{\tau+\Delta\tau}$$
$$\sigma'_{c(\tau+\Delta\tau)} = \tilde{\sigma}'_{c(\tau+\Delta\tau)}$$

(13) If $\left|f\left(\boldsymbol{\sigma}_{\tau+\Delta\tau}, \sigma'_{c(\tau+\Delta\tau)}\right)\right| > ftol$ the updated values need to be corrected back to the yield surface with appropriate algorithm.

(14) The new sub-step size is computed:

$$q = \min\left\{0.9\sqrt{\frac{stol}{R_{\tau+\Delta\tau}}}, 0.1\right\},$$
$$\Delta\tau \leftarrow q\Delta\tau,$$
$$\Delta\tau \leftarrow \tau + \Delta\tau.$$

(15) Run a check on the computed step size (it has to be larger than the minimum size) and ensure that integration stops when $\tau = 1$:

$$\Delta\tau \leftarrow \max\left\{\Delta\tau, \Delta\tau_{\min}\right\},$$
$$\Delta\tau \leftarrow \min\left\{\Delta\tau, 1-\tau\right\}.$$

(16) At the end of the increments $\Delta\boldsymbol{\varepsilon}$ and $\Delta\theta$, output stress state $\boldsymbol{\sigma}_1$ and hardening parameter σ'_{c1}. Update the void ratio and critical state parameter.

4.6. Numerical results

As seen above, the integration scheme allows us to independently control the applied total strains and the temperature, which represents an advance in soil thermo-plastic modelling. To test the algorithms, we first implemented the original scheme by Sloan (2001) and run simulations of several loading paths, which resulted correct. Next, we implemented the Modified Cam Clay thermo-plastic algorithm, and initially tested the model by applying isothermal loading (by setting to zero the temperature rate). These simulations proved again to be correct and that the model is able to cope with any loading path. An example simulation of isothermal oedometric compression is shown in Figure 38 and Figure 39. Starting from an arbitrary elastic stress state on the isotropic axis on the left hand side of apparent preconsolidation stress ($\sigma'_c = 300$ kPa), the soil element is strained vertically whilst imposing lateral confinement. Figure 38 shows the stress path in the MCC deviatoric plane, Figure 39 the loading path in the compression plane. It can be noticed in Figure 38 that the loading path approaches the yield surface, follows it towards the right for a while, to finally start to exhibit (at about *p'*=250 kPa, or Ln(*p'*)=5.5) plastic hardening (thus determining the enlargement of the yield locus) which is then indefinitely continued along a constant load path, without reaching the critical state. We remark that the initial part of the stress path in Figure 38 is not representative of a standard oedometer test, due to the initial conditions of our simulation: to reproduce over-consolidation, an isotropic apparent preconsolidation stress (consistently with the MCC framework) has been imposed as initial condition for an oedometric loading simulation. Had we also simulated the sample preparation by 1-D consolidation and subsequent elastic swelling, the loading path would have started at a higher *p'* in the isotropic axis, resulting in a smoother transition between the elastic and plastic states.

Finally, we tested the full potential of our thermo-elasto-plastic integration algorithm. The response of a soil element to different strain and temperature paths is demonstrated in Figure 40. For these example simulations, the following parameter values were chosen: $\nu = 0.3$, $\kappa = 0.02$, $\lambda = 0.2$, *OCR*=5, $\gamma = 0.3$, $\tilde{g} = 6 \cdot 10^{-3}$. The initial temperature, critical state parameter and void ratio were set respectively to $\theta_{ref} = 20$ °C, M_{ref}=0.8, $e_{ref} = 0.7$. The dashed line represents isothermal loading while the solid line represents thermo-mechanical loading, experiencing the same total straining as the isothermal case superimposed with a 40°C total temperature increase. The dash-dotted path was obtained by applying a higher temperature rate at the beginning (40°C of total increase concentrated during the first 1/20 of overall straining), followed by mechanical loading only. It is shown how the apparent preconsolidation stress decreases as temperature increases, and how the slope of the plastic loading path changes if temperature and mechanical strains are applied at the same time.

In Figure 41 numerical results are compared to some experimental data on three isothermal isotropic compression paths carried out at different temperatures (Laloui & Cekerevac, 2003). In accordance with the experimental data, for these simulations $\theta_{ref} = 22$ °C, $\kappa = 0.075$ and $\lambda = 0.11$. The red line simulates an isothermal loading path at ambient temperature. The black line represents a combined thermo-mechanical loading path to simulate the transition between two isothermal loading data sets, where temperature is increased from 22°C to 60°C alongside mechanical straining (path 0 to 2) while experiencing the same void ratio change as that obtained in Laloui and

Cekerevac's (2003) isobaric heating tests (path 0 to 1). After point 2, mechanical loading only follows. Good agreement with experimental data points is achieved in both cases.

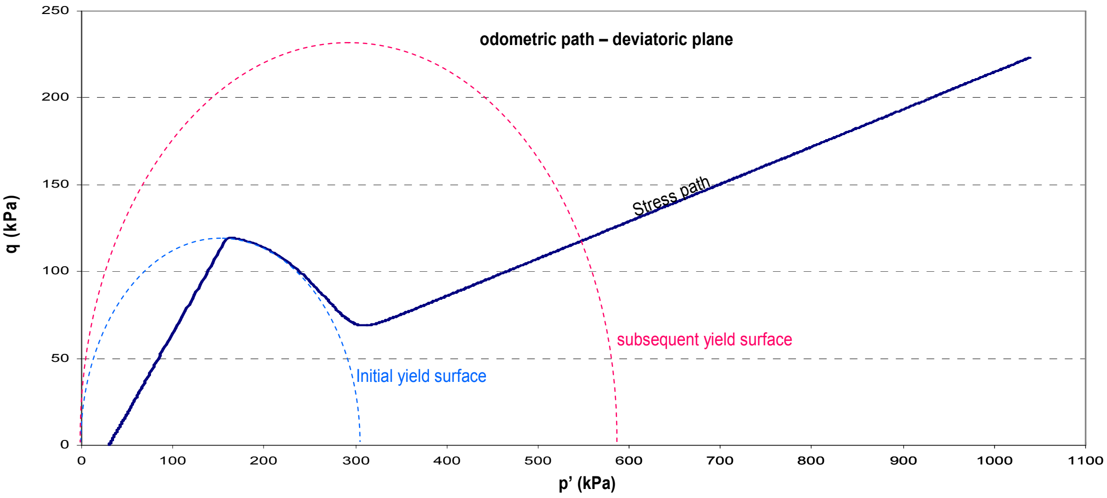

Figure 38. Numerical simulations with our code of isothermal oedometric compression of a soil element. Loading path in deviatoric plane (*p*', *q*)

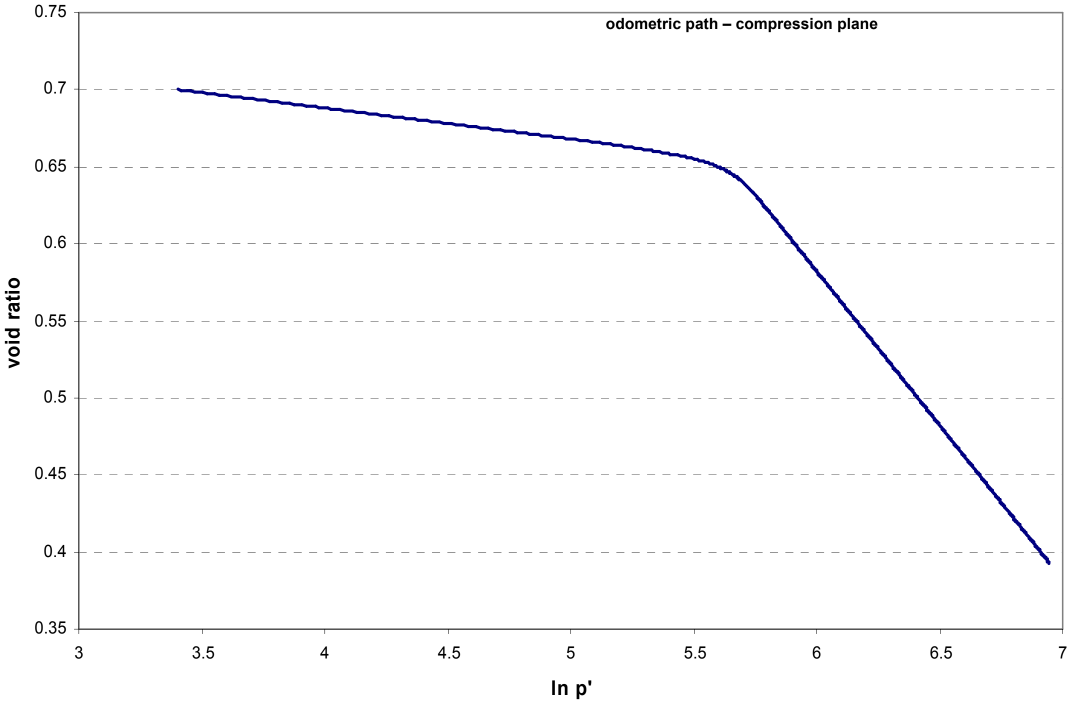

Figure 39. Numerical simulations with our code of isothermal oedometric compression of a soil element. Loading path in compression plane (ln(p'), e).

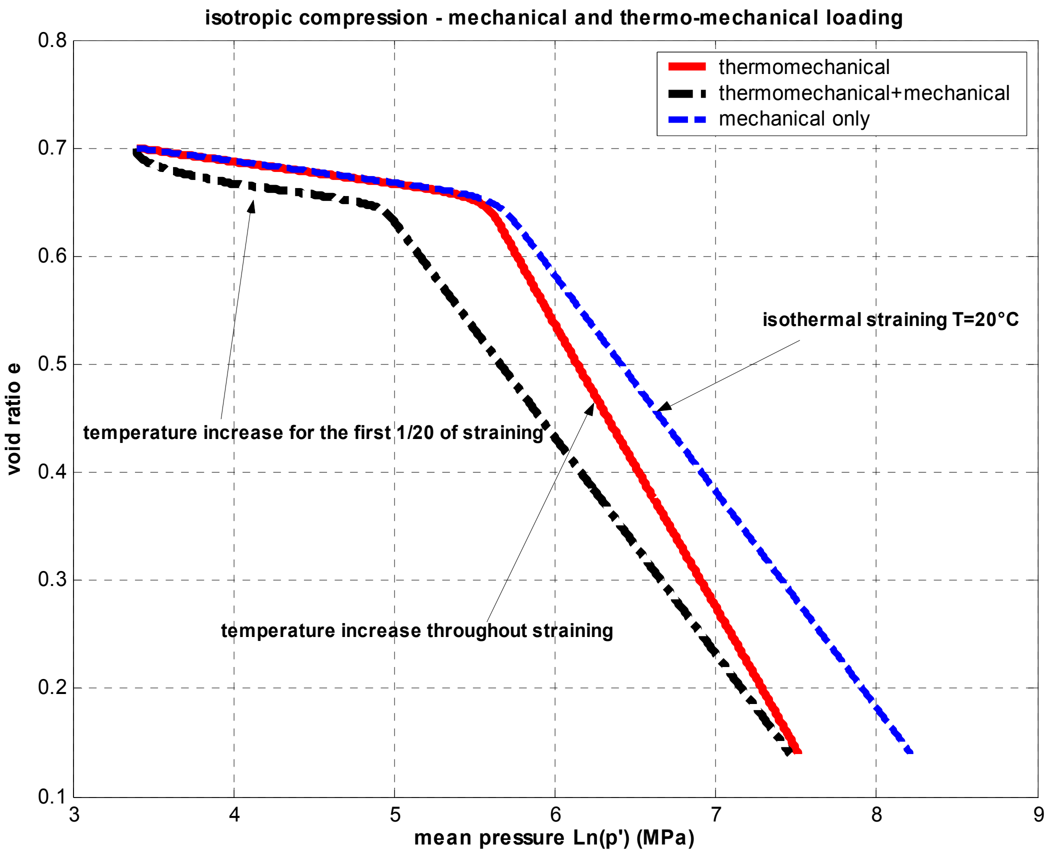

Figure 40. Numerical simulation of some thermo-mechanical isotropic paths. The dashed line represents isothermal loading (at 20°C), the solid line thermo-mechanical loading where temperature is increased from 20°C to 60°C, the dash-dotted path was obtained by applying a higher temperature rate (a 40°C increase during the first 1/20 of total loading), followed by mechanical loading only.

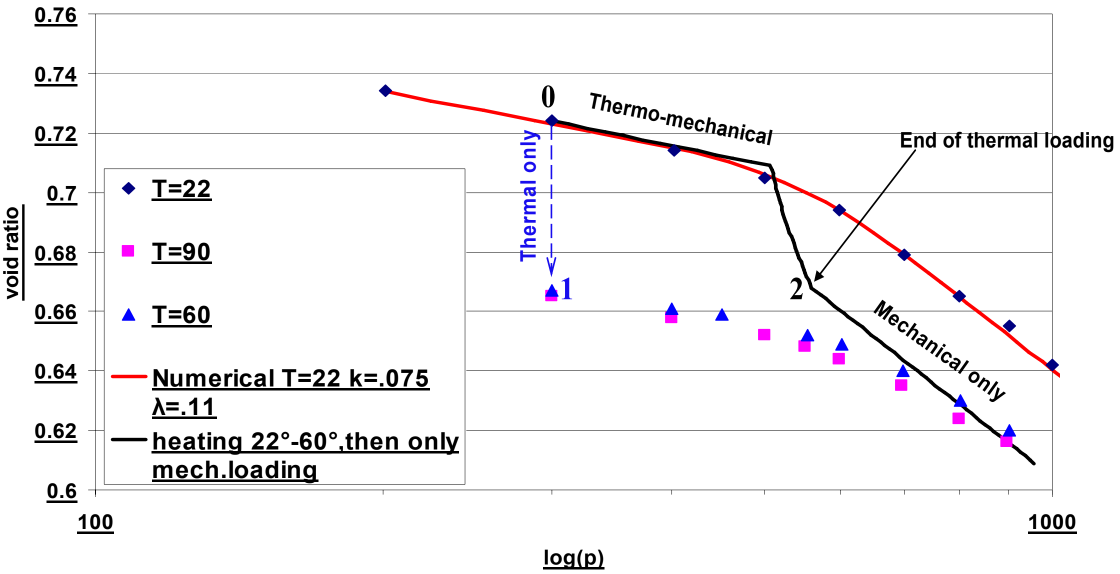

Figure 41. Simulation of isothermal loading and combined thermo-mechanical loading compared to experimental data of isothermal isotropic compression at different temperatures (data points from Laloui and Cekerevac, 2003). The black line simulates thermo-mechanical loading until temperature reaches 60 °C, followed by mechanical loading only. It can be seen how the state path moves between the two sets of data corresponding to isothermal compression at the respective temperatures.

Chapter 5. Modified landslide model

The system of governing equations for Vardoulakis' landslide model seen in Section 2.3.4 provides a 1-D analysis of the phenomenon, employing a simple Mohr-Coulomb yield locus as soil constitutive model. To provide a more realistic constitutive assumption, which can be more easily generalised for applications to a wider range of soils, we will now modify the landslide model governing equations to include the thermoplastic model described in Chapter 4. The three equations forming system (2.6) will be studied one by one, and changed to take into account the new constitutive law. After modification, the model will be ready for numerical implementation, and can be validated through the back-analysis of a catastrophic landslide case history. The large amount of information on the geological and geomechanical aspects of Vajont (cf. Section 2.1.4) makes it the ideal case study to back-analyse for this purpose.

5.1. Model assumptions and overview

The two main constitutive assumptions of the modified landslide model which are essential before a systematic description of the equations are those of plane strain and of critical state for the soil inside the shearband. Both are consistent with Vardoulakis (2000, 2002a).

According to the continuum mechanics definition, a state of plane strain exists at a point when one and only one of the principal strains is zero (Mase, 1970). In an elasto-plastic problem, plane strain implies in-plane deformation, i.e. the deformation field is identical in all planes perpendicular to the direction of the zero principal strain. With reference to Figure 42, in the shearband problem the direction of zero principal strain is the out-of-plane one, i.e. along axis y, while the x axis points in the direction of movement, and the z axis is taken perpendicular to it. Therefore, in plane strain the following conditions hold:

$$\begin{aligned} &\varepsilon_{yy} = 0 \\ &\gamma_{zy} = \gamma_{yz} = 0 \\ &\gamma_{xy} = \gamma_{yx} = 0 \end{aligned} \tag{5.1}$$

and the strain tensor is simplified to

$$\begin{pmatrix} \varepsilon_{xx} & \varepsilon_{xz} & 0 \\ \varepsilon_{xz} & \varepsilon_{zz} & 0 \\ 0 & 0 & 0 \end{pmatrix} = \begin{pmatrix} \varepsilon_{xx} & (1/2)\gamma_{xz} & 0 \\ (1/2)\gamma_{xz} & \varepsilon_{zz} & 0 \\ 0 & 0 & 0 \end{pmatrix}. \tag{5.2}$$

We also remark that, unlike Vardoulakis (2002a), the sign convention used here follows the standard soil mechanics one, where compressive deformations and stresses are taken as positive.

The assumption of critical state (CS) derives from considering the shearband soil to have already undergone large amounts of shear, since the analysis starts at incipient final collapse, so we can presume preceding creeping movements. It is therefore reasonable to assume that the soil has already undergone failure and mechanical hardening has fully developed. CS implies indefinite plastic shearing at constant specific volume. More precisely, in terms of triaxial variables, the condition of CS is attained when (cf. Muir Wood, 1990)

$$\frac{\partial p'}{\partial \varepsilon_q} = \frac{\partial q}{\partial \varepsilon_q} = \frac{\partial \mathrm{v}}{\partial \varepsilon_q} = 0. \tag{5.3}$$

According to the MCC thermoplastic model, in the (p, q) plane the critical state line (CSL) is the locus of critical states and joins the peak points of yield loci. The stress state of material points within the landslide shearband is thus represented by the CSL, so that the equation

$$q = Mp' \tag{5.4}$$

holds, and the stress state is 'locked' to the top of the yield surface at all times (cf. Figure 43). This allows us to relate the stress state to the apparent preconsolidation stress σ'_c representing the tip of the yield envelope, so that

$$p' = \sigma'_c/2, \tag{5.5}$$

and we can substitute (5.5) into (5.4) to directly relate the deviatoric stress to the apparent preconsolidation stress:

$$q = \frac{M\sigma'_c}{2}. \tag{5.6}$$

It is further assumed that the bulk of the slide moves as a rigid body with a speed $v_d(t)$, which constitutes the coupling variable between the two shearband equations and the dynamical equation. Moreover, velocity and acceleration components along the z axis are neglected. We finally remark that the small thickness of the band, compared to the slide dimensions, allows formulating the problem in one dimension along the lines of Vardoulakis (2002a): all variations in the x-direction (the direction of sliding) are neglected, i.e. $\frac{\partial u}{\partial x} = \frac{\partial \theta}{\partial x} = 0$, so that temperature and pore pressure changes will be assumed to take place along direction z only.

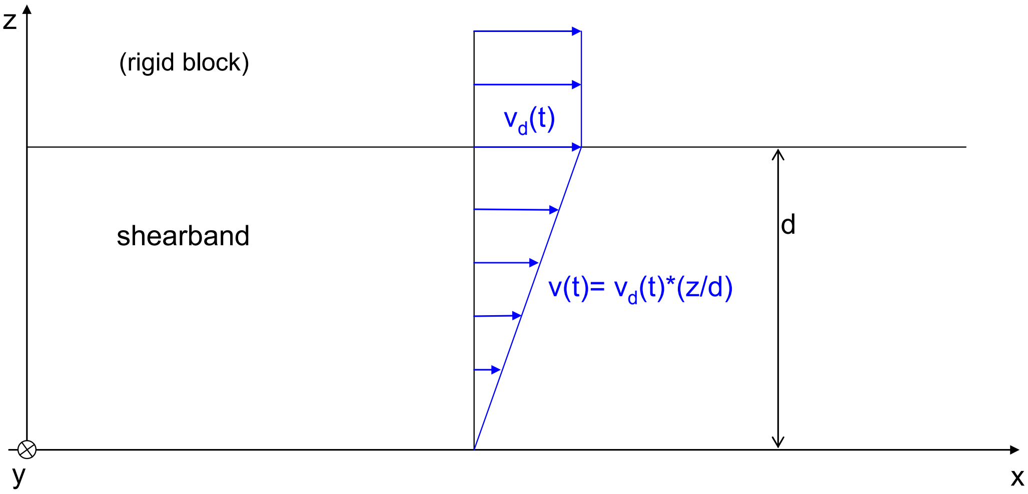

Figure 42. Scheme of the shearband with axis reference system. The out-of-plane direction is *y*.

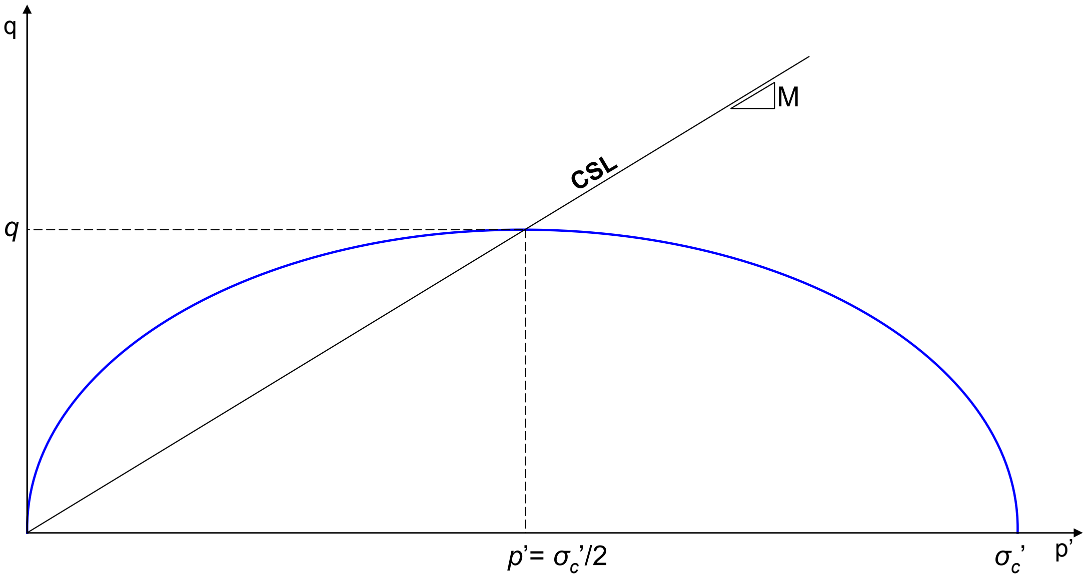

Figure 43. Sample stress state in critical state conditions, 'locked' at the peak point of the Modified Cam Clay ellipse.

5.2. Heat equation

The heat equation provides the time evolution of temperature (cf. Equation (2.1)):

$$\frac{\partial\theta}{\partial t} = k_m \frac{\partial^2\theta}{\partial z^2} + \frac{D}{C_f} \tag{5.7}$$

In the following, the modifications to (5.7) necessary to accommodate the new constitutive model of Chapter 4 are detailed.

The dissipation term, corresponding to the plastic work within the shearband, accounts for all heat generation, and is expressed as

$$D \approx \tau\dot{\gamma}^p \tag{5.8}$$

where the shear stress is $\tau = \mu\sigma'$, due to the assumed Mohr-Coulomb constitutive law, and the plastic shear deformation $\dot{\gamma}^p = \frac{\partial v}{\partial z}$. All dissipation within the fluid is neglected.

To employ the CS thermoplastic soil model, dissipation needs to be expressed in a generalised form.

Dissipation can be reformulated in the principal stress space as:

$$D = \sigma_1\dot{\varepsilon}_1^p + \sigma_2\dot{\varepsilon}_2^p + \sigma_3\dot{\varepsilon}_3^p . \tag{5.9}$$

Substituting the plastic strain rate components with the flow rule relationship (4.10) yields

$$D = \dot{\lambda}\left[\sigma_1\frac{\partial f}{\partial\sigma_1} + \sigma_2\frac{\partial f}{\partial\sigma_2} + \sigma_3\frac{\partial f}{\partial\sigma_3}\right] \tag{5.10}$$

where σ_1, σ_2 and σ_3 are the principal stresses, f is the yield locus (used also as a plastic potential) and $\dot{\lambda}$ is the plastic multiplier.

Expression (5.10) now needs to be specified in terms of the constitutive relationship. In principal stress space, the Modified Cam Clay yield surface f can be written in the general case of $\sigma_1' \neq \sigma_2' \neq \sigma_3'$ in terms of the three stress invariants, i.e. the mean principal effective stress *p'*, the stress deviator *J* and the Lode angle θ_L (e.g. see Potts and Zdravkovic, 1999):

$$f = J^2 - M_J^2 p'\left(\sigma_c' - p'\right) \tag{5.11}$$

where:

$$p' = \frac{1}{3}\left(\sigma_1' + \sigma_2' + \sigma_3'\right) \tag{5.12}$$

$$J = \frac{1}{\sqrt{6}}\sqrt{\left(\sigma_2' - \sigma_3'\right)^2 + \left(\sigma_3' - \sigma_1'\right)^2 + \left(\sigma_1' - \sigma_2'\right)^2} = \frac{q}{\sqrt{3}} \tag{5.13}$$

$$\theta_L = \arctan\left[\frac{1}{\sqrt{3}}\left(2\frac{\sigma_2' - \sigma_3'}{\sigma_1' - \sigma_3'} - 1\right)\right]. \tag{5.14}$$

In the above, M_J is a generalised critical state parameter depending on the Lode angle and the critical state angle of shearing resistance φ'_{cs}:

$$M_J = \frac{\sin\varphi'_{cs}}{\cos\theta_L + \frac{\sin\theta_L \sin\varphi'_{cs}}{\sqrt{3}}} \tag{5.15}$$

In plane strain conditions, it is normally assumed θ_L=0, so that (5.15) becomes

$$M_J = \sin\varphi'_{cs}. \tag{5.16}$$

The classic expression for the MCC yield surface adopted in Chapter 4 is

$$f = q^2 - M^2 p'\left(\sigma'_c - p'\right), \tag{5.17}$$

where, consistently with (5.13),

$$q = \sqrt{\frac{1}{2}\left[\left(\sigma'_2-\sigma'_3\right)^2+\left(\sigma'_3-\sigma'_1\right)^2+\left(\sigma'_1-\sigma'_2\right)^2\right]}. \tag{5.18}$$

As a consequence, expression (5.17) in terms of $\left(p',q\right)$ is equivalent to (5.11) only if

$$M = M_J\sqrt{3} = \sin\varphi'_{cs}\sqrt{3}. \tag{5.19}$$

We shall therefore adopt for the yield locus the form (5.17) together with expression (5.19) for the CS parameter throughout the analysis. The derivative of the yield surface with respect to the principal stress components can be expressed as a function of the invariants p and q as

$$\frac{\partial f}{\partial\sigma_i} = \frac{\partial f}{\partial p'}\frac{\partial p'}{\partial\sigma_i} + \frac{\partial f}{\partial q}\frac{\partial q}{\partial\sigma_i}. \tag{5.20}$$

From the definitions (5.12), (5.17) and (5.18) we can calculate the above derivatives as:

$$\frac{\partial f}{\partial p'} = M^2\left(2p' - \sigma'_c\right), \tag{5.21}$$

$$\frac{\partial p'}{\partial\sigma_i} = \frac{1}{3}, \tag{5.22}$$

$$\frac{\partial f}{\partial q} = 2q, \tag{5.23}$$

$$\frac{\partial q}{\partial\sigma_i} = \frac{3\left(\sigma_i - p'\right)}{2q}. \tag{5.24}$$

Recalling that the soil is at critical state, substituting (5.5) into Equation (5.21) yields

$$\frac{\partial f}{\partial p'} = 0. \tag{5.25}$$

By using equations (5.22)-(5.25) into (5.20) we get the equations (for i=1,2,3)

$$\frac{\partial f}{\partial\sigma_i} = 3\left(\sigma_i - p'\right), \tag{5.26}$$

which can be substituted into (5.10) to obtain, by employing the definition of mean effective stress (5.12):

$$\begin{aligned} D &= \dot{\lambda}\left[3\sigma_1\left(\sigma_1 - p'\right) + 3\sigma_2\left(\sigma_2 - p'\right) + 3\sigma_3\left(\sigma_3 - p'\right)\right] = \\ &= \dot{\lambda}\left[2\left(\sigma_1^2 + \sigma_2^2 + \sigma_3^2 - \sigma_1\sigma_2 - \sigma_1\sigma_3 - \sigma_2\sigma_3\right)\right] = \\ &= \dot{\lambda}\left[\left(\sigma_1 - \sigma_2\right)^2 + \left(\sigma_3 - \sigma_1\right)^2 + \left(\sigma_2 - \sigma_3\right)^2\right]. \end{aligned} \tag{5.27}$$

Recalling the definition of deviatoric stress (5.18), (5.27) becomes

$$D = 2\dot{\lambda}q^2, \tag{5.28}$$

which by substituting the CS condition (5.6) finally yields

$$D = 2\dot{\lambda}\left(\frac{M\sigma_c'}{2}\right)^2 = \frac{1}{2}\dot{\lambda}\left(M\sigma_c'\right)^2. \tag{5.29}$$

Equation (5.29) represents the dissipation term at CS for plane strain, in general stress space. It is now needed to specify the terms M, σ_c' and $\dot{\lambda}$ in relation to the thermoplastic CS model of Chapter 4. This is done in the following subsections, 5.2.1 to 5.2.3.

5.2.1. Material softening law

In CS soil mechanics, parameter M is constant, and in our case corresponds to the soil (measured) friction angle, $M = \sin\varphi'\sqrt{3}$ according to (5.19). On the other hand, prolonged and fast shearing along a defined failure plane often brings about a drop in the friction angle of clays, due to the aligning of the platy particles parallel to the direction of shearing, until the 'residual state' is reached. We may now adjust our CS framework in order to approximate such residual state behaviour, under constant volume conditions, by accounting for the reduction of friction angle φ' with displacement and velocity. This can be done following the strain- and strain-rate softening law proposed by Vardoulakis (2002a). Furthermore, according to the adopted thermoplastic model we may allow within the CS framework for possible thermal-friction softening behaviour, as observed in some soils and already discussed in Sections 3.4.3.3 and 4.4.1.

Regarding strain- and strain-rate friction softening (Section 2.3.4), we shall start from the simple laws defined by Vardoulakis (2002a) for the Vajont clay based on the ring shear experimental data of Tika and Hutchinson (1999). Such laws define the evolution of the friction coefficient $\hat{\mu}$, related to the soil mobilised friction angle as $\hat{\mu} = \tan\phi'$, as a hyperbolic function:

$$\hat{\mu} = \mu_r + \left(\mu_p - \mu_r\right)\frac{1}{1 + a_1\dfrac{x_d}{d}} \tag{5.30}$$

where

$$\mu_r = \mu_{rd} + \left(\mu_{rs} - \mu_{rd}\right)\frac{1}{1 + a_2\dfrac{v_d}{d}}. \tag{5.31}$$

In the above d is the shearband thickness, x_d the slide displacement and v_d the slide velocity, so that the (thickness-dependent) shear strain is $\gamma \approx \frac{x_d}{d}$ and its rate $\dot{\gamma} \approx \frac{v_d}{d}$. The limiting values μ_{rs} and μ_{rd} are respectively the static and dynamical residual friction coefficients, while μ_p is the initial value of friction coefficient and $a_1 = 0.114,\ a_2 = 0.103$ are numerical factors defining how quickly the static and dynamic coefficients respectively decrease with displacement and velocity. The material-friction softening critical state parameter $\hat{M}$ can be written using (5.30): since $\varphi' = \arctan\left(\hat{\mu}\right)$ and $M = \sin\varphi'\sqrt{3}$, we obtain

$$\hat{M} = \sqrt{3}\sin\left[\arctan\left(\hat{\mu}\right)\right]. \tag{5.32}$$

An alternative form of (5.32), which could be more convenient for algebraic manipulation, can be found through the trigonometric identity (e.g. see Abramowitz and Stegun, 1964)

$$\arctan\left(y\right) = \arcsin\left(\frac{y}{\sqrt{1+y^2}}\right) \tag{5.33}$$

which allows us to express (5.32) as

$$\hat{M} = \sqrt{3}\frac{\hat{\mu}}{\sqrt{1-\hat{\mu}^2}}. \tag{5.34}$$

Furthermore, we will allow for an additional mechanism of thermal-friction softening, by employing the linear law (4.2). The final expression for the critical state parameter is the result of superposition of the frictional displacement- ,velocity- and thermal-softening effects, so that parameter M starts from a reference value and decreases towards zero according to the following expression:

$$M(\gamma,\dot{\gamma},\theta) = \hat{M}\left(\gamma,\dot{\gamma}\right) - \tilde{g}\left(\theta - \theta_{ref}\right) \tag{5.35}$$

where θ_{ref} is the reference temperature and parameter $\tilde{g}$ is the rate of decrease of M with temperature, or 'thermal sensitivity', which can be calibrated on experimental data such as those reported in Figure 30.

It must be here observed that the thermal-friction softening mechanism, being linear, is not bounded from below and may lead to unrealistic negative, or excessively small, values for the friction coefficient. On the other hand, a linear decrease law is the simplest and most effective one available to interpret the scarce experimental data available. We therefore choose to adopt it and impose an arbitrary lower limit for M, rather than adopt a more complex law such as the exponential one proposed by Vardoulakis (2002b). In the absence of direct experimental evidence, the lower-bound value M_L is set equal to the dynamic residual value, $M_L = \sqrt{3}\sin\left[\arctan\left(\mu_{rd}\right)\right]$.

5.2.2. Thermal hardening law defining the stress state

The apparent preconsolidation stress σ_c', defining the size of the yield envelope, evolves with temperature and volumetric plastic strain according to the thermo-mechanical hardening law (4.1). However, at critical state its dependency is reduced to the thermal component only, since the plastic volumetric strain rate is zero.

We now need to allow for the presence of excess pore pressures within the shearband. This means adding a pore-pressure dependency to the hardening relationship, which had not been considered in Laloui's thermal model (Section 2.3) as that was derived in a context of fully drained loading. According to the effective stress principle, the mean effective stress can be written as

$$p' = p_0' - u \tag{5.36}$$

where $p_0' = p - u_H$ is the initial effective mean stress in the shearband before the occurrence of excess pore pressures, u_H being the equilibrium pore pressure. In critical state conditions, σ_c' uniquely defines the stress state since the latter is locked at the top of the yield envelope, at point $(\sigma_c'/2,\ M\sigma_c'/2)$ in the $\left(p,q\right)$ plane (Section 5.1). We can therefore rewrite (5.36), in view of (5.5), as

$$\sigma_c'\left(\theta,u\right) = \sigma_{cH}'\left(\theta\right) - 2u\,, \tag{5.37}$$

where according to (4.1),

$$\sigma_{cH}'\left(\theta\right) = \sigma_{c0}' \exp(\tilde{\beta}\varepsilon_v^p)\left[1 - \gamma\log\left(\theta/\theta_{ref}\right)\right]. \tag{5.38}$$

From the above we understand that CS conditions allow us to equivalently consider as the stress variable either the preconsolidation stress or the mean stress. If one wants to refer, as is more conventional, to the mean stress *p'*, the stress state during thermo-poro-mechanical loading can be expressed as

$$p'(\theta,u) = p'(\theta) - u \tag{5.39}$$

where $p'(\theta) = \sigma'_{cH}(\theta)/2$ according to (5.5).

A demonstration of the above constitutive assumptions is given in Figure 44, which shows a typical (effective) stress path of a material point within the shearband during catastrophic sliding. For clarity the contributions of the different mechanisms affecting the stress state are drawn separately, although they occur at the same time. In a generic time interval Δt during sliding, the stress state, locked at the top of the yield locus, follows the path 1-4. From state 1 to 2, thermal softening occurs as the locus shrinks due to a temperature increase, according to the hardening law (5.38). Path 2 to 3 is due to the occurrence of excess pore pressures, which reduces by Δu the effective mean stress (or equivalently, the apparent preconsolidation stress by $2\Delta u$). Finally, from 3 to 4 frictional softening occurs, causing a decrease in the slope of the CSL and a consequent further change in stress.

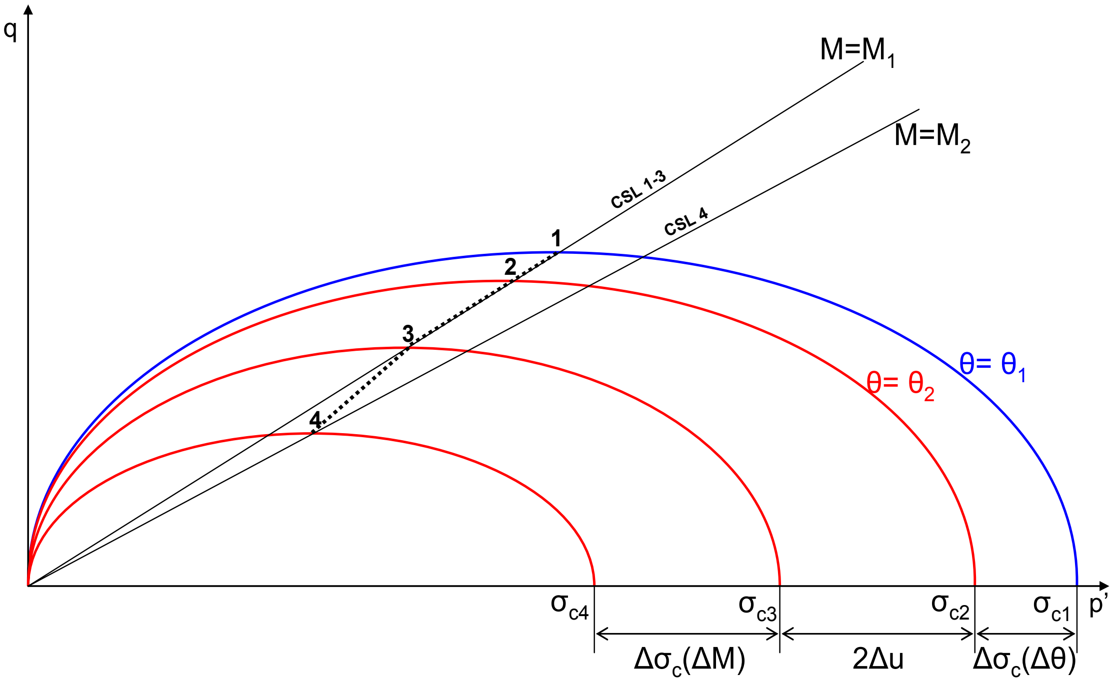

Figure 44. Effective stress paths of material points inside the shearband.

5.2.3. Plastic multiplier

The plastic multiplier in general stress space $\dot{\lambda}$ was calculated in Section 4.4.1 from the consistency condition, as

$$\dot{\lambda} = \frac{f_{\boldsymbol{\sigma}}\mathbf{D}^{me}\dot{\boldsymbol{\varepsilon}} + \left(f_{\theta} + 2\mathbf{D}^{te} f_{\boldsymbol{\sigma}}\right)\dot{\theta}}{f_{\boldsymbol{\sigma}}^{2}\mathbf{D}^{me} - f_{\varepsilon_v^p} f_{p'}}. \tag{5.40}$$

It is now convenient to express (5.40) in terms of stress invariants, for homogeneity of notation with the rest of the landslide model equations. No loss in generality occurs, since it is always possible, for isotropic materials, to split the stress tensor into a spherical and a deviatoric part (Mase, 1970). The terms featuring in (5.40) can be rewritten as:

$$f_{\boldsymbol{\sigma}}\mathbf{D}^{me}\dot{\boldsymbol{\varepsilon}} = Kf_p\dot{\varepsilon}_v + 3Gf_q\dot{\varepsilon}_q \tag{5.41}$$

$$2\mathbf{D}^{te} f_{\boldsymbol{\sigma}} = -2K\beta_s f_p \tag{5.42}$$

$$f_{\boldsymbol{\sigma}}^{2}\mathbf{D}^{me} = Kf_p^2 + 3Gf_q^2 \tag{5.43}$$

where the partial derivatives of the yield function, from Section 4.4.1 are:

$$\begin{aligned} f_{\theta} &= \frac{\sigma'_m \lambda p' M^2}{\theta} + 2\tilde{g}p'M\left\{\sigma'_m\left[1-\gamma\log\left(\theta/\theta_0\right)\right] - p'\right\} \\ f_{\varepsilon_v^p} &= -\sigma'_m p'\tilde{\beta}\left[1-\gamma\log\left(\theta/\theta_0\right)\right]M^2 \\ f_{p'} &= g_{p'} = M^2\left\{2p' - \sigma'_m\left[1-\gamma\log\left(\theta/\theta_0\right)\right]\right\} \\ f_q &= 2q \end{aligned} \tag{5.44}$$

In CS conditions, the first term on the RHS of (5.41) is zero since $\dot{\varepsilon}_v = 0$, so that the multiplier (5.40) becomes

$$\dot{\lambda} = F_0\dot{\varepsilon}_q + F_1\dot{\theta} \tag{5.45}$$

where

$$\begin{aligned} F_0 &= \frac{3Gf_q\dot{\varepsilon}_q}{\tilde{H}} \\ F_1 &= \frac{f_{\theta} - 2K\beta_s f_p}{\tilde{H}} \end{aligned} \tag{5.46}$$

and

$$\tilde{H} = Kf_p^2 + 3Gf_q^2 - f_{\varepsilon_v^p} f_{p'}. \tag{5.47}$$

The final step towards the incorporation of (5.45) into the landslide model is expressing the strain rate $\dot{\varepsilon}_q$ in terms of the variables of the 1-D shearband problem. A general form for the distortional (or deviatoric) strain rate is (e.g. see Muir Wood, 1990)

$$\dot{\varepsilon}_q = \frac{1}{3}\sqrt{2\left[\left(\dot{\varepsilon}_{yy} - \dot{\varepsilon}_{zz}\right)^2 + \left(\dot{\varepsilon}_{zz} - \dot{\varepsilon}_{xx}\right)^2 + \left(\dot{\varepsilon}_{xx} - \dot{\varepsilon}_{yy}\right)^2\right] + 3\left(\dot{\gamma}_{xy}^2 + \dot{\gamma}_{yz}^2 + \dot{\gamma}_{xz}^2\right)}. \quad (5.48)$$

In this case, due to plane strain conditions $\dot{\varepsilon}_{yy} = 0$ and $\dot{\gamma}_{zy} = \dot{\gamma}_{xy} = 0$. Moreover, 1-D hypotheses (Figure 42) imply that $\dot{\varepsilon}_{xx} = 0$, and since we are at critical state $\dot{\varepsilon}_v = \dot{\varepsilon}_{xx} + \dot{\varepsilon}_{yy} + \dot{\varepsilon}_{zz} = 0$, so that also $\dot{\varepsilon}_{zz} = 0$. Equation (5.48) is therefore reduced to

$$\dot{\varepsilon}_q = \frac{\sqrt{3}}{3}\dot{\gamma}_{zx} \quad (5.49)$$

where $\dot{\gamma}_{zx} = \frac{\partial v_x}{\partial z}$, and $v_x = v(z,t)$ is the velocity within the shearband in the direction of motion, which can be written, using the same assumptions discussed in Section 2.3.4.1, as

$$v(z,t) = v_d(t)\frac{z}{d} \quad (5.50)$$

so that (5.49) becomes

$$\dot{\varepsilon}_q = \frac{\sqrt{3}}{3}\frac{\partial v_x}{\partial z} = \frac{\sqrt{3}}{3}\frac{v_d(t)}{d}. \quad (5.51)$$

Substituting (5.51) into (5.45) yields the final expression for the thermo-plastic multiplier:

$$\dot{\lambda} = F_1\frac{\partial \theta}{\partial t} + F_2\frac{\partial v_x}{\partial z}. \quad (5.52)$$

Coefficients F_1 and $F_2 = F_0\frac{\sqrt{3}}{3}$ depend on the current temperature θ and pore pressure u through equations (5.46).

5.2.4. Final form of heat equation

All terms featuring in the dissipation term are now fully specified. The heat Equation (5.7), by adopting expression (5.29) for the dissipation, can then be written as

$$\frac{\partial \theta}{\partial t} = k_m\frac{\partial^2 \theta}{\partial z^2} + \frac{\dot{\lambda}\left(M\sigma'_c\right)^2}{2C_f} \quad (5.53)$$

or, by substituting (5.52),

$$\frac{\partial \theta}{\partial t} = k_m\frac{\partial^2 \theta}{\partial z^2} + \frac{\left(M\sigma'_c\right)^2}{2C_f}\left(F_1\frac{\partial \theta}{\partial t} + F_2\frac{\partial v_x}{\partial z}\right). \quad (5.54)$$

By collecting the terms multiplying the temperature rate we obtain

$$\frac{\partial \theta}{\partial t}\left(1-\frac{\left(M\sigma_c'\right)^2}{2C_f}F_1\right)=k_m\frac{\partial^2\theta}{\partial z^2}+\frac{\left(M\sigma_c'\right)^2 F_2}{2C_f}\frac{\partial v_x}{\partial z} \tag{5.55}$$

hence,

$$\frac{\partial \theta}{\partial t}=\frac{k_m}{1-\frac{\left(M\sigma_c'\right)^2}{2C_f}F_1}\frac{\partial^2\theta}{\partial z^2}+\frac{\left(M\sigma_c'\right)^2 F_2}{2C_f-\left(M\sigma_c'\right)^2 F_1}\frac{\partial v_x}{\partial z} \tag{5.56}$$

which, in view of (5.50), can be written as

$$\frac{\partial \theta}{\partial t}=D_i\frac{\partial^2\theta}{\partial z^2}+F_i\frac{v_d\left(t\right)}{d} \tag{5.57}$$

where

$$D_i=\frac{k_m}{1-\frac{\left(M\sigma_c'\right)^2}{2C_f}F_1}, \tag{5.58}$$

$$F_i=\frac{\left(M\sigma_c'\right)^2 F_2}{2C_f-\left(M\sigma_c'\right)^2 F_1}. \tag{5.59}$$

Coefficients D_i and F_i depend on pore pressure u, temperature θ and, if the material softening law (5.35) is taken into account, also on the shear strain γ and strain rate $\dot{\gamma}$. The final form for the heat diffusion-generation equation within the framework of thermal CS soil mechanics is given by (5.57). Compared to the original equation, (5.7), it can be noticed that the diffusion term is now non-linear: despite the original thermal diffusivity k_m being constant, it is divided by the temperature-dependent factor $\left(1-\frac{\left(M\sigma_c'\right)^2}{2C_f}F_1\right)$. Hence, defining the term D_i as a new thermal diffusivity allows us to formally define (5.57) a non-linear diffusion-generation equation.

5.3. Pore pressure equation

The pore pressure equation describes the time evolution of excess pore pressures within the shearband and its surroundings (cf. Section 2.3.4.1):

$$\frac{\partial u}{\partial t}=\frac{\partial}{\partial z}\left(c_v\frac{\partial u}{\partial z}\right)+\lambda_m\frac{\partial \theta}{\partial t}. \tag{5.60}$$

the structure of the consolidation coefficient c_v and the pressurisation coefficient λ_m will be now discussed in light of the proposed modifications to the constitutive framework.

5.3.1. Consolidation coefficient

The consolidation coefficient c_v is a function of soil compressibility and soil permeability. It can be expressed as

$$c_v = \frac{k_w}{g\rho_w c}, \tag{5.61}$$

where c is the soil compressibility, g the acceleration of gravity, ρ_w the pore-fluid density and k_w is Darcy's permeability coefficient, which is an increasing function of porosity and fluid density and inversely proportional to the dynamic viscosity of the fluid (see e.g. Powrie, 1997). Experimental results in Boom clay (Delage et al., 2000) showed that c_v for a clay is expected to be a weakly increasing function of temperature (Figure 45). Such small variation is due to two opposing effects: the soil permeability (in the sense of Darcy) increases with temperature, as a consequence of the thermal decrease of viscosity of the pore fluid, but this effect is compensated by a concurrent decrease of porosity.

Delage et al. (2000) suggest that the aforementioned thermal variation of c_v can be neglected, in line with other authors who investigated the thermal volumetric behaviour of clays (e.g., Habibagahi, 1977 and Towhata et al., 1995). Vardoulakis (2002a) on the other hand, to interpolate the experimental data of Delage et al. (2000) reported in Figure 45, proposes the exponential function

$$c_v = c_{v0} \exp\left(\theta/\theta_c\right) \tag{5.62}$$

where $c_{v0} = 6.346\times10^{-8}\,\mathrm{m}^2/\mathrm{s}$ and $\theta_c = 389.15\ °\mathrm{C}$. These experimental results according to Vardoulakis (2002a) are not representative of a deforming shearband undergoing pressurisation, and need to be adjusted to the considered 'elastic unloading' stress path in the landslide model, so c_v is recalculated as a function of the permeability and compressibility of the soil (Section 5.3.2.3) through Equation (5.61). This yields a still weakly increase of c_v with temperature, but at higher values (Figure 46) compared to Delage et al.'s (2000) results, given the relatively small value obtained for compressibility. Based on these data, Vardoulakis suggests a mean value for the consolidation coefficient of water-saturated clay:

$$\overline{c}_v = 7.3\times10^{-8}\ \mathrm{m}^2/\mathrm{s}. \tag{5.63}$$

The above considerations suggest that the variation of consolidation coefficient with temperature is not significant in our context. In fact, the thermal change of c_v at thermo-plastic states is less than an order of magnitude (Figure 45). This is also consistent with the fact that between 50°C and 100°C the dynamic viscosity of water is reduced by a factor of 2, while at the same time porosity is reduced by some 2% (Delage et al., 2000), thus determining an overall small permeability increase. In conclusion, in Equation (5.60) we may adopt the constant value (5.63). Alternatively, c_v may be calculated from Equation (5.61) if the (assumed constant) soil parameters k_w and c are known. Either way, the consolidation coefficient will be constant and can therefore be taken out of the partial derivative operator in (5.60):

$$\frac{\partial u}{\partial t} = \overline{c}_v \frac{\partial^2 u}{\partial z^2} + \lambda_m \frac{\partial \theta}{\partial t}. \tag{5.64}$$

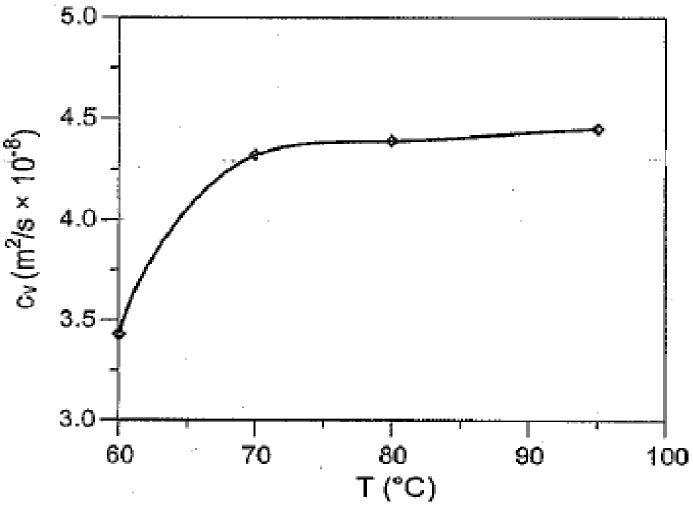

Figure 45. Experimental results showing the variation of the consolidation coefficient of a saturated clay with temperature (Delage et al., 2000).

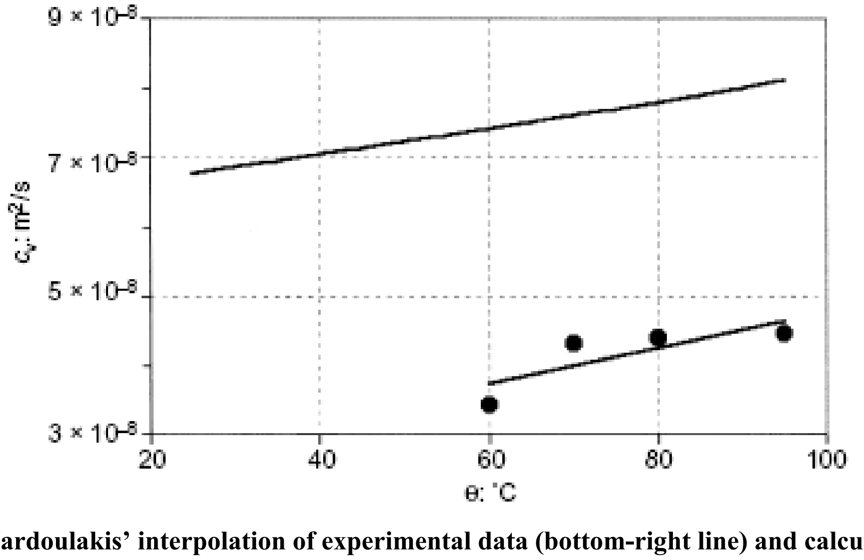

Figure 46. Vardoulakis' interpolation of experimental data (bottom-right line) and calculations according to the landslide model's assumptions (over-lying line) for the consolidation coefficient. From Vardoulakis (2002a).

5.3.2. Pressurisation coefficient and thermal volumetric behaviour of clay

The pressurisation coefficient is defined as the pore pressure increase due to a unit temperature increase in undrained and isochoric conditions. This definition is obtained by assuming that, for a soil with small permeability (as is that within the shearband) and for a short term analysis, pore water flow is negligible so that from (5.64) we obtain

$$\frac{\partial u}{\partial t} = \lambda_m \frac{\partial \theta}{\partial t}, \tag{5.65}$$

which yields the definition

$$\lambda_m = \left.\frac{\partial u}{\partial \theta}\right|_{\substack{Vol=const \\ undrained}}. \tag{5.66}$$

Vardoulakis (2000, 2002a) expresses coefficient λ_m in terms of the soil's thermal expansion coefficient α and the compressibility coefficient *c*, as

$$\lambda_m = \frac{\alpha}{c} \tag{5.67}$$

where:

$$\alpha = \alpha_m - \alpha_c \tag{5.68}$$

and α_m and α_c are the thermal expansion coefficient of the soil-water mixture and the thermal expansion coefficient of the soil skeleton respectively. This is also in line with Sulem et al. (2007).

It has been found experimentally (e.g. Hueckel and Baldi,1990; Laloui et al., 2005) that normally-consolidated clays in general, when heated under drained conditions exhibit a net volume reduction (cf. Section 2.3.3). This is due to an internal mechanism of micro-structural collapse, which in turn is due to changes in water adsorption by the clay particles and changes in the equilibrium between attractive and repulsive electrostatic forces between ions forming the 'double layer' at the clay particle scale (Campanella and Mitchell, 1968).

Many authors (e.g. Baldi et al., 1988 and 1991, Sultan, 1997; Modaressi and Laloui, 1997) reported that while normally-consolidated clays exhibit plastic contraction upon heating, over-consolidated clays tend to behave elastically and expand at the initial stages of heating, then subsequently show plastic contraction at higher temperatures. For this reason, experimental thermal loading paths are usually plotted for different OCRs (Figure 47). In Figure 48 we can see the experimental response to temperature cycling, highlighting the reversibility of (dilative) deformation of Boom clay at OCR=6.

The attainment of a 'transition temperature' at which plastic contraction starts in over-consolidated soils is evident in the change in slope of some of the plots describing isotropic heating tests at constant confining stress, when the soil's volumetric behaviour changes from dilative to contractive (Figure 47 and Figure 49).

As a summary of the important aspects of the thermal volumetric behaviour of clays, we find it useful to report here the experimental observations by Sultan et al. (2002) regarding the major thermo-elasto-plastic trends of clay's behaviour; these are in agreement with earlier findings (e.g. Demars and Charles, 1982, Baldi et al., 1988):

- The amount of plastic contraction of normally consolidated samples is independent of the applied mean effective stress;
- Thermal contraction during a test increases when the soil's OCR is lower, leading to pure contractive behaviour when OCR=1;
- The slope of the volumetric strain versus temperature curve in the cooling stage (i.e. the thermo-elastic expansion coefficient) is independent of the applied mean effective stress;
- The temperature at which transition between thermal expansion and contraction occurs decreases with OCR.

5.3.2.1. Determination of λ_m according to Vardoulakis

In light of the above experimental findings, Vardoulakis (2002a) proposes to describe the thermal volumetric behaviour of clay with a twofold expression for the expansion coefficient, depending on whether the current temperature is below or above the transition or "critical" temperature θ_{crit} :

$$\alpha_c = \begin{cases} \alpha_c^e & \text{if } \theta \le \theta_{crit} \\ \alpha_c^{ep} & \text{if } \theta > \theta_{crit} \end{cases} \tag{5.69}$$

where α_c^e denotes the elastic and α_c^{ep} the elasto-plastic thermal expansion coefficients of the soil skeleton. A constant value for the elastic thermal expansion coefficient is proposed (slope of A-B in Figure 49) which was found experimentally (Sultan, 1997) to be practically equal to the thermal expansion coefficient of the soil-water mixture α_m, calculated as

$$\alpha_m = (1-n)\alpha_s + n\alpha_w . \tag{5.70}$$

In the above n is the porosity, α_s the thermal expansion coefficient of clay particles and α_w that of pore water. Vardoulakis (2002a) suggests that also $\alpha_m \approx \alpha_c^e$ (which corresponds to coefficient β_s of Section 4.3), so that at elastic states (i.e. below the critical temperature), by applying (5.68) the soil's thermal expansion coefficient $\alpha = \alpha_m - \alpha_c = 0$.

At plastic states, by using the additive decomposition of the elasto-plastic coefficient into elastic and plastic contribution $\alpha_c^{ep} = \alpha_c^e + \alpha_c^p$, the thermal expansion coefficient from Equation (5.68) can be expressed as

$$\alpha = -\left(\alpha_c^{ep} - \alpha_c^e\right) = -\alpha_c^p \tag{5.71}$$

where α_c^{ep}, α_c^e and α_c^p are the elasto-plastic (i.e. slope of B-C in Figure 49), elastic and plastic expansion coefficients respectively. This leads to the following expression for the pressurisation coefficient (Vardoulakis 2002a):

$$\lambda_m = \begin{cases} 0 & \text{if } \theta \le \theta_{crit} \\ \dfrac{-\alpha_c^p}{c} & \text{if } \theta > \theta_{crit} \end{cases} \tag{5.72}$$

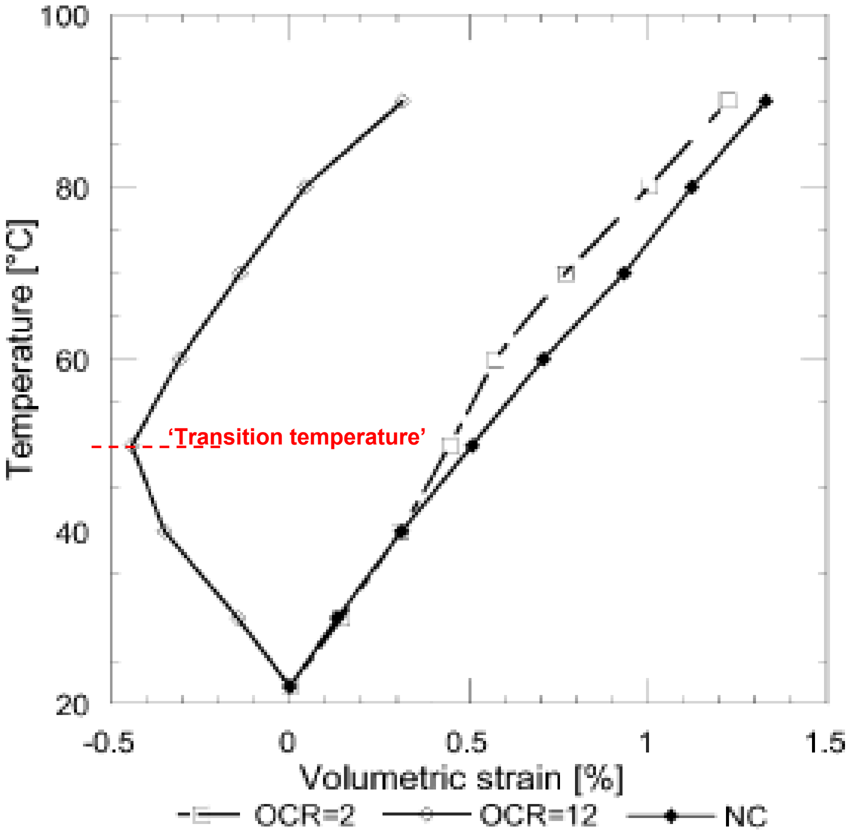

Figure 47. Experimentally observed volume changes from isotropic heating tests, at different OCRs, for a kaolin clay (from Laloui and Cekerevac, 2003).

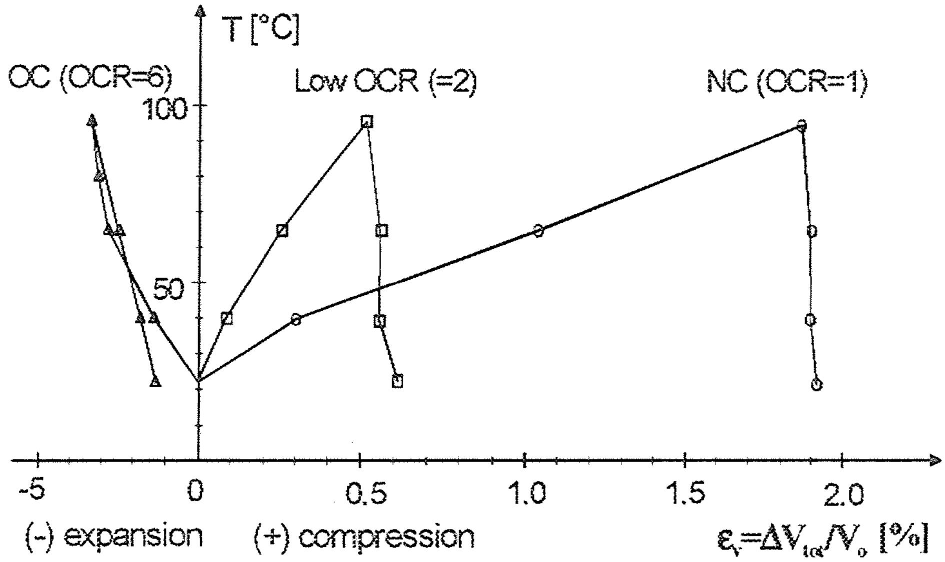

Figure 48. From Baldi et al. (1991). Volumetric response of Boom clay to drained isotropic heating/cooling tests, for different OCRs.

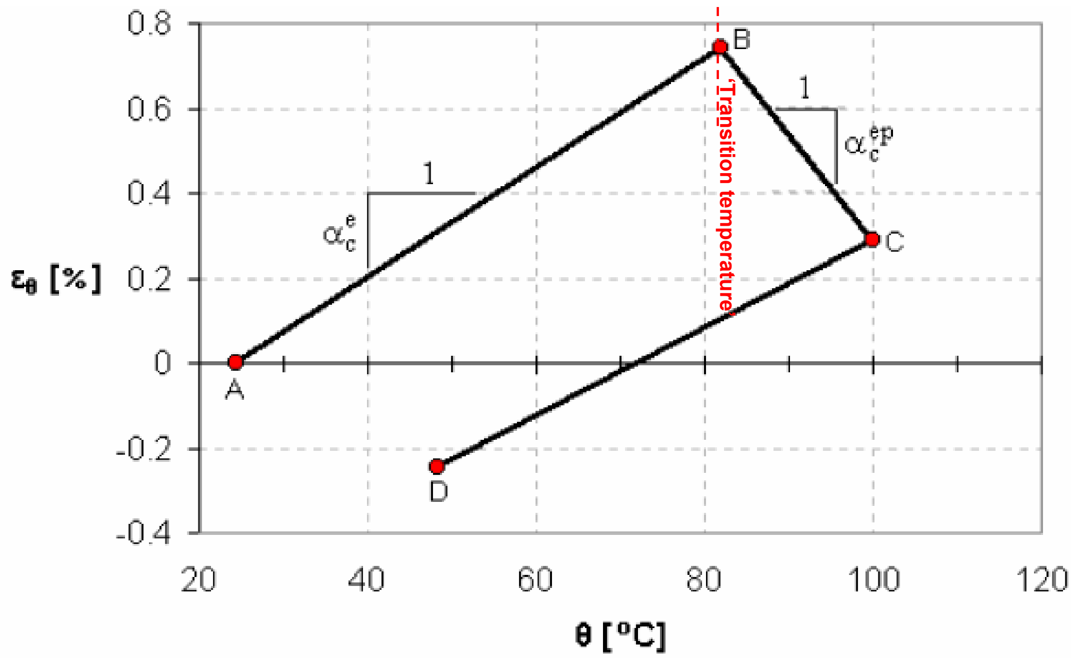

Figure 49. From Vardoulakis (2002a). Isotropic thermal volumetric deformation of an over-consolidated 'Boom clay' (OCR=12). The experimental data by Sultan (1997) have been interpolated with a bi-linear law by Vardoulakis (2002a). A-B represents the thermoelastic expansion, at B the 'transition' or 'critical' temperature is reached after which thermoplastic collapse (B-C) follows. CD represents the cooling phase and shows thermoelastic contraction.

The author also proposes the variation laws with OCR of critical temperature θ_{crit} and plastic contraction coefficient α_c^p (Vardoulakis, 2002a, equations (27) and (29)), based on interpolation of the experimental data obtained by Sultan (1997) on the thermal behaviour of Boom clay (Figure 50). It should be noted here that while for Sultan

(1997) the OCR is intended as the 'initial' one, i.e. the ratio between the isotropic preconsolidation stress and the (constant) confining stress adopted in the experiments, Vardoulakis seems to use 'current' values of OCR during thermo-mechanical loading, considering OCR to increase during the unloading of the soil skeleton as excess pore pressure develops, starting from a normally consolidated state. In other words, for Sultan et al. (2002)

$$\mathrm{OCR} = \sigma_c' \big/ p_0' \tag{5.73}$$

while for Vardoulakis (2002a, Equation (27))

$$\mathrm{OCR} = p_0' \Big/ \left(p_0' - u \right) \tag{5.74}$$

where p_0' is the isotropic mean stress at the start of loading, σ_c' the isotropic preconsolidation pressure and u the excess pore pressure, whose evolution is governed by Equation (5.60).

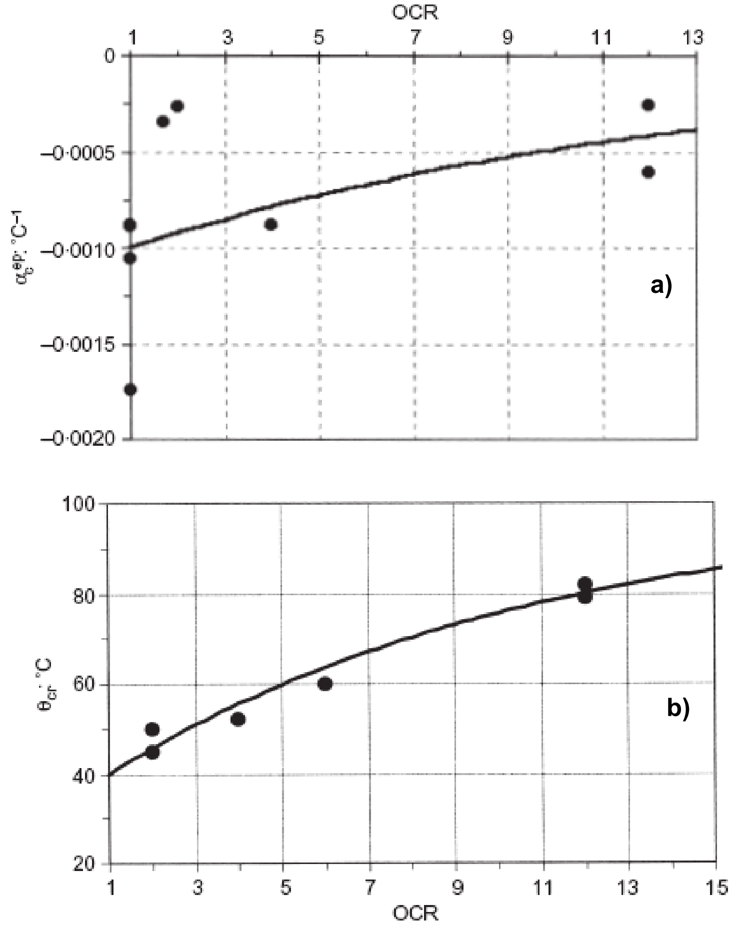

Figure 50. Data points from Sultan (1997) showing the dependency of the elasto-plastic thermal expansion coefficient (a) and critical temperature (b) on the soil's OCR; and relative interpolating lines (Vardoulakis 2002a). It can be noticed that, while the data on critical temperature show a clear trend, those regarding the elasto-plastic coefficient are rather scattered.

Vardoulakis (2002a), after the above considerations, remarks the yet large uncertainties in the determination of the value of pressurisation coefficient due to the lack of direct experimental data and suggests a mean value of $\bar{\lambda}_m = 0.06\ \text{MPa/°C}$, to be employed subject to condition (5.72) when the current temperature is above the "critical" one.

5.3.2.2. Determination of λ_m consistently with the new constitutive model

Within the framework of the constitutive model presented in Chapter 4, the soil's thermal behaviour discussed above exhibits some typical features: in purely elastic conditions the volumetric response of clay to heating is dilative and reversible, and depends only on coefficient $\beta_s = \alpha_c^e$; in elasto-plastic conditions, the volumetric response is more complex and is governed by the flow rule (4.11). In this context, the initial OCR is not a parameter of the problem, but merely an indicator on whether the state of the soil at the start of loading is elastic or plastic: for a NC soil, further (thermal or mechanical) loading immediately causes plastic flow, while for an OC soil it initially causes elastic (reversible) strains until the stress state engages the yield surface.

While Vardoulakis (2002a), in the absence of a constitutive law capable of accounting for the thermal behaviour of the soil, proposed an expression of λ_m based on the available experimental evidence (Equation (5.72)), this is not an option here. To be consistent with the thermo-plasticity framework proposed we have to derive the plastic contraction coefficient (leading to the calculation of λ_m according to Equation (5.67)) directly from the assumed constitutive model.

In fact, by definition the thermal expansion (or contraction) coefficient α_c in a strain-temperature constitutive relationship is the factor pre-multiplying the temperature rate:

$$\dot{\varepsilon}^{tep} = \frac{\partial \varepsilon}{\partial \theta}\frac{d\theta}{dt} = \alpha_c \frac{d\theta}{dt} \tag{5.75}$$

where $\dot{\varepsilon}^{tep}$ is the thermal contribution to the total thermo-mechanical strain rate

$$\dot{\varepsilon}^{tot} = \dot{\varepsilon}^{tep} + \dot{\varepsilon}^{mep}, \tag{5.76}$$

and $\dot{\varepsilon}^{mep}$ represents the mechanical contribution.

In the elastic regime, coefficient $\alpha_c = \alpha_c^e$ is identified from the elastic volumetric strain rate expression, as in Equation (4.15), and can be considered either constant, in first approximation (e.g. the coefficient α used in Mase, 1970, Section 6.9), or pressure- and temperature-dependent (coefficient β_s of Laloui and Cekerevac, 2003). Similarly, at plastic yield the thermo-plastic contraction coefficient α_c^{tp} (denoting the thermal only contribution to the global volumetric strain rate) coincides with the factor pre-multiplying the temperature rate on the right hand side of the plastic flow expression. Accordingly, from (4.11) we can write:

$$\dot{\boldsymbol{\varepsilon}}_v^p = \dot{\lambda}\left(\dot{\theta}, \dot{\varepsilon}\right)\frac{\partial f}{\partial p'}. \tag{5.77}$$

In the above, the plastic multiplier is given by Equation (5.40), which by substituting equations (5.41)-(5.43) becomes

$$\dot{\lambda} = \frac{Kf_p\dot{\varepsilon}_v + 3Gf_q\dot{\varepsilon}_q + \left(f_\theta - 2K\beta_s f_p\right)\dot{\theta}}{\tilde{H}}, \tag{5.78}$$

where H is specified by (5.47), and the partial derivatives of the yield surface are expressed by (5.44).

Before elaborating on the above expressions to calculate α_c^{tp}, we must impose isotropic loading conditions in order to be consistent with the experimental evidence and earlier findings in the literature, as discussed in Section 5.3.2.1. This means prescribing in this calculation that the stress state must lie at all times on the isotropic axis, at the tip of the yield envelope, so that

$$p' = \sigma_c'; \quad q = 0; \quad \dot{\varepsilon}_q = 0. \tag{5.79}$$

Substituting conditions (5.79) into (5.78) allows us to reformulate (5.77) as

$$\dot{\boldsymbol{\varepsilon}}_v^p = F_\theta\dot{\theta} + F_m\dot{\varepsilon}_v^m \tag{5.80}$$

where

$$F_\theta = \frac{f_\theta - 2K\beta_s f_p}{\tilde{H}}M^2\sigma_c' \tag{5.81}$$

is the factor representing the thermal contribution to volumetric plastic strain rates, and

$$F_m = \frac{Kf_p}{\tilde{H}}M^2\sigma_c' \tag{5.82}$$

represents the isotropic mechanical contribution to volumetric plastic strain rates.

The thermoplastic contraction coefficient is thus equal to factor F_θ. Recalling the derivatives (5.44) and applying conditions (5.79) yields

$$\begin{cases} f_\theta = \dfrac{\gamma \sigma_c'^2 M^2}{\theta\left[1-\gamma \log\left(\theta/\theta_{ref}\right)\right]} \\ f_{\varepsilon_v^p} = -\tilde{\beta} M^2 \sigma_c'^2 \\ f_{p'} = M^2 \sigma_c' \\ f_q = 0 \end{cases} . \tag{5.83}$$

Substituting (5.47) and (5.83) into (5.81) we obtain

$$\alpha_c^{tp} = F_\theta = \frac{\gamma \sigma_c' - 2K\theta\left[1-\gamma \log\left(\theta/\theta_{ref}\right)\right]\beta_s}{\theta\left[1-\gamma \log\left(\theta/\theta_{ref}\right)\right]\left(K+\tilde{\beta}\sigma_c'\right)} . \tag{5.84}$$

Recalling the definition of the bulk modulus (4.20), at isotropic conditions (5.79)

$$K = \frac{1+e}{\kappa}\sigma_c' ,$$

we can substitute it to (5.84), to obtain

$$\alpha_c^{tp}\left(\theta\right) = \frac{\gamma - 2\theta\left[1-\gamma \log\left(\theta/\theta_{ref}\right)\right]\dfrac{1+e}{\kappa}\beta_s}{\theta\left[1-\gamma \log\left(\theta/\theta_{ref}\right)\right]\left(\dfrac{1+e}{\kappa}+\tilde{\beta}\right)} \tag{5.85}$$

which by substituting definition (4.42) finally becomes

$$\alpha_c^{tp} = \frac{\lambda-\kappa}{\lambda}\left\{\frac{\gamma\ \kappa}{\left(1\text{+e}\right)\theta\left[1-\gamma \log\left(\theta/\theta_0\right)\right]} - 2\beta_s\right\} \tag{5.86}$$

The plastic contraction coefficient α_c^{tp} must be negative to be physically meaningful, and shows dependency on the current temperature level and some constant soil parameters, whose values are discussed in Section 5.5.3.

Expression (5.86) overcomes the concept of critical temperature introduced in Vardoulakis (2002a). In fact, thermal dependency of coefficient α_c^{tp} allows for a gradual soil skeleton collapse, rather than the sudden one prescribed by (5.72). There is no more need for the concept of a threshold temperature dividing thermoelastic from thermoplastic states if we adopt the form (5.86), as the constitutive model accounts for thermoplastic yield as soon as a temperature increase occurs, regardless of its magnitude, provided that the stress state lies on the yield envelope. This condition holds for the landslide model, where the loading state within the shearband is always plastic (Figure 44). As a consequence, in the landslide model instead of (5.72) we will adopt, for all temperature values,

$$\lambda_m\left(\theta\right) = \frac{-\alpha_c^{tp}\left(\theta\right)}{c} . \tag{5.87}$$

The above basic considerations for the interpretation of the thermal volumetric behaviour of soils incidentally provide us with an additional explanation for the occurrence of excess pore pressures (cf. Section 2.3.3): isotropic thermoplastic contraction of the soil measures how much the soil volume would collapse if this were possible. However, as already discussed, the soil within the shearband is at critical state and does not allow any volume change (Section 5.1): excess pore pressures develop as a consequence of the impossibility for the soil skeleton to thermally collapse.

5.3.2.3. Compressibility coefficient and mean stress

The calculation of pressurisation coefficient according to (5.87) is completed once the oedometric water saturated, drained compressibility coefficient c is determined (Vardoulakis 2002a).

First of all, it is necessary to express the effective mean stress p' as a function of the normal (vertical) stress σ'_n acting in the slip plane. In static conditions, which represent the initial conditions for the landslide model, σ'_n is calculated knowing the unit weights of the materials involved, the slide geometry and the seepage conditions. From this value of normal stress we can deduce the 'static' or initial value of the mean effective stress p'_0.

By resorting to linear elasticity, we may write Hooke's law in terms of the Young's modulus E and Poisson's ratio ν as follows:

$$\begin{cases} \varepsilon_{xx} = \dfrac{1}{E}\left(\sigma'_{xx} - \nu\sigma'_{yy} - \nu\sigma'_{zz}\right) \\ \varepsilon_{yy} = \dfrac{1}{E}\left(-\nu\sigma'_{xx} + \sigma'_{yy} - \nu\sigma'_{zz}\right) \\ \varepsilon_{zz} = \dfrac{1}{E}\left(-\nu\sigma'_{xx} - \nu\sigma'_{yy} + \sigma'_{zz}\right) \end{cases} \tag{5.88}$$

where the same axis geometry of Figure 42 is considered, hence the normal stress $\sigma'_n = \sigma'_{zz}$.

In oedometric conditions, $\varepsilon_{xx} = \varepsilon_{yy} = 0$, so that from the first two equations of (5.88) we get

$$\begin{cases} \sigma'_{xx} = \nu\left(\sigma'_{yy} + \sigma'_n\right) \\ \sigma'_{yy} = \nu\left(\sigma'_{xx} + \sigma'_n\right) \end{cases} \tag{5.89}$$

By additionally assuming for simplicity that $\sigma'_{xx} = \sigma'_n$ (Vardoulakis, 2000), we obtain from the second of (5.89) $\sigma'_{yy} = 2\nu\sigma'_n$. By substituting these expressions for the principal stress components in the definition of mean effective stress

$$p' = \frac{1}{3}\left(\sigma'_{xx} + \sigma'_{yy} + \sigma'_{zz}\right), \tag{5.90}$$

we finally obtain

$$p' = p'_0 = \frac{2}{3}\left(1+\nu\right)\sigma'_n. \tag{5.91}$$

The oedometric compressibility coefficient can be written as

$$c = nc_w + c_{sk} \tag{5.92}$$

where $n = e/(1+e)$ is the porosity of the soil, c_w the compressibility of water and c_{sk} the compressibility of the soil skeleton, obtained in one-dimensional conditions. Expression (5.92) is adopted in order to be consistent with Vardoulakis (2002a), although we remark that the first addend on the right hand side of the equation could be neglected, since c_w is typically two orders of magnitude smaller than c_{sk} and $0 < n \leq 1$. The latter can be thus expressed as

$$c_{sk} = \left(\frac{\partial \varepsilon}{\partial \sigma_v'}\right)_{\theta=const.} \tag{5.93}$$

which is equivalent to

$$c_{sk} = \left(c_{sw}\frac{\partial p'}{\partial \sigma_v'}\right)_{\theta=const.} \tag{5.94}$$

where

$$c_{sw} = \left(\frac{\partial \varepsilon}{\partial p'}\right)_{\theta=const.} \tag{5.95}$$

is the isotropic elastic ‘swelling’ soil compressibility, corresponding to the compression modulus in isotropic elastic unloading. This choice is justified by the fact that under conditions of effective stress reduction due to pore pressure increase (cf. Section 2.3.3), the soil skeleton practically undergoes elastic unloading (Vardoulakis 2000, 2002a, Ghabezloo and Sulem 2008). From (5.91) we deduce that

$$\frac{\partial p'}{\partial \sigma_v'} = \frac{2}{3}\left(1+\nu\right), \tag{5.96}$$

so that (5.94) becomes

$$c_{sk} = \frac{2}{3}(1+\nu)c_{sw} \tag{5.97}$$

In order to calculate (5.95) consistently with the proposed constitutive framework, we may resort to the equation of the soil's unloading-reloading line (URL) in the $(\ln p', \mathrm{v})$ compression plane:

$$\mathrm{v} = \mathrm{v}_0 - \kappa \ln(p') \tag{5.98}$$

where $\mathrm{v} = (1+e)$ is the specific volume, so that

$$\frac{d\mathrm{v}}{dp'} = -\frac{\kappa}{p'}. \tag{5.99}$$

Since an increment in specific volume produces an increment of volumetric strain

$$d\varepsilon_v = -\frac{d\mathrm{v}}{\mathrm{v}} \tag{5.100}$$

(see e.g. Muir Wood, 1990), where the negative sign comes from the soil mechanics convention that compressive strains are positive, we may substitute definition $d\mathrm{v} = -\mathrm{v} \cdot d\varepsilon_v$ into (5.99), to obtain

$$c_{sw} = \frac{\partial \varepsilon_v}{\partial p'} = \frac{\kappa}{\mathrm{v}p'} = \frac{\kappa}{(1+e)p'} \tag{5.101}$$

where we can set as mean effective stress in the shearband the static value, $p' = p'_0$.

By substituting (5.97) and (5.101) into (5.92), compressibility takes the form

$$c = \left(\frac{e}{1+e}\right)c_w + \frac{2\kappa(1+\nu)}{3p_0'(1+e)}. \tag{5.102}$$

5.4. Dynamical equation

The dynamical equation describes the time evolution of the landslide velocity (see also Section 2.3.4.2), when the soil mass is assumed to rotate as a rigid body with respect to the centre of a previously defined critical failure circle. By calculating the net driving moment of the mass assuming a constant normal stress (set equal to a mean value) acting along the whole failure circle, the linear acceleration of the slide can be expressed as (Vardoulakis, 2002a):

$$\frac{dv_d}{dt} = R\omega_0^2 \left(A(\mu_m) + \frac{u_d(t)}{p_c(\mu_m)} \right). \tag{5.103}$$

Parameter A is expressed as

$$A = A_0\left(1-\frac{\mu_m}{\mu_F}\right) \tag{5.104}$$

where $A_0=\left(D_F\ R\ R_D\right)/\left(\gamma_s I_p\right)$ is a (constant) function of the geometrical parameters of the considered failure circle section with:

D_F the resultant driving force (per unit length),

R the radius of the failure circle,

R_D the radius of the "friction circle" (Taylor, 1948),

γ_s the unit weight of the soil,

I_p the polar moment of inertia of the rotating rigid body.

Coefficient μ_F is the friction coefficient at incipient failure for the critical circle, while μ_m is the mobilised friction coefficient.

Parameter p_c in (5.103) is expressed as:

$$p_c=\frac{\gamma_s I_p}{R^3}\frac{1}{\left(\alpha-\alpha_1\right)\mu_m}=\frac{F_c}{\mu_m} \tag{5.105}$$

where $\left(\alpha-\alpha_1\right)$ is the epicentric angle, encompassing the part of the failure surface situated below the phreatic level (Figure 51).

In order to incorporate the frictional softening law (Section 5.2.1) into Equation (5.103), it is necessary to rewrite it in a more convenient form. The mobilised friction coefficient is $\mu_m=\tan\varphi'_m$, where φ'_m is the corresponding mobilised friction angle. According to (5.19), we can write

$$\mu_m=\tan\left[\arcsin\left(\frac{M}{\sqrt{3}}\right)\right]. \tag{5.106}$$

From the trigonometric identity

$$\arcsin\left(y\right)=\arctan\left(\frac{y}{\sqrt{1-y^2}}\right) \tag{5.107}$$

(e.g. see Abramowitz and Stegun, 1964), by setting $y=M/\sqrt{3}$ we deduce

$$\mu_m=\frac{M/\sqrt{3}}{\sqrt{1-\left(M/\sqrt{3}\right)^2}}=\frac{M}{\sqrt{3-M^2}} \tag{5.108}$$

where M is expressed by (5.35).

Substituting the above expressions of p_c, A and μ_m into (5.103) yields

$$\frac{dv_d}{dt} = R\omega_0^2 \left[A_0 - \frac{M}{\sqrt{3-M^2}} \left(\frac{A_0}{\mu_F} + \frac{u_d}{F_c} \right) \right] \tag{5.109}$$

where $u_d = u(z,t)\big|_{z=d}$. This is the last one of the set of governing equations for the landslide model, summarised below:

$$\begin{cases} \text{(I)} \quad \dfrac{\partial \theta}{\partial t} = D_i \dfrac{\partial^2 \theta}{\partial z^2} + F_i \dfrac{v_d(t)}{d} \\ \text{(II)} \quad \dfrac{\partial u}{\partial t} = \overline{c}_v \dfrac{\partial^2 u}{\partial z^2} + \lambda_m \dfrac{\partial \theta}{\partial t} \\ \text{(III)} \ \dfrac{dv_d}{dt} = R\omega_0^2 \left[A_0 - \dfrac{M}{\sqrt{3-M^2}} \left(\dfrac{A_0}{\mu_F} + \dfrac{u_d}{F_c} \right) \right] \end{cases} . \tag{5.110}$$

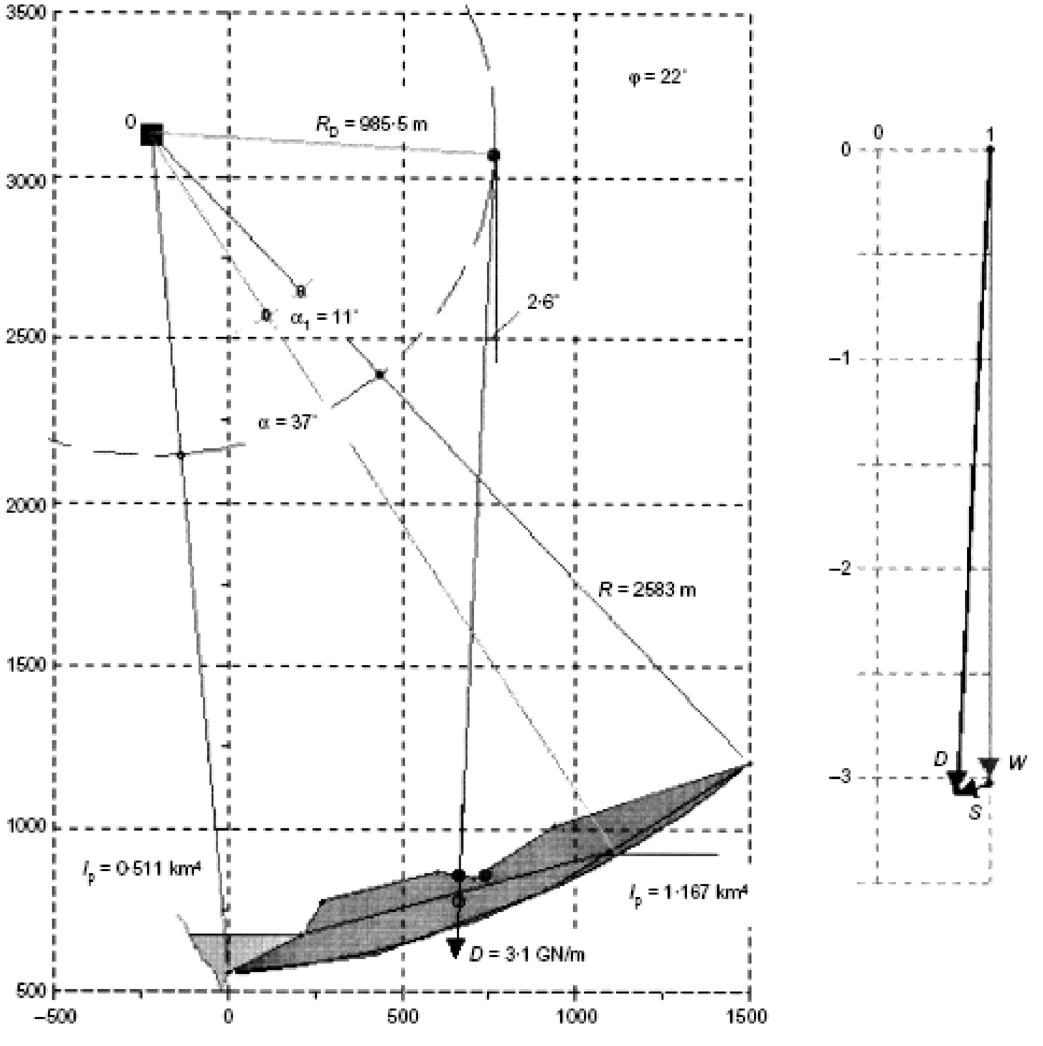

Figure 51. From Vardoulakis (2002a). Critical failure circle for 'section 6' of the Vajont slide. The epicentric angle represents the immersed part of the circular failure surface, and corresponds to the portion α- α_1=(37°-11°) in this case.

5.5. Numerical implementation

The first two equations of system (5.110) are nonlinear partial differential equations (PDEs) while the last one is in a nonlinear ordinary differential equation (ODE). They all need to be integrated with the necessary initial and boundary conditions. Due to the difference in the mathematical nature of the equations, different numerical integration schemes are now needed compared to those used in Section 4.5.1. We will resort to Finite-Difference techniques to provide approximation of the exact derivatives, as described hereafter.

5.5.1. Discussion on integration methods

Equations (5.110) (I) and (II) both describe the time evolution of a physical quantity (defining an 'initial value' problem), and they belong to the mathematical category of parabolic PDEs (e.g. see Hoffman, 2001): The solution in the domain of interest is found by marching forward in time from an initial state, taking the boundary conditions into account.

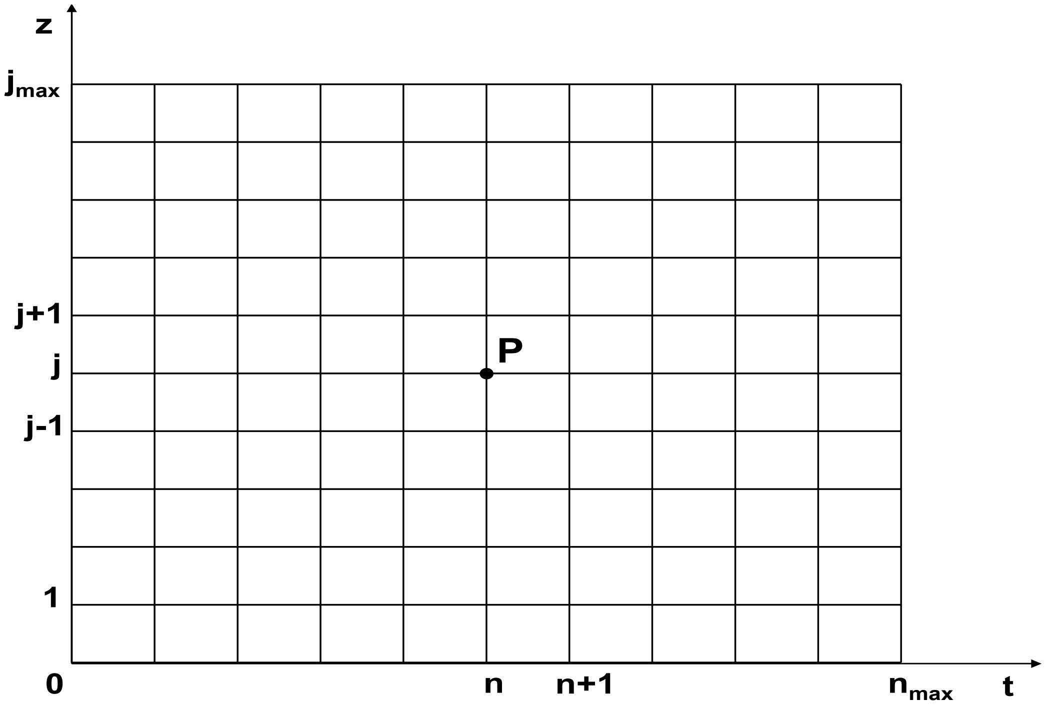

Figure 52. Sample finite difference grid, defining the discretised solution domain for a parabolic PDE.

The solution of PDEs describing such one-dimensional problems implies the subdivision of the time and space domain into a grid of discrete points (Figure 52), where the derivatives entering the problem are to be calculated. Similarly to those for ODEs (Section 4.5.1), existing integration methods for parabolic PDEs can be subdivided into explicit and implicit ones.

In explicit methods, the solution at a point *P* at time step *n*+1 depends only on the solution at neighbouring points at the previous time step *n*. Thus, at each integration step a small triangular area of the integration domain is involved in the calculation ('numerical domain of dependence' in Figure 53). In implicit methods, on the other hand, the solution at point *P* at time step *n*+1 depends on the solution at neighbouring points, both at time step *n*+1 and time step *n*. The numerical domain of dependence is in this case extended to the whole spatial range enclosed by time levels *n* and *n*+1 (Figure 54). While explicit methods involve the solution of a single equation in terms of known quantities, implicit ones require the solution of a system of equations to be found at each time-step.

Among the available methods, we consider three potentially suitable ones for the discretisation of equations (5.110):

- Forward-time centred-space (FTCS), explicit
- Backward-time centred-space (BTCS), implicit
- Crank-Nicholson (CN), implicit.

The FTCS method provides a first-order approximation in time and second-order approximation in space (cf. Section 4.5.1). This method is very straightforward to implement, as it does not require the solution of a system, implying less computational expense. However, stability is not guaranteed for explicit methods and a restriction in the size of the time-step is needed. In other words, the solution might not be bounded if the time-step is bigger than a threshold value, to be established through an appropriate stability analysis (e.g. see Press, 1988). The BTCS method overcomes this difficulty, as all implicit methods are unconditionally stable, despite requiring a fairly larger computational effort in order to handle the more complex algebra. The CN method still retains the stability advantages of BTCS, and improves on the accuracy since it provides a second-order approximation in time. The mathematical formulation here is more complicated, but the overall robustness is an undoubted advantage that would make this method the most suitable one for discretising equations (5.110). Nevertheless, the convenience of adopting CN should be reconsidered in light of the potential nonlinearity of the considered equations. In our case, equations (5.110) contain nonlinear terms as discussed in Sections 5.2 and 5.3.2, which constitute a considerable complication: for example, the variation of coefficient D_i in the spatial and temporal domain needs to be taken into account in the discretised formulas. In this context, adopting the FTCS method does not pose any numerical difficulty, since the nonlinear coefficients are evaluated at points where all the functions are known. On the other hand, if one of the implicit methods is to be considered, severe numerical problems arise as the coefficients will depend on unknown values of the involved variables. In this case, further mathematical elaboration would be needed following complex time linearisation methods (Hoffman, 2001), or attempting to perform analytical integration in order to reduce the problem to a tridiagonal system which could be solved numerically (Press, 1988).

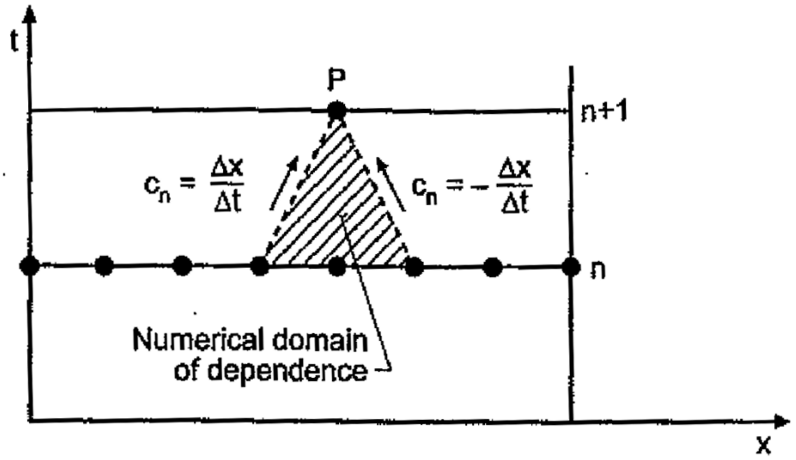

Figure 53. From Hoffman (2001). Numerical domain of dependence for explicit methods, for 1-D propagation PDEs. The spatial coordinate is *x*.

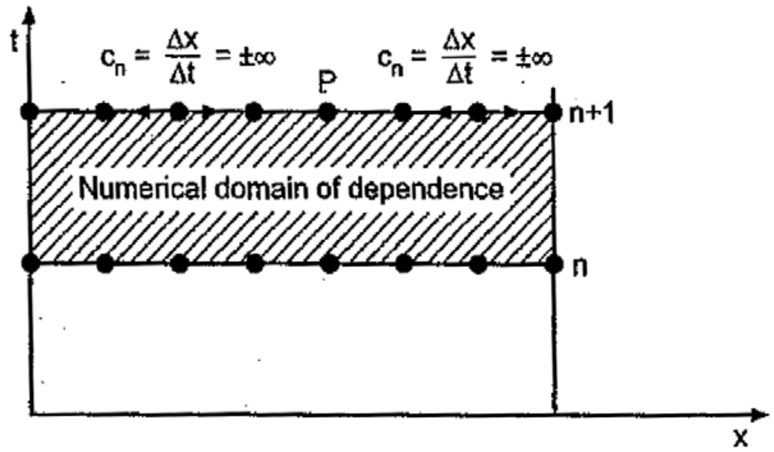

Figure 54. From Hoffman (2001). Numerical domain of dependence for implicit methods, for 1-D propagation PDEs. The spatial coordinate is *x*.

In conclusion, the presence of nonlinear coefficients, in addition to the existence of several couplings in equations (5.110), incline us to adopt the FTCS method. In fact, the additional effort of performing a stability analysis (strongly recommended for explicit methods) is largely compensated by the mathematical and numerical simplifications that explicit integration implies, compared to implicit methods.

5.5.2. Discretisation

The heat Equation (5.110)-(I) can be discretised with a FTCS scheme as

$$\frac{\theta_j^{n+1}-\theta_j^n}{\Delta t}=D_j^n\frac{\theta_{j+1}^n-2\theta_j^n+\theta_{j-1}^n}{\left(\Delta z\right)^2}+F_j^n\frac{v_d^n}{d} \tag{5.111}$$

where the subscripts denote the spatial position, superscripts the time value (Figure 52), Δt the time-step and Δz the spatial step amplitude. The 'current' values of space and time are respectively *j* and *n*. Since the involved coefficients are not constant but depend on the current values of temperature, pore pressure and velocity we have

$$D_j^n=D_i\left(\theta_j^n,u_j^n,v_d^n\right);\qquad F_j^n=F_i\left(\theta_j^n,u_j^n,v_d^n\right). \tag{5.112}$$

Similarly, the pore pressure Equation (5.110)-(II) can be approximated as

$$\frac{u_j^{n+1}-u_j^n}{\Delta t}=\overline{c}_v\frac{u_{j+1}^n-2u_j^n+u_{j-1}^n}{\left(\Delta z\right)^2}+\lambda_j^n\frac{\theta_j^{n+1}-\theta_j^n}{\Delta t} \tag{5.113}$$

where (5.111) can be substituted, to provide the finite difference approximation of the temperature rate. The same grid notation as above applies, coefficient $\overline{c}_v$ is taken constant and the pressurisation coefficient as shown in Section 5.3.2 depends on the current value of temperature:

$$\lambda_j^n=\lambda_m\left(\theta_j^n\right). \tag{5.114}$$

The dynamical equation is a uni-dimensional ODE and describes the variation over time of the problem quantities, while the spatial coordinate is fixed to the shearband-rigid block interface (*z*=*d*). Equation (5.110)-(III) can therefore be discretised using a standard 4th order Runge-Kutta (RK) method (Section 4.5.1). By defining the value of the time-derivative of the slide velocity (RHS of Equation (5.109)) at the generic time-step *i* as

$$f^i=R\omega_0^2\left[A_0-\frac{M\left(\theta_d^i,x_d^i,v_d^i\right)}{\sqrt{3-\left[M\left(\theta_d^i,x_d^i,v_d^i\right)\right]^2}}\left(\frac{A_0}{\mu_F}+\frac{u_d^i}{F_c}\right)\right], \tag{5.115}$$

we may write the 4th order RK approximation as

$$\frac{v_d^{n+1} - v_d^n}{\Delta t} = \frac{1}{6} f^n + \frac{2}{3} f^{n+1/2} + \frac{1}{6} f^{n+1} \tag{5.116}$$

where the variables at halfway time-step $\left(n+1/2\right)$, if the step size is reasonably small, may be logically calculated as $\theta_d^{n+1/2} = \frac{1}{2}\left(\theta_d^n + \theta_d^{n+1}\right)$, $u_d^{n+1/2} = \frac{1}{2}\left(u_d^n + u_d^{n+1}\right)$ and so on.

Equations (5.111), (5.113) and (5.116) can be integrated numerically in this same order, since despite the numerous couplings they may be solved explicitly in sequence: the first equation provides the value of θ_j^{n+1}, which is used in the second one to obtain the solution for u_j^{n+1}. Both values can then be used into the dynamical equation to find the slide velocity v_d^{n+1}.

The numerical procedure for solving Equation (5.116) depends on the kind of friction softening adopted: if all dependencies of the friction-softening law are taken into account, (5.116) becomes a nonlinear algebraic equation which must be solved iteratively (Section 5.5.7.3). If on the contrary we ignore the displacement and velocity dependence of parameter *M*, we may solve the equation directly (Section 5.5.7.2).

5.5.3. Choice of parameters for the Vajont case study

As an example we back-analyse the Vajont case with the modified landslide model, to asses its consistency with the available field observations and the calculations performed by Vardoulakis (2002a). The constant material and system parameters for our calculations are hence chosen, where possible, consistently with Vardoulakis (2002a). Our analysis will be hereafter carried out for 'Section 5' of the Vajont slide, whose parameters are summarised in Table 4.

The implementation of the thermoplastic model introduces a few additional parameters compared to Vardoulakis (2002a) which are separately discussed hereafter.

5.5.3.1. Void ratio

The void ratio at critical state *e* is calculated through the more conventional critical state soil parameter Γ, representing the soil's specific volume intercept at unit mean effective stress equal to 1 kPa. The CSL in the v-ln(*p*') plane is expressed as

$$\mathrm{v}_{cs} = (1+e) = \Gamma - \lambda \ln p'_{cs} \tag{5.117}$$

(e.g. Powrie, 1997) so that we may calculate

$$e = \Gamma - 1 - \lambda \ln(p'_{cs}) \tag{5.118}$$

where $p'_{cs} = p'_0$. It must be remarked here that expression (5.118) is unit-dependent, so if the value of Γ is given (as is most frequently) in kPa, the mean effective stress must be given in kPa as well.

Table 4. Material and system parameters chosen to back-analyse the Vajont landslide.

Soil density	ρ	$2.44*10^3$	Kg/m^3
Unit weight of the soil	γ_s	$23.89*10^3$	N/m^3
Unit weight of water	γ_w	$9.81*10^3$	N/m^3
Thermal constant	C_f	2.84	MPa/°C
Radius of the failure circle	R	1493	m
Radius of the "friction circle"	R_D	594.8	m
Polar moment of inertia of slide	I_p	0.511	km^4
Resultant driving force	D	3.94	GN/m
Slide geometry parameter	ω_0	$8.1*10^{-2}$	s^{-1}
Shearband thickness	d	$1.4*10^{-3}$	m
Reference temperature	θ_{ref}	12	°C
Soil thermal diffusivity coefficient	k_m	$1.45*10^{-7}$	m^2/s
Slope of URL of clay	κ	$4.3*10^{-2}$	-----
Slope of NCL of clay	λ	0.16	-----
Specific volume intercept of clay	Γ	2.8	kPa
Initial (mean) normal effective stress	σ'_n	2.38	MPa
Soil (drained) Poisson's ratio	v	0.2	-----
Compressibility of water	c_W	$4.93*10^{-4}$	MPa^{-1}
Incipient failure (peak) friction coefficient	μ_p	0.410	-----
Static residual friction coefficient	μ_{rs}	0.179	-----
Dynamic residual friction coefficient	μ_{rd}	0.077	-----

5.5.3.2. Isothermal preconsolidation stress

The isothermal value of apparent preconsolidation stress σ'_m, as defined from equation (4.34), is representative of the stress state at incipient sliding. Due to our assumptions of critical state, we deduce $\sigma'_m = 2p'_0$ (Section 5.2), where p'_0 is obtained from parameter σ'_n through Equation (5.91).

5.5.3.3. Plastic compressibility

The plastic compressibility modulus $\tilde{\beta}$, already discussed in Section 4.4.3, features in the expression of the plastic multiplier (5.40). It can be calculated in terms of the void ratio *e* and the soil parameters λ and κ, as defined in Equation (4.42).

5.5.3.4. Thermo-elastic expansion

The thermal expansion coefficient β_s has been given by Laloui et al. (2005) a temperature- and mean stress-dependent form, introducing a double source of nonlinearity in the elasticity relationship through two additional parameters. Although it is commonly accepted that β_s may slightly vary at different stress and temperature levels (e.g. see the 'elastic branch' in Figure 47), this dependency may be neglected because of the lack of direct experimental data and the mathematical simplifications brought about by adopting a linear thermoelastic law. Coefficient β_s thus in our case corresponds to the constant value of α_c^e discussed in Section 5.3.2, to be calculated as

$$\beta_s = (1-n)\alpha_s + n\alpha_w \tag{5.119}$$

where $n = e/(1+e)$ is the porosity of the soil, $\alpha_s = 3*10^{-5}$ °C^{-1} is the coefficient of thermal expansion for clay particles and $\alpha_w = 2.75*10^{-4}$ °C^{-1} that of water. As a result, $\beta_s = 7.41*10^{-5}$ °C^{-1}. This represents an average value for clays, in line with other experimental findings (e.g. see Delage et al., 2000, Sultan et al., 2002, Cui et al., 2000).

5.5.3.5. Thermal friction sensitivity

The rate of thermal friction softening $\tilde{g}$ may be calibrated using the (few) experimental data available on thermal-friction softening, with the awareness that this data is not necessarily representative of the Vajont clay. From Figure 30 we can extract an average slope of decrease of the friction angle with temperature: a decrease of $\Delta\varphi \simeq 10°$, corresponding to $\Delta M \approx 0.36$ occurs over a temperature increase of $\Delta\theta \simeq 60°\text{C}$. We deduce $10^{-3} \le \tilde{g} \le 10^{-2}$.

5.5.3.6. Thermal softening parameter 'γ' and resulting values of the pressurisation coefficient

The material parameter γ that controls the 'rapidity' of thermal softening (i.e. the decrease of the apparent preconsolidation stress with temperature), comes from Laloui's hardening relationship and can be chosen within a relatively wide range. Laloui et al. (2003) presented some experimentally measured values of γ for different clays, from which we may deduce a range of $5\times10^{-3}\leq\gamma\leq5\times10^{-1}$. This parameter also appears in the expression (5.84) of the thermoplastic contraction coefficient: while it is difficult and fairly uncommon to measure γ, the other parameters featuring in (5.84) represent standard, well-established geotechnical properties. It is therefore reasonable to first assign a sensible value to all other parameters and define γ last, based on overall consistency arguments, also due to the lack of information regarding thermal softening properties of the Vajont clay.

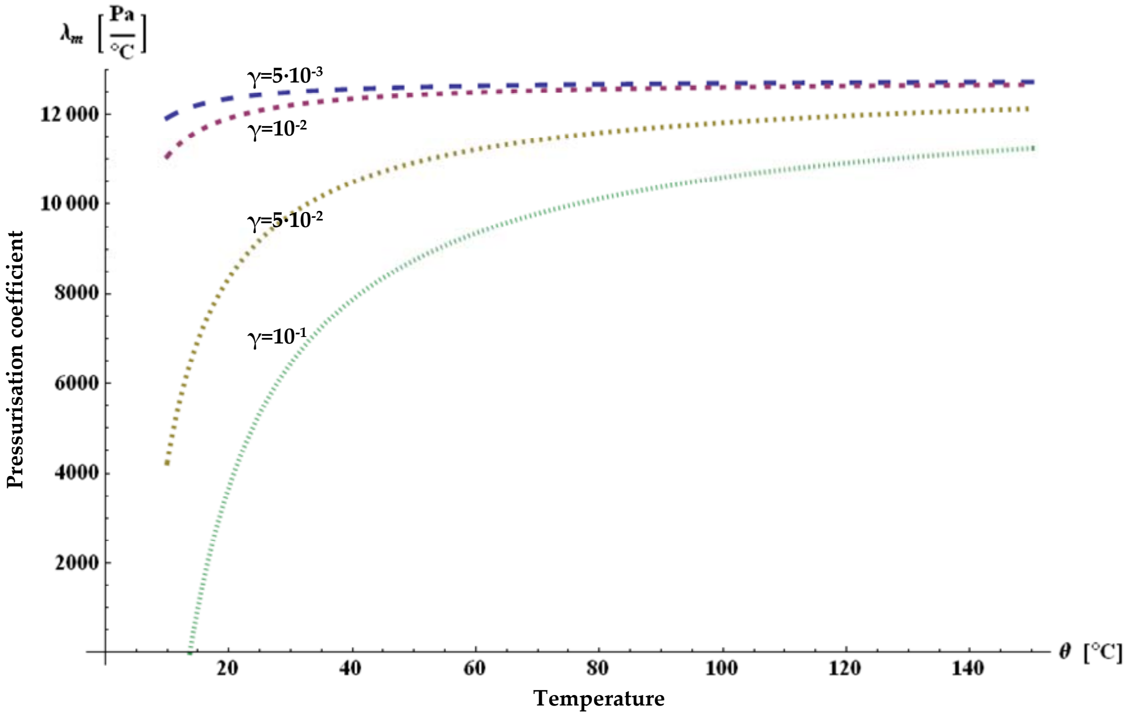

Figure 55. Calculation of pressurisation coefficient λ_m as a function of temperature, for four different values of the thermal softening parameter γ.

The correct value of γ in our case must be selected, all other parameters being chosen, in order to respect the conditions that the thermoplastic contraction coefficient α_c^{tp} be negative for all values of temperature, and that consequently the resulting pressurisation coefficient (5.87) is positive and assumes values that are in line with the earlier findings.

Numerical experimentation on the function $\lambda_m(\theta)$ was thus carried out for $\theta = 10 - 150\ \ ^\circ\mathrm{C}$, applying the parameter settings of Section 5.5.3. It was found that the values assumed by λ_m are higher and more realistic if a value of γ is chosen towards the lower end of the above established range. Figure 55 shows that for decreasing values of γ, the variation of pressurisation coefficient over temperature is sensibly smaller and tends to an average value $\overline{\lambda}_m \approx 0.012$ MPa which agrees with the range of measured values for clay reported in the literature (Section 2.3.3), and is also not far from that proposed by Vardoulakis (Section 5.3.2.1).

It appears therefore reasonable to complete the definition of function $\lambda_m(\theta)$ for our calculations by assigning the lower-mid-range value $\gamma = 10^{-2}$.

5.5.4. Well-posedness of the heat equation

Expression (5.110)-(I) is a diffusion-generation equation for temperature where, unlike Vardoulakis (2002a), the diffusivity coefficient varies non-linearly with temperature and pore pressure as

$$D_i = \frac{k_m}{1 - \dfrac{\left[M(\theta,\gamma,\dot{\gamma})\sigma'_c(\theta)\right]^2}{2C_f} F_1(\theta,u)} . \tag{5.120}$$

In fact, due to the introduction of constitutive thermo-plasticity and possible thermal-friction softening, the problem is now governed by a diffusivity D_i that is not constant and that can, theoretically at least, assume negative values. This would imply mathematical ill-posedness of the equation and inability to solve it. To ensure that this does not happen and that the problem remains well-posed, the sign of the coefficient D_i was calculated for a wide range of values of its parameters and the temperature range $0<\theta<1000$ °C. Diffusivity proved to be always positive for all values examined of the parameters involved, showing very little variation around the original value of the soil thermal diffusivity, $k_m=1.45*10^{-7}$ m^2/sec. The parameter ranges used are: $10^{-8} \le \tilde{g} \le 10^{-1}$ for the thermal sensitivity, $0.25 \le M_{ref} \le 0.85$ and $0.1 \le \sigma'_m \le 10$MPa for the critical state parameter and the preconsolidation stress respectively at ambient temperature, $5 \le \tilde{\beta} \le 20$ for the plastic compressibility, $10^{-3} \le \kappa \le 5 \cdot 10^{-2}$ for the slope of the elastic compression line, $0.15 \leq \nu \leq 0.45$ for the Poisson's ratio, $0.2 \leq e \leq 1.5$ for the void ratio and $0.005 \leq \gamma \leq 0.5$ for the parameter-γ of the thermoplastic model. In Figure 56 an example of this calculation for the given temperature range, at mid-range values of the involved parameters, is shown.

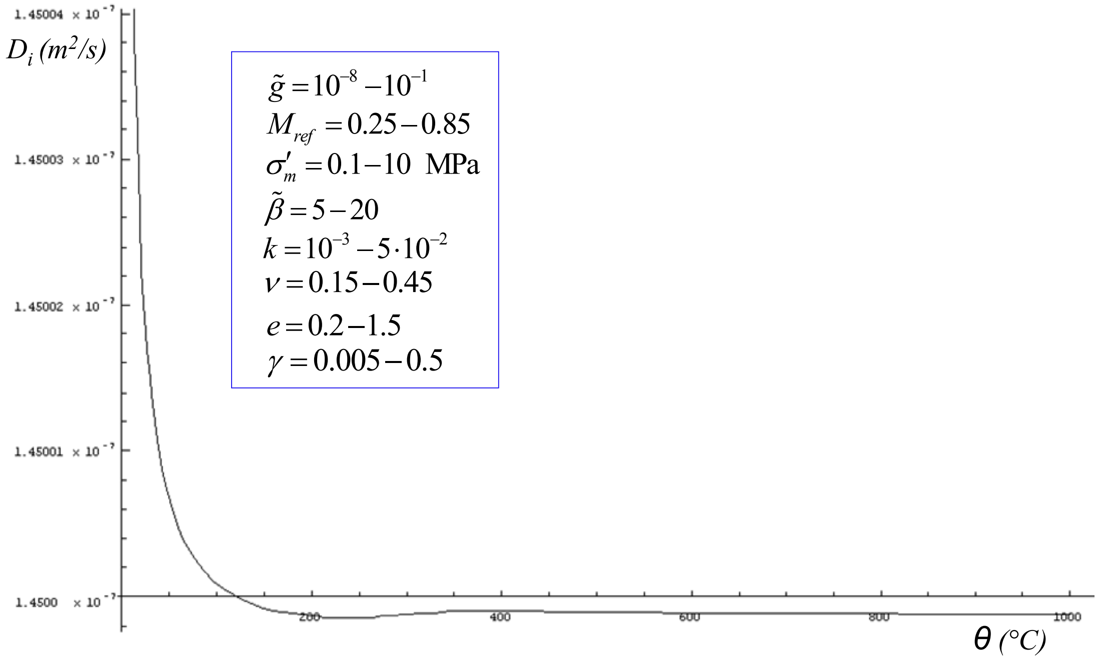

Figure 56. Calculation of the sign of coefficient D_i for mid-range values of involved parameters (whose typical ranges are listed in the framed box) and temperature ranging between 0 and 1000 °C.

5.5.5. Time-step analysis

As mentioned in Section 5.5.1, the explicit integration scheme employed will be numerically unstable if the adopted time-step Δt is larger than a limit value. A stability analysis is recommended whenever explicit schemes are employed.

Among the various techniques available for performing stability analysis of a finite difference approximation of a PDE, the von Neumann method (e.g. see Hoffman, 2002) is one of the simplest and most widely used. For a 1-D parabolic equation having the general form like the heat and pore pressure equations at hand,

$$\frac{\partial f}{\partial t} = \beta(z,t)\frac{\partial^2 f}{\partial z^2} + g(z,t) \qquad (5.121)$$

where f is the considered variable, z the spatial coordinate, β the diffusivity and g the source (generation) term, the corresponding finite difference scheme (cf. Section 5.5.2) is

$$\frac{f_j^{n+1}-f_j^n}{\Delta t}=\beta_j^n\frac{f_{j+1}^n-f_j^n+f_{j-1}^n}{\left(\Delta z\right)^2}+g_j^n. \tag{5.122}$$

The stability condition of the finite difference scheme (5.122) based on the von Neumann stability analysis is (e.g. see Press, 1988)

$$\Delta t\le\frac{\left(\Delta z\right)^2}{2\beta}. \tag{5.123}$$

However, the above stability criterion applies to linear PDEs only (Hoffman, 2002), i.e. when $\beta_j^n=\beta=\text{constant}$, while nonlinear PDEs need a more complex local linearisation procedure before being analysed for stability.

Since in our case the governing equations are formally nonlinear, as a first check we performed some numerical experimentation, by identifying a threshold value for Δt (at given Δx) below which the numerical results are unaffected by changes in time-step. For the Vajont back-analysis calculations, a safe, small enough value of the time-step, for the chosen spatial resolution of $\Delta z=0.02\text{mm}$ was found to be $\Delta t=10^{-4}$ s.

Nevertheless, by taking a closer look at the results we notice that the coefficients featuring in the PDEs are constant or virtually so. In fact, on Section 5.3.1 we have chosen to take the consolidation coefficient $\overline{c}_v$ constant, given the weakness of its temperature dependence. Moreover, in Section 5.5.4 we have shown the minor variability of the diffusivity D_i: since its magnitude of variation is of the order of 10^{-12} along a 1000°C temperature span (Figure 56), this coefficient remains for all practical purposes equal to the original thermal diffusivity value of k_m=1.45*10^{-7}, i.e. $D_i\cong k_m$. In this context, the need for local linearization disappears and we may directly carry out a stability analysis, to decide the maximum time-step size that can be employed whilst respecting condition (5.123).

For the finite difference pore pressure Equation (5.113), the stability condition becomes

$$\Delta t\le\frac{\left(\Delta z\right)^2}{2\overline{c}_v} \tag{5.124}$$

where $\overline{c}_v$ has the form (5.61) and the spatial step Δz, for practical purposes, in our numerical code is a function of the imposed shearband thickness d, $\Delta z=d/w$ where w is the (integer) number of spatial subdivisions desired within the shearband thickness.

For the finite difference heat Equation (5.111), the stability condition is

$$\Delta t \leq \frac{(\Delta z)^2}{2k_m} \tag{5.125}$$

where Δz is the same as in (5.124).

The time-step choice is then defined by the condition

$$\Delta t_{\max} \leq \min\left[\frac{(\Delta z)^2}{2k_m}, \frac{(\Delta z)^2}{2\overline{c}_v}\right]. \tag{5.126}$$

By substituting into (5.126) the values chosen for Vajont of $\Delta z = 0.02\times10^{-3}\,\mathrm{m}$, $k_m = 1.45\times10^{-7}\,\mathrm{m}^2/\mathrm{s}$ and $\overline{c}_v = 7.3\times10^{-8}\,\mathrm{m}^2/\mathrm{s}$ (Section 5.3.1) we obtain

$$\Delta t_{\max} \leq 10^{-3}$$

which confirms that indeed the 'safe' value $\Delta t = 10^{-4}$ found through numerical experimentation respects the stability criterion.

5.5.6. Initial and boundary conditions

The finite difference equations (Section 5.5.2) are integrated in a spatial domain composed of the shearband thickness and the surrounding clayey soil. In fact, as anticipated in Section 2.1.4.1 the shearband is assumed to be embedded in a clay layer of the same characteristics, whose thickness is much larger than the band dimensions. In other words, the band merely marks the boundaries of strain localisation, in an otherwise thicker clayey layer. Shear strain and consequent heat production will occur within the localisation band only. The 1-D spatial domain is here set to be 10 times the thickness of the shearband and assumed to be uniform in hydraulic and geotechnical properties. In line with Vardoulakis (2002a), the assumption is made that at large distance from the band (i.e. at the domain boundaries) the excess pore pressure is zero and the temperature is equal to the ambient one:

$$u(\pm\infty, t) = 0; \quad \theta(\pm\infty, t) = \theta_{ref}\,. \tag{5.127}$$

The velocity profile through the thickness domain (as discussed in Section 2.3.4.1, see Figure 57) is defined as:

$$\begin{cases} v = 0 & \mathrm{z} \in [-\infty, 0] \\ v = v_d(\mathrm{t})\dfrac{\mathrm{z}}{\mathrm{d}} & \mathrm{z} \in [0, d] \\ v = v_d(\mathrm{t}) & \mathrm{z} \in [d, +\infty] \end{cases}. \tag{5.128}$$

Initial conditions are:

$$\theta(z,0)=\theta_{ref};\quad u(z,0)=0;\quad v(z,0)=0. \tag{5.129}$$

In order to initiate the movement, the sliding mass needs to be unbalanced from its limit equilibrium. This can be achieved numerically by assuming an arbitrarily small reduction of the limit equilibrium friction angle. Following Vardoulakis (2002a), such reduction is chosen to be of 0.1%.

For a time window of 10 seconds after movement initiation, corresponding to a computed value of displacement not exceedingly large ($x_d < 120\text{m}$) so that the assumption of rigid-body remains reasonable, the model equations were integrated numerically. Results are presented hereafter.

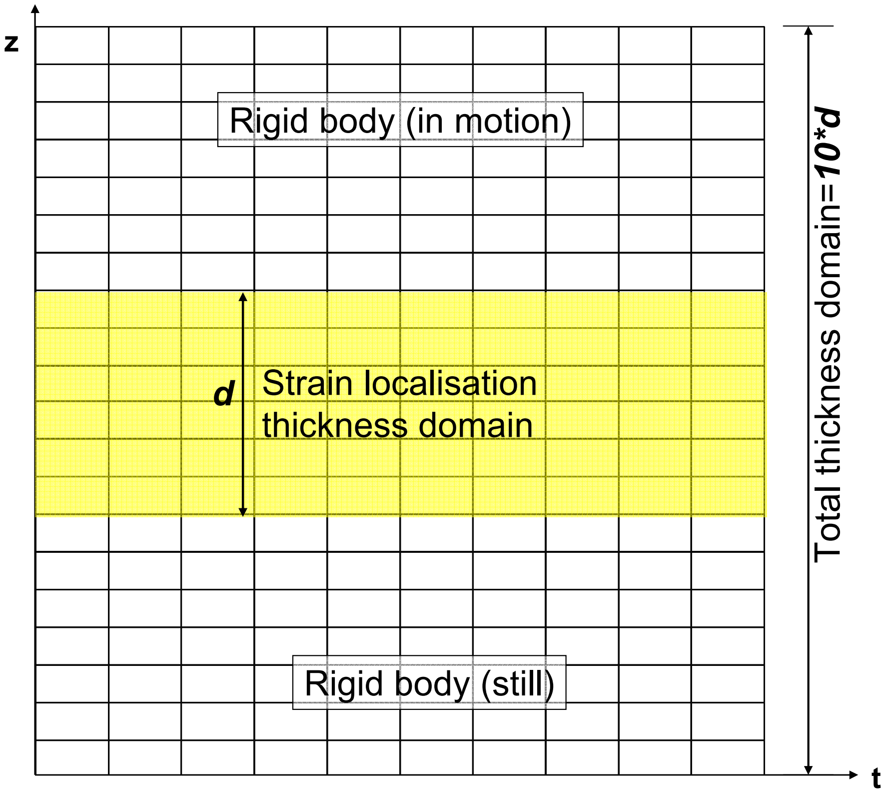

Figure 57. Finite difference grid showing the thickness domain of integration. The shearband is a strain localisation zone of thickness *d*, embedded in an otherwise homogeneous soil layer of total thickness 10*d*. The soil below the shearband is still, while the soil at the top of the shearband moves at the velocity v_d, characteristic of the landslide overburden.

5.5.7. Numerical results for Vajont

5.5.7.1. Vaporisation threshold

Before starting the computations, we should here remark that our model ceases to be valid as soon as the temperature within the shearband reaches the evaporation limit of the pore water for the current pressure. After this transition point, the governing equations would need substantial modifications since the energy balance should account for the evaporation heat, and fluid flow would take place under conditions of partial saturation. Within the so-called "undrained-adiabatic limit", Vardoulakis (2000) showed that the presence of vapour would decrease the fluid compressibility and result in the reduction of excess pore pressure and apparent frictional softening. Such effects would arguably only have a minor influence on the acquired speed of the landslide. Nevertheless, since the model's assumptions will break down as soon as the vaporisation threshold is attained, our simulations will be considered well-founded as long as the maximum temperature $\theta_{\max}$ reached in the slip plane remains below the threshold temperature θ_{vap}. This threshold may be calculated from the phase change line of water

$$p_{cr} \approx 62\left(\theta_{vap} + 273.15\right)_k \exp\left(-\frac{4650}{\theta_{vap} + 273.15}\right) \tag{5.130}$$

(Vardoulakis, 2000), where θ_{vap} is the critical temperature in °C and p_{cr} the critical pressure in MPa. In the Vajont case, by setting as p_{cr} the maximum pore pressure that can be reached, $p_{cr} \approx \sigma_n' = 2.38$ MPa and solving (5.130) for θ_{vap} we get as vaporisation threshold temperature $\theta_{vap} \approx 210$ °C. We anticipate here that in our calculations condition $\theta_{\max} < \theta_{vap}$ always holds.

5.5.7.2. Case of thermal-only friction softening

We will start the analysis from the simpler case of thermal-only friction softening (TFS), since the concern was raised that this feature may lead to mathematical ill-posedness for the heat equation. By neglecting strain- and strain-rate softening as a first step, we will be able to investigate more efficiently the potential impact of TFS, which constitutes the most novel, and least established, feature of the proposed soil model. In this context, expression (5.35) becomes

$$M(\cancel{\gamma}, \cancel{\dot{\gamma}}, \theta) = M_{ref} - \tilde{g}\left(\theta - \theta_{ref}\right) \tag{5.131}$$

where $M_{ref} = 0.657$ is the reference value of critical state parameter, corresponding to the friction angle at incipient sliding (Table 4) through formula (5.19). Thermal sensitivity, in light of the considerations in Section 5.5.3, is chosen as $\tilde{g} = 10^{-2}$.

Adopting relationship (5.131) allows us to solve Equation (5.116) directly, since all terms on the RHS depend on known values of the problem variables.

With these settings, temperature and pore pressure were computed at each grid-point of the spatial domain, and isochrones through the domain were produced at significant time values (Figure 58 and Figure 59). It can be seen that temperature inside the shearband reaches about 145 °C after 10 seconds (about 8 seconds after the outbreak of acceleration, as can be seen from the velocity profile in Figure 60). This is well below the water vaporisation threshold at the given pressure, as pointed out in Section 5.5.7.1. The overburden corresponds to an initial vertical effective stress of 2.38 MPa which, as a consequence of the effective stress principle, is also the maximum value that excess pore pressure can reach. It can be seen that this value is approached as excess pore pressures overtops 2 MPa after 10 s from slide triggering.

In Figure 60 and Figure 61 the corresponding computed slide velocity and displacement are plotted. From the velocity plot we can distinguish the slide 'triggering point' (at *t*=0, due to the 0.1% reduction of the incipient failure friction angle, cf. Section 5.5.6) and the slide's (catastrophic) 'activation point', here set at $t \approx 1.8$ s, when the acceleration of the mass abruptly increases. In fact, the velocity profile shows negligible increase up to $t \simeq 2$ s, followed by a rapid kick at $t \simeq 3$ s which corresponds to a substantial increase in the pressurisation rate, as can be seen in Figure 59.

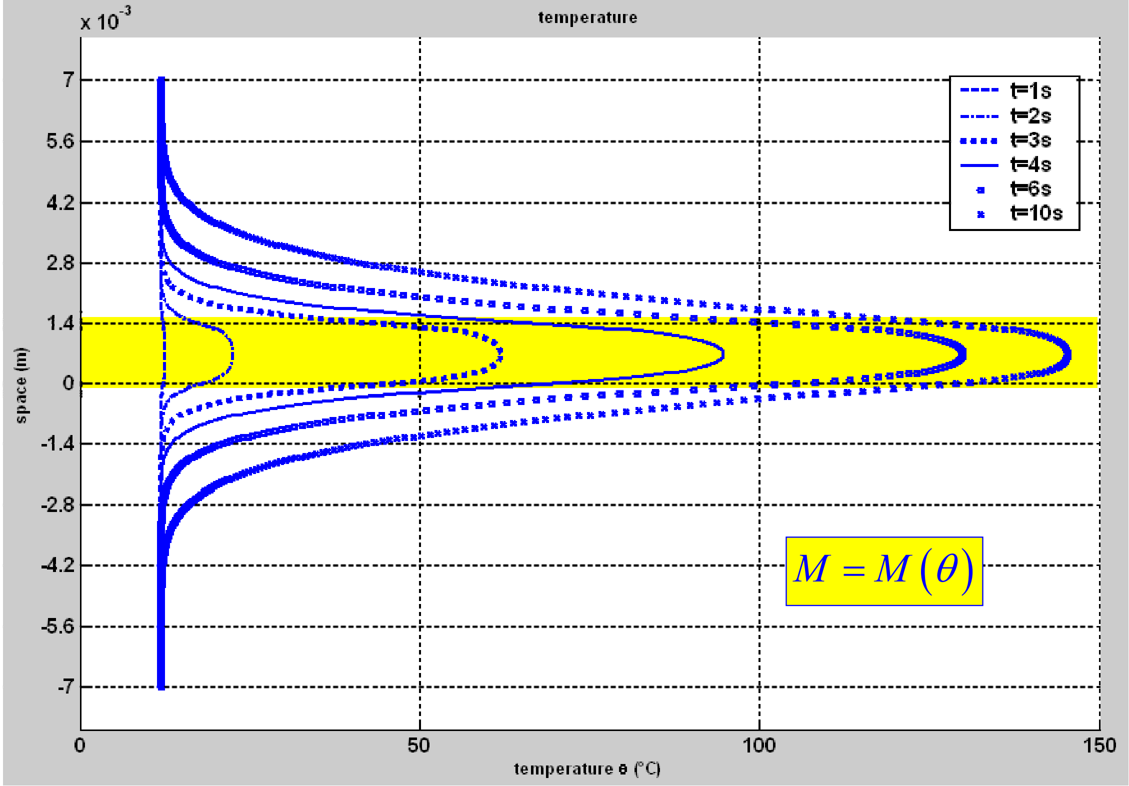

Figure 58. Temperature isochrones within the shearband and its surroundings, for the case of thermal-only friction softening. The shearband area, where strain localisation takes place, is shaded.

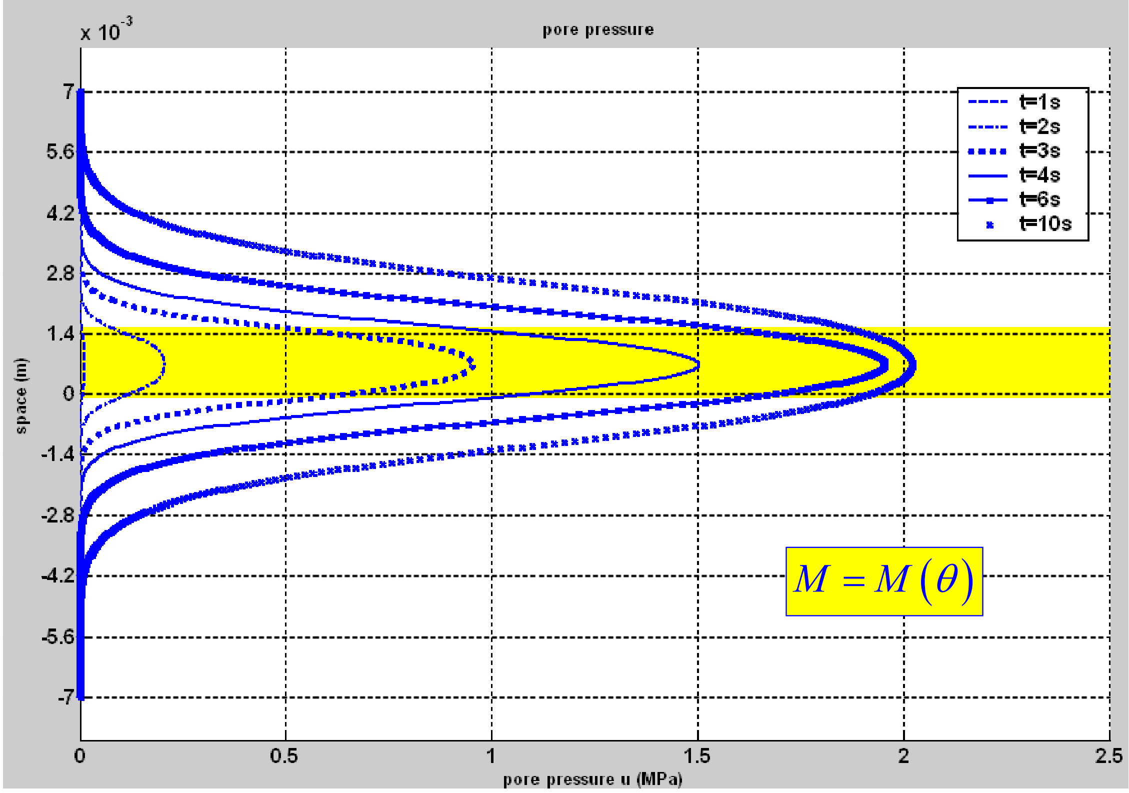

Figure 59. Pore pressure isochrones within the shearband and its surroundings, for the case of thermal-only friction softening. The shearband area, where strain localisation takes place, is shaded.

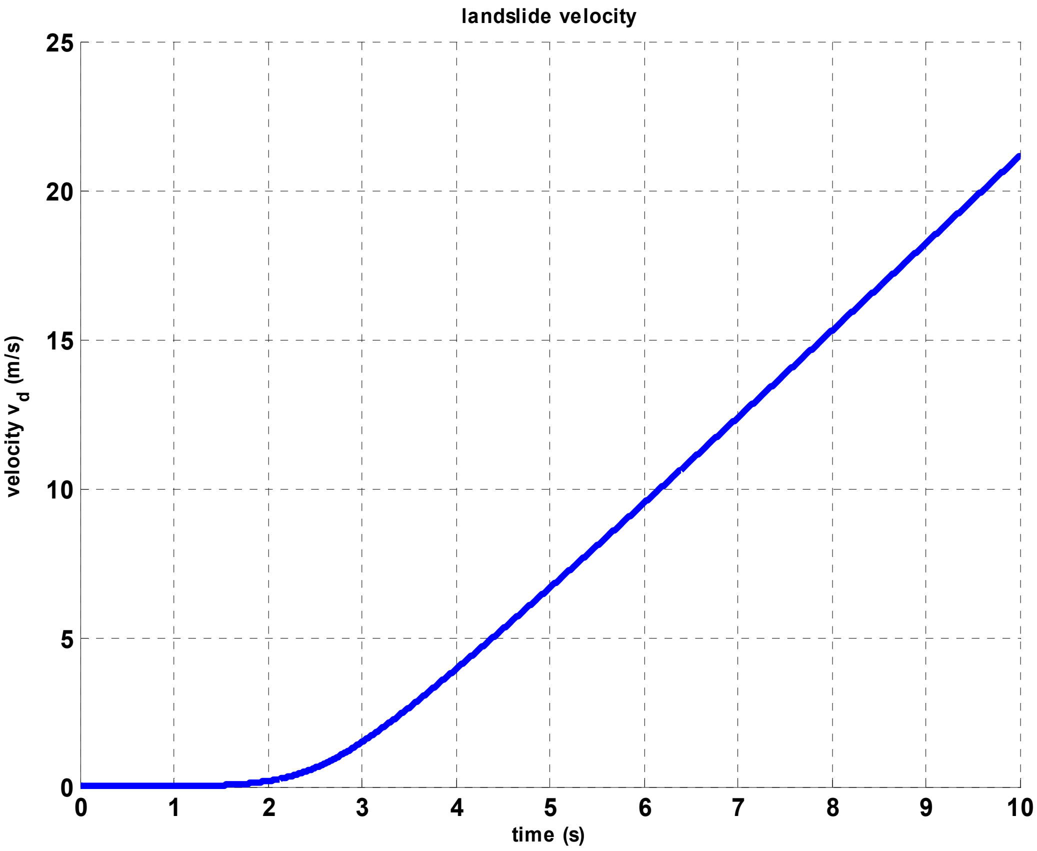

Figure 60. Slide velocity profile for the case of thermal-only friction softening.

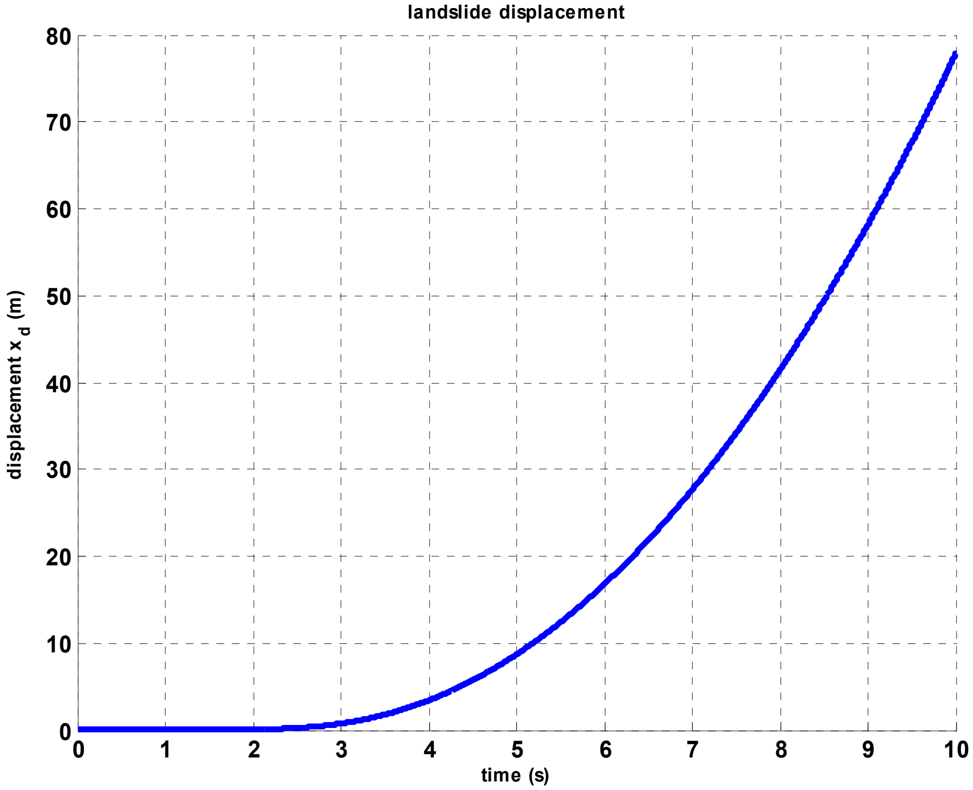

Figure 61. Slide displacement profile for the case of thermal-only friction softening.

5.5.7.3. Case of 'full' friction softening

We will now analyse the most general case, where the critical state parameter depends on displacement, velocity and temperature as expressed by Equation (5.35). As a result, the discretised dynamical Equation (5.116) cannot be solved directly for v_d^{n+1}, since this unknown value also unavoidably appears on the RHS of the equation as a consequence of velocity friction-softening. An iterative procedure is now required to solve the dynamical equation: starting from an approximate trial solution, an algorithm is needed to refine the value until convergence is achieved within some pre-specified accuracy. Among the many available methods to find a bracketed root of a mono-dimensional function, the so-called Ridders method was chosen (Press et al., 1988). This has clear advantages in our case with respect to the more famous Newton-Rhapson method, as it does not require the awkward computation of the derivative of the involved function. Ridders method constitutes an enhanced variant of the 'false position' method, widely employed when the function at hand is known to be smooth near a root. Considering the physics of the problem at hand and previous results on computed sliding velocities (e.g.

Vardoulakis, 2002a), we can reasonably assert that $v_d(t)$ is a growing function of time, so that at each step we may easily set two bracketing values, v_L and v_R within which the new value of velocity v_d^{n+1} lies: the previous value ($v_L = v_d^n$), and a reasonably higher value ($v_R = 10 \cdot v_d^n$). Numerical implementation of this method ensured convergence in a few iteration steps.

In Figure 62 and Figure 63 the temperature and pore pressure isochrones are plotted for this case of ‘full’ friction softening (FFS), in Figure 64 and Figure 65 the velocity and displacement profiles are plotted for a time window of 10 seconds after triggering. In comparison with the TFS case, we can observe that:

- Sliding is activated earlier here (after about half a second from triggering as opposed to ~ 2 seconds in TFS case, as can be seen by comparing Figure 64 and Figure 60), as a result of the ‘full’ softening law providing a quicker decrease of the friction angle alongside temperature, displacement and velocity.

- A higher final velocity is reached, $v_{(t=10s)}$=26.3 m/s as opposed to 21 m/s in TFS case. This depends on the above mentioned earlier ‘activation’ of the slide, implying a longer overall time of catastrophic sliding for the FFS case. For the same reason, also displacement after 10 seconds is substantially larger (119.5 m)

- A higher maximum temperature ($\theta_{\max} = 147.7$°C) is reached within the shearband at t=10 seconds, due to the larger accumulated shear strain and consequent larger dissipation, which governs the heat generation term. Nevertheless, this value is not substantially larger than TFS case ($\theta_{\max} = 145.5$°C) since at the same time the friction angle decreases more rapidly, so that the dissipation function is not significantly increased.
- A velocity of about 20 m/s is reached about 7.5 seconds after activation of catastrophic sliding in both cases.
- A displacement of about 80m is reached about 7.5 seconds after activation of catastrophic sliding in both cases.

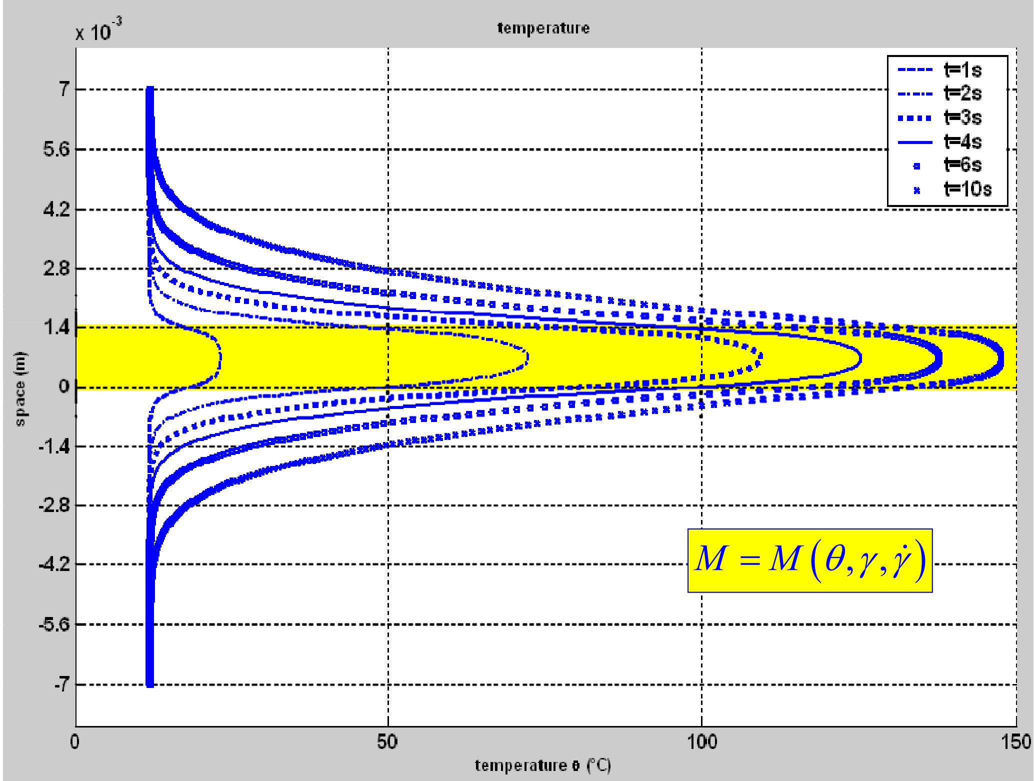

Figure 62. Temperature isochrones within the shearband and its surroundings, for the case of full friction softening. The shearband area, where strain localisation takes place, is shaded.

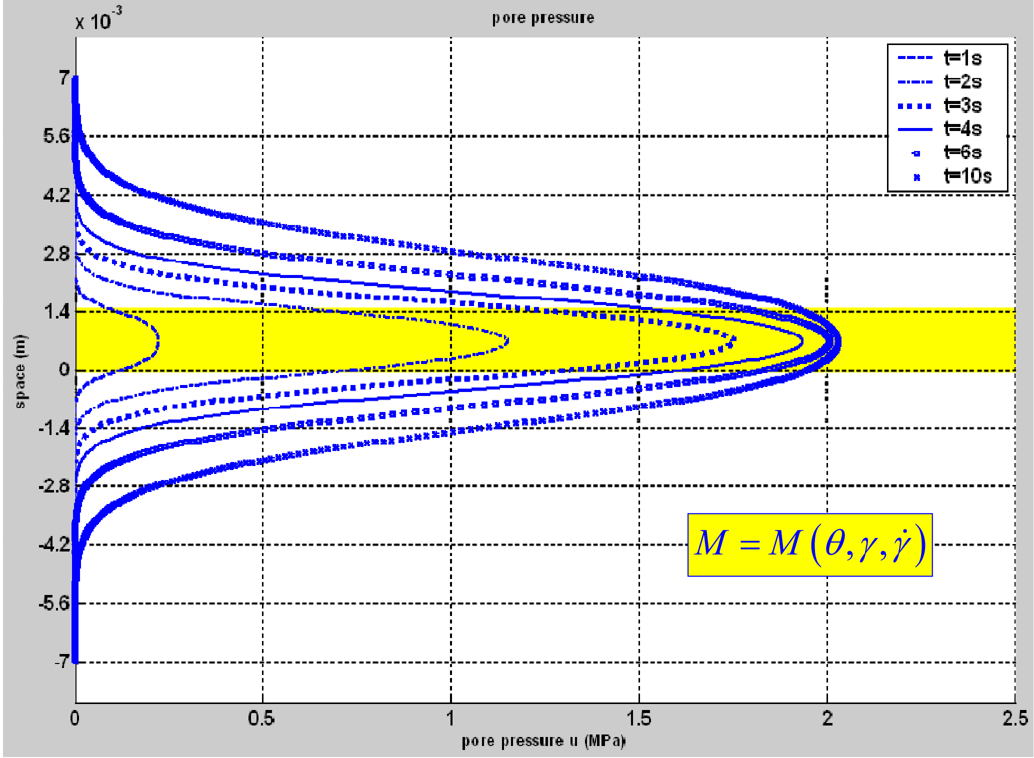

Figure 63. Pore pressure isochrones within the shearband and its surroundings, for the case of full friction softening. The shearband area, where strain localisation takes place, is shaded.

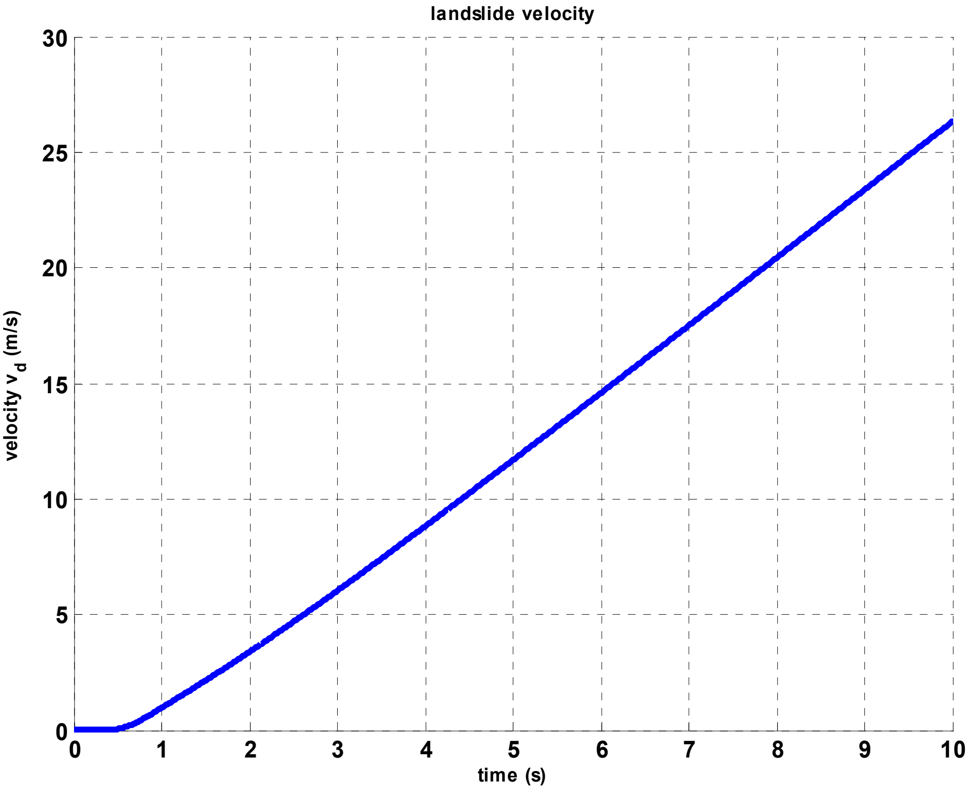

Figure 64. slide velocity profile for the case of full friction softening.

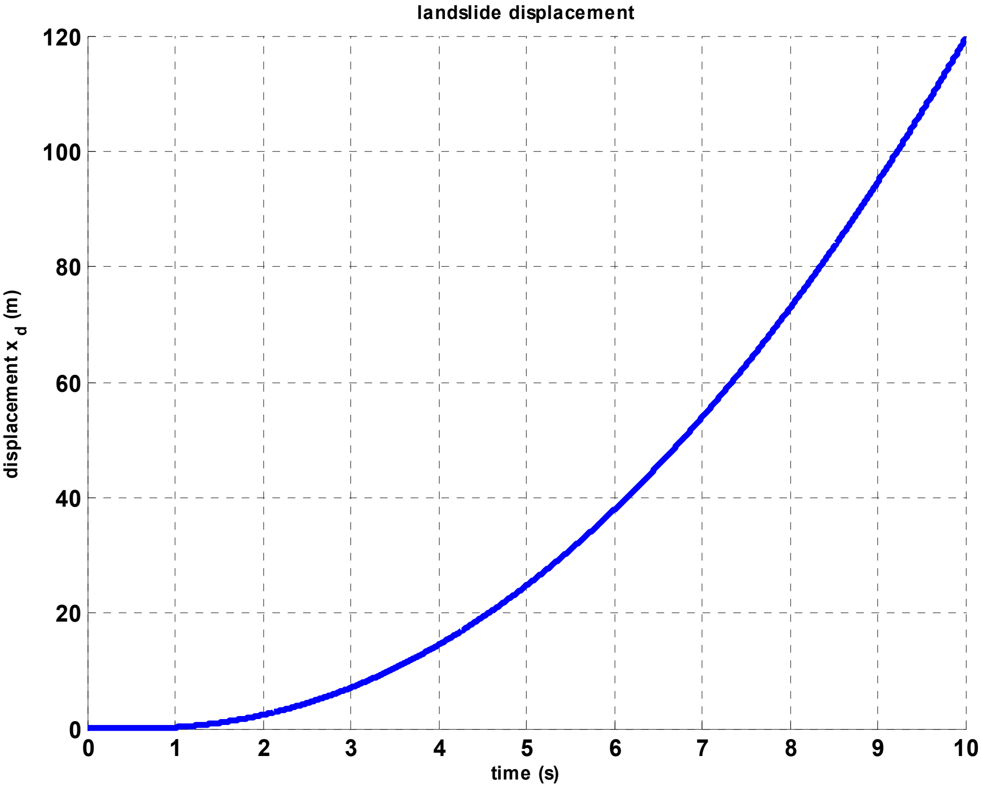

Figure 65. Slide displacement profile for the case of full friction softening.

5.5.7.4. Case of absent thermal friction softening

In order to assess the relative importance of the two main components of the FFS law (thermal-dependence and strain-, strain rate- dependence) in the predicted values of sliding velocity, it is now worth considering the case of absent thermal friction softening (ATS), as proposed by Vardoulakis (2002a). This is easily achieved by setting $\tilde{g}=0$ in the friction-softening law (5.35). Results for temperature and pore pressure isochrones are plotted in Figure 66 and Figure 67, velocity and displacement profiles are plotted in Figure 68 and Figure 69.

By examining the graphs we cannot notice any appreciable difference with the case of FFS. The calculated values for maximum temperature, pore pressure, slide velocity and displacement are in fact smaller than those obtained for full softening by 0.5-1%, which is negligible for our purposes. The comparison of results obtained for the three examined friction-softening scenarios highlights the substantially more important role played by strain- and strain rate-friction softening in determining the slide activation, and is due to the specific form of the softening law (5.35): the decrease of M towards the residual value according to the (twofold) hyperbolic law $\hat{M}(\gamma,\dot{\gamma})$ is so fast that no perceptible difference is brought about by superimposing the linear decrease law $M(\theta)$.

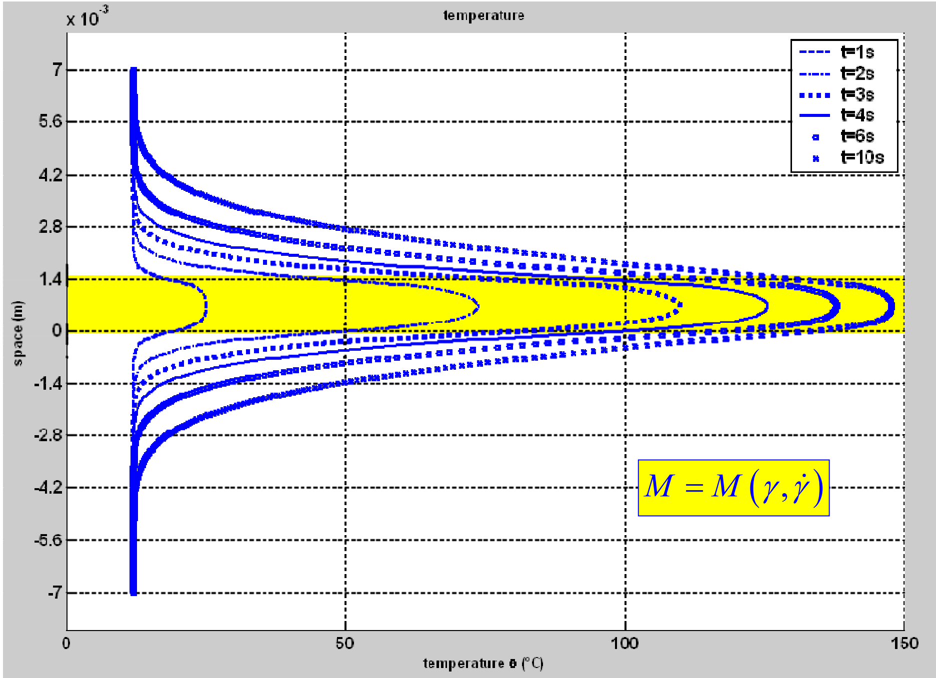

Figure 66. Temperature isochrones within the shearband and its surroundings, for the case of displacement and velocity softening only. The shearband area, where strain localisation takes place, is shaded.

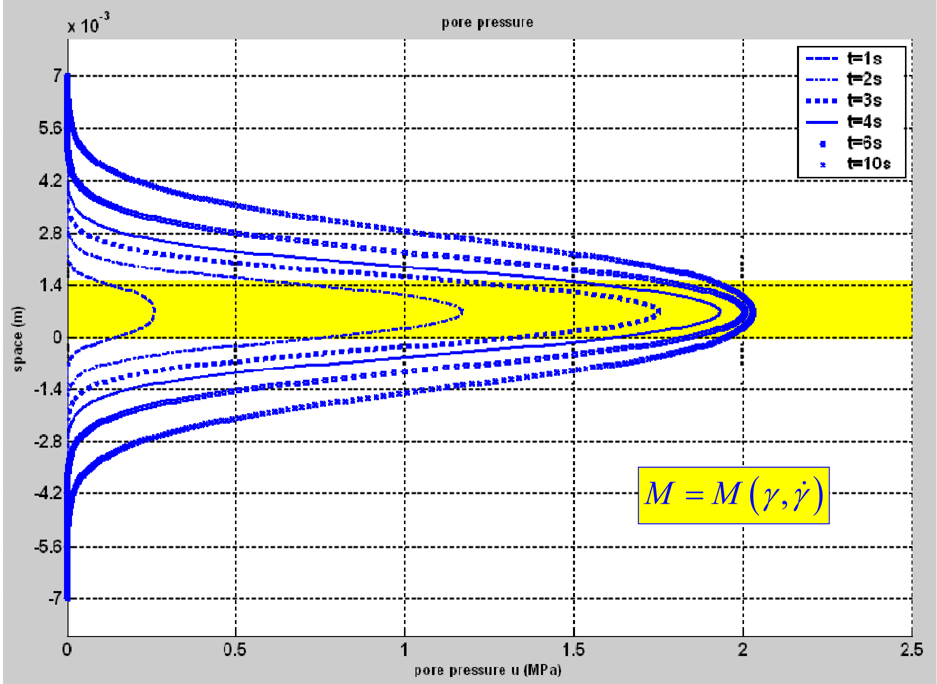

Figure 67. Pore pressure isochrones within the shearband and its surroundings, for the case of displacement and velocity softening only. The shearband area, where strain localisation takes place, is shaded.

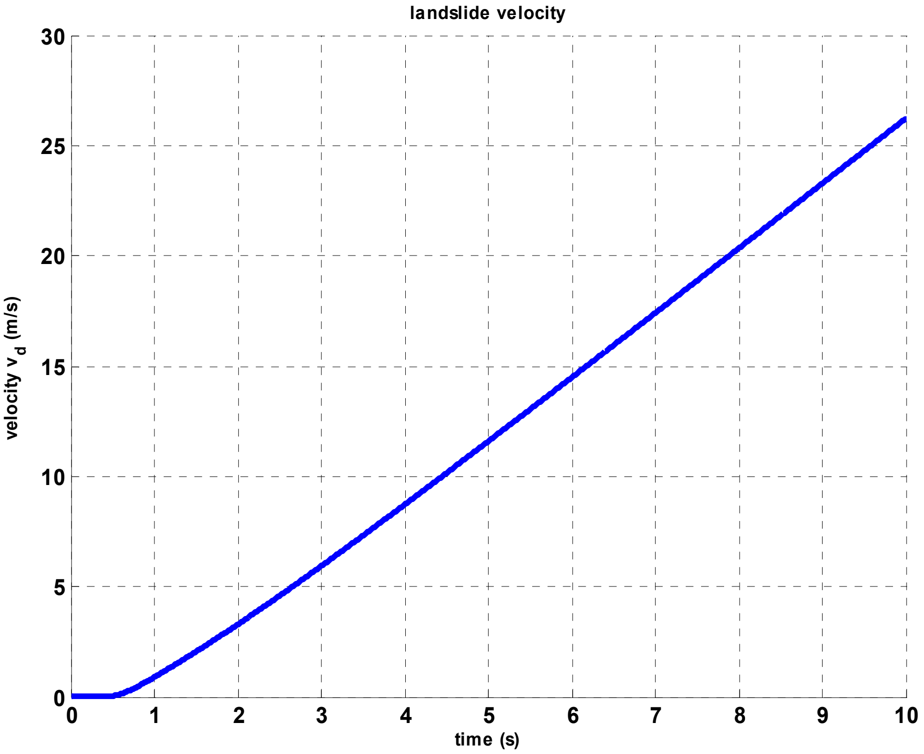

Figure 68. slide velocity profile for the case of displacement and velocity softening only.

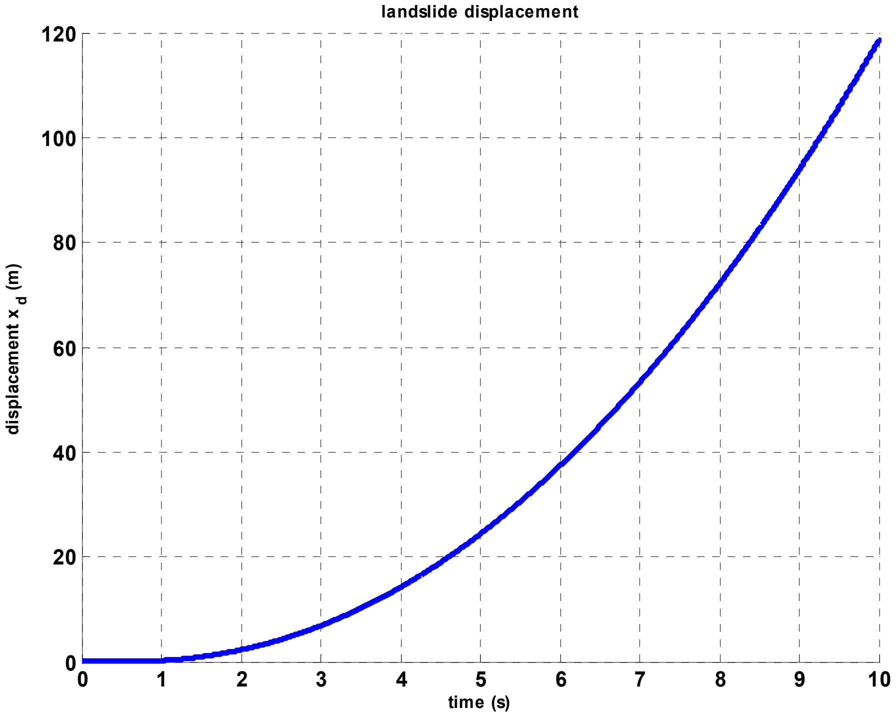

Figure 69. Slide displacement profile for the case of displacement and velocity softening only.

5.5.7.5. Discussion on numerical results

All simulations reported in the last three sections predict a similar behaviour and magnitude of results to those observed in Vajont, and are in accordance with those calculated by the strain and strain-rate softening model of Vardoulakis (2002a). In particular, a predicted final velocity of 20-25 m/s is in the bulk of the reported observations for the Vajont slide (Hendron and Patton, 1985).

The TFS simulation shows that thermal-friction softening alone can indeed account for catastrophic sliding, being potentially an important mechanism. Our choice for thermal sensitivity of $\tilde{g} = 10^{-2}$ proved to be reasonable, as it leads to realistic predictions and matches with the available data on thermal-friction softening. On the other hand, the simulations for the case of TFS should be only seen as an example to investigate the impact of the newly introduced mechanism, since a realistic simulation must account for the better established strain and strain-rate softening mechanisms. Such mechanisms were included in the FFS and ATS simulations, which led to almost identical predictions. By employing the hyperbolic strain- and strain rate-friction softening law into the modified landslide model, slide activation for the Vajont case is anticipated to $t \sim 0.5$ seconds, and the influence of an additional thermal friction softening mechanism is negligible. The outbreak of catastrophic acceleration in this case is anticipated by some 1.5 seconds compared to Vardoulakis' (2002a) calculations, as a result of a quicker development of thermal pressurisation brought about by our constitutive thermo-plastic modifications.

We may conclude that the numerical results presented give realistic predictions for the final collapse phase of the Vajont case history, thus providing an essential validation stage for our landslide model. On the other hand, it is worth recalling that the intermittent, creep-like sliding phases of Vajont that preceded the catastrophic run-out phase (cf. Section 2.1.4.2) cannot be reproduced by this model.

Chapter 6. Generalisation to infinite slope geometry

The results presented in Section 5.5.7 showed that the modified landslide model is comprehensive and able to predict realistic values for the velocity of the Vajont slide. The simulation of the Vajont case, which is the best documented catastrophic sliding event in the literature, was a necessary validation step for the model, which can be now employed to develop more general analyses.

The dynamical equation presented in Section 5.4 was derived from a friction circle analysis, which presumes rotational failure for the sliding body and a constant average vertical stress acting on the slip plane. Such assumptions were necessary to back-analyse the Vajont case, known to have slid along an approximately circular rupture surface. However, in order to provide a simple enough model that will allow us to explore the impact of frictional heating and the role of different parameters, we will now consider a more general geometry: the infinite slope.

6.1. Infinite slope analysis

The infinite slope or 'block-on-slope' idealisation consists of assuming the slope to be uniform and of infinite extent (see e.g. Powrie, 1997). The slip plane is parallel to the surface of the slope at a depth *H*. A unit length of slope is considered in the analysis, and for a given geometry the gravity and seepage forces acting on it determine its safety factor, if we are concerned about the stability of the slope (static analysis), or its acceleration, if we are conducting a post-failure (dynamic) analysis. In Figure 70 the infinite slope geometry is shown.

6.1.1. Static analysis to determine incipient failure conditions

The landslide model is dynamic and assumes 'incipient failure' as initial condition for the mobilised strength. The limit equilibrium stress state, according to Coulomb's law $\tau = \mu\sigma'$ is such that

$$\mu_{mob} = \tan\phi'_{mob} = \frac{\tau_{zx,ult}}{\sigma'_{zz}} \tag{6.1}$$

where $\sigma'_{zz} = \sigma'_n$ is the normal effective stress on the slip plane, τ_{zx} the ultimate shear stress and ϕ'_{mob} is the soil's friction angle at limit equilibrium. The values of normal and shear stress can be obtained by considering equilibrium of forces in both z and x directions.

Along z we obtain:

$$\sigma'_n = W \cos\beta - u_H \tag{6.2}$$

where u_H is the initial pore pressure, and the weight of the slice $W = \gamma_s H$, where γ_s is the unit weight of the overburden.

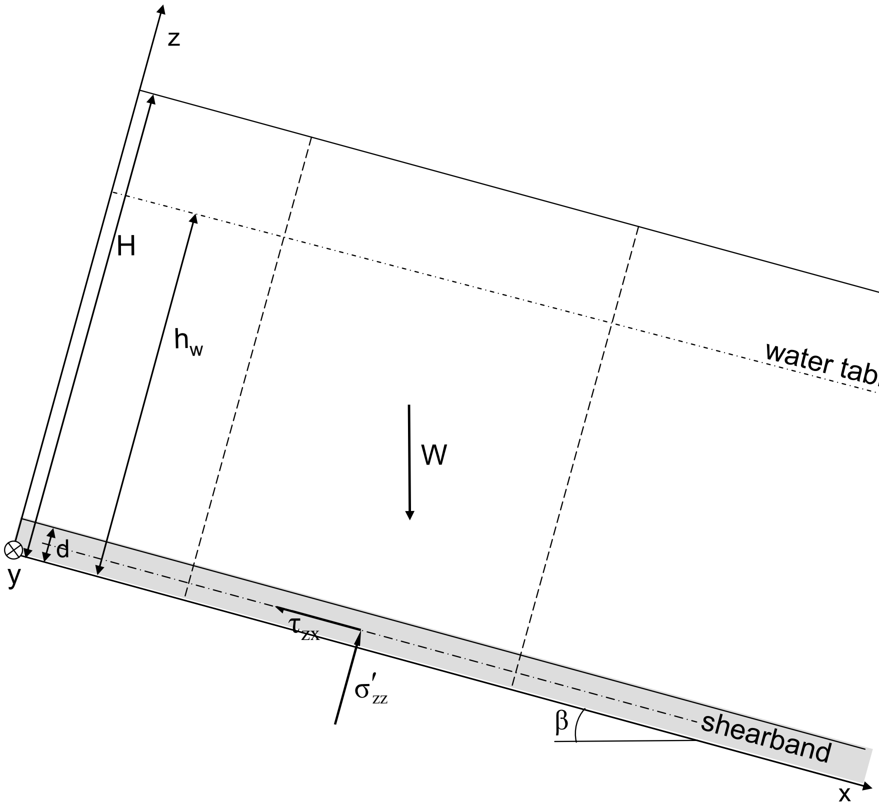

Figure 70. Infinite slope geometry. The shearband (shaded) has negligible thickness compared to that of the overburden, i.e. *H»d*. The slope inclination with respect to horizontal is *β*.

Equilibrium along x yields:

$$\tau_{zx} = W \sin\beta \tag{6.3}$$

so that from (6.1) we obtain

$$\tan\phi'_{mob} = \mu_0 = \frac{\gamma_s H \sin\beta}{\gamma_s H \cos\beta - u_H}\,. \tag{6.4}$$

The value of u_H depends on the groundwater conditions within the slope. As an example, we will now consider the simple (although not most general, as we will discuss in Section 7.3) case of groundwater flow parallel to the slope. In this case,

$$u_H = h_w \gamma_w \cos\beta \tag{6.5}$$

where γ_w is the unit weight of water and h_w the height of the water table above the slip plane. From (6.4) we may finally calculate the limit equilibrium friction angle as

$$\phi'_{mob} = \arctan\left(\frac{\gamma_s H}{\gamma_s H - \gamma_w h_w} \tan\beta \right). \tag{6.6}$$

With such initial configuration, a small perturbation to equilibrium is needed to trigger the movement of the slide. This can be done, for example, by reducing the obtained value of ϕ'_{mob} by some 0.1% as it was done for the Vajont simulation (Section 5.5.6).

6.1.2. Dynamic analysis

The considered block is subjected after triggering to an acceleration driven by gravity. The dynamic equation for the block along the *x* axis can be derived from Newton's second law of motion

$$F_x = m \frac{dv_x}{dt}, \tag{6.7}$$

where the mass of the 1-D block of Figure 70, knowing its volume$=\left(1 \cdot 1 \cdot H\right)$, the overburden's unit weight γ_s and the acceleration of gravity *g*, is

$$m = H \frac{\gamma_s}{g}. \tag{6.8}$$

From dynamic equilibrium, the force that applies in the direction of movement is the result of the imbalance between the gravity component along *x* and the resisting force in the slip plane due to friction and pore pressure:

$$F_x = \left(\gamma_s H \sin\beta - \tau_{zx} \right) \tag{6.9}$$

where the shear stress τ_{zx}, taken at mid-plane of the shearband where pressurisation is expected to be maximum, is derived from Coulomb's law. We may write

$$\tau_{zx}\left(t\right) = \hat{\mu} \sigma'_n \tag{6.10}$$

where $\hat{\mu} = \hat{\mu}\left(t\right)$ is the (potentially softening) friction coefficient (Section 5.2.1), and $\sigma'_n = \sigma'_n\left(t\right)$ the current normal effective stress which depends on the current values of excess pore pressure and temperature, consistently with the current stress state in the shearband (Section 6.1.3, Figure 44).

By substituting (6.8) and (6.9) into (6.7) we can finally write the dynamic equation for the infinite slope:

$$\frac{dv_x}{dt} = g\left[\sin\beta - \frac{\tau_{zx}(t)}{\gamma_s H}\right]. \tag{6.11}$$

At incipient failure, representing the model's initial conditions, the shear stress is

$$\tau_{zx}\big|_{t=0} = \tau_0 = \mu_0 \sigma'_{n0} \tag{6.12}$$

where μ_0 is given by expression (6.4), and σ'_{n0} by (6.2). This yields $dv_x/dt = 0$, hence the need to introduce a perturbation (cf. Section 6.1.1). After initiation of the slide movement, acceleration evolves with $\tau_{zx}(t)$.

6.1.3. Stress state assumptions

In Section 5.3.2.3 we deduced the value of mean effective stress from that of normal stress on the slip plane from the simplifying assumption that $\sigma'_{xx} = \sigma'_{zz}$ (cf. Figure 70 for the axis notation). This assumption was made along the lines of Vardoulakis (2000, 2002a), with the primary aim of validating our simulations against the calculations for the case of Vajont reported there. However, it is more realistic in soil mechanics to assume that it is the two in-plane stresses that are equal, i.e. $\sigma'_{xx} = \sigma'_{yy}$. Therefore, in the context of generalising the landslide model, it appears more appropriate to calculate the relationship between normal stress and mean effective stress as follows.

Similarly to Section 5.3.2.3, from Hooke's law in oedometric conditions we derive equations

$$\begin{cases} \sigma'_{xx} = \nu\left(\sigma'_{yy} + \sigma'_{zz}\right) \\ \sigma'_{yy} = \nu\left(\sigma'_{xx} + \sigma'_{zz}\right) \end{cases} \tag{6.13}$$

from which we obtain, by assuming $\sigma'_{xx} = \sigma'_{yy}$,

$$\sigma'_{xx} = \sigma'_{yy} = \left(\frac{\nu}{1-\nu}\right)\sigma'_{zz}. \tag{6.14}$$

Hence, from the definition of mean effective stress

$$p' = \frac{1}{3}\left(\sigma'_{xx} + \sigma'_{yy} + \sigma'_{zz}\right), \tag{6.15}$$

we obtain

$$\sigma'_{zz} = \sigma'_n = 3\left(\frac{1-\nu}{1+\nu}\right)p'. \tag{6.16}$$

From (6.16) we may calculate the current vertical effective stress acting on the shearband from the current mean effective stress, given by expression (5.39). Furthermore, we may calculate the initial mean effective stress from the initial normal effective stress (6.2) as

$$p'_0 = \frac{1}{3}\left(\frac{1+\nu}{1-\nu}\right)\sigma'_{n0} \tag{6.17}$$

Following the same reasoning as in Section 5.3.2.3, from (6.17) we obtain a new expression for the compressibility coefficient. The compressibility of the soil skeleton from (5.94) becomes

$$c_{sk} = \frac{1}{3}\left(\frac{1+\nu}{1-\nu}\right)c_{sw} \tag{6.18}$$

and (5.92) leads to the following expression for soil compressibility:

$$c = nc_w + \frac{\kappa(1+\nu)}{3p_0'(1-\nu)(1+e)}. \tag{6.19}$$

6.2. Numerical implementation

The infinite slope model contains the same heat and pore pressure equations as the model of the rotational case (Chapter 5), and a new dynamical equation defined by (6.11). To simulate the time evolution of temperature, excess pore pressure and slide velocity it is then necessary to integrate numerically the following system:

$$\begin{cases} \text{(I)} \quad \dfrac{\partial\theta}{\partial t} = D_i \dfrac{\partial^2\theta}{\partial z^2} + F_i \dfrac{v_d(t)}{d} \\ \text{(II)} \quad \dfrac{\partial u}{\partial t} = \bar{c}_v \dfrac{\partial^2 u}{\partial z^2} + \lambda_m \dfrac{\partial\theta}{\partial t} \\ \text{(III)} \quad \dfrac{dv_b}{dt} = g\left[\sin\beta - \dfrac{\hat{\mu}\sigma'_n}{\gamma_s H}\right] \end{cases} \tag{6.20}$$

Discretisation of governing equations (6.20) is done along the lines of Section 5.5.2. Also in this case, the dynamical Equation (6.20)-(III) is a one-dimensional ODE, describing the variation over time of the velocity of the block (hence the subscript *b*). Similarly to Equation (5.115), the slide acceleration at the generic i^{th} time-step is expressed by function f^i:

$$f^i = g\left[\sin\beta - \frac{\hat{\mu}\left(\theta^i, x_b^i, v_b^i\right)\sigma_n'\left(\theta^i, u^i\right)}{\gamma_s H}\right]. \tag{6.21}$$

In the general case the stress depends on the current temperature and pore pressure at the shearband mid-plane, and the friction coefficient depends on temperature, the displacement and the velocity of the block. We can discretise the dynamical equation with the 4th order Runge-Kutta approximation as:

$$\frac{v_b^{n+1} - v_b^n}{\Delta t} = \frac{1}{6} f^n + \frac{2}{3} f^{n+1/2} + \frac{1}{6} f^{n+1}, \tag{6.22}$$

and proceed to integration in the same way as detailed in Section 5.5.2. Given the dependence on velocity of function (6.21), the discretised Runge-Kutta Equation (6.22) cannot be solved directly for v_b^{n+1}. The equation is therefore solved iteratively, using the Ridders method to advance the solution (cf. Section 5.5.7.3).

The same considerations regarding the well-posedness of the heat equation hold for the infinite slope model; carrying out the analysis of Section 5.5.4 shows that the infinite slide model too remains well-posed for a very wide range of possible material values. Also the stability analysis described in Section 5.5.5 is still relevant and valid for the infinite slope model, as the heat and pore pressure equations remain unchanged compared to the circular failure model of Chapter 5. This stability analysis is implemented in our numerical code in order to automatically choose, before the start of simulations, the computationally cheapest (i.e., the largest) time-step that complies with condition (5.125).

6.3. Back-analysis of the Jiufengershan slide

The infinite slope model as presented above can now be applied to back-analyse other case histories. The landslide of Jiufengershan (Section 2.1.4.5) appears to best suit the purpose, because a) its planar geometry can be effectively represented by a block-on-slope model, b) sufficient geomechanical data (although not as abundant as for the case of Vajont) are available for a first-approximation simulation, and c) a pre-existing dynamic numerical analisys (Chang et al., 2005a) provides us with some reference values for a critical comparison.

6.3.1. Overview of the slide

The Jiufengershan landslide was triggered by the 1999 Chi-Chi earthquake in Taiwan. It affected weathered rock and soil materials, which quickly slid along the bedding plane, initially in a coherent manner and subsequently in a flow-like fashion (Chang et al., 2005a), for a total of 1 km. The slip surface developed along a pre-existing bedding fault, constituted of alternating beds of dark gray shale and muddy sandstone. Bedding-parallel clay seams of 1-6 cm in thickness were found in the slip plane throughout the slope, with clear slickensides and dip-slip striations (Wang et al., 2003).

The presence of frictionites in the slip plane of this slide (Section 2.3.1) proves the occurrence of frictional heating which must have locally reached, in areas where direct rock-to-rock contact was possible, temperatures in excess of 1000 °C (Chang et al., 2005a). Moreover, the authors observe the possible occurrence of pore pressure build-up when the permeability of the shear zone is low, as is the case for clay. Evidence of pore water pressurisation in the shear zone was found through field observations, as adjacent rock joints were found to be “filled with sheared mud injected from nearby saturated clay layers that experienced fluidisation during the avalanche” (Chang et al., 2005a).

Based on the above observations, Chang et al. (2005a) proposed a simple block-on-slope thermo-mechanical model (cf. Section 2.3.2) which was employed to simulate the landslide dynamics during the seismic triggering stage and the final collapse phase. The authors proposed a back-calculation of the slide velocity and of temperature, pore pressure and shear stress within the slip plane. These calculations show that the catastrophic evolution of the slide (termed by the authors “avalanche regime”) can be reproduced as soon as the thermal absorption coefficient, representing the fraction of frictional energy that is transformed into heat, is above a threshold value. Nevertheless, as pointed out in Section 2.3.2, the model equations of Chang et al. (2005a) do not seem able to interpret in a physically well-based manner the landslide motion coupled with the equations for heat flow and pore pressure diffusion across the shear zone, hence the need for a more comprehensive understanding that the infinite slope model can provide.

6.3.2. Selection of parameters

The available data on the geometry and relevant geomechanical properties of the Jiufengershan slide, reported by Chang et al. (2005a), Shou and Wang (2003) and Wang et al. (2003), are reported in Table 5.

Table 5. Field data of Jiufengershan slide.

Unit weight of water	γ_w	$9.81*10^3$	N/m^3
Unit weight of the overburden	γ_s	$24.525*10^3$	N/m^3
Slope inclination	β	20	degrees
Slide thickness	H	50	m
Average shearband thickness	d	$1*10^{-2}$	m
Height of water table	h_w	30	m

In Table 4 parameter *d* has been assigned the value of 1 cm as this is the observed average thickness of the shearband, found to vary between 1 mm and 10 cm (Chang et al., 2005a). The water table height is assigned the average value h_w=30 m after Chang et al. (2005a), which implies, within the framework of an infinite slope geometry, that the flow lines are assumed parallel to the slope (cf. Section 6.1.1).

Laboratory investigations were carried out to determine the strength properties (i.e. cohesion and friction angle at peak, residual and weathered state) of materials involved in sliding, although these are only available for the Changhuken shale formation (Shou and Wang 2003). The reported field observations (Huang et al., 2001) suggest that the slip occurred along the bedding plane separating the Changhuken formation (shale interbedded with thin sandstone layers) and the Shihmen formation (thick sandstone). The presence of clayey layers with clear slip striations intercalated between the aforementioned rock formations (Wang et al., 2003) suggests that the slip occurred at the interface between rock and the clay seams, similarly to the Vajont case (as described by Hendron and Patton, 1985). We will therefore assume that also in this case the deformation was localised within one of the clay layers. X-ray analysis revealed that the main minerals constituting this soil were quartz, feldspar, chlorite, illite and a small amount of chlorite/smectite (Wang et al., 2003); however, no information is available on the geotechnical properties of the clay. In our case the friction angle at critical state, representing incipient failure, is calculated by substituting the values of Table 5 into the initial condition (6.6), resulting to $\phi'_{cs} = 27.4°$. The initial normal effective stress is calculated as $\sigma_n{}' = 0.876$ MPa using Equation (6.2). Mid-range values can be selected for the clay properties κ, λ and Γ, extracted from a range of known values for different clays (cf. Schofield and Wroth, 1968 and Table 7), in view of the fact that the model is not sensitive to these values (cf. Section 7.4.2.1). The thermo-mechanical properties of the soil, namely the thermo-elastic expansion coefficient β_s, the thermal diffusivity k_m and the thermal constant C_f do not vary significantly for different types of soil (cf. Alexandre et al., 1999, Vardoulakis, 2002a and Section 5.5.3.4). In the absence of better data, they can be assigned the same values as for the Vajont case (Section 5.5.3). The reference temperature θ_{ref} can be set to 25°C to match the initial temperature in the simulations of Chang et al. (2005a, Fig. 5), and appears reasonably higher than that of Vajont considering the climatic differences between central Taiwan and the Alps.

In absence of direct measurements, the soil permeability can be set to an average value representative of clayey soils, $k_w = 10^{-11}$ m/s, which was adopted also in the case of Vajont (Section 5.5.3). The thermal softening parameter γ, following the same reasoning of Section 5.5.3.6 can be assigned the lower-mid-range value $\gamma = 10^{-2}$. Furthermore, since no information is available on the friction-softening properties of the Jiufengershan soil, parameters $\tilde{g}$, a_1 and a_2 (Section 5.2.1) are all set to zero for a first-attempt simulation. The void ratio, isothermal preconsolidation stress and plastic compressibility may be calculated as explained in Sections 5.5.3.1, 5.5.3.2 and 5.5.3.3 respectively. The above parameters are summarised in Table 6.

Table 6. Choice of parameters for Jiufengershan slide.

Slope of URL of clay	κ	$4.5*10^{-2}$	-----
Slope of NCL of clay	λ	0.17	-----
Specific volume intercept of clay	Γ	3.2	kPa
Soil (drained) Poisson's ratio	ν	0.3	-----
Compressibility of water	c_w	$4.93*10^{-4}$	MPa^{-1}
Reference temperature	θ_{ref}	25	°C
Soil thermal diffusivity coefficient	k_m	$1.45*10^{-7}$	m^2/s
Thermo-elastic expansion coefficient	β_s	$7.41*10^{-5}$	$°C^{-1}$
Thermal constant	C_f	2.84	Mpa/°C
Soil permeability	k_w	10^{-11}	m/s
Thermal softening parameter	γ	10^{-2}	-----
Calculated friction angle at CS	ϕ'_{cs}	27.4	degrees
Calculated initial normal effective stress	σ_n'	0.876	MPa

6.3.3. Seismic triggering phase: undrained failure

The seismic triggering phase of Jiufengershan was simulated by Chang et al. (2005a) by resorting to the approach of Newmark (1965) modified with thermo-mechanical considerations. The evolution of displacements and loss of shear strength of the sliding block during earthquake shaking, based on the available accelerogram records (Huang et al., 2003), was calculated. An estimation of the pore pressure and temperature evolution in the slip plane was also given by Chang et al. (2005a), showing no major increase of these quantities until about 50 seconds after the event initiation (30 seconds after the actual start of the seismic shock), which we may consider as the reference time approximately marking the end of the slide triggering phase. After this point, once the slide has fully developed the rates of increase of temperature and pore pressure grow drastically, demonstrating the onset of thermo-mechanical collapse due to rapid vanishing of the shear resistance at the slip plane. These simulations can be seen in Figure 71, where we inserted a vertical line to differentiate, approximately, the seismic triggering phase (from t=20s to t=50s) from the thermo-mechanical collapse phase (from t=50s to t=70s). Such subdivision of Chang et al.'s (2005a) results facilitates a critical comparison with our simulations: our landslide model can interpret the final catastrophic acceleration phase, whereas it cannot be employed to simulate the "stick-slip behaviour" which is typical of the co-seismic inertial displacements (Chang et al., 2005a). Instead, we hereby provide a general description of the seismic failure phase within the framework of critical state soil mechanics.

Based on the landslide model assumptions (Chapter 5), the shearband soil is at critical state at the onset of catastrophic collapse. Before the earthquake, the rock and soil of Jiufengershan are assumed to be intact (Chang et al., 2005a). It is reasonable to assume that during seismic shaking the material reached failure in an undrained manner. In other words, the loading path assumed for the shearband soil is horizontal in the $\left(\ln p', \mathrm{v}\right)$ plane, starting from initial conditions and reaching critical state at constant specific volume, building up excess pore pressures that cannot be dissipated due to the rapidity of shearing. A sample state path for undrained seismic failure is drawn in Figure 72a, where the soil before the earthquake is assumed to be isotropically and normally consolidated. Figure 72b illustrates undrained failure for the case of an initially over-consolidated soil.

The calculation of the excess pore pressure to failure u_f (Figure 72) is straightforward once the soil parameters Γ, λ, κ and the initial values p_0' and $OCR = \sigma_{c0}' / p_0'$ are known. In fact, parameter N_p can be obtained as

$$N_p = \Gamma + \lambda - \kappa \tag{6.23}$$

(see e.g. Powrie, 1997), and if *OCR*=1 the initial specific volume can be calculated from the equation of the isotropic normal-consolidation line (iso-NCL) as

$$\mathrm{v}_0 = N_p - \lambda \ln p_0' . \tag{6.24}$$

If *OCR*>1 instead, the specific volume corresponding to the normally consolidated state v_1 is obtained from the equation of the iso-NCL as

$$\mathrm{v}_1 = N_p - \lambda \ln\left(OCR \cdot p_0'\right) \tag{6.25}$$

and the initial specific volume is calculated from the equation of the unloading-reloading line (URL) as

$$\mathrm{v}_0 = \mathrm{v}_1 + \kappa \ln\left(OCR\right). \tag{6.26}$$

In either case, from the equation of the critical state line (csl) we may calculate the effective mean stress at critical state as

$$p_{cs}' = \exp\left(\frac{\Gamma - \mathrm{v}_0}{\lambda}\right), \tag{6.27}$$

from which we deduce

$$u_f = p_0' - p_{cs}' . \tag{6.28}$$

For the case history of Jiufengershan only p_0' is available from field data, while parameters Γ, λ, κ have been assigned mid-range values (Table 6) and *OCR* is not known. In order to assess the importance of the parameters in the calculation of the excess pore pressure to failure, u_f was calculated starting from the known field stress $p_0' = 437.9\,\mathrm{kPa}$ for three sample clays of known properties (Schofield and Wroth, 1968) and for different values of *OCR* (Table 7). It emerges that the involved soil parameters, most notably *OCR*, have a substantial influence in the value of u_f. For this reason, we cannot reliably calculate u_f for Jiufengershan based on the imposed mid-range values. However, we notice that the value of $u_{f0} \sim 70\,\mathrm{kPa}$ computed by Chang et al. (2005a) (In Figure 71, U_p is increased from ~235 to ~305 kPa during the seismic triggering phase) is not unreasonable for undrained failure at the given field pressure.

Consequently, we will adopt $u_{f0} = 70\,\text{kPa}$ as the value of excess pore pressure at the start of the catastrophic collapse phase.

Due to frictional heating resulting from co-seismic slip, we can expect the temperature at the base of the slide to be higher than the ambient one (θ_{ref}=25°C, cf. Section 6.3.2) after 30 seconds of seismic shaking (i.e. within the time window Δt_s=20-50s in Figure 71). In fact, the calculations of Chang et al. (2005a) predict for this stage a 20°C temperature increase (from about 298 to 318 °K in Figure 71). Consistently, as initial temperature for the catastrophic landslide model we may set $\theta_0 = 45$ °C.

Table 7. Combinations of parameters for which the excess pore pressure to failure is calculated.

Soil type	Γ	λ	κ	*OCR*	u_f (kPa)
London clay	2.76	0.16	0.06	1	203.5
London clay	2.76	0.16	0.06	1.5	135.9
London clay	2.76	0.16	0.06	2	76.4
London clay	2.76	0.16	0.06	2.5	22.3
Weald clay	2.06	0.09	0.035	1	200.2
Weald clay	2.06	0.09	0.035	2	74.9
Kaolin clay	3.767	0.26	0.05	1	242.6
Kaolin clay	3.767	0.26	0.05	2	96.1

6.3.4. Catastrophic collapse phase

The final collapse phase of Jiufengershan, corresponding to Chang et al.'s (2005a) "avalanche regime", was simulated by numerically integrating the infinite slope model (Section 6.2), employing the relevant parameter values (Section 6.3.2) and initial conditions (Section 6.3.3). Within the shearband, initial temperature is set to $\theta_0 = 45$ °C while the initial total pore pressure is the sum of the pre-earthquake pore pressure (Equation (6.5)) and that resulting from undrained shear u_{f0}, a total of $u_0 = u_H + u_{f0} \simeq 305\,\text{kPa}$ (roughly corresponding to Chang et al.'s (2005a) value of U_p at t=50s in Figure 71). The initial velocity is set to zero as the slide movement is numerically initiated by a minute reduction of the friction angle from its limit equilibrium value (Section 6.1.1).

Temperature and excess pore pressure were computed at each grid-point of the spatial domain, and isochrones through the domain were produced at key time values, for a time window of 20 seconds after initiation (Figure 73 and Figure 74). Compared to the isochrones computed for Vajont (Figure 66 and Figure 67) where the initial normal stress was higher (2.38 MPa vs 0.876 MPa of this case), the rate of production of both temperature and pore pressure is here smaller: after 10s from initiation, at the shearband mid-plane $\theta \simeq 55\,°\mathrm{C}$ and $u \simeq 60\,\mathrm{kPa}$. In both graphs, the flat profile of the isochrones within the shearband for *t*=20s reveals the asymptotic convergence to a steady state for heat production: temperature reaches the maximum value $\theta_{\max} \simeq 134\,°\mathrm{C}$ as the shearband soil liquefies due to full pressurisation and the shear stress tends to zero. This is best illustrated in Figure 75, where the computed excess pore pressure and shear stress at the shearband mid-plane are plotted against time: the weakening of shear resistance is closely related to the raise of excess pore pressure, and the rates of both functions tend to zero after *t*=18s.

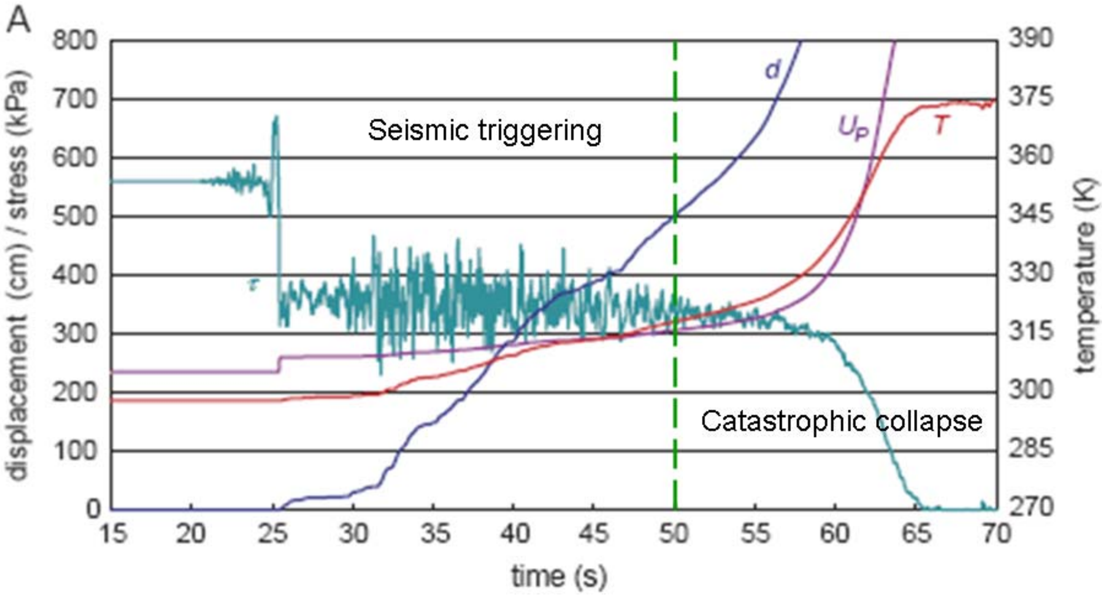

Figure 71. From Chang et al. (2005a). Simulation of the time evolution of shear stress (τ), displacement (d), temperature (T) and pore pressure (U_p) for the Jiufengershan slide in the catastrophic case scenario (avalanche regime). The seismic triggering phase, where the increase of pore pressure and temperature is not significant, lasts up to about 50 seconds, after which the drastic build-up of both T and U_p determines catastrophic collapse due to rapid vanishing of the shear strength. The vertical dashed line marks the approximate boundary between the two phases.

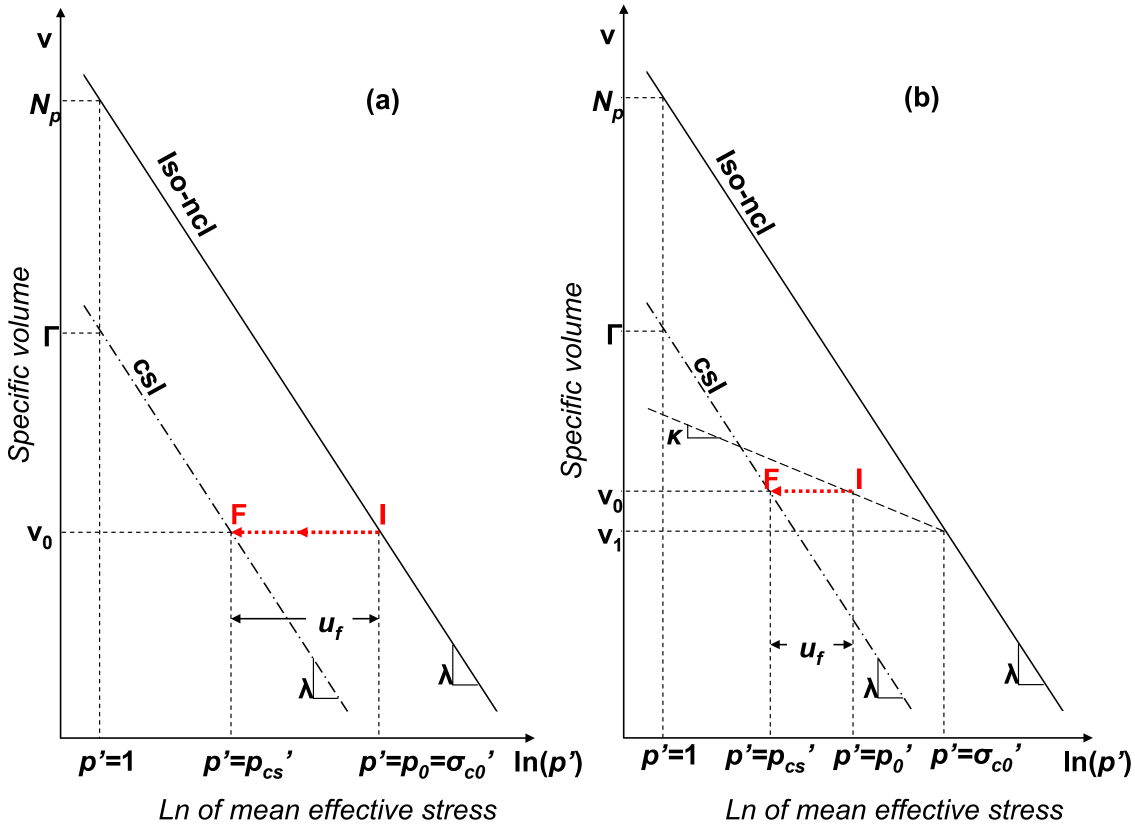

Figure 72. Sample stress paths of undrained failure from the initial undisturbed state (I) to the final critical state (F) in the compression plane, for the two cases of (a) initially NC soil and (b) initially OC soil.

In Figure 76 and Figure 77 the slide velocity and displacement are plotted against time. After 10s from initiation, we obtain $v_b \simeq 0.9\,\mathrm{m/s}$ and $x_b \simeq 1.6\,\mathrm{m}$, denoting a slower acceleration in comparison to Vajont (Figure 68 and Figure 69). Nevertheless, the reduction of shear strength is such that only 10 seconds later (at t=20s) also Jiufengershan attains a velocity of 25 m/s, thus undergoing an equally catastrophic evolution.

Field observations suggest that the maximum displacement of the Jiufengershan slide was 1 km, and the maximum velocity reached was about 80 m/s, at a stage when the mass could have lost its integrity and moved in a flow-like fashion (Chang et al., 2005a). Nevertheless, this later-stage evolution appears to be well reproduced with the infinite slope model: by extending our simulations to a time of 40 seconds after initiation (Figure 78), we calculate a velocity of about 80 m/s after a displacement of 1000m.

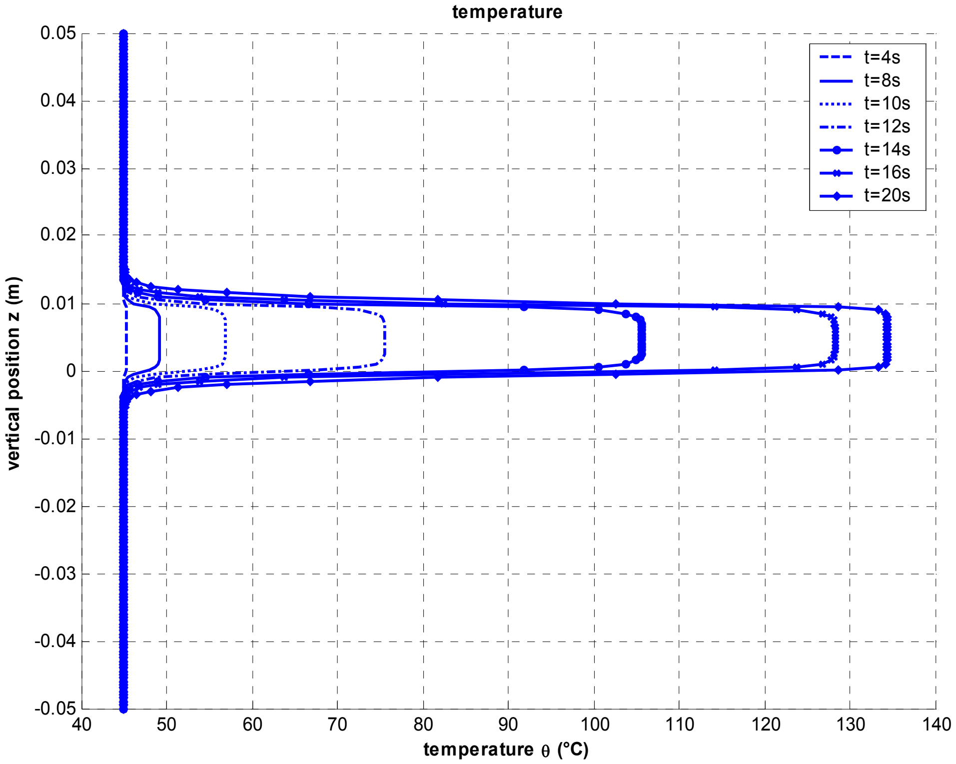

Figure 73. Temperature isochrones from our calculations to interpret the catastrophic collapse phase of Jiufengershan.

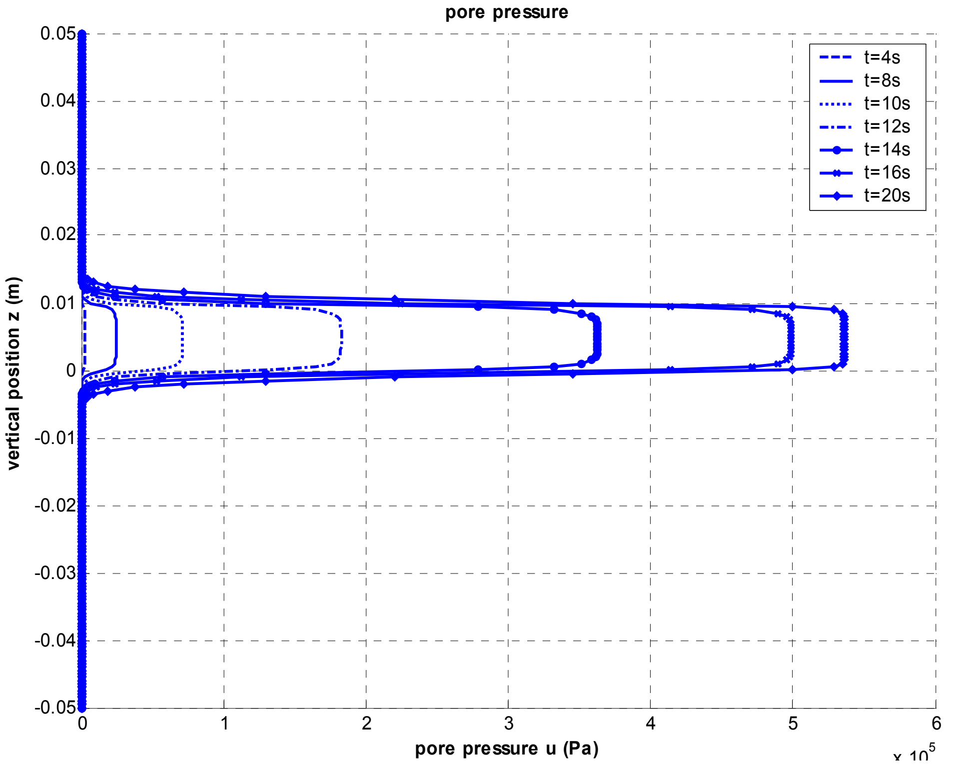

Figure 74. Excess pore pressure isochrones from our calculations to interpret the catastrophic collapse phase of Jiufengershan.

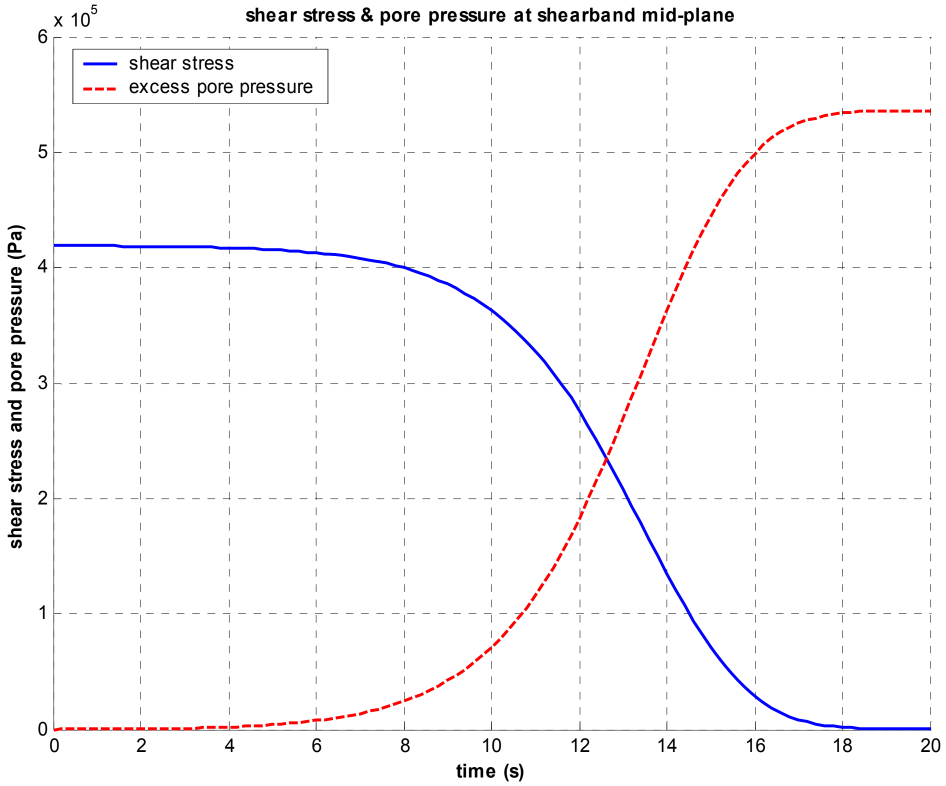

Figure 75. Computed shear stress and excess pore pressure at the shearband mid-plane as a function of time.

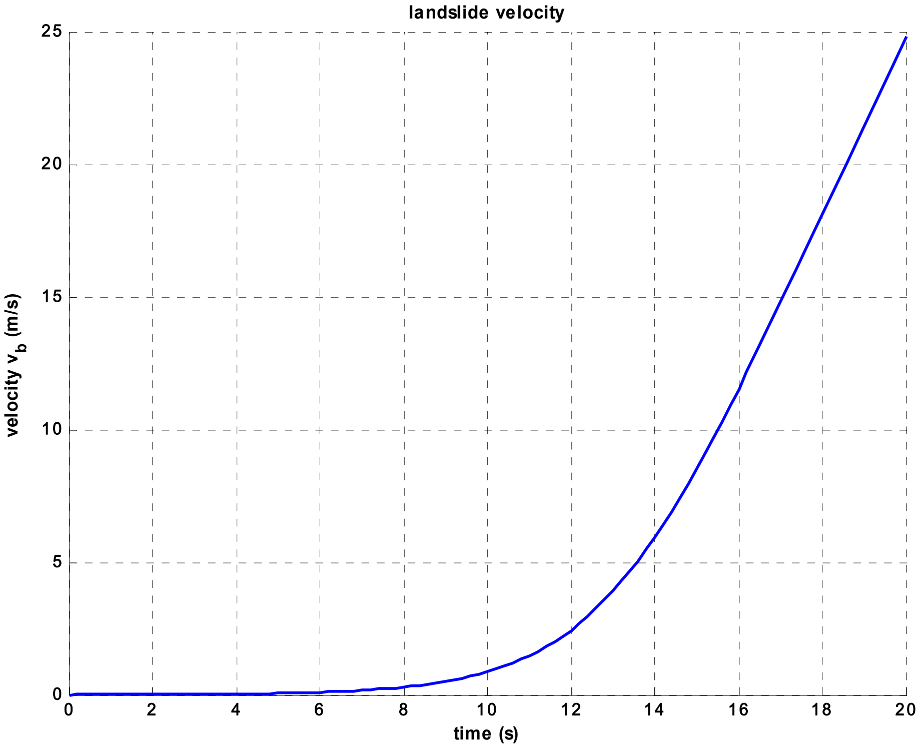

Figure 76. Computed velocity profile to simulate the catastrophic collapse phase of the Jiufengershan slide.

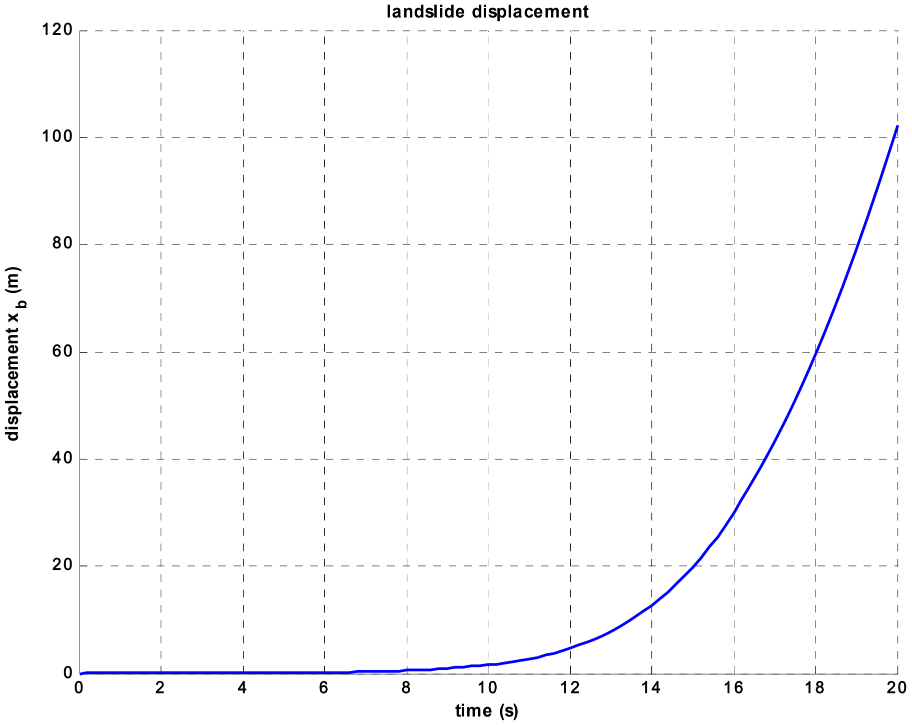

Figure 77. Computed displacement profile to simulate the catastrophic collapse phase of the Jiufengershan slide.

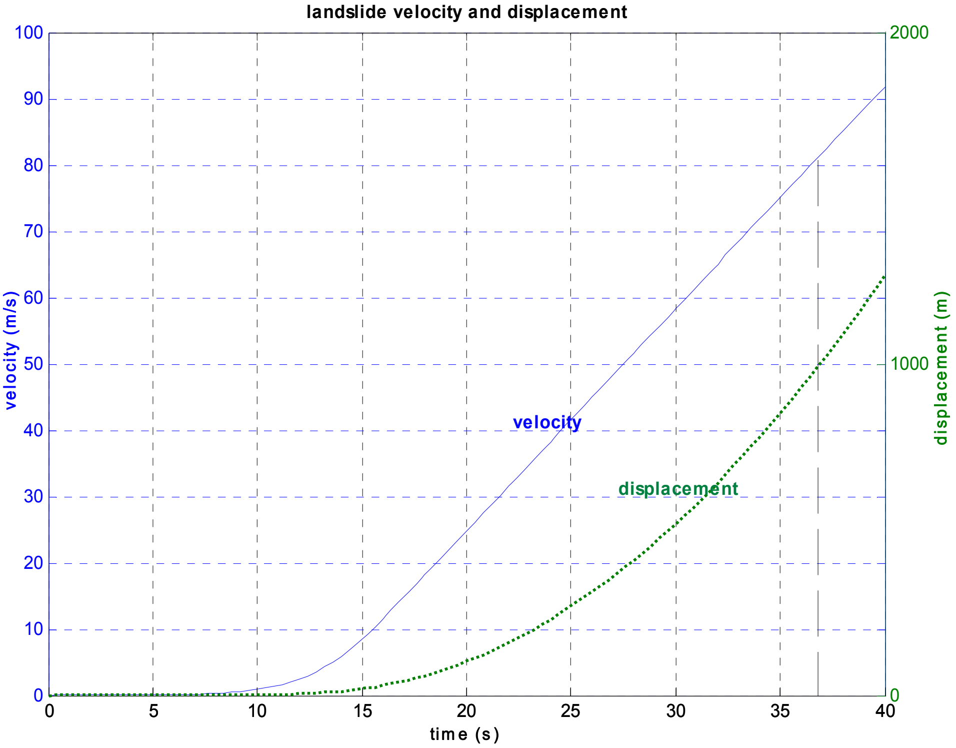

Figure 78. Computed velocity and displacement of the Jiufengershan slide, plotted against time for the first 40 seconds of catastrophic collapse. The vertical dashed line marks the reaching of 1km of displacement, roughly corresponding to a velocity of 80 m/s.

Furthermore, the calculations of Chang et al.'s (2005a) shown in Figure 71 were plotted in the same figure with our simulations, in order to carry out a systematic comparison. As explained in Section 6.3.3, our simulations should start at *t*=50s of the temporal axis of Chang et al.'s (2005a) calculations, in order to be compared to the 'catastrophic collapse' part. In Figure 79, Figure 80 and Figure 81 respectively the temperature, the total pore pressure and the shear stress acting in the mid-plane of the shearband are plotted for both models.

We notice that our simulations predict a considerably higher maximum temperature, which nevertheless remains below the vaporisation threshold, hence no phase change of the water is expected to take place. The threshold temperature θ_{vap} may be calculated along the lines of Section 5.5.7.1: by setting as p_{cr} the maximum total pore pressure reached, $p_{cr} = U_{\max} \approx 0.84$ MPa (cf. Figure 80) and solving Equation (5.130) for θ_{vap} we get as vaporisation threshold temperature $\theta_{vap} \approx 166\,°\mathrm{C}$. Moreover, our calculations predict the total pore pressure to stabilise around the maximum value $U_{\max} \approx 0.84$ MPa, showing that this variable is in fact upper-bounded by the initial normal effective stress ($\sigma_n' \simeq 0.87$ MPa), while the corresponding pore pressure profile calculated by Chang et al. (2005a) seems to keep increasing indefinitely.

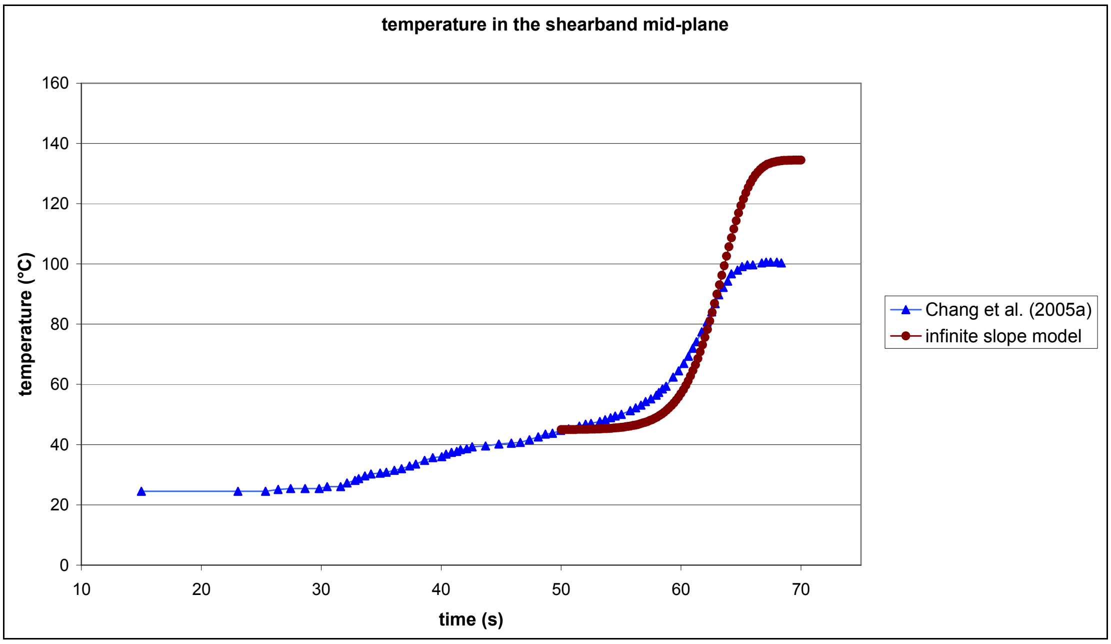

Figure 79. Comparison between our simulations and those of Chang et al. (2005a) of the temperature profile at the shearband mid-plane of the Jiufengershan landslide.

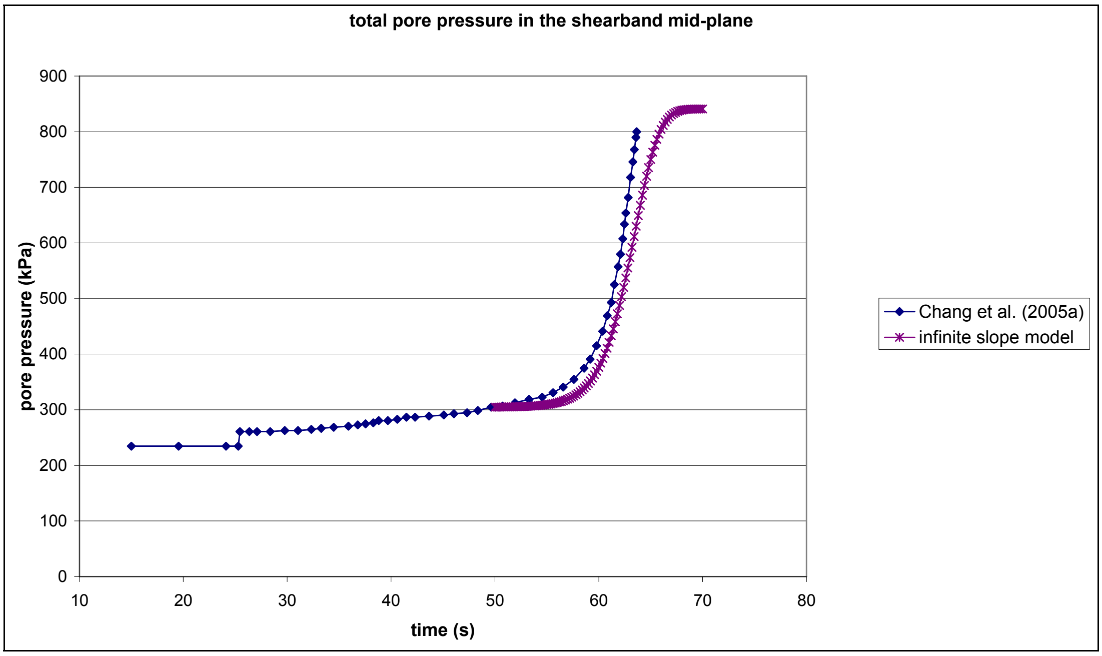

Figure 80. Comparison between our simulations and those of Chang et al. (2005a) of the total pore pressure profile at the shearband mid-plane of the Jiufengershan landslide.

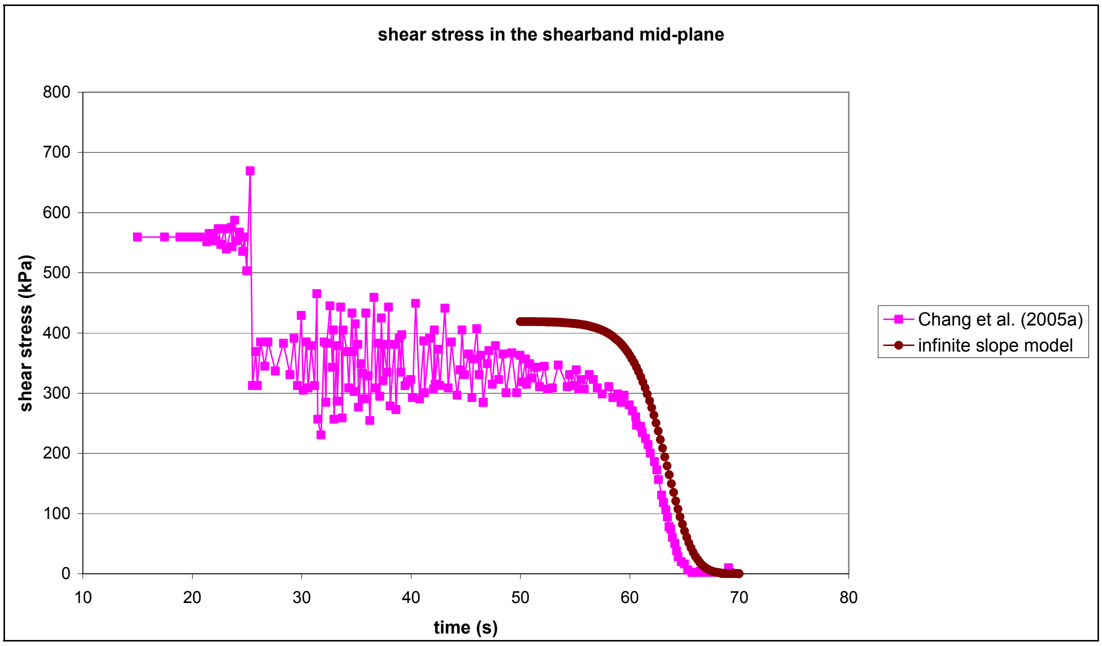

Figure 81. Comparison between our simulations and those of Chang et al. (2005a) of the shear stress profile at the shearband mid-plane of the Jiufengershan landslide.

We also notice in Figure 81 that the initial value of shear stress according to our incipient failure calculations plausibly falls in between Chang et al.'s (2005a) pre- and post-rupture values; and the computed catastrophic evolution of shear stress is very similar in the two cases.

6.3.5. Cases of friction-softening soil and thinner shearband

As we will show in Section 7.4.2.1, the predictions of catastrophic collapse carried out with our model are not substantially sensitive to the choice of standard soil parameters such as Γ, λ, and κ. On the other hand, some parameters that are not always easy to determine, like the shearband thickness *d* and the friction softening properties (static and dynamic residual friction angles and rates of softening) may drastically affect the predicted values. As an example, we will explore hereafter the effect of allowing for friction-softening and that of assuming a thinner shearband in the Jiufengershan simulations.

While the literature lacks information on typical values related to the dynamical friction-softening of clays, some trends can be found on the static residual friction angle (Section 2.1.4). For the Jiufengershan clay, we may assume that the latter is around 10°, as is typical of soils with 50% clay fraction (Skempton, 1985). As an example, in our simulation we will allow the friction angle to decrease with displacement only, assuming for the rate of static softening, in the absence of better information, the same value as for Vajont (cf. Section 5.2.1 and 5.5.3). By using for the other parameters the same values as in Section 6.3.2, the simulations were run for a total time window of 20 seconds. The resulting temperature and pore pressure isochrones are shown in Figure 82 and Figure 83, and are similar to those in Section 6.3.4 (Figure 73 and Figure 74), but the effect of the rapid decrease of friction with displacement is evident in the variable slope of the shear stress plot (Figure 84): an initial, very steep branch due to friction softening is followed by a relatively milder one, representing the continuation of the shear resistance weakening due to pressurisation, towards the asymptotic attainment of a liquefaction state, after *t*=12s. By comparing the shear stress and excess pore pressure plots of Figure 84 to those in Figure 75 we notice that pressurisation is now more rapid, due to more rapid frictional heating (Figure 85). In fact the rates of velocity and displacement are heavily affected by material softening, as the slide reaches 500m at a speed of almost 60 m/s after 20 seconds from initiation (Figure 86).

The effect of the shearband thickness on our calculations is shown by choosing for *d* the lower-range value of 1mm (Chang et al., 2005a) whilst keeping all other parameters as described in Section 6.3.2: more localised shearing causes (compared to the results in Section 6.3.4) heating and pressurisation to be more concentrated around the shearband mid-plane (Figure 87 and Figure 88). Also, thermal pressurisation is quicker, as in this case full pressurisation is attained after only 8s (Figure 89). The acceleration is also higher, as velocity reaches about 50 m/s at *t*=20s (Figure 90).

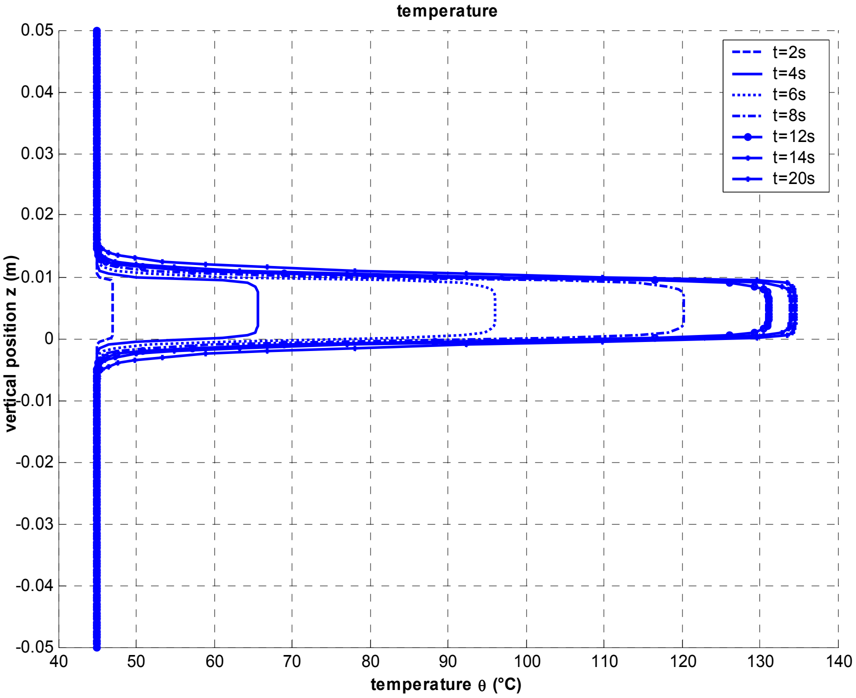

Figure 82. Temperature isochrones from our calculations to interpret the catastrophic collapse phase of Jiufengershan, in the case of friction-softening soil.

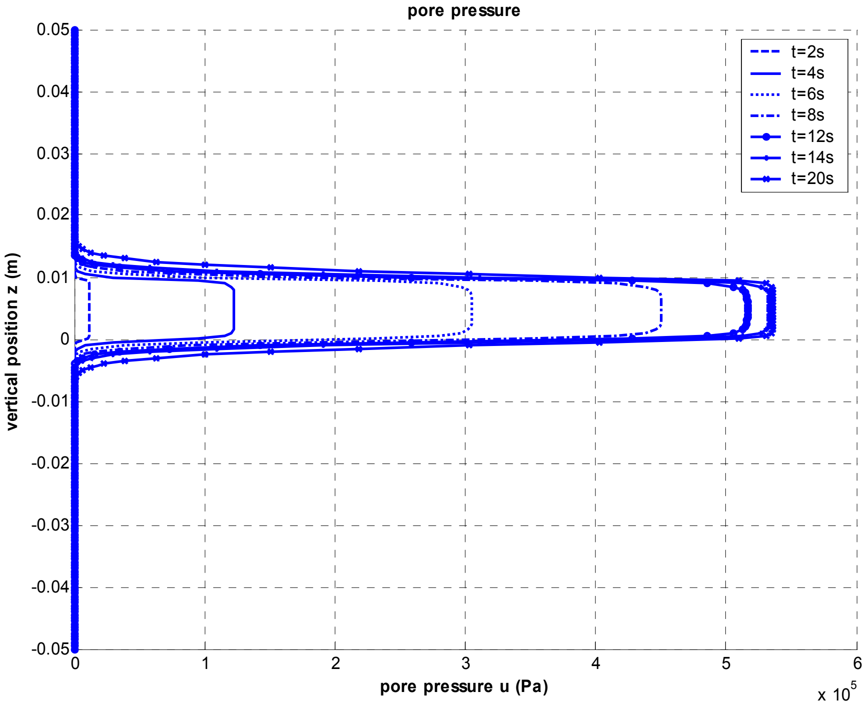

Figure 83. Excess pore pressure isochrones from our calculations to interpret the catastrophic collapse phase of Jiufengershan, in the case of friction-softening soil.

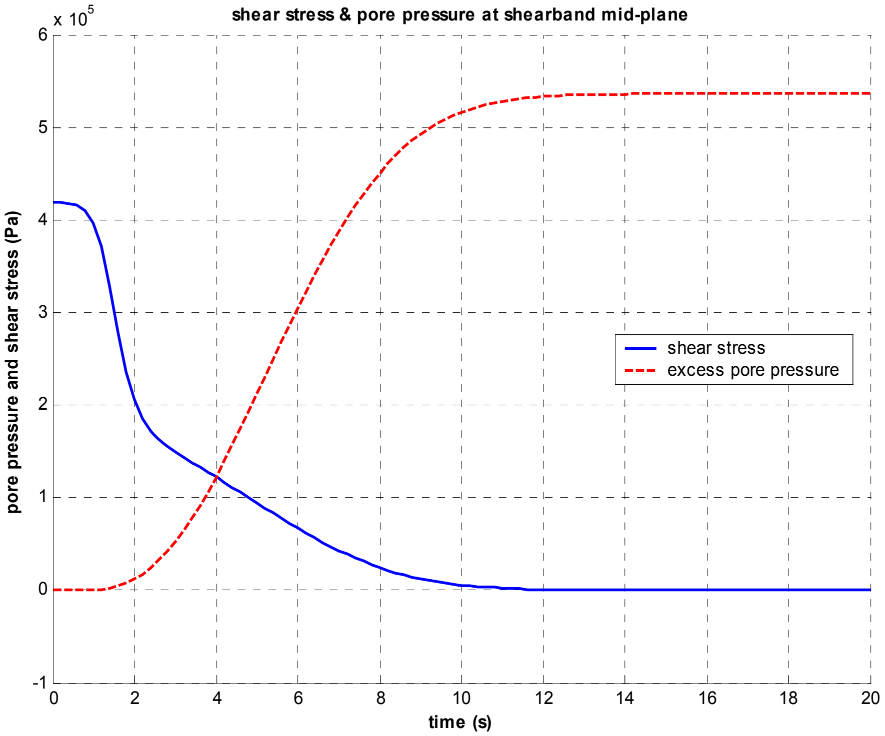

Figure 84. Computed shear stress and excess pore pressure at the shearband mid-plane as a function of time, in the case of friction-softening soil.

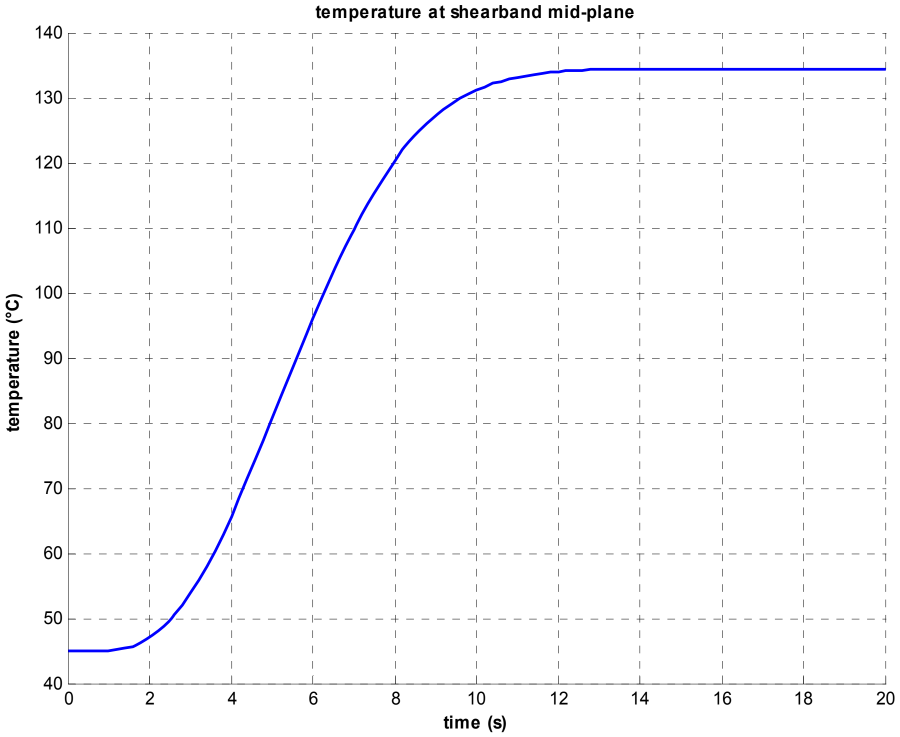

Figure 85. Computed temperature at the shearband mid-plane as a function of time, in the case of friction-softening soil.

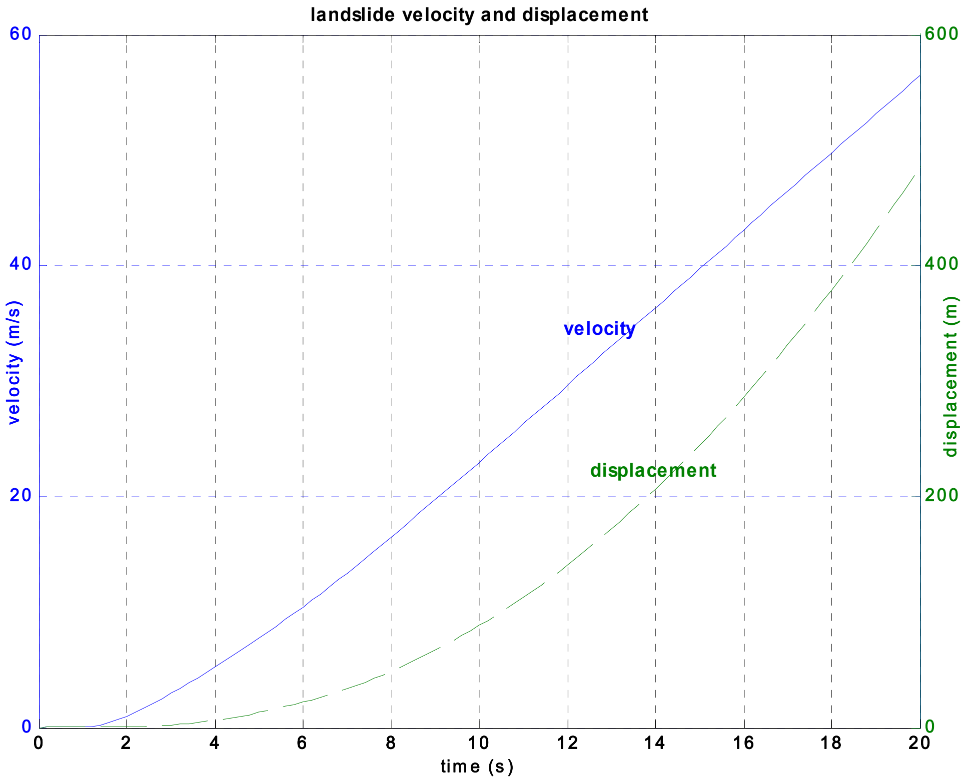

Figure 86. Computed velocity and displacement of the Jiufengershan slide, plotted against time for the first 20 seconds of catastrophic collapse, in the case of friction-softening soil.

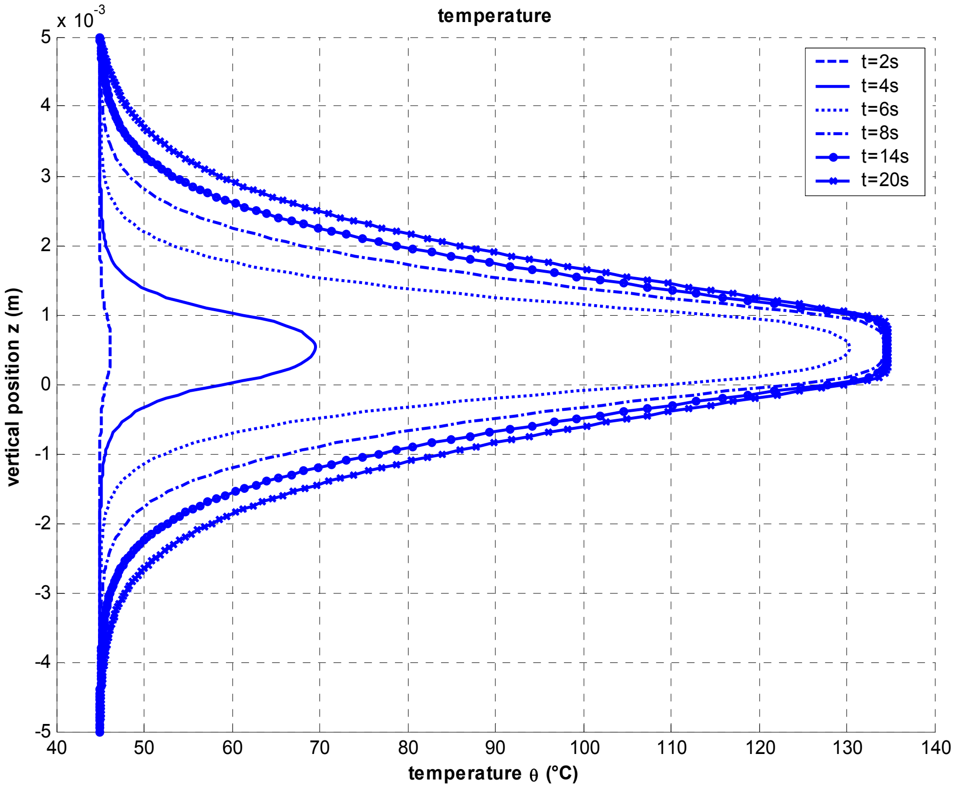

Figure 87. Temperature isochrones from our calculations to interpret the catastrophic collapse phase of Jiufengershan, in the case of thinner shearband (*d*=1mm instead of 1cm).

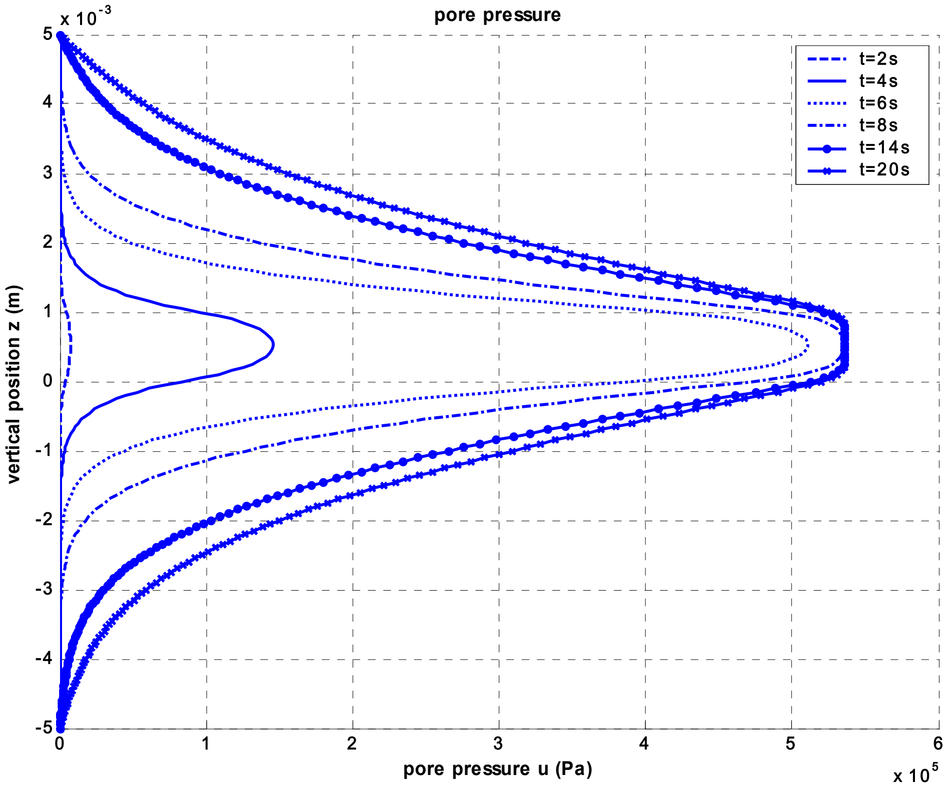

Figure 88. Excess pore pressure isochrones from our calculations to interpret the catastrophic collapse phase of Jiufengershan, in the case of thinner shearband (*d*=1mm instead of 1cm).

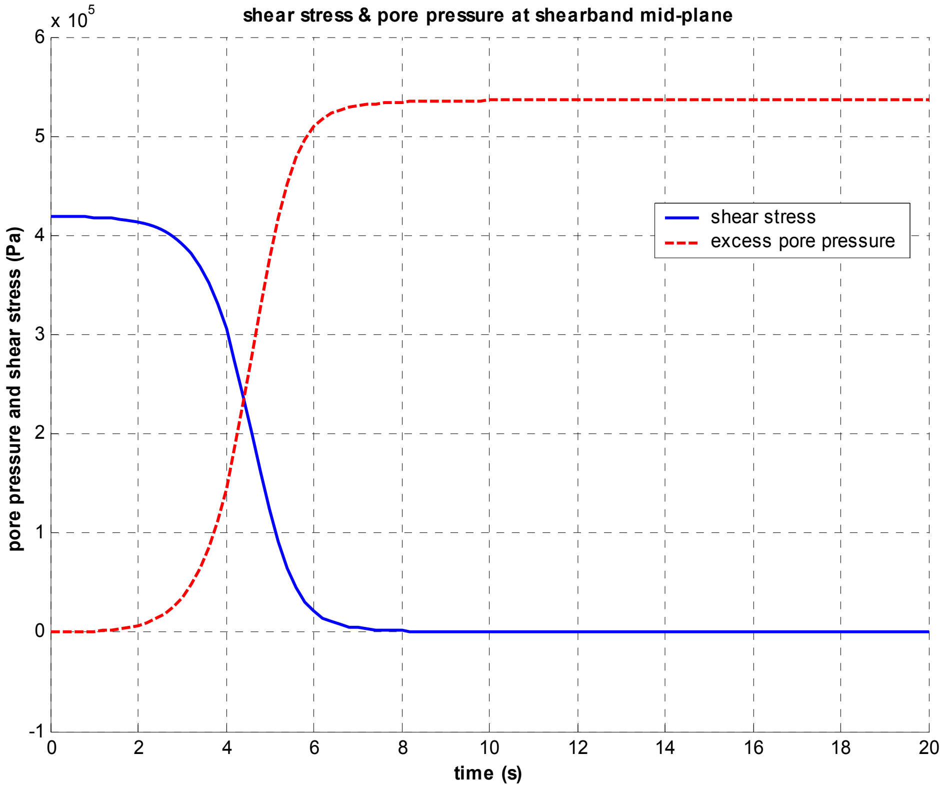

Figure 89. Computed shear stress and excess pore pressure at the shearband mid-plane as a function of time, in the case of thinner shearband (*d*=1mm instead of 1cm).

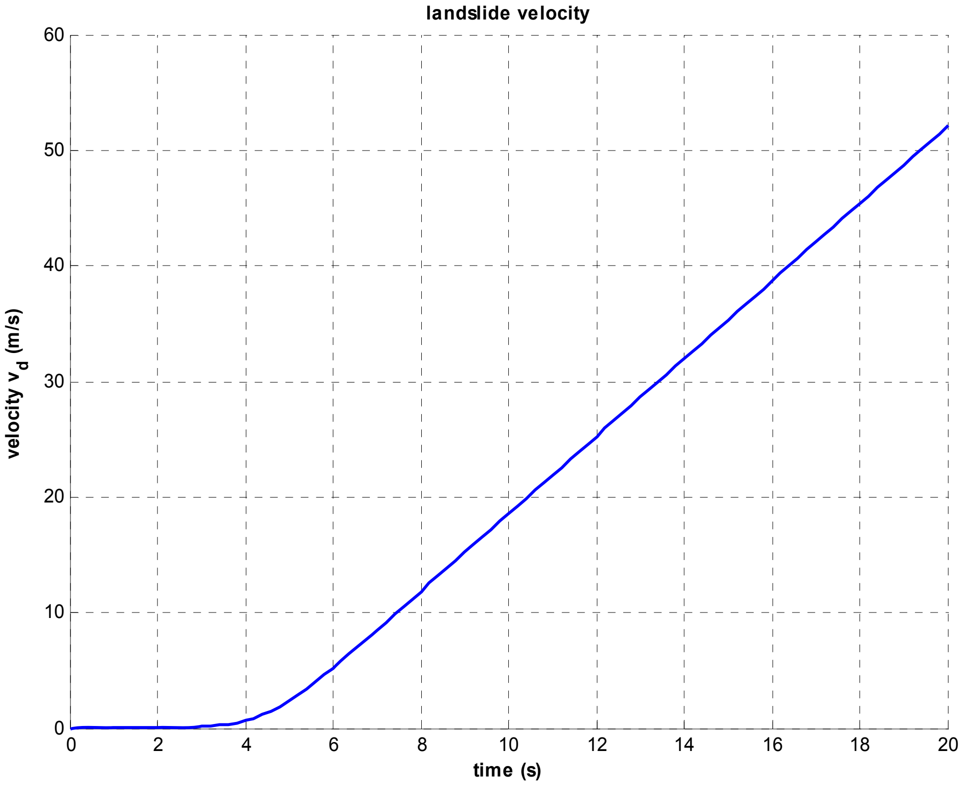

Figure 90. Computed velocity profile to simulate the catastrophic collapse phase of the Jiufengershan slide, in the case of thinner shearband (*d*=1mm instead of 1cm).

Chapter 7. Parametric analysis to determine the critical conditions to catastrophic failure

After validating the infinite slope model with the back-analysis of the Jiufengershan case history (Chapter 6), we may employ it to carry out a more general dynamic analysis, with the aim of identifying the most important parameters that make a slope prone to catastrophic failure. This is done by carrying out a number of simulations using the landslide model while independently varying each relevant geometrical and geomechanical property of the slide within a realistic range. Exploring all significant combinations of parameters will allow us to determine the ones which maximise the predicted slide velocity, i.e. those exacerbating the catastrophic character of the slide.

7.1. On the definition of 'catastrophic' slide

It has been shown in Chapter 6 that the infinite slope model is able to interpret the dynamics of the final collapse phase of a landslide by calculating, among other relevant quantities, the time evolution of the slide velocity. The velocity that a slide can reach is indeed one of the key attributes to determine its destructive potential or, in other words, to define how catastrophic a slide can be. Of particular interest to civil protection issues is the slide acceleration, as predicting it can be critical to planning evacuation measures. However, as discussed in Section 2.1.2, there cannot be a unique definition of 'catastrophic' slide, due to the wide variety of contexts in which landslides occur.

A criterion enabling us to formally discern between dangerous and non-dangerous cases could still be established, based on the velocity reached by a slide after a certain distance. For example, we could consider catastrophic any landslide that after 10 metres of displacement reaches a velocity of 3 m/min (i.e., 0.05 m/s) or more. The latter value constitutes the threshold velocity for 'very rapid' slides in the IUGS velocity classification (Table 2); while 10 metres can arguably be considered, in first approximation, a distance large enough for a slide to be noticed, and maybe small enough to avoid major damage. Such a criterion can be useful when a potentially unstable slope is considered and, all relevant field data being available, a prediction of the dynamic evolution of the slide is attempted. On the other hand, our main aim is to establish a general rule, enabling us to identify the most important properties that make a slope prone to be catastrophic. This rule can be established through the dynamical simulation of a series of possible landslide case scenarios, in order to determine a ranking of importance of the involved parameters in making a slide more dangerous. In this context, the need for a threshold is overcome as we will need to classify the parameters in order of importance with respect to their influence in maximising the slope velocity, regardless of its value. For this purpose, in our parametric analysis the simulation output to be elaborated upon can simply be the velocity v_τ, reached after a certain time τ from the initiation of movement. We may set $\tau = 10\,\mathrm{s}$, a small enough value that allows us to save computational time, yet long enough for the development of full pressurisation in the most catastrophic cases, as seen in our previous simulations (cf. Chapters 5 and 6).

It is also worth remarking here that the infinite slope model is conceived to interpret a landslide's final collapse, thus excluding any preliminary creeping phase that may occur. Our analysis will then aim to assess whether a potentially unstable slope is bound to acquire unexpectedly high velocities, rather than estimate its long-term stability.

As a preliminary example of the unexpected influence of commonly measured landslide properties in the predicted dynamics we can consider the variation of the depth *H* of the slide. This parameter is irrelevant in the dynamic evolution of a slide if we neglect pressurisation, as can be seen by re-writing Equation (6.11) for the case of zero excess pore pressure:

$$a = \frac{dv_x}{dt} = g\left[\sin\beta - \tan\phi'\left(\cos\beta - \frac{u_H}{\gamma_s H}\right)\right] \tag{7.1}$$

In the above, *H* features in the denominator of the last term on the right hand side, which is constant and dependent on the initial conditions only. In this case the evolution of acceleration *a* only depends on whether or not the soil exhibits friction-softening, through the term $\left(\tan\phi'\right)$. If instead thermal pressurisation is taken into account, the rate of production of excess pore pressure will increase with *H* since, everything else being equal, the dissipation term (Section 5.2) will be higher for a thicker overburden. This means that slides with a deeper rupture surface will be more bound to accelerate catastrophically. This is shown in Figure 91, where results of a set of infinite slope simulations are presented. The simulations were run using mid-range values for the involved parameters (see Section 7.2 and Table 8) and varying the thickness *H* only. The velocity profile for the first 10 seconds from slide initiation is plotted for thicknesses ranging from 50 to 400 metres, both with and without thermal pressurisation. Calculations relative to the latter case all lead to the same prediction, represented by the thin dashed line at the bottom of the plot. The velocity reached after 10s in this case is of the order of metres/hour, while if thermo-mechanical effects are taken into account the velocity after 10s increases with *H* by several orders of magnitude, up to 10 m/s in the extreme case of *H*=400m.

The above example highlights the need for a systematic study, since in the framework of the thermo-mechanical infinite slope model other parameters might be unexpectedly important in the catastrophic evolution of a slide. The parameteric analysis is presented hereafter.

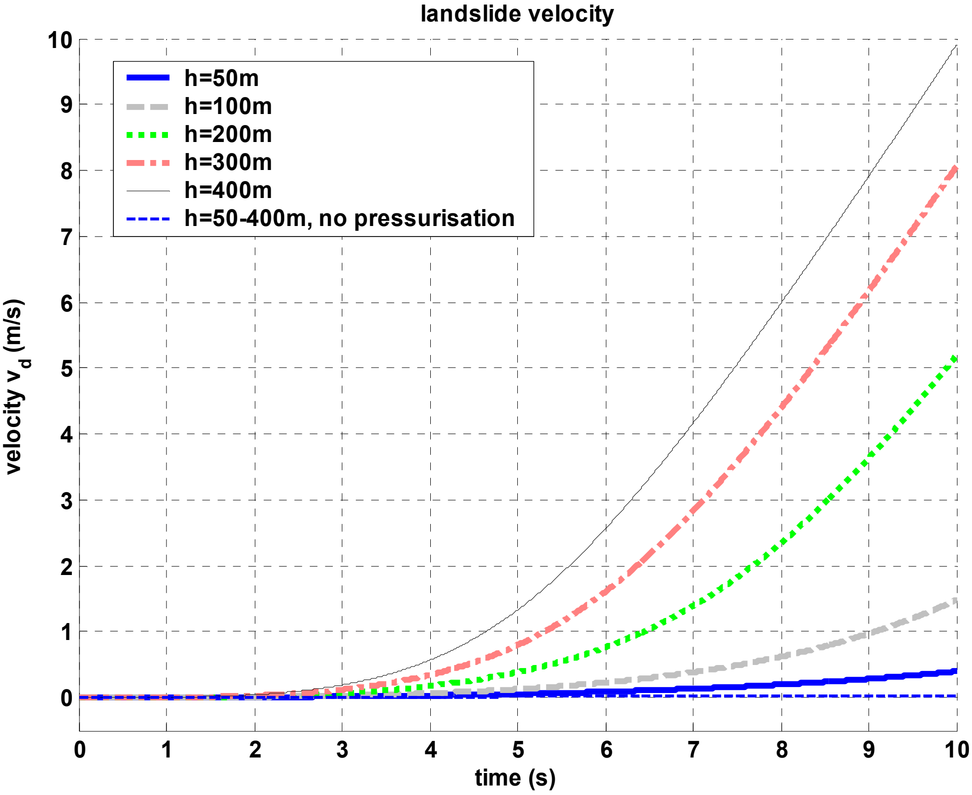

Figure 91. Preliminary study on the effect of the overburden thickness *H* on the slide velocity.

7.2. Choice of parameters and their range

7.2.1. Selected parameters

The main parameters involved in the dynamic analysis of a landslide are listed in Section 6.3.2. Of these, the properties that are bound to exhibit more variability for different landslide cases will be chosen hereafter as parameters for our study. A set of representative combinations of such parameters will be chosen to carry out velocity simulations using the infinite slope model. The results will then be analysed in order to assess the relative importance of the involved parameters in making the slide prone to catastrophic collapse (cf. Section 7.4).

Among all the model parameters, we will surely include in our analysis those describing the geometry of the infinite slope: the slide thickness (or depth) H and the slope inclination β which are standard stability analysis quantities, along with the less common shearband thickness d, introduced with the thermo-mechanical model. Regarding the geotechnical properties of the soil, we will consider as variables κ, λ and Γ, whose range is quite well established. The effects of material friction-softening (whose importance to the slide dynamics has already been established in the back-analyses carried out in Sections 5.5.7.4 and 6.3.5) will be taken into account through the critical state, residual static and residual dynamic friction angles ϕ_{cs}, ϕ_{rs} and ϕ_{rd} as well as the static and dynamic softening rates a_1 and a_2. Finally, we will include in the analysis the soil permeability k_w, expected to affect the pore pressure diffusion, and the material parameter γ since, despite the uncertainties in its determination, it allows us to explore the impact of the newly introduced mechanism of thermo-plastic softening in the dynamical behaviour of landslides.

7.2.2. Range of selected parameters

After selecting the variables to be examined in our analysis, realistic ranges for them must be established.

We shall consider $5 \le H \le 250$ m, 5 metres being a reasonable lower-bound value and 250 m representing the maximum depth at which a slip plane has been detected in deep-seated slides (Petley and Allison, 1996). The range chosen for the slope inclination, expected to affect the driving force due to gravity, is $15 \le \beta \le 35\,°$ (cf. landslide database in the Appendix and Section 2.1.4) while for the shearband thickness we assume $0.3 \le d \le 3$ mm, based on the observations by Vardoulakis (2002a) that this value should be a few hundreds of micrometres, the value of 1.4mm chosen for Vajont (Section 2.3.4) being a mid-range setting. Based on the measured properties of three typical clayey soils (cf. Schofield and Wroth, 1968) as seen in Table 7, we can set $3\times10^{-2} \le \kappa \le 6\times10^{-2}$, $9\times10^{-2} \le \lambda \le 2.6\times10^{-1}$ and $2.8 \le \Gamma \le 3.8$. The ranges of characteristic friction angles may be determined on the basis of the available data from shear tests on clays (cf. Skempton, 1985, and Section 2.1.4): $20 \le \phi_{cs} \le 32\,°$,

$10 \le \phi_{rs} \le 20$ ° and $4 \le \phi_{rd} \le 10$ °. The rates of friction-softening, on the other hand, have hardly ever been estimated in the literature, hence we will select for both a_1 and a_2 a broad range, representing all possible scenarios spanning from the extremely slow to the very sudden softening case: $10^{-5} \le a_1 \le 10^{3}$, $10^{-5} \le a_2 \le 10^{3}$. From the few available data on the friction-softening behaviour of clays (Skempton, 1985, Lehane and Jardine, 1992 and Tikka and Hutchinson, 1999) we may deduce that a reasonable mid-range value for both a_1 and a_2 is 0.1, as proposed by Vardoulakis (2002a) for the Vajont clay. Permeability is assumed to vary as $10^{-13} \le k_w \le 10^{-6}$ m/s, the upper-bound value representing fissured clays (cf. Powrie, 1997) and the lower-bound one representing a uniform clay whose permeability has decreased due to prolonged shearing and consequent alignment of the platy particles parallel to the direction of motion (Vardoulakis, 2000). The range chosen for the parameter γ of the thermoplastic model is $10^{-3} \le \gamma \le 10^{-1}$, in agreement with the range experimentally observed whilst ensuring the calculation of realistic values for the pressurisation coefficient (cf. Section 5.5.3.6).

7.2.3. Parameters that are kept constant

The parameters involved in the landslide model (Section 6.3.2) that do not exhibit in nature a high variability, or that are not expected to influence the results with their variation will be kept constant in our parametric analysis. In particular, the soil thermal properties β_s, k_m and C_f are assigned a mean value which is typical of clays (Section 6.3.2), the Poisson's ratio ν is set equal to the mean value 0.3 and the rate of thermal-friction softening $\tilde{g}$ is set to zero, due to the lack of information on this phenomenon and to its ascertained secondary importance to static and dynamic material friction softening (Section 5.5.7.4). The reference temperature θ_{ref} can be set to 20°C, representing a mean value between the initial temperature of the Vajont simulation and that of the Jiufengershan simulation. The compressibility of water c_w, the unit weight of water γ_w and the unit weight of the overburden γ_s are assigned the same values as in Section 6.3.2, which can be considered representative of average conditions.

7.3. Generalisation of initial conditions

The static analysis leading to the determination of incipient failure conditions for the infinite slope as presented in Section 6.1.1 is appropriate for the back-analysis of Jiufengershan, but lacks generality as far as the assumed groundwater conditions are concerned. With the twofold purpose of being able to better explore the slope parameters' space and of being more representative of a sample planar landslide, we will now consider the slope to be waterlogged, with a generic seepage angle α_s. This situation is illustrated in Figure 92, showing a long slope of inclination β through which water flows at inclination α_s. The intersection of the equipotential with the top flowline determines the relevant equipotential level h_w, i.e. the level that water would reach in an open-end standpipe. From the geometry of Figure 92, the following trigonometric relationship can be deduced (cf. Bolton, 1991):

$$\frac{\mathrm{BC}}{\mathrm{BD}}=\frac{h_w}{H/\cos\beta}=\frac{1}{1+\tan\alpha_s+\tan\beta}. \tag{7.2}$$

The above can be employed to calculate the pore pressure $u_H=\gamma_w h_w$ as a function of the seepage angle, as

$$u_H=\frac{\gamma_w H}{\left(1+\tan\alpha_s+\tan\beta\right)\cos\beta}. \tag{7.3}$$

Substituting the above in the incipient failure condition for the infinite slope (6.4) yields

$$\tan\phi'_{mob}=\frac{\tan\beta}{\left[1-\dfrac{\gamma_w}{\gamma\left(\cos\beta\right)^2\left(1+\tan\alpha_s\tan\beta\right)}\right]}. \tag{7.4}$$

In the above, both the critical state friction angle, corresponding to ϕ'_{mob} and the slope angle β are selected parameters for our parametric analysis (Section 7.2.1). Incipient failure conditions will be therefore determined by calculating the seepage angle that satisfies (7.4), all other values being fixed. This can be done by solving Equation (7.4) for α_s, hence obtaining the following expression:

$$\alpha_s=\arctan\left\{\frac{\tan\phi'_{mob}\left[-\gamma+\gamma_w\left(1+\tan^2\beta\right)\right]+\gamma\tan\beta}{\gamma\tan\beta\left(\tan\phi'_{mob}-\tan\beta\right)}\right\} \tag{7.5}$$

where $-90°\le\alpha_s\le 90°$. The seepage angle α_s is taken zero at the horizontal and positive clockwise. The case of stabilising seepage ($90°\le\alpha_s\le 180°$) is admitted in our parametric analysis, in order to respect the incipient failure condition (7.4) when the slope angle β is chosen to be larger than the friction angle ϕ'_{mob}. Although rather unrealistic, the case $\beta>\phi'_{mob}$ is included in our parametric analysis since we investigate the influence of both β and ϕ'_{mob} independently, and the incipient failure conditions will not anyway affect the results of our dynamical (post-failure) study (Section 7.4). If

$\beta > \phi'_{mob}$ the resulting α_s will be greater than 90°, however, due to the nature of function arctangent, Equation (7.5) yields $\alpha_s = \alpha_{neg} < 0$ instead. This limitation is overcome numerically by setting, whenever $\beta > \phi'_{mob}$,

$$\alpha_s = \pi + \alpha_{neg}, \tag{7.6}$$

which allows us to calculate the correct value of $\alpha_s \in [90°, 180°]$.

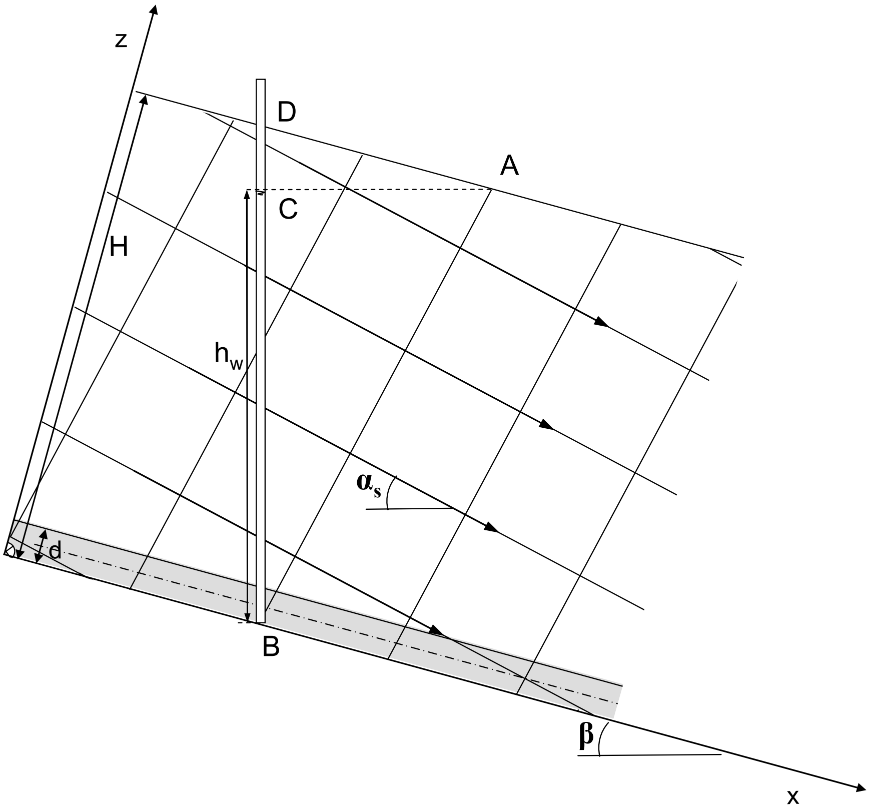

Figure 92. Scheme of an infinite slope of inclination *β* through which water is flowing at inclination *α_s*. An open-end standpipe is represented to highlight the equipotential level relevant to points situated along segment AB.

As discussed in Section 6.1.1, with the initial configuration described by Equation (6.4) a perturbation of the incipient failure conditions is needed to trigger the movement of the slide. This can be done by increasing by a small Δu_H the limit equilibrium value of u_H, as obtained by substituting (7.5) into (7.3). For example, we may set $\Delta u_H = 0.01$ Pa.

7.4. Parametric analysis

7.4.1. Factorial vs. Taguchi analysis

With the parametric analysis we aim to explore systematically the influence of all 13 factors described in Section 7.2.1 in the dynamical evolution of a landslide. In other words, we ideally want to run one infinite slope simulation for each of the possible combinations of the selected parameters, and analyse the results statistically to determine which factors are most influential in causing large slide velocities. Since the involved parameters are continuously measurable variables, for each of them we need to define the levels, i.e. the set of values that each parameter can assume (within the respective range) during our study. For a first-attempt, general-purpose analysis, we can reasonably select three levels for each parameter, that will enable us to effectively explore the impact of the variables: the upper-bound, the lower-bound and a mid-range value. Considering the physics of the problem at hand, this choice is justified by the likelihood that the variables involved will have a more quantifiable effect in the results when they are set to an extreme value, the mid-range setting being useful to evaluate any non-linearity that may arise over each parameter's range. The 13 parameters discussed in Section 7.2.1 are summarised in Table 8, along with the 3 selected levels "min", "med", "max" (cf. Section 7.2.2).

Table 8. Parameters selected for the parametric study and their levels.

Parameter	**Level**			**Units**
	min	**med**	**max**	
Slope inclination: β	15	25	35	degrees
permeability: k_w	1.00E-013	1.00E-009	1.00E-006	m/s
Slide thickness: H	5	130	250	m
Slip zone thickness: d	3.00E-004	1.00E-003	3.00E-003	m
Thermal softening parameter: γ	1.00E-003	1.00E-002	1.00E-001	-------
Critical state fric. angle.: φ_{cs}	20	25	32	degrees
Static res. fric. angle: φ_{rs}	10	15	20	degrees
Dynamic res. fric. angle: φ_{rd}	4	8	10	degrees
Static softening parameter: a_1	1.00E-05	0.1	1.00E+03	-------
Dynamic softening parameter: a_2	1.00E-05	0.1	1.00E+03	-------
Specific volume intercept: Γ	2.8	3.2	3.8	-------
Slope of κ-line: κ	3.00E-02	4.50E-02	6.00E-02	-------
Slope of λ-line: λ	9.00E-02	1.70E-01	2.60E-01	-------

In order to design our parametric analysis we may resort to the concepts of Experimental Design, a branch of Engineering Statistics that deals with deliberately changing one or more variables in a process, in order to observe the effect that the changes have on one or more response variables (e.g. see NIST/SEMATECH, 2003). In our case, the process is the landslide simulation, the variables are the 13 selected parameters, and the response variable is the calculated velocity after 10 seconds from slide initiation.

Once the significant process variables have been selected together with the relevant levels, the type of experimental design must be chosen, among the many available, based on the objectives of the experiment and the number of factors to be investigated. The most straightforward method is a design in which every setting of every factor appears with every setting of every other factor, called the full factorial method. This implies running an experiment (i.e. a simulation) for each of the possible combinations of parameters. The number of needed experiments in this case is N^p, where N is the number of levels chosen for each variable and p the number of variables. With the settings of Table 8, the number of simulations that we need for a full factorial analysis is then $3^{13} = 1{,}594{,}323$. Considering that the computational time for a 10-seconds simulation with our infinite slope numerical code varies between 1 minute and 1 week, depending on the resulting time-step from the stability analysis (in turn depending on the value of key parameters such as the permeability k_w and the shearband thickness d, cf. Section 5.5.5), a full factorial analysis is impractical.

Several other methods are available in the literature, notably the ‘randomised’ and the ‘fractional factorial’ designs (e.g. see NIST/SEMATECH, 2003), involving a reduction of the needed number of experiments compared to a full factorial analysis. While the randomised design, if applied to our case, may lead to an incorrect interpretation of the physical phenomena involved, a fractional factorial analysis would be extremely complicated from the point of view of statistical design, whilst not necessarily allowing us to save much computational time.

The method that was found to best suit our purposes due to its robustness, flexibility and simplicity, is the renowned Taguchi method (e.g., Taguchi et al., 1989, Peace, 1993). The experimental strategy within the framework of Taguchi is based on orthogonal arrays (Section 7.4.2), defining the number of experiments needed to explore all statistically significant parameters’ combinations. With our settings of 13 parameters and 3 levels (Table 8), a Taguchi analysis will need only 27 simulations to be completed, to which some basic statistical analysis of results will have to follow. The practicality of this method is apparent, also considering that it is possible to perform verification runs (see Section 7.4.2.2) to double-check the reliability of the analysis' results. We elaborate on the Taguchi method in the next section.

7.4.2. A general Taguchi analysis

The theory of the Taguchi experimental design will be illustrated hereafter, alongside its application to the infinite slope parametric analysis outlined in Table 8.

A fundamental step in the design of our analysis is the definition of a suitable orthogonal array, i.e., a 2-dimensional matrix defining the variables' settings for each of the experiments needed. Each row of the matrix contains the list of settings for all parameters in one experiment. Each column corresponds to one of the variables, and contains all the values that this variable will be assigned during the experiments. As an example a generic orthogonal array for a 3-variable, 2-level analysis is reported in Table 9, where α, β and γ indicate the variables, the *H*'s and *L*'s the two levels decided for each parameter (e.g. a 'high' and 'low' value within a range) and the numbers on the leftmost column denote the number of experimental runs (or equivalently, the number of combinations of factors). We observe that in this sample scenario only 4 runs are needed to explore the significant combinations of 3 parameters with two levels, instead of the 2^3=8 runs needed in a full factorial analysis.

Table 9. Sample orthogonal array containing the settings for a 3-parameter, 2-level analysis.

Experiment n.\ **parameter**	**α**	**β**	**γ**
1	L_α	L_β	L_γ
2	L_α	H_β	H_γ
3	H_α	L_β	H_γ
4	H_α	H_β	L_γ

Orthogonal arrays must respond to specific requirements, and they cannot be created with any chosen combination of parameters and levels. The fundamental property of these matrices is statistical independence (Peace, 1993): not only within each column is present an equal number of occurrences for each level (e.g. in Table 9, in each column both level *H* and level *L* appear twice), but also the columns are interrelated (orthogonal) between one another; i.e. for each level within one column, each level within any other column will occur an equal number of times as well. The latter property is better illustrated by looking at a bigger orthogonal array such as that reported in Table 10: by looking for example at column γ, we see that factor γ occurs 4 times at level *L* and four times at level *H*. If we now look at column α we see that for γ at level *L*, factor α is set to level *L* twice and to level *H* twice. Likewise, for γ at level *H* factor α is set to level *L* twice and to level *H* twice. By looking at column ε we notice the same relationship between columns γ and ε. This property holds between all columns of all orthogonal arrays and is crucial to statistical independence. As we will see in Section 7.4.2.1 with the level average analysis, a factor has a strong impact on the output variable if the results associated with one of its levels are very different from the results associated with another one of its levels. Since, due to the orthogonality between columns described above, the levels of the other factors occur an equal number of times for each level of the strong factor, any effect of these other factors will be cancelled out in the computation of the effect of the strong factor. This implies that an estimation of the effect of any one particular factor will tend to be accurate and reproducible, because the estimated effect does not include the influence of other factors (Peace, 1993).

Table 10. Orthogonal array for a 7-parameter, 2-level analysis where the levels in three samples columns are shaded with different tones to illustrate the feature of orthogonality between columns.

Experiment n.\ **parameter**	**α**	**β**	**γ**	**δ**	**ε**	**ζ**	**η**
1	L_α	L_β	L_γ	L_δ	L_ε	L_ζ	L_η
2	L_α	L_β	L_γ	H_δ	H_ε	H_ζ	H_η
3	L_α	H_β	H_γ	L_δ	L_ε	H_ζ	H_η
4	L_α	H_β	H_γ	H_δ	H_ε	L_ζ	L_η
5	H_α	L_β	H_γ	L_δ	H_ε	L_ζ	H_η
6	H_α	L_β	H_γ	H_δ	L_ε	H_ζ	L_η
7	H_α	H_β	L_γ	L_δ	H_ε	H_ζ	L_η
8	H_α	H_β	L_γ	H_δ	L_ε	L_ζ	H_η

The usual nomenclature for describing orthogonal arrays is $L_A(B^C)$, where A denotes the number of experimental runs (i.e., of combinations of factors) needed, B identifies the number of levels within each column and C represents the number of columns (i.e., of parameters) of the matrix. Each orthogonal array is characterised by a certain number of degrees of freedom *D*, denoting the number of comparisons between factors required, and can be calculated as $D = (\mathrm{B}-1)\cdot\mathrm{C}$. In standard orthogonal arrays, the rule $\mathrm{A} = D + 1$ also applies, so the number of combinations needed is a function of the number of levels and of that of parameters: $A = 1 + (B-1) \cdot C$. This is straightforward to verify, for example, in the $\mathrm{L}_4\left(2^3\right)$ array of Table 9 and the $\mathrm{L}_8\left(2^7\right)$ array of Table 10.

The Taguchi method also requires to account for any interactions between factors, defined as the situations in which two or more factors acting together have a different effect on the output variable than the effect of each factor acting individually: potential interactions should be identified and appropriately modelled in the orthogonal array (a special procedure is needed to account for the interaction between factors). In order to avoid this complication, the parameters and the relative levels for our analysis were chosen (Section 7.2) with the aim of avoiding interactions. For example, the ranges of the three friction angles ϕ_{cs}, ϕ_{rs} and ϕ_{rd} were chosen contiguous, but not overlapping. Moreover, the lower-bound level of the friction-softening rates a_1 and a_2 was chosen very small but not zero, otherwise during the experiments it would rule out the effect of the residual friction angles, thus giving rise to an unnecessary interaction.

Having made sure to avoid interactions in our design, which we are anyway able to double-check with confirmation runs at the end of our analysis, we may now look for a suitable array to carry out our 13-parameter, 3-level analysis (cf. Table 8). Fortunately, the conventional orthogonal array $\mathrm{L}_{27}\left(3^{13}\right)$ is readily available in the literature, and can be filled in with our factors' settings to finalise the design of our parametric study. The resulting array is shown in Table 11, where a column has been added at the extreme right to specify the output of the simulations for each row, i.e., the calculated slide velocities after 10s from triggering. These rather heterogeneous velocity values constitute the 'raw data' of the Taguchi parametric study, to which some statistical post-processing needs to be applied in order to extract the results of our analysis, as will be shown in the next Section.

7.4.2.1. Level average analysis

The statistical technique called level average analysis is appropriate for interpreting the experiment data when, like in our case, the monitored factors have been defined in terms of continuously measurable variables. The scope of level average analysis is to identify the strongest effects, and determine the combination of factors affecting the target variable the most (Peace, 1993).

First, we must calculate the average simulation result for each level of each factor. This is performed by taking the arithmetic mean, for each column, of the results v_i pertaining to a specific level only, and repeating this procedure for each level of each column. In our case, with reference to Table 11, we may calculate the average result for factor β, at level "min" (corresponding to β=15°) as follows:

$$\begin{aligned}&\bar{\beta}_{\min} = \left(\sum_{i=1}^{9} v_i\right)\bigg/ 9 = \\ &= \frac{1.52+17.94+18.68+17.24+18.55+2.32+13.45+0.85+18.69}{9} = \\ &= 12.14 \text{ m/s.}\end{aligned} \tag{7.7}$$

Similarly, the average result for factor β at level "med" (corresponding to β=25°) is

$$\bar{\beta}_{\text{med}} = \left(\sum_{i=10}^{18} v_i\right)\bigg/ 9 = 20.63 \text{ m/s}, \tag{7.8}$$

and that for the same factor at level "max" (corresponding to β=35°) is

$$\bar{\beta}_{\max} = \left(\sum_{i=19}^{27} v_i\right)\bigg/ 9 = 29.48 \text{ m/s}. \tag{7.9}$$

Next, the effect of factor β is quantified by taking the absolute difference $\Delta\beta$ between the highest and lowest average results:

$$\Delta\beta = \left|\bar{\beta}_{\min} - \bar{\beta}_{\max}\right| = 17.34 \text{ m/s}. \tag{7.10}$$

We remark that in this type of analysis the average result corresponding to the "max" parameter setting is not necessarily the highest and that corresponding to the "min" setting the lowest. Any of the average results could be the highest. In fact, by calculating in the same way the average results for the soil permeability (from the second column of the array in Table 11) we obtain:

$$\bar{k}_{w,\min} = \left[\left(\sum_{i=1}^{3} v_i\right) + \left(\sum_{i=10}^{12} v_i\right) + \left(\sum_{i=19}^{21} v_i\right)\right]\bigg/ 9 = 27.46 \text{ m/s} \tag{7.11}$$

$$\bar{k}_{w,\text{med}} = \left[\left(\sum_{i=4}^{6} v_i\right) + \left(\sum_{i=13}^{15} v_i\right) + \left(\sum_{i=22}^{24} v_i\right)\right]\bigg/ 9 = 16.61 \text{ m/s} \tag{7.12}$$

$$\bar{k}_{w,\max} = \left[\left(\sum_{i=7}^{9} v_i\right) + \left(\sum_{i=16}^{18} v_i\right) + \left(\sum_{i=25}^{27} v_i\right)\right]\bigg/ 9 = 18.18 \text{ m/s}. \tag{7.13}$$

The resulting effect of parameter k_w is

$$\Delta k_w = \left|\bar{k}_{w,\min} - \bar{k}_{w,\max}\right| = 10.85 \text{ m/s}. \tag{7.14}$$

As a further example, calculating the same quantities for parameter a_2 (corresponding to the tenth column of the array in Table 11) yields:

$$\bar{a}_{2,\min} = \frac{v_1 + v_6 + v_8 + v_{11} + v_{13} + v_{18} + v_{21} + v_{23} + v_{25}}{9} = 16.77 \text{ m/s} \tag{7.15}$$

$$\overline{a}_{2,\mathrm{med}} = \frac{v_2+v_4+v_9+v_{12}+v_{14}+v_{16}+v_{19}+v_{24}+v_{26}}{9} = 24.73\ \mathrm{m/s} \tag{7.16}$$

$$\overline{a}_{2,\max} = \frac{v_3+v_5+v_7+v_{10}+v_{15}+v_{17}+v_{20}+v_{22}+v_{27}}{9} = 20.75\ \mathrm{m/s} \tag{7.17}$$

The resulting effect of parameter a_2 is smaller than the previous two:

$$\Delta a_2 = \left|\overline{a}_{2,\min} - \overline{a}_{2,\mathrm{med}}\right| = 7.96\ \mathrm{m/s}\,. \tag{7.18}$$

The same procedure is followed for each of the remaining 10 parameters of Table 11, and the results are summarised in the response table (Table 12).

The next step is to identify the strong effects, by ranking the factors from the largest to the smallest absolute difference. This is done in the last row of Table 12, and constitutes the main result of our parametric analysis.

A rule of thumb of level average analysis is to consider roughly the top half of the ranked parameters to have a significant impact on the results (Peace, 1993). We may consider the top-five factors as those that surely have a significant influence in the slide velocity, namely (1) the static friction-softening rate a_1, (2) the slope inclination β, (3) the soil permeability k_w, (4) the dynamic residual friction angle ϕ_{rd} and (5) the slide thickness *H*. This choice is demonstrated to be a valid one by the reliability check performed in the next section.

7.4.2.2. Reliability check

It is now possible to perform a check on the reliability of our statistical study by computing an estimate of the predicted response based on the above selected levels of the dominant parameters (Peace, 1993).

First, we compute the overall average $\overline{v}$ from the results of Table 11 as

$$\overline{v} = \sum_{i=1}^{27} v_i = 20.75\ \mathrm{m/s}\,. \tag{7.19}$$

Next, we calculate a predicted average velocity $\overline{v}^*$, quantity that incorporates the effect on the overall average of each one of the 5 dominant factors (Peace, 1993):

$$\begin{aligned}\overline{v}^* = \overline{v} + \left(\overline{a}_{1,\max} - \overline{v}\right) + \left(\overline{\beta}_{\max} - \overline{v}\right) + \left(\overline{k}_{w,\min} - \overline{v}\right) + \\ + \left(\overline{\phi}_{rd,\min} - \overline{v}\right) + \left(\overline{H}_{\max} - \overline{v}\right) = 56.22\ \mathrm{m/s}\end{aligned} \tag{7.20}$$

In other words, $\overline{v}^*$ is the average $\overline{v}$ plus all the fluctuations from the average $\overline{v}$ caused by setting the dominant parameters to their most influential values. Since all such fluctuations are positive, $\overline{v}^*$ is larger than $\overline{v}$. The numerical results from the most influential parameter settings employed in (7.20), corresponding to the lowest setting for k_w and ϕ_{rd} and the highest setting for a_1, β and H, are shaded in Table 12. By calculating $\overline{v}^*$ we statistically simulate the case scenario that maximises the slide velocity, thus providing a prediction for the most dangerous parameters settings.

The final step of our reliability check is to conduct a confirmation run with the infinite slope code, by adopting the most influential parameter settings identified above while setting all remaining parameters to their mid-range level (Table 13). Our parametric analysis can be considered successful if the result v_c of the confirmation run is higher than the overall average $\overline{v}$, and reasonably close to the prediction average $\overline{v}^*$.

The velocity after 10s from triggering resulting from our confirmation run is $v_c = 51.2$ m/s. We observe that this value is very close to that calculated in (7.20), especially if compared to the much larger fluctuations from the average exhibited by the results of Table 11.

In order to check the validity of our choice to consider only the top five parameters in the ranking of Table 12 as the significant ones in the catastrophic evolution of a slide, we can now consider significant the top seven parameters instead, thus including also factors a_2 and κ in the calculation of the prediction average, and check whether their impact is strong enough to yield a prediction average closer to the confirmation run's result. Following the above outlined procedure, in this case we obtain $\overline{v}^* = 64.4$ m/s. The confirmation run, carried out by adopting the most influential parameter settings of the above top seven parameters, yields $v_c = 52$ m/s. The much wider discrepancy between these two values corroborates our initial choice of considering significant only the first 5 factors.

We may conclude that indeed, the important factors in making a slope prone to catastrophic failure are a_1, β, k_w, ϕ_{rd} and H.

7.4.2.3. Discussion of the results

The outcome of our parametric study is the ranking in order of importance of the involved landslide properties in causing catastrophic sliding, as reported in Section 7.4.2.1: among all the classified parameters, the first 5 can be deemed to have a key role in maximising the landslide velocity.

Table 11. Orthogonal array for the infinite slide parametric analysis.

Exp/param	β	k_w	H	d	γ	φ_{cs}	φ_{rs}	φ_{rd}	a_1	a_2	Γ	k	λ	Results: velocity *v* after 10s (m/s)
1	15	1.00E-13	5	3.00E-04	1.00E-03	20	10	4	1.00E-05	1.00E-05	2.8	3.00E-02	9.00E-02	1.52
2	15	1.00E-13	5	3.00E-04	1.00E-02	25	15	8	1.00E-01	1.00E-01	3.2	4.50E-02	1.70E-01	17.94
3	15	1.00E-13	5	3.00E-04	1.00E-01	32	20	10	1.00E+03	1.00E+03	3.8	6.00E-02	2.60E-01	18.68
4	15	1.00E-09	130	1.00E-03	1.00E-03	20	10	8	1.00E-01	1.00E-01	3.8	6.00E-02	2.60E-01	17.24
5	15	1.00E-09	130	1.00E-03	1.00E-02	25	15	10	1.00E+03	1.00E+03	2.8	3.00E-02	9.00E-02	18.55
6	15	1.00E-09	130	1.00E-03	1.00E-01	32	20	4	1.00E-05	1.00E-05	3.2	4.50E-02	1.70E-01	2.32
7	15	1.00E-06	250	3.00E-03	1.00E-03	20	10	10	1.00E+03	1.00E+03	3.2	4.50E-02	1.70E-01	13.45
8	15	1.00E-06	250	3.00E-03	1.00E-02	25	15	4	1.00E-05	1.00E-05	3.8	6.00E-02	2.60E-01	0.85
9	15	1.00E-06	250	3.00E-03	1.00E-01	32	20	8	1.00E-01	1.00E-01	2.8	3.00E-02	9.00E-02	18.69
10	25	1.00E-13	130	3.00E-03	1.00E-03	25	20	4	1.00E-01	1.00E+03	2.8	4.50E-02	2.60E-01	29.25
11	25	1.00E-13	130	3.00E-03	1.00E-02	32	10	8	1.00E+03	1.00E-05	3.2	6.00E-02	9.00E-02	33.45
12	25	1.00E-13	130	3.00E-03	1.00E-01	20	15	10	1.00E-05	1.00E-01	3.8	3.00E-02	1.70E-01	13.75
13	25	1.00E-09	250	3.00E-04	1.00E-03	25	20	8	1.00E+03	1.00E-05	3.8	3.00E-02	1.70E-01	20.02
14	25	1.00E-09	250	3.00E-04	1.00E-02	32	10	10	1.00E-05	1.00E-01	2.8	4.50E-02	2.60E-01	7.8
15	25	1.00E-09	250	3.00E-04	1.00E-01	20	15	4	1.00E-01	1.00E+03	3.2	6.00E-02	9.00E-02	33.36
16	25	1.00E-06	5	1.00E-03	1.00E-03	25	20	10	1.00E-05	1.00E-01	3.2	6.00E-02	9.00E-02	4.00E-05
17	25	1.00E-06	5	1.00E-03	1.00E-02	32	10	4	1.00E-01	1.00E+03	3.8	3.00E-02	1.70E-01	35.85
18	25	1.00E-06	5	1.00E-03	1.00E-01	20	15	8	1.00E+03	1.00E-05	2.8	4.50E-02	2.60E-01	12.15
19	35	1.00E-13	250	1.00E-03	1.00E-03	32	15	4	1.00E+03	1.00E-01	2.8	6.00E-02	1.70E-01	53.25
20	35	1.00E-13	250	1.00E-03	1.00E-02	20	20	8	1.00E-05	1.00E+03	3.2	3.00E-02	2.60E-01	33.89
21	35	1.00E-13	250	1.00E-03	1.00E-01	25	10	10	1.00E-01	1.00E-05	3.8	4.50E-02	9.00E-02	45.4
22	35	1.00E-09	5	3.00E-03	1.00E-03	32	15	8	1.00E-05	1.00E+03	3.8	4.50E-02	9.00E-02	1.11
23	35	1.00E-09	5	3.00E-03	1.00E-02	20	20	10	1.00E-01	1.00E-05	2.8	6.00E-02	1.70E-01	0.69
24	35	1.00E-09	5	3.00E-03	1.00E-01	25	10	4	1.00E+03	1.00E-01	3.2	3.00E-02	2.60E-01	48.38
25	35	1.00E-06	130	3.00E-04	1.00E-03	32	15	10	1.00E-01	1.00E-05	3.2	3.00E-02	2.60E-01	34.53
26	35	1.00E-06	130	3.00E-04	1.00E-02	20	20	4	1.00E+03	1.00E-01	3.8	4.50E-02	9.00E-02	45.51
27	35	1.00E-06	130	3.00E-04	1.00E-01	25	10	8	1.00E-05	1.00E+03	2.8	6.00E-02	1.70E-01	2.58

Table 12. Response table of our 13-parameter landslide model Taguchi analysis.

RESPONSE TABLE (slide velocity in m/s after t=10 seconds from triggering)													
Level/par.	β	k_w	H	d	γ	φ_{cs}	φ_{rs}	φ_{rd}	a_1	a_2	Γ	k	λ
Min	12.14	27.46	15.15	20.22	18.93	19.06	21.53	27.81	7.09	16.77	16.05	25.02	21.95
Med	20.63	16.61	21.91	24.29	21.61	20.33	20.61	17.45	25.88	24.73	22.83	19.44	17.76
Max	29.48	18.18	25.19	17.74	21.70	22.85	18.78	16.98	29.27	20.75	22.05	17.79	22.53
Effect of parameter (Delta)	**17.34**	**10.85**	**10.04**	**6.56**	**2.77**	**3.79**	**2.74**	**10.83**	**22.18**	**7.96**	**6.77**	**7.23**	**4.77**
Ranking	**2**	**3**	**5**	9	12	11	13	**4**	**1**	6	8	7	10

Table 13. Parameter settings for the confirmation run of our general Taguchi analysis.

Exp/param	β_{max}	$k_{w,min}$	H_{max}	d_{med}	γ_{med}	$\varphi_{cs,med}$	$\varphi_{rs,med}$	$\varphi_{rd,min}$	$a_{1,max}$	$a_{2,med}$	Γ_{med}	k_{med}	λ_{med}
Confirmation run	35	1.00E-13	250	1.00E-003	1.00E-002	25	15	4	1.00E+03	0.1	3.2	4.50E-02	1.70E-01

The worst-case scenario for a planar slide is represented by the parameter combination of Table 13: a potentially unstable slope is bound to be most catastrophic if the soil's static softening rate, the inclination and the thickness of the slope are very large, and the soil's permeability and dynamic residual friction angle are very small. Of these five properties, a_1, β and ϕ_{rd} are independent of thermal effects, thus constituting important factors in standard landslide analyses as well. The strong influence of a_1 and ϕ_{rd} is explained by observing that while thermal pressurisation needs a certain time to cause liquefaction, material friction-softening fully develops within a few centimetres of displacement after the initiation of movement (cf. Section 6.3.5, and Vardoulakis, 2002a). Besides, the slope inclination is understandably crucial in the landslide dynamics as it determines the magnitude of the driving force. On the other hand, parameters k_w and H deserve more attention, as they have been introduced by the thermo-mechanical model, and are not normally considered in landslide prevention practice. The most important one of the two parameters is k_w, which affects pore pressure diffusion: a low soil permeability implies a poor dissipation of the excess pore pressure within the shearband, thus promoting the reduction of shear resistance. The influence of parameter H, determining the amount of dissipation as anticipated in Section 7.1, is plausibly second to permeability: despite the amount of frictional heat that may be produced, if pore pressure does not build up no strength loss will be caused (in the absence of friction softening).

The above observations are useful as a guidance for field investigations on potentially unstable large slopes: by measuring or estimating the aforementioned five key properties, it is possible to determine whether or not the slope is bound to evolve catastrophically. The slope's inclination and depth of the slip plane may be easier to detect, while for a_1 and ϕ_{rd} it is necessary to collect samples and run laboratory tests, more specifically dynamic ring shear tests such as those performed by Tika and Hutchinson (1999). Despite the possibility to measure the permeability k_w in-situ, this should be avoided since the presence of fractures would lead to an overestimation of the shearband permeability, in turn leading to underestimation of thermal pressurisation. Moreover, the permeability of most clays is likely to decrease as the soil approaches residual state, due to the alignment of the platy particles parallel to the direction of motion (cf. Section 7.2.2). Thus, in order to obtain more sensible information it might be more appropriate to run a laboratory permeability test on a sample that has previously undergone prolonged shearing.

7.4.3. A Taguchi analysis focusing on thermo-mechanical effects

The analysis of Section 7.4.2.1 involved 13 parameters of different nature, that can be grouped into 'thermo-mechanical' and 'standard' parameters, depending on whether or not they are relevant of a thermo-mechanical analysis only, as opposed to a standard stability analysis. Some of the thermo-mechanical parameters, namely the shearband thickness d and the thermal softening parameter γ, have been left out of the list of key factors, as the level average analysis showed that their influence is weak. However, in cases where the standard parameters assume 'non-catastrophic' values (i.e., values that minimise the velocity such as moderate/absent friction softening and moderate slope angle) the thermo-mechanical factors will have a yet more important role in the catastrophic evolution of a slide. In order to corroborate the conclusions drawn in Section 7.4.2.3, it is useful to carry out a parametric study focused on the thermo-mechanical parameters only. This will also allow us to assess whether these parameters can be decisive in making catastrophic a slide that would be otherwise (i.e., with a standard analysis) predicted to be non-catastrophic. The analysis can be performed by means of a standard $L_9\left(3^4\right)$ orthogonal array, where thermo-mechanical factors k_w, H, d, γ are varied within the relevant ranges while the remaining 9 factors of Table 8 are kept constant.

7.4.3.1. Level average analysis

The 3 levels chosen for the 4 parameters are the same as those involved in the analysis of Section 7.4.2, whereas mid-range values are assigned to β, ϕ_{cs}, Γ, κ, λ and, in order to simulate a safer scenario in terms of loss of resistance to movement, friction-softening is ruled out by setting the relative rates to zero. With such settings (summarised in Table 14) we aim to explore the role of only thermo-mechanical phenomena in the catastrophic development of a slide, since the values assigned to the standard parameters, featuring in a standard dynamic equation would result in a slow slide acceleration.

As the number of experiments needed is now smaller, we may run longer simulations in order for the output to conform to the criterion for catastrophic velocity proposed in Section 7.1: the output velocity is that reached by the slide after 10 metres of displacement. The relative orthogonal array is reported in Table 15.

Next, following the procedure described in Section 7.4.2, a level average analysis is carried out, as summarised in Table 16.

Table 14. Parameter levels for the 4-parameter Taguchi analysis.

Parameters	**State**			**Units**
	Min	**Med**	**Max**	
Permeability: k_w	1.00E-013	1.00E-009	1.00E-006	m/s
Slide thickness: H	5	130	250	m
Slip zone thickness: d	3.00E-004	1.00E-003	3.00E-003	m
Th. softening parameter: γ	1.00E-003	1.00E-002	1.00E-001	-------
Fixed properties	**Value**			**Units**
Slope inclination: β	25			degrees
Peak fric. angle.: φ_p	25			degrees
Static res. fric. angle: φ_{rs}	-------			-------
Dynamic res. fric. angle: φ_{rd}	------			-------
Static softening parameter: a_1	0.00E+00			-------
Dynamic softening parameter: a_2	0.00E+00			-------
Specific volume intercept: Γ	3.2			-------
Slope of κ-line: κ	4.50E-02			-------
Slope of λ-line: λ	1.70E-01			-------

Table 15. Orthogonal array for the infinite slide 4-parameter analysis.

Exp/param	kw	H	d	γ	velocity at 10m (m/s)
1	1.00E-013	5	3.00E-004	1.00E-003	1.46
2	1.00E-013	130	1.00E-003	1.00E-002	6.02
3	1.00E-013	250	3.00E-003	1.00E-001	5.2
4	1.00E-009	5	1.00E-003	1.00E-001	0.82
5	1.00E-009	130	3.00E-003	1.00E-003	3.8
6	1.00E-009	250	3.00E-004	1.00E-002	1.97
7	1.00E-006	5	3.00E-003	1.00E-002	0.03
8	1.00E-006	130	3.00E-004	1.00E-001	1.62E-03
9	1.00E-006	250	1.00E-003	1.00E-003	1.23E-03

Table 16. Response of the level average analysis.

RESPONSE TABLE (slide velocity after 10m displacement)				
Lev/param	kw	H	d	γ
Min	4.227	0.770	1.144	1.754
Med	2.197	3.274	2.280	2.673
Max	0.011	2.390	3.010	2.007
Effect of parameter (Delta)	4.216	2.504	1.866	0.920
ranking	1	2	3	4

7.4.3.2. Results and discussion

The outcome of the level average analysis (Table 16) is indeed a confirmation of the results obtained from the 13-parameter analysis (13PA). The order of importance of the thermo-mechanical factors is: (1) permeability (which came third in 13PA), (2) slide thickness (which came fifth in 13PA), (3) shearband thickness (which came ninth in 13PA), (4) thermal softening parameter (which came twelfth in 13PA). In fact, the thermo-mechanical parameters alone can make the difference between a catastrophic and a non-catastrophic case: experiments 7, 8 and 9 in Table 15, in which permeability is high thus ruling out thermal pressurisation, yield values of velocity after 10m that are below the catastrophic velocity threshold of 0.05 m/s (cf. Section 7.1). In contrast, simulations 1-6 of Table 15 can be regarded as cases of ‘thermo-mechanical collapse’, i.e. cases in which the catastrophic evolution of the slide, when the velocity after 10m exceeds the threshold considered, is brought about by thermo-mechanical phenomena.

It is now worth recalling a rule of thumb of level average analysis (Section 7.4.2.1): due to the statistical nature of the results, only about half of the parameters in the ranking can be considered to have a significant effect (Peace, 1993). By examining the results of the above 4-parameter analysis in light of this criterion, we have confirmation that the only two properties which are worth determining for assessing the danger of thermo-mechanical collapse are the permeability of the soil and the thickness of the slide. Fortunately, these two properties coincide with the best-established and easiest ones to quantify in the field. The measurement of H implies the detection of an existing rupture surface or a reasonable assumption, based on local geology and in-situ conditions, of where a rupture surface would be expected to develop. The permeability k_w of the soil expected to be involved in shearing can be estimated by means of a specific permeability test (cf. Section 7.4.2.3). On the other hand, the shearband thickness is of uncertain determination and has hardly ever been directly measured (e.g. see Morgenstern and Tschalenko, 1967, Vardoulakis, 2002a and Section 2.3.4) and parameter γ would require non-standard thermally controlled triaxial tests (Laloui and Cekerevac, 2003).

The above observations allow us to conclude that, in order to assess whether a potentially unstable slope is bound to exhibit thermo-mechanical collapse, the depth of the slip plane and the permeability of the soil therein should be estimated or measured. We may estimate, as a guidance, that if the permeability falls in the (lower) range $10^{-9} \le k_w \le 10^{-13}$ m/s and the depth in the (higher) range $130 \le H \le 250$ m, there is a high risk of thermo-mechanical collapse; thus the slide may assume unexpectedly high velocities, despite possibly retaining its coherence of mass, and pose a higher threat to populations and the environment than expected from a traditional stability analysis. In fact, landslides of this type constitute a higher threat not only because, once rupture has taken place, they allow less time for evacuation of the population, but also for the potential creation of tsunamis or flood surges in case the mass comes into contact with a body of water.

On the other hand, it is rather difficult to employ the thermo-mechanical model to accurately predict the time evolution of the slide's velocity in the real case of a potentially unstable slope. This is because of the difficulty and cost of measuring all the relevant parameters before a landslide takes place, but also because a one-dimensional model cannot account for the numerous morphological constraints and inhomogeneities that influence the dynamical evolution of a slide. Nevertheless, for civil protection purposes it may be enough to calculate the order of magnitude of velocity that the slide can reach after a certain displacement. This could be done, within limits (Section 7.5), with the thermo-mechanical model presented in this work.

7.5. Limitations of the infinite slope model

Although most of the limitations of the infinite slope thermo-mechanical model have been already highlighted throughout this work, it is worth summarising them here, in order to better identify the future direction of research in this subject (cf. Chapter 8).

An evident drawback of the model is its inability to capture creep, which often precedes catastrophic collapse in large-scale, deep-seated landslides (cf. Section 2.1.4.2). In fact, the structure of the dynamic equation does not allow any velocity reduction or rate effects. For this reason, on the one hand the model is unable to predict stick-slip or decelerated types of movement, and on the other hand it cannot interpret excessively long run-out sliding, in which possibly viscous effects (along with topographical constraints) may prevent the velocity from increasing indefinitely. The model is reliable for interpreting the slide dynamics within a displacement interval that greatly depends on the specific case under study, but can be set as an example to about 200 metres for large, deep-seated landslides like Vajont. Another reason for which the model cannot be employed for velocity predictions beyond a certain run-out distance is that, rather frequently, beyond a threshold displacement, large-scale landslides transform into a flow-like phenomenon, implying the end of validity for the hypothesis of coherence of mass that allowed us to employ the block-on-slope model.

Furthermore, the inability of our model to capture creep is linked to the random nature of the triggering condition for the dynamic equation: a minute decrease $-\Delta\phi'$ of the mobilised friction angle (Section 6.1.1) or a minute increase Δu_H of the pore pressure (Section 7.3) is imposed to trigger the slide movement. Numerical experimentation was performed to assess the sensitivity of the model response to such incipient failure conditions. It was found that the predicted v_{10s} (velocity after 10s from triggering) is substantially affected by the value chosen for Δu_H if thermal pressurisation is not considered, i.e. in cases when the calculated v_{10s} is very small (order of magnitude of 10^{-6}-10^{-4} m/s), and negligibly affected when pressurisation is active and the calculated v_{10s} is large (order of magnitude of 10 m/s). More specifically, for a variation of Δu_H from 10^{-5} to 1 Pa, we obtain a variation in the predicted velocity of 0.01-5% (thus negligible to our purposes) for the cases when thermal pressurisation is considered, and of more than 100% when thermal pressurisation is ruled out. The sensitivity to the triggering condition Δu_H in any case diminishes for increasing slide thickness H and overburden's unit weight γ_s, as can be deduced by looking at the last term on the right hand side of Equation (7.1).

The above results make us reconsider the values of velocity after ten metres calculated in the last three rows of Table 15, when high permeability excludes thermal pressurisation, and lead us to conclude that although the calculated order of magnitudes are reliable, the values themselves are not. This in turn justifies our reluctance in adopting a (yet difficult to establish) threshold value for a catastrophic sliding velocity in our analysis (cf. Section 7.1); and further confirms that the most fruitful use of our model is estimating, by looking at a few key parameters, whether or not catastrophic collapse can occur, rather than predicting the timescale of the phenomenon.

We should finally remark that the model cannot be trusted if the predicted temperature exceeds the vaporisation threshold at the given pressure (cf. Section 5.5.7.1), as the thermo-dynamical assumptions behind the governing equations will cease to be valid. This has been checked for our simulations and proved never to be the case, although it might happen for cases of very thick and heavy overburden, higher friction angles and thinner shearbands. In such cases, the calculated values should be considered invalid as soon as vaporisation starts. This, however, would not necessarily affect the indicative value of the velocity predictions, as in most cases of thermo-mechanical collapse the acceleration of the slide evolves in the first few seconds and soon becomes constant, possibly before the temperature reaches the vaporisation threshold.

Chapter 8. Conclusions and future work

8.1. General conclusions

In this work we investigated the role of frictional heating in the development of catastrophic landslides. In particular:

- Landslide case histories and existing landslide models were critically reviewed, special attention being given to catastrophic landslides. For terrestrial landslides, typical ranges of certain soil properties such as residual static friction angles and of in-situ conditions like slope inclinations were identified, whereas other parameters (e.g. thermal-friction softening rates, residual dynamic friction angles) were found to be scarcely available in the literature. Furthermore, the most representative cases of coherent catastrophic landsliding were identified, among which the best-documented ones turned out to be the Vajont and Jiufengershan cases.
- Existing thermo-elasto-plastic constitutive soil models were reviewed. Due to its simpler formulation and the fewer material parameters, the model proposed by Laloui et al. (2005) was found to be the most suitable to be incorporated in a thermo-mechanical landslide model.
- A generalised thermo-plastic constitutive model was developed, based on re-deriving the constitutive law proposed by Laloui et al. (2005) in a standard plasticity framework, with a general stress space formulation. The model was then discretised using a refined explicit scheme, and validated by reproducing experimental thermo-mechanical loading paths.
- An improved landslide model based on that proposed by Vardoulakis (2002) was developed accounting for frictional heating, thermal pressurisation and including the above thermo-plastic generalised constitutive law for the soil. The model was discretised using an explicit scheme, and validated by successfully back-analysing the Vajont landslide. It also emerged that the newly introduced thermal friction softening mechanism is of secondary importance to the catastrophic acceleration of a slide compared to the better established mechanisms of static and dynamic material friction softening.

- The landslide model was generalised to an infinite slope geometry, discretised and validated by back-analysing the translational catastrophic landslide case of Jiufengershan.
- A parametric study to systematically investigate the development of catastrophic failure in uniform slopes was carried out. It was found that the most influential parameters in promoting catastrophic collapse are (1) the static friction-softening rate a_1, (2) the slope inclination β, (3) the soil permeability k_w, (4) the dynamic residual friction angle ϕ_{rd} and (5) the overburden thickness H. The most dangerous situation is when a_1, β and H are very large and k_w and ϕ_{rd} are very low. Of the above, 'thermo-mechanical parameters' k_w and H deserve more attention as they have been introduced by the thermo-mechanical model and are not normally considered in standard stability analyses of uniform slopes. A second parametric study was performed to demonstrate that thermo-mechanical parameters alone can make a difference between a relatively non-catastrophic event and a catastrophic one. Hence, further insight into the design of landslide risk mitigation measures is gained if, in addition to the standard site investigations, the permeability of the soil is measured and the depth of an existing or expected failure surface is measured or estimated respectively.

8.2. Recommendations for further research

A major limitation of the model developed in this work is that it disregards a landslide's creep-like activity before the final collapse phase, thus being unable to predict the overall timescale of a slide's failure. This may be overcome by integrating the model developed with another one that is able to interpret creep from a thermo-mechanical point of view, such as the analytical asymptotic model proposed by Veveakis et al. (2007). Coupling the two models would require special attention to the critical phase of transition between the creeping regime described by one model and the final collapse described by the other. A crack propagation analysis would probably be required to model the formation of the shearband and the evolution of its thickness.

A further enhancement could be brought about by generalising the above thermo-mechanical model to a 2-D finite element analysis. This may also involve the implementation of interface elements, for correctly modelling the interface between the two substructures constituted by the bedrock and the overburden. The shearband would be confined within the interface element and the same constitutive model for the interface element and the surrounding soil could be used.

The above improvements could lead to the development of a more general modelling tool, able to capture the dynamic emergence of progressive thermo-mechanical failure, from the inception of rupture to the final catastrophic collapse, in slopes of arbitrary geometry due to different initiation events.

Appendix

In the following, a database of relevant landslide case studies is presented. Each case study is summarised in a table and is assigned a number, for ease of reference in Section 2.1.4.

1) Jiufengershan landslide (Shou and Wang, 2003, Wang et al., 2003, Chang et al., 2005a, Chang et al., 2005b)

Type of sliding event	Rockslide/avalanche
Sliding characteristics	Translational slide consisting of large blocks that were rapidly broken up to form an avalanche as the material was pulverized in transit
Estimated dimensions of mobilized mass	Volume ~42 x 10^6 m^3. 50-60 m thick, 1.5 km long.
Run-out length	~1 km
Sliding speed	Estimated from model (Chang et al., 2005_a) max velocity: ~80 m/s
Physical and mechanical properties	Average properties of the *shale* involved in sliding: Density ρ=2500 Kg/m^3 Residual Cohesion c'_{rs}=25 kPa Friction angle φ'_{rs}=27.3°
Materials involved in sliding	Thick-bedded muddy sandstone with subordinate shale
Slip surface characteristics	Parallel to the bedding plane, alternating beds of dark gray shale and sandstone, with 1-6 cm thick clay seams intercalated in the alternating beds showing dip slip striations. The thickness of the shear zone is 1 mm-10 cm, mean value 1 cm (Chang et al., 2005_a)
Mineralogy of slip surface	The clay seams consist of quartz, feldspar, chlorite, illite and a small amount of likely chlorite/smectite mixed layer clay minerals (same minerals as host rock). A thin layer of pseudotachlyte (glass material) was observed along some areas of the basal shear surface. Chang et al. (2005a) suggest that this material was formed by frictional heating during the sliding process (minimum estimated temperature for pseudotachlyte formation 1100-1600 °C)
Extra information	• Evidence of high pore-pressures in the shear zone. • Evidence of frictional heating in the slip plane, as shown by the presence of a pseudotachylites along some areas of the basal shear surface, formed by frictional heating during the sliding process.

2) La Clapiere landslide (Sornette et al., 2004, Helmstetter et al., 2004, Cappa et al., 2004, Follacci et al., 1988)

Type of sliding event	Rockslide
Sliding characteristics	Slow, accelerating creep of coherent mass for decades. Rotational-like sliding shape (Follacci et al., 1988), multiple progressive fracturing.
Estimated dimensions of mobilized mass	Volume ~50 x 10^6 m^3. Width ~1000 m. 50 m high escarpment.
Run-out length	<100 m
Sliding speed	• Increase from 0.5 m/year in the 1950-1960 period to 1.5 m/year in the 1975-1982 period. • Dramatic increase between 1986 and 1988, up to 80 mm/day in summer 1987 and 90 mm/day in October 1987. • Decrease and stabilization in displacement rate (to some meters/year) since 1988 (Sornette et al., 2004)
Physical and mechanical properties	NA
Materials involved in sliding	Mostly gneiss rock
Slip surface characteristics	No defined slip surface. An 80 m-thick gneiss bed provides a stronger level compared with the rest of relatively weak and fractured gneiss; the two lithological entities are characterized by a change in mica content which is associated with a change of the peak strength (Follacci et al., 1988).
Mineralogy of slip surface	NA

3) Ok Ma dam 1984 landslide (Griffiths et al., 2004)

Type of sliding event	Rock and earth slide
Sliding characteristics	Repeated, short-reach downslope movement of coherent mass on pre-existing shear surfaces
Estimated dimensions of mobilized mass	Volume ~35 x 10^6 m^3.
Run-out length	~21 m
Sliding speed	Max. 5.2 m/h
Physical and mechanical properties	Average properties of some shear surfaces in the sliding mass: Assumed residual cohesion c'_{rs}=0 kPa Static residual friction coefficient φ'_{rs}=16° Liquid limit=38% Plastic limit=23%

Materials involved in sliding	Hard 40-100 m thick limestone rock-cap overlying 1000 m thick mudstone (bedded dark grey silty mudstone and clayey siltstone, with occasional calcareous beds)
Slip surface characteristics	Not uniquely defined shear surface
Mineralogy of slip surface	From a Clay-silt sample taken from a *possible shear zone*: 45% Clay, of which: 20% smectite 15% kaolinite 65% illite

4) Kuzulu landslide (Gokceoglu et al., 2005)

Type of sliding event	Landslide/earthflow
Sliding characteristics	Initial rotational failure followed by flow of the earth material from the accumulation zone
Estimated dimensions of mobilized mass	Volume ~12.5 x 10^6 m^3.
Run-out length	~1800 m
Sliding speed	Earthflow velocity ~6 m/s
Physical and mechanical properties	NA
Materials involved in sliding	Volcanic regolith
Slip surface characteristics	NA
Mineralogy of slip surface	NA

5) Shazou landslide (Zhou, 2000)

Type of sliding event	Landslide
Sliding characteristics	Short-reach sliding
Estimated dimensions of mobilized mass	Volume ~0.035 x 10^6 m^3. Width ~30-78 m, length ~25-50 m, thickness ~3-21 m
Run-out length	~6 m
Sliding speed	NA
Physical and mechanical properties	From probable shearplane: Cohesion $c'_{rs} = 0$ kPa friction coefficient $\varphi'_{rs} = 18°$
Materials involved in sliding	Silt-clay. Pebble-gravel, sand layers and eroded phyllite

Slip surface characteristics	NA
Mineralogy of slip surface	NA

6) Casanuova landslide (Catalano et al., 2000)

Type of sliding event	Earthslide
Sliding characteristics	Translational, reactivation of an old quiescent landslide
Estimated dimensions of mobilized mass	Thickness ~70 m, length ~ 1 km
Run-out length	200 m
Sliding speed	Max slip rate ~2 mm/day
Physical and mechanical properties	Cohesion $c'=0$ kPa Residual friction angle $\varphi'_{rs}=8°$
Materials involved in sliding	Destructured arenaceous and marly formations
Slip surface characteristics	Slickensided softened clay layer, 10-50 cm thick
Mineralogy of slip surface	NA

7) Caramanico landslide (Buccolini and Sciarra, 1996)

Type of sliding event	Complex (Rockslide/lateral spreads/flow)
Sliding characteristics	Rotational failure in reactivated area
Estimated dimensions of mobilized mass	Volume ~10^7 m^3
Run-out length	NA
Sliding speed	NA
Physical and mechanical properties	Marly clays of the substratum Unit weigth $\gamma=21.3\text{-}23.7$ kN/m^2 Water content ~10% Compressibility index=0.06-0.08 Liquid limit =32-74% Plasticity index ~50% Rsidual friction angle $\varphi'_{rs}=17.5°$
Materials involved in sliding	Series of marly-silty and arenaceous-sandy lythotypes
Slip surface characteristics	Marly clay
Mineralogy of slip surface	13-29 % $CaCO_3$

8) Valette landslide (Van Beek and Van Asch, 1996, Antoine et al., 1988)

Type of sliding event	Complex
Sliding characteristics	Succession of interrelated mass movements, rotational slide and earthflow
Estimated dimensions of mobilized mass	Depth of rotational slide ~20 m, total volume ~3 x 10^6 m^3
Run-out length	1 km for the earthflow
Sliding speed	Max ~1 m/day for the rotational landslide
Physical and mechanical properties	Residual friction angle φ_{rs}'=24.5° Residual cohesion c_{rs}'=0 kPa Plasticity index=10-25%
Materials involved in sliding	Flysch and moranic material
Slip surface characteristics	Remoulded moranic material (weathered "terres noires"), inclination 18°, depth 20 m
Mineralogy of slip surface	Calcite 20-40% Quartz 10-30% Illite 20-40% Chlorite 10-30%

9) Abbotsford landslide (Bell and Pettinga, 1988)

Type of sliding event	Landslip
Sliding characteristics	Two principal sliding blocks separated by a medial shear zone and a series of debris flows
Estimated dimensions of mobilized mass	Area ~18 ha., Volume ~5.4 x 10^6 m^3
Run-out length	~50 m
Sliding speed	15 mm/day for 20 days, then 30 cm/day for the last 10 days *before* failure
Physical and mechanical properties	In the shear plane: Residual cohesion c_{rs}' =0-5 kPa Residual friction angle φ_{rs}'= 8-10°
Materials involved in sliding	Overlying cohesionless "green island" sand and Pleistocene colluvium and loess deposits, irregularly mantling the gently-dipping (6-10°) tertiary soft rocks
Slip surface characteristics	Organic-rich highly plastic clay, only ~50 mm thick
Mineralogy of slip surface	Montmorillonite-rich

10) Landslide in China (Huang and Wang, 1988)

Type of sliding event	Large-scale rockslide

Sliding characteristics	Coherent translational sliding, then broken up in large blocks
Estimated dimensions of mobilized mass	Area ~0.2 km^2., Volume ~31.7 x 10^6 m^3, length ~750 m, width ~300 m.
Run-out length	~550 m
Sliding speed	High velocity, not determined
Physical and mechanical properties	Compressive strength of rock mass =18 Mpa Friction angle of the joint corresponding to the slip surface φ'=32°
Materials involved in sliding	Granite
Slip surface characteristics	Gently inclined (28°) joint set
Mineralogy of slip surface	NA
Extra information	• Evidence of high-speed sliding due to long run-out of such a huge rock mass • Inferred average temperature on the slip surface: 310 °C • A "block rolling friction mechanism" is assumed to explain the high sliding speed of the rock mass

11) Furre landslide (Hutchinson, 1961)

Type of sliding event	Translational earthslide
Sliding characteristics	A mainly cohesionless mass slid as a single intact flake on a thin layer of quick clay
Estimated dimensions of mobilized mass	Area ~180,000 m^2., Volume ~3 x 10^6 m^3, length ~300 m, width ~850 m.
Run-out length	~90 m
Sliding speed	NA
Physical and mechanical properties	Shear surface: Peak friction angle φ_p'=25°
Materials involved in sliding	Post-glacial and deltaic deposits
Slip surface characteristics	Layer of very quick clay, 2-10 cm thick, flat and gently inclined (6°-9°)
Mineralogy of slip surface	Main constituents of the quick clay, in descending order of quantity: Chamosite (of chlorite type) Illite Inactive minerals of quartz and feldspar

12) Usoy landslide (Gaziev, 1984)

Type of sliding event	Very large rockslide
Sliding characteristics	Earthquake-induced coherent sliding
Estimated dimensions of mobilized mass	Volume ~2 x 10^9 m^3
Run-out length	NA
Sliding speed	NA
Physical and mechanical properties	Back-calculated values: Residual cohesion c'_{rs} =0 kPa Residual friction angle φ'_{rs}= 28°
Materials involved in sliding	Sedimentary rocks
Slip surface characteristics	NA
Mineralogy of slip surface	NA
Extra information	Proposed explanation for the low friction angle is a “self lubrication” mechanism of crushing and dispersion of the rock material in the shear zone

13) Chana landslide (Zhongyou, 1984)

Type of sliding event	Translational rockslide
Sliding characteristics	The sliding body moved in two consecutive blocks
Estimated dimensions of mobilized mass	Volume ~ 10^8 m^3, thickness ~20-70 m, length 3000 m, max. width 1600 m
Run-out length	Max ~2000 m
Sliding speed	Max ~30 m/s
Physical and mechanical properties	Intact rock mass: c'=10-100 T/m^2 φ'=32-38° Discontinuities where sliding took place: c'=1-10 T/m^2 φ'=5-10°
Materials involved in sliding	Lacustrine semi-rock strata consisting of siltstones and mudstones
Slip surface characteristics	Thin layers of green-grey shales
Mineralogy of slip surface	NA
Extra information	The author proposes “self-lubrication” as an explanation for such a long run-out

14) Landslides in Fukushima, Japan (Okura et al., 2003)

Type of sliding event	Earthslides/debris slides
Sliding characteristics	Long run-out translational movement
Estimated dimensions of mobilized mass	Volumes ranging from 10^2 to 1.5 x 10^3 m^3
Run-out length	NA
Sliding speed	NA
Physical and mechanical properties	Average properties of *slip surfaces*: Density ρ=0.55-0.85 g/cm^3 Friction coefficient μ'=0.5-0.8
Materials involved in sliding	Thick layer of welded pyroclastic rock overlaid with a loam layer of 0.5-2 m thickness.
Slip surface characteristics	NA
Mineralogy of slip surface	NA

15) Las Colinas landslide (Crosta et al., 2005)

Type of sliding event	Debris avalanche
Sliding characteristics	Very long run-out flow-like movement
Estimated dimensions of mobilized mass	Volume ~0.18 x 10^6 m^3.
Run-out length	~800 m
Sliding speed	NA
Physical and mechanical properties	Only available for the debris layers
Materials involved in sliding	Stratified, loose volcanic deposits
Slip surface characteristics	NA
Mineralogy of slip surface	NA

16) Val Pola landslide (Crosta et al., 2004)

Type of sliding event	Rockslide/avalanche
Sliding characteristics	A large mass detached from a prehistoric landslide area, with a multi-planar wedge geometry, then, after impacting against a rocky escarpment, transformed into a flow-like movement, of which the front part run up 300 m on the opposite valley side

Estimated dimensions of mobilized mass	Volume ~40 x 10^6 m^3.
Run-out length	~1200 m
Sliding speed	Max estimated speed 108 m/s
Physical and mechanical properties	Only available for the deposit
Materials involved in sliding	Gneiss intruded by gabbro and diorite overlain by thin glacial and colluvial deposits
Slip surface characteristics	NA
Mineralogy of slip surface	NA

17) Tochiyama landslide (Chihara et al., 1994)

Type of sliding event	Complex, deep-seated movement
Sliding characteristics	Long-term creeping
Estimated dimensions of mobilized mass	Width ~50-1100 m, length ~2 km, max. thickness ~60 m
Run-out length	NA
Sliding speed	4.3 cm/yr from 1907 to 1983, 19 cm/yr afterwards.
Physical and mechanical properties	NA
Materials involved in sliding	Bedrock: sandstone and mudstone of the flysch type
Slip surface characteristics	NA
Mineralogy of slip surface	NA
Extra information	Likeliness to evolve into a very rapid landslide, by comparison with the adjacent Maseguchi landslide.

18) Vagnhärad landslide (Andersson et al., 2000)

Type of sliding event	Landslide
Sliding characteristics	NA
Estimated dimensions of mobilized mass	Length ~100 m, max. thickness ~10 m
Run-out length	200 m
Sliding speed	NA

Physical and mechanical properties	Liquid limit=50-80% Bulk density=1.8 t/m^3 Peak shear strength parameters: φ_p' = 30° c_p' = 2 kPa
Materials involved in sliding	Post-glacial clay and glacial clay with varves and layers of silt
Slip surface characteristics	Swedish soft silty clay
Mineralogy of slip surface	NA

19) St. Boniface landslide (Demers and Robitaille, 2000)

Type of sliding event	Retrogressive slide
Sliding characteristics	NA
Estimated dimensions of mobilized mass	Surface of ~14 ha., width ~1500 m, length ~1 km
Run-out length	150 m
Sliding speed	NA
Physical and mechanical properties	NA
Materials involved in sliding	Clay overlain by a 10m thick sand layer
Slip surface characteristics	Failure surface “not uniform” and “controlled by contrasting mechanical properties of the soil”
Mineralogy of slip surface	NA

20) Piemonte 1994 landslides (Bandis et al., 1996)

Type of sliding event	Small-scale rock-block slides
Sliding characteristics	NA
Estimated dimensions of mobilized mass	Average depth ~10 m, Volumes < 10^3 m^3
Run-out length	NA
Sliding speed	Variable between a few m/h to some hundred m/h
Physical and mechanical properties	Shear surface material Unit weigth γ=24 kN/m^2 Back-calculated residual friction angle φ'_{rs}=10-15°
Materials involved in sliding	Marly-silty and arenaceous-sandy lythotypes

Slip surface characteristics	Gently inclined at 8-10°, thin (5-20 mm) Silty-clayey materials, with grain-size distribution 65-75% silt, 20-25% clay, 5-10% sand.
Mineralogy of slip surface	Inclusions of muscovite

21) 1987 Belluno province landslide (Turrini et al., 1996)

Type of sliding event	Rotational slip/earthflow
Sliding characteristics	Active for a long period, repeated creeping movements of some portions of the slope
Estimated dimensions of mobilized mass	Volume ~10^4 m^3
Run-out length	~20 m
Sliding speed	NA
Physical and mechanical properties	for the "soil involved in sliding" (Turrini et al., 1996): Unit weight γ=23 kN/m^2 friction angle φ'=35° cohesion c'=60 kPa
Materials involved in sliding	Sequence of thin sandy strata alternated with thick clayey layers, all completely reworked by previous movements.
Slip surface characteristics	NA
Mineralogy of slip surface	Clay 15-25% Silt 25-70% $CaCO_3$ 10%

22) Chiampo valley landslide (Favaretti et al., 1996)

Type of sliding event	Translational landslide
Sliding characteristics	NA
Estimated dimensions of mobilized mass	Thickness ~10 m, length ~200 m
Run-out length	NA
Sliding speed	NA
Physical and mechanical properties	Peak shear strength parameters c_p' =20-30 kPa φ_p'= 20-25° Residual shear strength parameters c'_{rs} =0 φ'_{rs} ~18°
Materials involved in sliding	Clayey soils, including gravels and cobbles. The clayey matrix has medium to high plasticity and activity
Slip surface characteristics	NA

Mineralogy of slip surface	NA

23) Poggio Ferrato landslide (Braga et al., 2003)

Type of sliding event	Complex earthslide/earthflow
Sliding characteristics	Movement started as roto-translational and evolved into an earthflow, possible presence of deep-seated movement
Estimated dimensions of mobilized mass	Width 30-250 m, area 9 x 10^4 m
Run-out length	1.5 km for the earthflow
Sliding speed	NA
Physical and mechanical properties	“chaotic complex” (fissured stiff clay shales with embedded limestone and marlstone): Residual friction angle φ_{res}’=10-12°
Materials involved in sliding	Fractured rigid sandstone plate lying on a deformable marly-clayey substratum (Clay >40%)
Slip surface characteristics	No well-defined defined surface
Mineralogy of slip surface	NA

24) Landslide in China #2 (Huang and Zhang, 1988)

Type of sliding event	Rockslide
Sliding characteristics	NA
Estimated dimensions of mobilized mass	Volume ~100 x 10^6 m^3
Run-out length	NA
Sliding speed	High velocity, not determined
Physical and mechanical properties	Peak friction angle of faults φ_p’=33°
Materials involved in sliding	Metamorphic quartz-sandstone layers and clayey slates
Slip surface characteristics	Gently inclined faults observed in the clay-slate
Mineralogy of slip surface	NA

Extra information	- Evidence of high-speed sliding due to long run-out of such a huge rock mass - Inferred average temperature on the slip surface: 350 °C - A mathematical simulation of the landslide mechanism which takes into account the temperature rise is proposed by the authors

25) Edgerton landslide (Cruden et al., 1995)

Type of sliding event	Complex
Sliding characteristics	Evolution from reactivated, multiple and rapid rockslide to slow earthflow
Estimated dimensions of mobilized mass	Volume ~10^6 m^3
Run-out length	NA
Sliding speed	NA
Physical and mechanical properties	Bentonitic claystone: Natural moisture content=20-24% Liquid limit=100-125% Plasticity index=55-80% Peak shear strength parameters: c_p' =7 kPa φ_p'= 35° Residual shear strength parameters: c'_{rs} =0 kPa φ'_{rs}= 9°
Materials involved in sliding	Bedrock of marine claystones, siltstones and deltaic sandstones, overlain by till
Slip surface characteristics	Bentonitic claystone
Mineralogy of slip surface	Dominant mineral in the clay fraction: montmorillonite

26) Madipo landslide (Zhongyou, 1984)

Type of sliding event	Translational rockslide
Sliding characteristics	The sliding body moved in four consecutive blocks
Estimated dimensions of mobilized mass	Volume ~ 10^6 m^3, thickness ~20 m, length 300 m, width 220 m
Run-out length	240 m in horizontal direction, 60 m in vertical
Sliding speed	Max ~28 m/s

Physical and mechanical properties	Intact rock mass: c_p'=5-20 T/m^2 φ_p'=20-40° Discontinuities where sliding took place: c_{rs}'=0.2-2 T/m^2 φ_{rs}'=3-5°
Materials involved in sliding	Lacustrine semi-rock strata consisting of siltstones, mudstones and shales, total thickness ~200 m
Slip surface characteristics	NA
Mineralogy of slip surface	NA
Extra information	The author proposes "self-lubrication" as an explanation for such a long run-out

27) New Rara landslide (Hasmi and Haq Izhar, 1984)

Type of sliding event	Translational landslide
Sliding characteristics	NA
Estimated dimensions of mobilized mass	Width ~120 m, length ~300 m
Run-out length	NA
Sliding speed	NA
Physical and mechanical properties	In the slip plane: Liquid limit=36% Plastic limit=22% Plasticity index=14% Peak strength parameters: c_p'=12 kPa φ_p'=29° Residual values: c_{rs}'=0 kPa φ_{rs}'=18°
Materials involved in sliding	Clay with fragments of sandstone, siltstone and claystone
Slip surface characteristics	Clayey silt, polished, slickensided, with high plasticity.
Mineralogy of slip surface	20% sand 50% silt 30% clay

28) Ancona landslide (Hegg, 1984)

Type of sliding event	Translational landslide
Sliding characteristics	NA

Estimated dimensions of mobilized mass	Max width ~1.7 km, area ~340 ha, thickness=80m.
Run-out length	<50 m
Sliding speed	NA
Physical and mechanical properties	Marly clay Unit weight γ ~2 g/cm^3 Plastic index =20-40% Peak friction angle φ_p'=21-25° Peak cohesion c_p'=0-180 kPa Residual friction angle φ_{rs}'=16-19°
Materials involved in sliding	Cover of sandy and silty clay ~10 m thick, followed by Pleistocene deposits of marly-silty clays and carbonate sands, and Pliocene base layers of heavily overconsolidated marly clay
Slip surface characteristics	Principally, heavily overconsolidated marly clay
Mineralogy of slip surface	Clay 40-60% $CaCO_3$ 30-60%

29) Vajont landslide (Muller, 1964, Tika and Hutchinson, 1999, Muller and Fairhurst, 1968, Hendron and Patton, 1985, Vardoulakis, 2002a.)

Type of sliding event	Rockslide
Sliding characteristics	Very fast deep-seated rotational sliding
Estimated dimensions of mobilized mass	Volume ~250 x 10^6 m^3, 40-250 m thick, average thickness~120m
Run-out length	450-500 m
Sliding speed	25-30 m/s
Physical and mechanical properties	Clay in the slip plane: Peak friction angle φ_p'=22° Residual friction angle: static value φ_{rs}' = 8-10°; dynamic value φ_{rd}'=6.6° (Tikka and Hutchinson, 1999)
Materials involved in sliding	Rock formations composed mainly of limestone and marly limestone, with clay intercalations
Slip surface characteristics	Approximately circular shape, with slope varying from 30° at rear scarp to 0° at the toe. Silty-clayey material.
Mineralogy of slip surface	Clay ~50%, of which 50% illite-smectite, <5% kaolinite Calcite 40% Quartz <5%

30) Goldau landslide (Erismann, 1979, Thuro et al., 2005, Thuro et al., 2008)

Type of sliding event	Rockslide

Sliding characteristics	Translational, failure along bedding plane dipping (15°-30°) parallel to topography
Estimated dimensions of mobilized mass	Volume ~40 x 10^6 m^3
Run-out length	Vertical travel: 800 m
Sliding speed	NA
Physical and mechanical properties	Unit weight of overburden ~2.7 x 10^3 Kg/m^3
Materials involved in sliding	Carbonate rocks, conglomerates
Slip surface characteristics	Failure occurred along bedding plane contacts between the conglomerates and the underlying marls
Mineralogy of slip surface	NA
Extra information	Self-lubrication originated by rock melting has been suggested (Erismann, 1979) to explain long run-out

31) Koefels landslide (Erismann, 1979, Erismann and Abele, 2001, Sorensen and Bauer, 2003)

Type of sliding event	Rockslide
Sliding characteristics	Translational sliding
Estimated dimensions of mobilized mass	Volume ~2.3 x 10^9 m^3
Run-out length	Vertical travel 320 m, displacement >1 km
Sliding speed	~50 m/s after 1 km of displacement
Physical and mechanical properties	Unit weight of overburden ~2.25 x 10^3 Kg/m^3
Materials involved in sliding	Gneiss
Slip surface characteristics	NA
Mineralogy of slip surface	NA
Extra information	Evidence of fused rock (pumice formations), frictional heating suggested (Erismann and Abele, 2001, Sorensen and Bauer, 2003)

32) Huascaràn slide (Erismann and Abele, 2001)

Type of sliding event	Rockslide/avalanche
Sliding characteristics	Extremely fast and long run-out compound sliding

Estimated dimensions of mobilized mass	Volume ~40 x 10^6 m^3
Run-out length	10 km
Sliding speed	Average velocity ~67 m/s
Physical and mechanical properties	Unit weight of overburden ~1.25 x 10^3 Kg/m^3
Materials involved in sliding	Rock, mud, ice
Slip surface characteristics	NA
Mineralogy of slip surface	NA
Extra information	Various self-lubrication mechanisms proposed, among which rock and ice melting caused by frictional heating

33) Sale Mountain slide (Miao et al., 2001, Zhang et al., 2002)

Type of sliding event	rockslide
Sliding characteristics	Chair-shaped: upper part rotational, lower part translational
Estimated dimensions of mobilized mass	Volume ~30 x 10^6 m^3, length 1600 m, width 1100 m. Average slope angle of main scarp: 70°
Run-out length	1050 m
Sliding speed	~20 m/s
Physical and mechanical properties	Unit weight of overburden ~1.8 x 10^3 Kg/m^3
Materials involved in sliding	Loess, mudstones, siltstones
Slip surface characteristics	~2 mm thick
Mineralogy of slip surface	NA
Extra information	• The entire sliding process lasted less than 1 min. • Evidence of frictional heating, allegedly reaching temperatures of 600 °C locally in the slip plane • The overburden preserved its integrity during sliding: a person on it travelled uninjured for ~1 km by holding a tree trunk.

34) Qiangjiangping landslide (Wen et al., 2004, Luo et al., 2008, Yueping, 2008)

Type of sliding event	Coherent earth/rock slide
Sliding characteristics	Translational, tongue-shaped

Estimated dimensions of mobilized mass	Volume ~24 x 10^6 m^3, length 1200 m, width 1000 m. Average slope angle: 35°
Run-out length	120 m
Sliding speed	1 m/s on average
Physical and mechanical properties	Unit weight ~1.96 x 10^3 Kg/m^3 Water content=19.6 %
Materials involved in sliding	Siltstone, mudstone and shale
Slip surface characteristics	Occurred in carbonaceous shale, 20-30 cm thick.
Mineralogy of slip surface	NA

35) Campo Vallemaggia slide (Bonzanigo et al., 2007)

Type of sliding event	Deep-seated landslide
Sliding characteristics	Creeping translational movement
Estimated dimensions of mobilized mass	Volume ~800 x 10^6 m^3, max thickness=300 m
Run-out length	30 m in 100 years
Sliding speed	~5 cm/year
Physical and mechanical properties	Unit weight γ~22 kN/m^3 Overall rock permeability k_w=10^{-7}-10^{-5}
Materials involved in sliding	Several rock units, among which gneiss and schists. Presence of chlorite and clays
Slip surface characteristics	Moderately dipping basal shear zone
Mineralogy of slip surface	NA

36) La Frasse landslide (Tacher et al., 2005)

Type of sliding event	Deep-seated rockslide
Sliding characteristics	Composite creeping movement, has been active for millennia
Estimated dimensions of mobilized mass	Volume ~42 x 10^6 m^3, thickness=40-80 m
Run-out length	Some metres
Sliding speed	Upper part:10-15 cm/year Lower part: 20-60 cm/year Mean velocity at geological scale: 7 cm/year

Physical and mechanical properties	Permeability of shale matrix $\sim 10^{-7}$ m/s
Materials involved in sliding	Sandstones and clay schists, shale
Slip surface characteristics	NA
Mineralogy of slip surface	NA

37) Triesenberg landslide (Francois et al., 2005)

Type of sliding event	Rockslide
Sliding characteristics	Translational
Estimated dimensions of mobilized mass	Volume $\sim 37 \times 10^6$ m^3, thickness=10-20 m
Run-out length	Some metres
Sliding speed	0-3 cm/year
Physical and mechanical properties	Peak friction angle for the clay φ_p'~25° Field permeability $k_w \sim 10^{-4}$
Materials involved in sliding	Bedrock: schist, limestone, sandstone, flysch
Slip surface characteristics	Mean inclination 24°, normally-consolidated clayey soil
Mineralogy of slip surface	NA

References

Abramowitz, M. and I. A. Stegun (1964). Handbook of mathematical functions with formulas, graphs, and mathematical tables. Washington, U.S. Govt. Print. Off.

Agliardi, F., G. Crosta, et al. (2001). "Structural constraints on deep-seated slope deformation kinematics." Engineering Geology **59**(1-2): 83-102.

Alexandre, J., F. Saboya, et al. (1999). "Photoacoustic thermal characterization of kaolinite clays." Analyst **124**(8): 1209-1214.

Anderson, D. L. (1980). An earthquake induced heat mechanism to explain the loss of strength of large rock and earth slides. Proceedings of the International conference on engineering for protection from natural disasters, Bangkok.

Andersson, H., P. E. Bengtsson, et al. (2000). The landslide at Vagnharad in Sweden. Proceedings of the 8th international Symposium on Landslides, Cardiff, Thomas Thelford.

Antoine, P., D. Fabre, et al. (1988). Propriètès gèotechniques de quelques ensembles gèologiques propices aux glissements de terrains. Proceedings of the 5th International Symposium on Landslides, Lausanne.

Azzoni, A., S. Chiesa, et al. (1992). "The Valpola Landslide." Engineering Geology **33**(1): 59-70.

Baldi, G., T. Hueckel, et al. (1988). "Thermal Volume Changes of the Mineral Water-System in Low-Porosity Clay Soils." Canadian Geotechnical Journal **25**(4): 807-825.

Baldi, G., T. Hueckel, et al. (1991). Developments in modelling of thermo-hydro-geomechanical behaviour of Boom clay and clay-based buffer materials, Report EUR 13365, Commission of the European Communities, Nuclear science and technology.

Bandis, S. C., G. Delmonaco, et al. (1996). Landslide phenomena during the extreme meteorological event of 4-6 November 1994 in the Piemonte Region in N Italy. Proceedings of the 7th International Symposium on Landslides. K. Senneset**:** 623-628.

Baraza, J., H. J. Lee, et al. (1990). "Geotechnical Characteristics and Slope Stability on the Ebro Margin, Western Mediterranean." Marine Geology **95**(3-4): 379-393.

Bell, D. H. and J. R. Pettinga (1988). Bedding-Controlled Landslides in New-Zealand Soft Rock Terrain. Proceedings of the 5th International Symposium on Landslides.

Bentley, S. P. and H. J. Siddle (1996). "Landslide research in the South Wales coalfield." Engineering Geology **43**(1): 65-80.

Bojanowski, A. (2007). Als der Berg in den See fiel. Süddeutsche Zeitung **248**.

Bonzanigo, L., E. Eberhardt, et al. (2007). "Long-term investigation of a deep-seated creeping landslide in crystalline rock. Part I. Geological and hydromechanical factors controlling the Campo Vallemaggia landslide." Canadian Geotechnical Journal **44**(10): 1157-1180.

Booth, J. S., D. W. O'Leary, et al. (1991). U.S. Atlantic continental slope landslides: their distribution, general attributes, and implications. U. S. D. o. t. interior, U.S. Geological Survey.

Borja, R. I. and S. R. Lee (1990). "Cam Clay Plasticity .1. Implicit Integration of Elastoplastic Constitutive Relations." Computer Methods in Applied Mechanics and Engineering **78**(1): 49-72.

Braga, G., C. Messina, et al. (2003). Study of a complex landslide movement for risk assessment: the example of the poggio ferrato landslide (northern Italy). Proc. International Conference on Fast Slope Movements: Prediction and Prevention for Risk Mitigation. Napoli, AGI.

Buccolini, M. and N. Sciarra (1996). The Caramanico Landslide (Abruzzo, Italy). Seventh International Symposium on Landslides, Trondheim, Balkema.

Bugge, T., R. H. Belderson, et al. (1988). "The Storegga Slide." Philosophical Transactions of the Royal Society of London Series a-Mathematical Physical and Engineering Sciences **325**(1586): 357-&.

Campanella, R. G., J. K. Mitchell, et al. (1968). Influence of temperature variations on soil behavior. Berkeley, University of California, Institute of Transportation and Traffic Engineering, Soil Mechanics and Bituminous Materials Research Laboratory.

Canals, M., G. Lastras, et al. (2004). "Slope failure dynamics and impacts from seafloor and shallow sub-seafloor geophysical data: case studies from the COSTA project." Marine Geology **213**(1-4): 9-72.

Cappa, F., Y. Guglielmi, et al. (2004). "Hydromechanical modeling of a large moving rock slope inferred from slope levelling coupled to spring long-term hydrochemical monitoring: Example of the La Clapie're landslide (Southern Alps, France)." Journal of Hydrology **291**(1-2): 67-90.

Catalano, A., V. Chieppa, et al. (2000). Interacion between dams and landslides: three case histories. 8th int. Symposium on Landslides, Cardiff, Thomas Thelford.

Chang, K. J., A. Taboada, et al. (2005a). "Analysis of landsliding by earthquake shaking using a block-on-slope thermo-mechanical model: Example of Jiufengershan landslide, central Taiwan." Engineering Geology **80**(1-2): 151-163.

Chang, K. J., A. Taboada, et al. (2005b). "Geological and morphological study of the Jiufengershan landslide triggered by the Chi-Chi Taiwan earthquake." Geomorphology **71**(3-4): 293-309.

Chihara, K., S. Iwanaga, et al. (1994). "Geohistorical Development of the Tochiyama Landslide in North-Central Japan." Engineering Geology **38**(3-4): 205-219.

Cornforth, D. H. and J. A. Lowell (1996). The 1994 submarine slope failure at Skagway, Alaska. Seventh International Symposium on Landslides, Trondheim, Balkema.

Corominas, J. (1996). "The angle of reach as a mobility index for small and large landslides." Canadian Geotechnical Journal **33**(2): 260-271.

Crosta, G. B. and F. Agliardi (2002). "How to obtain alert velocity thresholds for large rockslides." Physics and Chemistry of the Earth **27**(36): 1557-1565.

Crosta, G. B., H. Chen, et al. (2004). "Replay of the 1987 Val Pola Landslide, Italian Alps." Geomorphology **60**(1-2): 127-146.

Crosta, G. B., S. Imposimato, et al. (2005). "Small fast-moving flow-like landslides in volcanic deposits: The 2001 Las Colinas Landslide (El Salvador)." Engineering Geology **79**(3-4): 185-214.

Cruden, D. M., Z. Y. Lu, et al. (1997). "The 1939 Montagneuse River landslide, Alberta." Canadian Geotechnical Journal **34**(5): 799-810.

Cruden, D. M., S. Thomson, et al. (1995). "The Edgerton landslides." Canadian Geotechnical Journal **32**(6): 989-1001.

Cui, Y. J., N. Sultan, et al. (2000). "A thermomechanical model for saturated clays." Canadian Geotechnical Journal **37**(3): 607-620.

De Blasio, F. V. and A. Elverhoi (2008). "A model for frictional melt production beneath large rock avalanches." Journal of Geophysical Research-Earth Surface **113**(F2).

Delage, P., N. Sultan, et al. (2000). "On the thermal consolidation of Boom clay." Canadian Geotechnical Journal **37**(2): 343-354.

Demars, K. R. and R. D. Charles (1982). "Soil Volume Changes Induced by Temperature Cycling." Canadian Geotechnical Journal **19**(2): 188-194.

Demers, D. and D. Robitaille (2000). The St. Boniface landslide of April 1996: A large retrogressive landslide in sensitive clay with little flow component. Proceedings of the 8th international Symposium on Landslides, Cardiff, Thomas Thelford.

Desgagnes, P., J. Locat, et al. (2000). Geotechnical properties of a mass flow deposit on the Hudson Apron, off New Jersey, U.S.A. 53rd Canadian Geotechnical Conference, Montreal.

Despax, D. (1976). Etude de l'influence de la temperature sur les proprietés des argiles saturées. Thése de doctorat. Grenoble, Université de Grenoble.

Dowell, M. and P. Jarratt (1972). "The "Pegasus" method for computing the root of an equation." BIT Numerical Mathematics **12**(4): 503-508.

Erismann, T. H. (1979). "Mechanisms of Large Landslides." Rock Mechanics **12**: 15-46.

Erismann, T. H. and G. Abele (2001). Dynamics of Rockslides and Rockfalls. Berlin Heidelberg, Springer-Verlag.

Evans, S. G. and J. V. DeGraff (2002). Catastrophic landslides : effects, occurrence, and mechanisms. Boulder, CO, Geological Society of America.

Favaretti, M., P. Previatello, et al. (1996). A case history of a translational landslide in the Chiampo Valley (Italy). Proceedings of the 7th International Symposium on Landslides. K. Senneset**:** 1219-1224.

Fleming, R. W., S. D. Ellen, et al. (1989). "Transformation of Dilative and Contractive Landslide Debris into Debris Flows - an Example from Marin County, California." Engineering Geology **27**(1-4): 201-223.

Follacci, J. P., P. Guardia, et al. (1988). Geodynamic framework of La Clapière landslide (Maritime Alps, France). Proceedings of the 5th International Symposium on Landslides, Lausanne.

Forsberg, C. F. and J. Locat (2005). "Mineralogical and microstructural development of the sediments on the Mid-Norwegian margin." Marine and Petroleum Geology **22**(1-2): 109-122.

Francois, B., L. Tacher, et al. (2007). "Numerical modelling of the hydrogeological and geomechanical behaviour of a large slope movement: the Triesenberg landslide (Liechtenstein)." Canadian Geotechnical Journal **44**: 840-857.

Gaziev, E. (1984). Study of the Usoy landslide in Pamir. IV International Symposium on Landslides Toronto.

Ghabezloo, S. and J. Sulem (2008). "Stress dependent thermal pressurization of a fluid-saturated rock." Rock Mechanics and Rock Engineering.

Gokceoglu, C., H. Sonmez, et al. (2005). "The 17 March 2005 Kuzulu landslide (Sivas, Turkey) and landslide-susceptibility map of its near vicinity." Engineering Geology **81**(1): 65-83.

Griffiths, J. S., J. N. Hutchinson, et al. (2004). "The reactivation of a landslide during the construction of the Ok Ma tailings dam, Papua New Guinea." Quarterly Journal of Engineering Geology and Hydrogeology **37**: 173-186.

Guadagno, F. M. and S. Perriello Zampelli (2000). Triggering mechanisms of the Landslides that inundated Sarno, Quindici, Siano, and Bracigliano (S. Italy) on

May 5-6, 1998. Proceedings of the 8th international Symposium on Landslides, Cardiff, Thomas Thelford.

Guzzetti, F. (2000). "Landslide fatalities and the evaluation of landslide risk in Italy." Engineering Geology **58**(2): 89-107.

Guzzetti, F., C. P. Stark, et al. (2005). "Evaluation of flood and landslide risk to the population of Italy." Environmental Management **36**(1): 15-36.

Habib, P. (1975). "Production of gaseous pore pressure during rock slides." Rock Mechanics and Rock Engineering **7**(4): 193-197.

Habibagahi, K. (1977). "Temperature effect and the concept of effective void ratio." Indian Geotechnical Journal **1**: 14-34.

Hampton, M. A., H. J. Lee, et al. (1996). "Submarine landslides." Reviews of Geophysics **34**(1): 33-59.

Hegg, U. (1984). Case history of a large coastal landslide in pliocene clays. Proc. IV International Symposium on Landslides Toronto.

Helmstetter, A., D. Sornette, et al. (2004). "Slider block friction model for landslides: Application to Vaiont and La Clapiere landslides." Journal of Geophysical Research-Solid Earth **109**(B2).

Hendron, A. J. and F. D. Patton (1985). The Vaiont slide, a geotehnical analysis based on new geologic observations of the failure surface. Technical Report GL-85-5. Washington, DC, Department of the Army US Corps of Engineers.

Hendron, A. J. and F. D. Patton (1987). "The Vaiont Slide - a Geotechnical Analysis Based on New Geologic Observations of the Failure Surface." Engineering Geology **24**(1-4): 475-491.

Hicher, P. Y. (1974). Etude des proprietés mechaniques des argiles à l'aide d'essais triaxiaux, influence de la vitesse et de la temperature. Report of the soil mechanics laboratory. Paris, Ecole Centrale de Paris.

Hoffman, J. D. (2001). Numerical methods for engineers and scientists. New York Marcel Dekker.

Huang, C. C., Y. H. Lee, et al. (2001). "Influence of surface-normal ground acceleration on the initiation of the Jih-Feng-Erh-Shan landslide during the 1999 Chi-Chi, Taiwan, earthquake." Bulletin of the Seismological Society of America **91**(5): 953-958.

Huang, R. Q. and S. T. Wang (1988). Rolling Friction Mechanism for the High-Speed Motion of a Large-Scale Landslide. Proceedings of the 5th International Symposium on Landslides. C. Bonnard**:** 187-191.

Huang, R. Q. and Z. Y. Zhang (1988). Analysis and Mathematical Simulation of a Large Landslide Formed by Composite Mechanism. Proceedings of the 5th International Symposium on Landslides. C. Bonnard**:** 673-678.

Hueckel, T. and G. Baldi (1990). "Thermoplasticity of Saturated Clays - Experimental Constitutive Study." Journal of Geotechnical Engineering-Asce **116**(12): 1778-1796.

Hueckel, T. and M. Borsetto (1990). "Thermoplasticity of Saturated Soils and Shales - Constitutive-Equations." Journal of Geotechnical Engineering-Asce **116**(12): 1765-1777.

Hueckel, T. and A. Peano (1987). "Some geotechnical aspects of radioactive waste isolation in continental clays." Computers and Geotechnics **3**: 157-182.

Hueckel, T. and R. Pellegrini (1989). Modelling of thermal failure of saturated clays. Proceedings of Numerical Models in Geomechanics, Elsevier.

Hueckel, T. and R. Pellegrini (1991). "Thermoplastic modelling of undrained failure of saturated clay due to heating." Soils and Foundations **31**(3): 1-16.

Huhnerbach, V. and D. G. Masson (2004). "Landslides in the North Atlantic and its adjacent seas: an analysis of their morphology, setting and behaviour." Marine Geology **213**(1-4): 343-362.

Hunter, G. J. and R. Fell (2003). Mechanics of failure of soil slopes leading to "rapid" failure. Proc. International Conference on Fast Slope Movements: Prediction and Prevention for Risk Mitigation Napoli, AGI.

Hurlimann, M., A. Ledesma, et al. (1999). "Conditions favouring catastrophic landslides on Tenerife (Canary Islands)." Terra Nova **11**(2-3): 106-111.

Hutchinson, J. N. (1961). "A landslide on a thin layer of quick clay at Furre, Central Norway." Géotechnique **11**: 69–94.

Hutchinson, J. N. (1988). Morphological and Geotechnical parameters of Landslides in relation to Geology and Hydrogeology. V Intl Symposium on Landslides, Lausanne.

IUGS - International working group, L. (1995). "A suggested method for describing the rate of movement of a landslide." Bullettin of the International Association of Engineering Geology **52**: 75-78.

Kilburn, C. R. J. and D. N. Petley (2003). "Forecasting giant, catastrophic slope collapse: lessons from Vajont, Northern Italy." Geomorphology **54**(1-2): 21-32.

Koiter, W. T. (1960). General theorems for elastic-plastic solids. Progress in solid mechanics. I. N. S. a. R. Hill. Amsterdam**:** 167-221.

Kvalstad, T. J., L. Andresen, et al. (2005a). "The Storegga slide: evaluation of triggering sources and slide mechanics." Marine and Petroleum Geology **22**(1-2): 245-256.

Kvalstad, T. J., F. Nadim, et al. (2005b). "Soil conditions and slope stability in the Ormen Lange area." Marine and Petroleum Geology **22**(1-2): 299-310.

Laloui, L. (2001). "Thermo-mechanical behaviour of soils." Environmental geomechanics **5**: 809-843.

Laloui, L. and C. Cekerevac (2003). "Thermo-plasticity of clays: An isotropic yield mechanism." Computers and Geotechnics **30**(8): 649-660.

Laloui, L., C. Cekerevac, et al. (2005). "Constitutive modelling of the thermo-plastic behaviour of soils." Revue Europeenne de genie civil **9**(5-6): 635-650.

Laloui, L., C. Cekerevac, et al. (2002). Thermo-plasticity of clays: a simple constitutive approach. Environmental geomechanics - Monte Verita` 2002. L.Vulliet.

Lee, E. M., D. K. C. Jones, et al. (2000). The landslide environment of Great Britain. Proceedings of the 8th international Symposium on Landslides
Cardiff, Thomas Thelford.

Lee, H. J., W. C. Schwab, et al. (1991). Submarine Landslides: an introduction. U. S. D. o. t. interior, U.S. Geological Survey.

Legros, F. (2002). "The mobility of long-runout landslides." Engineering Geology **63**(3-4): 301-331.

Legros, F., J. M. Cantagrel, et al. (2000). "Pseudotachylyte (frictionite) at the base of the Arequipa volcanic landslide deposit (Peru): Implications for emplacement mechanisms." Journal of Geology **108**(5): 601-611.

Lehane, B. M. and R. J. Jardine (1992). "Residual Strength Characteristics of Bothkennar Clay." Geotechnique **42**(2): 363-367.

Leroueil, S., J. Locat, et al. (1996). Geotechnical characterization of slope movements. Proceedings of the 7th International Symposium on Landslides. K. Senneset**:** 53-74.

Lin, A. M., A. L. Chen, et al. (2001). "Frictional fusion due to coseismic landsliding during the 1999 Chi-Chi (Taiwan) M-L 7.3 earthquake." Geophysical Research Letters **28**: 4011-4014.

Locat, J. and H. J. Lee (2000). Submarine Landslides: Advances and Challenges. 8th int. Symposium on Landslides, Cardiff, Thomas Thelford.

Luo, X., A. Che, et al. (2008). Failure mechanism of slipping zone soil of the Qiangjiangping landslide in the Three Gorges reservoir area: A study based on Dead Load test. Proceedings of the 10th International Symposium on Landslides and Engineered Slopes, Xi'An, China, Taylor and Francis.

Lykousis, V., G. Roussakis, et al. (2002). "Sliding and regional slope stability in active margins: North Aegean Trough (Mediterranean)." Marine Geology **186**(3-4): 281-298.

Mandel, J. (1965). "Une generalisation de la theorie de Koiter." International Journal of Solid Structures **1**: 273-295.

Marques, M. E. S., S. Leroueil, et al. (2004). "Viscous behaviour of St-Roch-de-l'Achigan clay, Quebec." Canadian Geotechnical Journal **41**(1): 25-38.

Martinez, J. F., J. Cartwright, et al. (2005). "3D seismic interpretation of slump complexes: examples from the continental margin of Israel." Basin Research **17**(1): 83-108.

Masch, L., H. R. Wenk, et al. (1985). "Electron-Microscopy Study of Hyalomylonites - Evidence for Frictional Melting in Landslides." Tectonophysics **115**(1-2): 131-160.

Mase, G. E. (1970). Schaum's outline of theory and problems of continuum mechanics. New York, McGraw-Hill.

Modaressi, H. and L. Laloui (1997). "A thermo-viscoplastic constitutive model for clays." International Journal for Numerical and Analytical Methods in Geomechanics **21**(5): 313-335.

Morgenstern, N. R. and J. S. Tschalenko (1967). "Microscopic structures in kaolin subjected to direct shear." Géotechnique **17**(4): 309-328.

Muir Wood, D. (1990). Soil behaviour and critical state soil mechanics, Cambridge university press.

Muller, L. (1964). "The rock slide in the Vaiont valley." Felsmech. Ingenieurgeol. **2**: 148-212.

Muller, L. and C. Fairhurst (1968). "New Considerations on the Vaiont Slide " Rock Mech Eng Geol **VI**(1-2).

NIST/SEMATECH. (2003, 18/07/2006). "e-Handbook of Statistical Methods." from http://www.itl.nist.gov/div898/handbook/.

Okura, Y., H. Kitahara, et al. (2003). "Topography and volume effects on travel distance of surface failure." Engineering Geology **67**(3-4): 243-254.

Oyagi, N., M. Sorriso-Valvo, et al. (1994). "Introduction to the Special Issue of the Symposium on Deep-Seated Landslides and Large-Scale Rock Avalanches." Engineering Geology **38**(3-4): 187-188.

Pastor, M., O. C. Zienkiewicz, et al. (1990). "Generalized Plasticity and the Modeling of Soil Behavior." International Journal for Numerical and Analytical Methods in Geomechanics **14**(3): 151-190.

Peace, G. S. (1993). Taguchi methods : a hands-on approach. Reading, Mass., Addison-Wesley.

Petley, D. N. and R. J. Allison (1997). "The mechanics of deep-seated landslides." Earth Surface Processes and Landforms **22**(8): 747-758.

Polloni, G., P. Aleotti, et al. (1996). Heavy rain triggered landslides in the Piemonte region (Italy). Proceedings of the 7th International Symposium on Landslides. K. Senneset. Trondheim, Balkema**:** 1955-1960.

Potts, D. M. and L. Zdravkovic (1999). Finite element analysis in geotechnical engineering : theory. London; Reston, VA, Telford ; Distributed by ASCE Press.

Powrie, W. (1997). Soil mechanics : concepts and applications. London; New York, E & FN Spon.

Prager, W. (1958). "Non-isothermal plastic deformation." Bol. Konike Nederl. Acad. Wet. **8**(61/3): 176-182.

Press, W. H., B. P. Flannery, et al. (1988). Numerical recipes in C : the art of scientific computing. Cambridge [Cambridgeshire]; New York, Cambridge University Press.

Prior, D. (1988). Subaqueous Landslides. Proceedings of the 5th International Symposium on Landslides.

Puzrin, A. M. and L. N. Germanovich (2005). "The growth of shear bands in the catastrophic failure of soils." Proceedings of the Royal Society a-Mathematical Physical and Engineering Sciences **461**(2056): 1199-1228.

Rice, J. R. (2006). "Heating and weakening of faults during earthquake slip." Journal of Geophysical Research-Part B-Solid Earth **111**(B5): 29 pp.-29 pp.

Roberts, J. A. and A. Cramp (1996). "Sediment stability on the western flanks of the Canary Islands." Marine Geology **134**(1-2): 13-30.

Robinet, J. C., A. Rahbaoui, et al. (1996). "A constitutive thermomechanical model for saturated clays." Engineering Geology **41**(1-4): 145-169.

Roscoe, K. and J. Burland (1968). On generalized stress strain behaviour of wet clay, Cambridge University Press.

Roscoe, K. and A. N. Schofield (1963). Mechanical behaviour of an idealised 'wet' clay. Proc. European Conf. on soil Mechanics and Foundation Engineering, Wiesbaden.

Sangrey, D. A. (1977). "Marine Geotechnology - State of the Art." Marine Geotechnology **2**: 45-80.

Schofield, A. N. and C. P. Wroth (1968). Critical State Soil Mechanics. London, McGraw Hill.

Schrefler, B. (2005). "Finite element analysis of strain localization in multiphase materials." from http://alert.epfl.ch/Archive/ALERT2005/s/slides/Schrefler_aussois2005-localization-sent.pdf.

Shou, K. J. and C. F. Wang (2003). "Analysis of the Chiufengershan landslide triggered by the 1999 Chi-Chi earthquake in Taiwan." Engineering Geology **68**(3-4): 237-250.

Shreve, R. L. (1966). "Sherman Landslide, Alaska." Science, new series **154**(3757): 1639-1643.

Shuzui, H. (2000). Landslide classification based on the Properties of Slip Surface. 8th int. Symposium on Landslides, Cardiff, Thomas Thelford.

Silva, A. J., C. D. P. Baxter, et al. (2004). "Investigation of mass wasting on the continental slope and rise." Marine Geology **203**(3-4): 355-366.

Skempton, A. W. (1985). "Residual Strength of Clays in Landslides, Folded Strata and the Laboratory." Geotechnique **35**(1): 3-18.

Sloan, S. W., A. J. Abbo, et al. (2001). "Refined explicit integration of elastoplastic models with automatic error control." Engineering Computations **18**(1-2): 121-154.

Sørensen, S.-A. and B. Bauer (2003). "On the dynamics of the Köfels sturzstrom." Geomorphology **54**(1-2): 11-19.

Sornette, D., A. Helmstetter, et al. (2004). "Towards landslide predictions: two case studies." Physica a-Statistical Mechanics and Its Applications **338**(3-4): 605-632.

Stead, D. (2003). "Dynamics of Rockslides and Rockfalls - T.H. Erismann and G. Abele. Springer-Verlag Berlin Heidelberg, 2001. 316 pages. ISBN 3-540-67198-6. Hardbound." Engineering geology. **66**(3): 320.

Strom, A. L. (1996). Some morphological types of long-runout rockslides: Effect of the relief on their mechanism and on the rockslide deposits distribution. Seventh International Symposium on Landslides, Trondheim, Balkema.

Sulem, J., P. Lazar, et al. (2007). "Thermo-poro-mechanical properties of clayey gouge and application to rapid fault shearing." International Journal for Numerical and Analytical Methods in Geomechanics **31**(3): 523-540.

Sulem, J., I. Vardoulakis, et al. (2004). "Experimental characterization of the thermo-poro-mechanical properties of the Aegion Fault gouge." Comptes Rendus Geoscience **336**(4-5): 455-466.

Sulem, J., I. Vardoulakis, et al. (2005). "Thermo-poro-mechanical properties of the Aigion fault clayey gouge - Application to the analysis of shear heating and fluid pressurization." Soils and Foundations **45**(2): 97-108.

Sultan, N. (1997). Etude du comportement thermo-mèchanique de l'argile de Boom: expériences et modélisation. Thèse de doctorat. ENPC. Paris, CERMES.

Sultan, N., P. Delage, et al. (2001). Temperature effects on the volume change behaviour of Boom clay. Workshop on Key Issues in Waste Isolation Research, Barcelona, Spain, Elsevier Science Bv.

Sultan, N., P. Delage, et al. (2002). "Temperature effects on the volume change behaviour of Boom clay." Engineering Geology **64**(2-3): 135-145.

Tacher, L., C. Bonnard, et al. (2005). "Modelling the behaviour of a large landslide with respect to hydrogeological and geomechanical parameter heterogeneity." Landslides **2**(1): 3-14.

Taguchi, G. and O. Asian Productivity (1986). Introduction to quality engineering; designing quality into products and processes. White Plains, N.Y.; Dearborn, Mich., Unipub/Quality Resources; American Supplier Institute.

Taguchi, G., M. El Sayed, et al. (1989). Quality Engineering and quality systems. New York, McGraw-Hill.

Tarchi, D., N. Casagli, et al. (2003). "Landslide monitoring by using ground-based SAR interferometry: an example of application to the Tessina landslide in Italy." Engineering Geology **68**(1-2): 15-30.

Taylor, D. W. (1948). Fundamentals of soil mechanics. New York, J. Wiley.

Thuro, K., C. Berner, et al. (2005). Der Bergsturz von Goldau 1806 - Versagensmechanismen in wechsellagernden Konglomeraten und Mergeln. Veroffentlichungen von der 15. Tagung fur Ingenieurgeologie : Erlangen, 06. - 09. April 2005 ; (Proceedings of the 15th Conference on Engineering Geology), Erlangen.

Tika, T. E. and J. N. Hutchinson (1999). "Ring shear tests on soil from the Vaiont landslide slip surface." Geotechnique **49**(1): 59-74.

Tinti, S., F. Zaniboni, et al. (2007). Tsunamigenic landslides in the western Corinth Gulf: Numerical scenarios. 3rd International Symposium on Submarine Mass Movements and Their Consequences, Santorini, GREECE, Springer.

Towhata, I., P. Kuntiwattanakul, et al. (1995). "Discussion on volume change of clays induced by heating as observed in consolidation tests (Towhata and al. 1993)." Soils and Foundations **35**(3): 124-127.

Troncone, A. (2005). "Numerical analysis of a landslide in soils with strain-softening behaviour." Geotechnique **55**(8): 585-596.

Turrini, M. C., F. Fiorani, et al. (1996). Analysis of a landslide in a complex formation. Proceedings of the 7th International Symposium on Landslides. K. Senneset: 913-918.

Urgeles, R., D. Leynaud, et al. (2006). "Back-analysis and failure mechanisms of a large submarine slide on the ebro slope, NW Mediterranean." Marine Geology **226**(3-4): 185-206.

Van Beek, L. P. H. and T. W. J. Van Asch (1996). The mobility characteristics of the Valette landslide. Seventh International Symposium on Landslides, Trondheim, Balkema.

Van Genuchten, P. M. B. (1988). Intermittent sliding of a landslide in varved clays. Proceedings of the 5th International Symposium on Landslides, Lausanne.

Vardoulakis, I. (2000). "Catastrophic landslides due to frictional heating of the failure plane." Mechanics of Cohesive-Frictional Materials **5**(6): 443-467.

Vardoulakis, I. (2001). Thermo-poro-mechanical analysis of rapid fault deformation. International Conference on Micromechanics of Granular Media, Sendai, Japan, Rotterdam: Balkema.

Vardoulakis, I. (2002a). "Dynamic thermo-poro-mechanical analysis of catastrophic landslides." Geotechnique **52**(3): 157-171.

Vardoulakis, I. (2002b). "Steady shear and thermal run-away in clayey gouges." International Journal of Solids and Structures **39**(13-14): 3831-3844.

Vardoulakis, I. (2003). "Dynamic thermo-poro-mechanical analysis of catastrophic landslides." Geotechnique **53**(5): 523-524.

Vardoulakis, I. and J. Sulem (1995). Bifurcation analysis in Geomechanics. Glasgow, Chapman & Hall.

Varnes, D. J. (1978). "Slope movement types and processes." Special report, Washington D.C.: Transportation research board, National Academy of sciences(176): 11-33.

Veveakis, E., I. Vardoulakis, et al. (2007). "Thermoporomechanics of creeping landslides: The 1963 Vaiont slide, northern Italy." Journal of Geophysical Research-Earth Surface **112**(F3).

Voight, B. and C. Faust (1982). "Frictional Heat and Strength Loss in Some Rapid Landslides." Geotechnique **32**(1): 43-54.

Voight, B. and C. Faust (1992). "Frictional Heat and Strength Loss in Some Rapid Landslides - Error Correction and Affirmation of Mechanism for the Vaiont Landslide." Geotechnique **42**(4): 641-643.

Wang, W. N., M. Chigira, et al. (2003). "Geological and geomorphological precursors of the Chiu-fen-erh-shan landslide triggered by the Chi-chi earthquake in central Taiwan." Engineering Geology **69**(1-2): 1-13.

Wen, B., S. Wang, et al. (2004). "Characteristics of rapid giant landslides in China." Landslides **1**(4): 247-261.

Whalley, W. B., G. R. Douglas, et al. (1983). "The Magnitude and Frequency of Large Rockslides in Iceland in the Post-Glacial." Geografiska Annaler Series a-Physical Geography **65**(1-2): 99-110.

Wibberley, C. A. J. and T. Shimamoto (2005). "Earthquake slip weakening and asperities explained by thermal pressurization." Nature **436**(7051): 689-692.

Wieczorek, G. F., M. Jakob, et al. (2003). Preliminary assessment of landslide-induced wave hazards: Tidal Inlet, Glacier Bay National Park, Alaska, U. S. Geological Survey Open-File Report 03-100.

Wilson, A. J., W. Murphy, et al. (2000). Some obsevations on the Geotechnics and movement of Large Volume Earth Flows in Alpine Regions. Proceedings of the 8th international Symposium on Landslides, Cardiff, Thomas Thelford.

Yueping, Y. (2008). Landslides in China - Selected case studies. Beijing, China Land Press.

Zhang, Z. Y., S. M. Chen, et al. (2002). 1983 Sale Mountain landslide, Gansu Province, China. Catastrophic Landslides: Effects, Occurrence, and Mechanisms. J. V. D. Stephen G. Evans**:** 149-163.

Zhongyou, L. (1984). Examples of rapid landslides in semi-rock strata. IV International Symposium on Landslides Toronto.

Zhou, Y. (2000). Research and treatment of Shazou Landslide, Sichuan. Proceedings of the 8th international Symposium on Landslides, Cardiff, Thomas Thelford.